The Effects Of Alloying And Grain Size On Fatigue Life Behavior, Cyclic Stress-Strain Behavior, and Microstructural Evolution Of Unalloyed Mg and A Mg-Al Alloy

by

Aeriel D. Murphy-Leonard

A dissertation submitted in partial fulfillment
of the requirements for the degree of
Doctor of Philosophy
(Materials Science and Engineering)
in the University of Michigan
2019

Doctoral Committee:

Professor John E. Allison, Chair
Professor Emeritus J. Wayne Jones
Professor Amit Misra
Associate Professor Veera Sundararaghavan
Professor Katsuyo Thornton

Aeriel D. Murphy-Leonard

aerielm@umich.edu

ORCID iD: 0000-0002-5822-5312

For all the women who have inspired me
especially,
Collin, Ruth, and Dornell

ACKNOWLEDGEMENTS

This dissertation would not be possible without the village of people who have showered me with love, support, and encouragement throughout graduate school. I will forever be thankful for each and every one of you!

First, I would like to thank God for all his many blessings and showing me favor even when I did not deserve it. My completion of this journey is a true testament of his unfailing love.

To my PhD advisor, Professor John Allison, I will never be able to thank you enough for your academic, emotional, and financial support and encouragement throughout my time as your student. I am beyond blessed to have had someone in my life who challenged me to be a better student, researcher, and leader. Thank you for always seeing the light in me when I was struggling to see it in myself. You will truly be missed. I owe a special thanks to my committee member, Professor Wayne Jones for his mentorship and both academic and emotional support throughout graduate school. I am also thankful for my other committee members: Professor Katsuyo Thornton, Professor Amit Misra and Professor Veera Sundararaghavan, their technical advice and guidance has been essential in the completion of my dissertation work. I would also like to thank Bruce Williams and all the other staff at Canmet Materials for providing the materials discussed throughout this dissertation.

My high energy diffraction experiments at the Cornell High Energy Synchrotron Source (CHESS) would not have been possible without the support of Dr. Darren Pagan, Dr. Armand Beaudoin, and Professor Matthew Miller. Thank you for the valuable discussions, help with experimental set-ups, and assistance in the analysis of experimental data gathered at CHESS. I also feel indebted to my groupmates, Dr. Tracy Berman and Dr. Qianying Shi for assisting me with my CHESS experiments for two years. I will forever be thankful for your commitment to the success of my research.

I owe many thanks to many fellow students and colleagues who made the Gerstacker lab a wonderful and positive work environment for many years: Dr. Qianying Shi, Dr. Tracy Berman, Dr. Alfred Okello, Dr. Jason Geathers, Dr. Vir Nirankari, Dr. Erin Deda, Dr. Anna Trump, , Dr. Jiashi Miao, Dr. Xianfeng Ma, Alan Githens, Zhihua Huang, Jacob Garves, Zhenjie Yao, and Duncan Greeley. I also owe a special thanks to John Lasecki for his technical assistance with equipment especially the MTS frames. My fatigue experiments would have not been possible without his help and valuable expertise.

I owe many thanks to my family for all their love and guidance. My achievements during my time at Michigan would not have been possible without the love, support, and sacrifices of my mom, Collin Lashley, who has dedicated her entire life to my success. Thank you for teaching me to be a warrior! I would also like to thank my dad, Artis Murphy, for his encouragement, love, and support throughout my life. I would like to recognize my grandmothers, Dornell Parker and Ruth Murphy, for always inspiring me to be a kind and dependable person. Thank you to my grandad for teaching me the importance of using my voice and staying true to myself. Thank you to my brothers Aquanta Parker and Kejuan Riley for lifting me up when I was down and allowing me to boss you around for 28 years!! I am extremely thankful for my niece and nephew, Erin and Grant Parker, for always being my sunshine on a cloudy day, teaching me responsibility, patience, and humility, and for being my daily inspiration.

I would like to thank my many close friends who have supported me through the highs and lows of graduate school. To my best friend and sister, Sheridan Wiggins, thank you for your love and friendship throughout the years. Thank you for keeping me sane and grounded when I was struggling and for believing in me when I couldn't believe in myself. I also owe special thanks to Lakaia Jackson for being the true definition of a best friend and sister and for all your encouragement throughout graduate school. I would also like to thank Dr. Ciara Sivels and soon-to-be Dr. Autumn Bullard for making graduate school a wonderful experience. WE MADE IT!!

Finally, I would like to thank my wonderful and supportive husband, Matt, for your patience, love, and understanding. Thank you for being a listening ear and my biggest fan. I am blessed to have you in my life and I am excited to start this next journey with you by my side!

TABLE OF CONTENTS

LIST OF TABLES

LIST OF FIGURES

LIST OF APPENDICES

ABSTRACT

Mg and Mg alloys are important materials in structural applications where light weighting is important since the material exhibits an excellent strength to weight ratio and has a lower density than alloys such as Al and Ti. The formation of these materials requires thermomechanical processing during which the material undergoes deformation and then subsequent annealing which leads to recrystallization and grain growth. Both of these mechanisms have a significant influence on the cyclic stress-strain response and the fatigue life during cyclic loading. Therefore, understanding the influence of grain size and alloying on the microstructural evolution that occurs during annealing and its effect on low cycle fatigue behavior is important for increased use of these materials in structural applications. The influence of grain size and alloying on the microstructural evolution that occurs during static recrystallization and grain growth and its effect on the mechanical behavior during fatigue is being investigated. It is widely understood that grain characteristics (e.g. size and crystallographic orientation) can have a significant effect on the mechanical behavior of metallic materials. The static recrystallization behavior of unalloyed Mg and Mg-4Al was characterized over a range of annealing temperatures. The electron backscatter diffraction grain orientation spread technique was used to quantify the level of recrystallization at various annealing times.

Recrystallization kinetics were characterized using the Johnson-Mehl-Avrami-Kolomogorov (JMAK) relationship and it was found that two sequential annealing stages exist. Stage 1 involves heterogeneous nucleation of recrystallization in regions with a high stored energy, including twins and grain boundaries. During Stage 2, recrystallization occurred predominately in the interior of deformed grains with incomplete recrystallization generally observed even at annealing times in excess of two weeks. Increasing the starting grain size in the unalloyed Mg condition led to a significant delay in recrystallization. The addition of Al had minimal effect on the recrystallization kinetics of Mg. To understand the influence of grain size and alloying on mechanical behavior, low cycle fatigue experiments using in-situ and ex-situ techniques were performed. The twinning and detwinning behavior of extruded fine-grained unalloyed Mg and Mg-4Al was investigated using in-situ high energy x-ray diffraction (HEXD) under displacement controlled, fully-reversed low cycle fatigue conditions. Measurements were conducted at three levels of applied strain. At cycle strains greater than 0.5%, tension-compression loop asymmetry was observed during cyclic loading which can be related to twinning during the compressive portion of the cycles followed by detwinning during the unloading (from peak compression) and tensile loading portions of the cycles. The twinning and detwinning were characterized by monitoring the evolution of x-ray diffractions peaks associated with the basal {0002} planes throughout a cycle. It was determined that the stress needed to initiate twinning during compression was independent of grain size and Al addition and that the stress needed for complete detwinning was closely related to the twin volume fraction. Ex-situ, strain-controlled LCF experiments were performed on both fine and coarse grained unalloyed

Mg alloys as well as Mg-4Al. It was also found that for a given total strain amplitude the fatigue life was slightly increased in the fine-grained unalloyed Mg condition.

CHAPTER 1
INTRODUCTION

In the U.S. automotive industry, the transition from conventional steel components to advanced light-weight materials has created exciting challenges and research pathways in structural materials science [1-3]. The transportation industry is responsible for 28% of the US energy consumption and is heavily dependent on petroleum sources [2]. A recent report by the US Department of Energy found that reducing the vehicle weight by 10% can lead to a 6-8% improvement of fuel efficiency [3]. The deployment of light-weight materials has the ability to improve fuel efficiency and energy consumption of automobiles and thus more research and development is needed. The use of light-weight materials in the automotive industry is limited by performance, manufacturability, and cost which is greatly influenced by microstructure (grain size, crystallographic texture) and materials properties (fatigue strength, fatigue lifetime) [1]. Magnesium (Mg) alloys, show great promise in vehicle weight reduction due to their lightness (two-thirds the density of Aluminum), good castability, and great machinability but have many limitations that need increased attention [1]. During thermomechanical processing of Mg, a strong basal texture is formed due in part to its lack of five independent slip systems. The strong basal texture generally leads to limited absolute strength, poor ductility, and poor room temperature formability of Mg and Mg alloys. Due to this lack of independent slip systems, mechanical twinning emerges as a dominant deformation mode, leading to pronounced texture development, differences in

tension and compression strength during fatigue, and a heterogeneous microstructure during thermomechanical processing. This complex deformation behavior makes it difficult to create computational models needed to predict materials properties and behavior which are imperative to shorten the time for alloy design. The limited absolute strength and ductility of these materials creates a challenge when replacing high strength aluminum and steel alloys in automobiles. For increased use in high-performing structural applications, wrought Mg alloys for use in components such as extruded profiles, forgings, and rolled sheets need to be developed which provide a higher strength and ductility.

The key metallurgical aspects for improving both strength and ductility of these materials are a homogeneous microstructure as well as a grain size and crystallographic texture that promotes uniform plastic deformation and weakens the basal texture formed during processing. The current work aims at aiding in the development of fatigue resistant wrought Mg alloys by improving the fundamental relationships between microstructure (texture, recrystallization and grain growth) and mechanical behavior (fatigue, cyclic stress-strain response). My first approach is to understand the texture development and nucleation and growth of grains that occur during static recrystallization (RX) by combining phase field simulations with experimental investigation including electron back scatter diffraction (EBSD) and optical microscopy. EBSD data provides information on grain size evolution, grain orientation, and texture evolution which can be related to recrystallization and grain growth as well as twinning. The second aspect of my research is to understand the influence of the microstructure (grain size and morphology, texture) on cyclic stress-strain response,

and lifetime by experimental investigation including low cycle fatigue as well as experiments that combine both synchrotron diffraction and fatigue experiments. In-situ synchrotron diffraction is a unique technique allowing the examination of real-time microstructural changes that occur during cyclic loading throughout the bulk material.

The development of accurate, fundamental relationships between the microstructure and mechanical behavior of Mg alloys is needed to increase their use in structural applications; and also build both computational and analytical models that help predict microstructure and materials properties of these alloys. If we can better understand the relationships between microstructure and mechanical behavior of magnesium, we can design and create workable Mg alloys needed to improve and advance the U.S. automobile industry.

The work presented in this document is a part of the Predictive Integrated Structural Materials Science (PRISMS) Center at the University of Michigan and focuses on the physical and mechanical metallurgy of Mg and Mg alloys during either thermomechanical processing or cyclic loading. The goal of the center is to develop a unique scientific platform to enable accelerated predictive materials science for structural metals through the integration of computational codes and experimental research. As such, the PRISMS Center is developing a framework and capability that represents the next generation of Integrated Computational Materials Engineering (ICME), that is, using integrated multi-scale models and experiments to accelerate the development of new ICME tools and materials. The center focuses on four important mechanisms in materials science: Precipitation Use-Case, Recrystallization Use-Case,

Tensile Behavior Use-Case and the Fatigue Use-Case. The research presented here is an important experimental component of the Recrystallization and Fatigue use-cases.

In the recrystallization use case, microstructural phenomena including recrystallization and grain growth are quantified as a function of processing parameters such as temperature and time using the Johnson-Mehl-Avrami-Kolomogorov relationship and parabolic grain growth equation, respectively. The experimental results from the processing-microstructure relationships are used parameterize crystal plasticity and phase field models to develop predictive computational tools. For the fatigue use case, deformation structures such as twinning are characterized during cyclic loading using in-situ synchrotron diffraction. Information including the stresses needed to initiate twinning and detwinning as well as the twin volume fraction can be quantified for many cycles or until the end of life. This enables us to quantitatively characterize the influence of twinning and detwinning on loop shape and the tension-compression strength asymmetry. Experimental data from both in-situ and ex-situ techniques are integrated into crystal plasticity and dislocation dynamics models to predict cyclic stress-strain response and lifetime during cyclic loading.

The overall goal of this dissertation work was to develop a fundamental understanding of the influence of microstructural features on the mechanisms of recrystallization, grain growth, low cycle fatigue behavior, and the cyclic stress-strain response in unalloyed Mg and a Mg-Al alloy. The specific objectives of this dissertation work were to:

1. Characterize the influence of deformation mechanisms such as twinning, detwinning, and dislocation slip on the cyclic stress strain behavior in

unalloyed Mg and Mg-4Al using in-situ synchrotron diffraction and post mortem electron back scatter diffraction;

2. Determine the influence of aluminum addition and grain size on cyclic stress strain behavior and low cycle fatigue behavior in magnesium;
3. Determine the effects of annealing conditions including temperature and time on recrystallization and grain growth kinetics in extruded and as-cast unalloyed Mg and Mg-4Al, respectively;
4. Identify the microstructural features such as grain size and twinning that control the kinetics of recrystallization in unalloyed Mg and Mg-4Al.

Chapter 2 provides a review of the literature that is relevant to the present work including studies involving the fatigue behavior, recrystallization kinetics and grain growth behavior of various Mg alloys as well as a discussion on advanced in-situ characterization techniques. Chapters 3, 4, 5, 6, and 7 represent studies prepared for publication, resulting in some repetition of background information provided in each chapter. The results of a study using in-situ high energy x-ray diffraction during low cycle fatigue on unalloyed Mg to quantify twinning and detwinning as well as the CSS response is discussed in Chapter 3. Chapter 4 represents a detailed description of a similar study using Mg-4Al and a comparative discussion on the influence of Al on twinning-detwinning and CSS behavior. A detailed study of the effect of Al addition and grain size on CSS and LCF behavior during ex-situ low cycle fatigue experiments is outlined in Chapter 5. The influence of alloying and grain size during recrystallization and grain growth are outlined in Chapters 6 and 7. Chapter 6 presents a thorough investigation on the static recrystallization behavior and kinetics of Mg-4Al and

unalloyed Mg. The influence of alloying on grain growth behavior is discussed in Chapter 7. Finally, conclusion and recommendations for future work are outlined in Chapter 8.

References

1. J. Hirsch, T. Al-Samman, Superior light metals by texture engineering: optimized aluminum and magnesium alloys for automotive applications, Acta Materialia 61 (2013) 818-843
2. F.A Mirza, D.L. Chen, Fatigue of rare earth containing Mg alloys: a review, Fat. Fract. Eng. Mater. Struct. 37 (2014) 831-853
3. W.J. Joost, Reducing the vehicle weight and improving US energy efficiency using ICME, JOM 64 (2012) 1032-1038

CHAPTER 2
LITERATURE REVIEW AND BACKGROUND

In this chapter, a review of the literature relevant to understanding the goals and objectives outlined in Chapter 1, the experimental methods and techniques, and the results of the current work is discussed. Section 1 describes the deformation processes of magnesium. Section 2 provides a general description of fatigue focusing on low-cycle fatigue. In Section 3, the fatigue properties observed in magnesium are discussed specifically the cyclic stress-strain response and the role of microstructure and twinning in fatigue behavior as well as advanced characterization techniques used to study this behavior. Finally, Section 4 describes the concepts of recrystallization and grain growth focusing on the role of microstructure on the kinetics in magnesium.

2.1. Deformation In Mg and Mg Alloys

2.1.1 Dislocation Slip

In Mg alloys there are four active slip systems. The most dominant and easiest to activate is <a> slip on the basal (0001) plane where the critical resolved shear stress (CRSS) is 0.5-1 MPa in unalloyed Mg [1-2]. The other slip systems -- prismatic <a> slip, pyramidal <a> slip, and pyramidal <c+a> slip -- require much higher stresses to activate during deformation [3]. The activation of certain slip systems depends on the initial texture of the material. During c-axis compression basal slip alone cannot accommodate plastic deformation and requires the activation of non-basal slip systems [4]. Transmission Electron Microscopy (TEM) studies have shown that during c-axis

compression plastic deformation is accommodated by pyramidal <c+a> dislocations with Burger's vectors along the$\langle 11\bar{2}3\rangle$ direction [5-7]. In Mg, <c+a> dislocations either glide on the $\{10\bar{1}1\}$ pyramidal I slip planes or $\{11\bar{2}2\}$ pyramidal II slip planes [4]. Studies have shown that c-axis deformation is accommodated by glide of pyramidal II dislocations [4,6,8-9]. However, Tang et al showed that <c+a> dislocations nucleate and glide on pyramidal I planes but can cross-slip to pyramidal II planes at higher stresses [10]. A Mg single crystal study by Xie et al found that during c-axis compression deformation was dominated by pyramidal II dislocation slip [4].

During compression normal to the c-axis, straining is accommodated by deformation twinning which is discussed in greater detail in the next section. But during tension, the orientation of the lattice is hard with respect to basal slip and plastic deformation is accommodated by the harder deformation mechanisms such as prismatic <a> and pyramidal <c+a> dislocation slip as well as compression twinning resulting in a high hardening rate until the maximum tensile stress is reached [10]. In these cases, both slip and twinning influence the macroscopic stress-strain response in the material and have an influence on the fatigue behavior which will be discussed later.

2.1.2 Twinning

In hexagonal close packed (HCP) metals and alloys, twinning plays an important role during deformation, especially in Mg alloys where non-basal slip systems are not easily activated [11-12]. In most cases, the initial texture and c/a ratio influence the twinning behavior of these materials. As stated earlier, Mg has four slip systems where pyramidal <c+a> slip allows for straining along the c-axis but is difficult to activate at room temperature [13,14]. Therefore, in order to satisfy the Von Mises requirement for

five independent deformation systems, secondary deformation mechanisms such as mechanical twinning contribute as the fifth deformation mode and allow for straining along the c-axis at room temperature.

The mechanism of twin nucleation and expansion has been studied using both experimental and computational techniques [15-24]. Several studies on Mg, Zr, and Ti have found that twins more than likely nucleate from grain boundaries since the formation of the twin nucleus and its growth require both large defect structures and high internal stresses [18,20-21]. Using molecular dynamics simulations, Wang et al found that a stable $\{10\bar{1}2\}$ nucleus was only formed when the multiple twinning dislocations it contained glided simultaneously [15]. The stacking of multiple twinning dislocations requires separation of defects with a Burger's vector much larger than that of the twinning dislocation into a set of boundary dislocations [15,23]. Since grain boundaries including triple and quadruple joints contain large internal stresses they can support the nucleation and expansion of twins [23]. Once a twin is formed, a new crystallographic orientation is introduced within the twin and into the grain [24]. As a result, the slip systems preferred within the twin can be different than those of the parent grain [24]. Because of this twin boundaries act as barriers to dislocation motion and depending on the orientation of the slip system and the twin boundary, the obstacle can be stronger for one slip system than another [24-25]. This changes the localized stress state generated within the twin and the surrounding matrix and can create a stress concentration within the twin proximity [24-25]. These highly localized stresses produced by twins, influence recrystallization kinetics where stored energy is the driving force and fatigue and fracture behavior, which will be discussed in future sections.

In cyclic loading of Mg alloys both twinning and slip work together to accommodate plastic deformation [26]. However, the mechanisms for nucleation and growth of lattice dislocations and twinning dislocations are different and influence the stress state in the material [26]. It is understood that the activation of lattice dislocations is easier than that of twinning dislocations, but the mobility of twinning dislocations is much higher [15, 27-29]. As a result, plastic deformation within twins is controlled by shearing of twinning dislocations while that of the matrix is controlled by dislocation slip [26]. This leads to plastic deformation being higher in the twin than in the matrix resulting in the stress state near the growing twin and that far away from the twin to be different. In other words, the shear stress near the growing twin has an opposite sign of the shear stress in the matrix far away from the twin [26]. The opposite sign stress near the twin is referred to as a back stress [26]. The ability for the twin to grow is influenced by this back stress and its growth is slowed down significantly if the back stress continues to increase [26]. Initiating slips in the opposite direction of the twinning shear or the external load can reduce the magnitude of the back stress and promote further twin growth [26].

In Mg alloys, there are three common twinning modes: the primary $\{10\bar{1}2\}\langle 10\bar{1}1\rangle$ extension twins, $\{10\bar{1}1\}\langle 10\bar{1}2\rangle$ compression twins, and double twins that form when compression twins undergo tension twinning [30-31]. Both extension twins and compression twins reorient the crystal lattice differently. Extension twins reorient the crystal lattice by 86° about the $\langle 11\bar{2}0\rangle$ axis while compression twins result in a 56° rotation around the $\langle 11\bar{2}0\rangle$ axis. Depending on the twinning mode the twin lamellae can

vary in size and abundance. In Mg alloys extension twins are generally thick, abundant, and readily observed while compression twins are thin, scarce, and hard to detect. The c/a ratio determines whether the dominant twinning mode will be tensile or compressive [32]. In unalloyed Mg and Mg alloys where the c/a ratio of 1.62 is less than the ideal value of 1.633, {10-12} <10-11> extension twinning is the dominant deformation mode, where extension along the c-axis can be accommodated, but not contractions along that same direction [33-34]. Due to this, during mechanical loading the tensile yield strength is significantly higher than the compressive yield strength [35] producing a Bauschinger effect [35-44].

2.1.3 Detwinning

The initial texture also influences deformation in Mg and Mg alloys [12]. In most wrought Mg alloys, the initial texture places the c-axis in most grains normal to the working direction, where during compression along this direction extension twinning is activated but not during tension along the same axis [12]. As stated previously, during favorable loading extension twinning causes an 86.3 reorientation of the crystal lattice. Thus, during subsequent reversed loading or unloading, detwinning of twinned regions can occur and the basal pole is reoriented from the twin back to the matrix [45]. In other words, twinned regions may disappear and/or become narrower [45]. Detwinning is mainly controlled by the migration of twin boundaries into the twins via glide of twinning dislocations, leading to a propagation of the parent grains into twinned grains [46]. Wu et al showed using grain mapping via in-situ synchrotron diffraction that during detwinning the parent grain was completely recovered via the migration of twinning dislocations from an untwinned region into a twinned region [45]. They also found that

the reoriented grain had a different lattice orientation that the parent grain. Similar studies have shown that the orientation after detwinning is complete, is hard with respect to basal slip and demands the activation of harder non-basal dislocation slip or compressive twinning [47]. It is also understood that detwinning requires a lesser activation stress than twinning since the twin already exists and no nucleation is needed [46]. Detwinning also requires a lower stress than that needed to cause growth of the twin. This is because the back stress formed in the alloy matrix during twin formation is an additional driving force for detwinning [48].

2.2. Fatigue

Fatigue is the failure of a material due repeated cycles of applied load. It is understood that materials subjected to cyclic loading will fail at stresses and strains much lower than those needed to cause failure under a single application of load [49]. This has made fatigue an important topic in aerospace, automobile, naval, and other applications where structural materials are heavily used [49].

Fatigue normally progresses in different stages: 1). Crack-free stage, 2). Crack nucleation/initiation, 3). Crack growth, and 4). Coalescence of cracks. During the crack-free stage dislocations move and/or are generated leading to cyclic softening or hardening [49]. As the dislocation density increases slip bands form, which become sites for crack initiation. During the crack-growth stage, short cracks advance throughout the material [49]. How the cracks propagate is heavily dependent on the microstructure (grain boundaries, precipitates, and orientation of basal planes. Once microscopic cracks grow and coalesce into dominant cracks, failure eventually occurs in the material [49].

Low-cycle fatigue (LCF) occurs at cycles less than 10^5 under conditions where the strain and stress amplitudes exceed the elastic limit of a material [49]. It is usually performed to study the evolution of plastic deformation mechanisms throughout the entire fatigue lifetime and gives insight to the cyclic stress-strain response of a material during the different stages of loading [49].

LCF experiments can be performed under load-controlled or strain-controlled conditions but in most cases strain-controlled conditions are used. This is because in structural components, plastic deformation is concentrated in specific areas due to discontinuities, notches, and sharp corners leading to build up of plastic strain in these regions eventually leading to the initiation of cracks and crack growth resulting in fracture [49]. During cyclic loading, deformation accumulates throughout the entire volume of the material and the stress-strain response varies from cycle to cycle. The materials response to this deformation is known as cyclic stress-strain (CSS) behavior [49]. The CSS behavior is usually characterized as cyclic hardening or cyclic softening. The CSS behavior is controlled by Interactions between dislocations and microstructural features such as grain boundaries and twin boundaries as well as other dislocations. As cycling proceeds, the dislocation density may increase resulting in hardening. During softening, dislocations interact with each other, annihilate, and rearrange during testing. The CSS behavior can be influenced by many factors such as grain size, cold working, and precipitate size and volume fraction [49].

Low-cycle fatigue data is usually plotted as a stress-strain hysteresis loop, which is shown in Figure 2.1 [49]. Figure 2.2 shows a material experiencing cyclic softening, where the stress is decreasing from cycle to cycle and a material experiencing

hardening where there is an increase in stress from cycle to cycle [49]. Low cycle fatigue parameters are quantified using the equation for the total strain amplitude [49]. The total strain amplitude can be expressed in terms of the elastic strain amplitude $\left(\frac{\Delta\varepsilon_e}{2}\right)$ and plastic strain amplitude $\left(\frac{\Delta\varepsilon_p}{2}\right)$.

$$\left(\frac{\Delta\varepsilon_t}{2}\right) = \left(\frac{\Delta\varepsilon_e}{2}\right) + \left(\frac{\Delta\varepsilon_p}{2}\right) \qquad [1]$$

The elastic strain amplitude can be expressed as the Basquin equation

$$\left(\frac{\Delta\varepsilon_e}{2}\right) = \frac{\Delta\sigma}{2E} = \frac{\sigma_f'\left(2N_f\right)^b}{E} \qquad [2]$$

and the second term of equation 2 is known as the Coffin-Manson (CM) relationship

$$\left(\frac{\Delta\varepsilon_p}{2}\right) = \varepsilon_f'\left(2N_f\right)^c \qquad [3]$$

Therefore equation 2 can be rewritten as a function of these relationships.

$$\left(\frac{\Delta\varepsilon_t}{2}\right) = \frac{\sigma_f'\left(2N_f\right)^b}{E} + \varepsilon_f'\left(2N_f\right)^c \qquad [4]$$

where σ_f' is the fatigue strength coefficient, N_f is the fatigue life, b is the fatigue strength exponent, E is the Young's Modulus, ε_f' is the fatigue ductility coefficient and c is the fatigue ductility exponent. The fatigue strength exponent can be determined by plotting $\log\frac{\Delta\varepsilon_e}{2}$ vs. $\log N_f$ and measuring the slope of the line. The fatigue ductility exponent can be calculated by plotting the $\log\frac{\Delta\varepsilon_p}{2}$ vs. $\log N_f$ and measuring the slope of the line.

2.3. Fatigue in Magnesium

The fatigue behavior of wrought Mg and Mg alloys is characterized by a strong in-plane tension-compression (T-C) asymmetry [43]. This anisotropic behavior has been attributed to the limited number of independent slip systems as well as deformation

twinning and detwinning on the $\{10\bar{1}2\}$ planes along the $\langle 10\bar{1}1\rangle$ directions [15-24]. During cyclic loading of Mg alloys three dominant deformation mechanisms govern the stress-strain hysteresis loop: 1). Slip dominated deformation, 2). Twinning dominated deformation, and 3). Detwinning dominated deformation. During initial tension, the slip-dominated mode is active and the flow curve resembles a normal concave down shape with a smooth elasto-plastic transition as well as a high yield stress [50-53]. When the material is loaded in compression, the twinning mode is activated and the flow curve exhibits an atypical concave up shape with an abrupt elasto-plastic transition followed by a low hardening rate due to twinning as well as a lower yield stress [47,50,52]. Lastly, when the load is reversed deformation is dominated by detwinning and the flow curve resembles a normal tensile stress-strain curve [50]. Once detwinning is exhausted, dislocation motion is much easier and the plastic flow is comparable to that of the slip mode [50]. In most cases, twins remain in the material at the end of a cycle and detwinning is exhausted upon reloading in tension. During tensile reloading the stress at which detwinning is exhausted and post-detwinning plastic flow begins is represented by an inflection point in the flow curve [47]. In other words, within a fatigue cycle, twinning and detwinning occur alternately while slip works with both twinning and detwinning to accommodate plastic deformation [15-24].

The T-C asymmetry exists because the stresses needed to initiate twinning are higher than those needed to promote detwinning, which was discussed in Section 2. The alternate occurrence of twinning and detwinning leads to an abnormally shaped hysteresis loop where the tensile yield stress is higher than the compressive yield stress [35-42,44,47,50]. A comparison of between a symmetric (red) and abnormal (blue)

hysteresis loop is shown in Figure 2.3 [37]. Q. Yu et al reported an abnormal hysteresis loop during LCF of unalloyed Mg where the stresses in tension were much higher than those in compression [37]. Begum et al also showed that during LCF of the Mg alloy, AZ31 the hysteresis loop was asymmetrical at the beginning of fatigue life with pronounced yielding in compression [38].

Other studies have shown that the asymmetry in Mg and Mg alloys is linked to the total strain amplitude and at lower strain amplitudes the asymmetry is greatly reduced [36-39]. Yu et al found during LCF of unalloyed Mg that an increase in twinning at high strain amplitudes (1.0%) led to an asymmetric loop shape while at lower strain amplitudes (0.12%) where slip was the dominant deformation mode the loop shape was symmetric (Figure 2.4) [36]. Begum et al showed that the T-C asymmetry decreased with strain amplitudes during LCF of AZ31 and related this behavior to a reduction in twinning [38]. At a strain amplitude of 0.1% and 0.2% the ratio between the maximum stresses in both tension and compression was almost one and at 0.6% the ratio was 0.64 [39]. This can be seen in the hysteresis loops in Figure 2.5 [39].

The tension-compression asymmetry caused by twinning-detwinning can be reduced by adding alloying elements, especially rare-earth (RE) elements [40]. RE elements help produce random textures, which decreases texture intensities and therefore allows basal slip to occur more readily in grains in which the resolved shear stress is appropriately aligned [54-55]. Yang et.al. found during HCF of a RE Mg alloy, GW123K the yield asymmetry was reduced when compared to AZ31 which was related to the random texture produced in the RE alloy [56]. The pole figures for both allows can be seen in Figure 2.6, where AZ31 displayed a strong basal texture [56].

Studies on LCF of RE Mg alloys such as Mg-10Gd-3Y-0.5Zr, Mg-3Nd-0.2Zn-0.5Zr, and Mg-8Gd-3Y-0.5Zr found that a weakened basal texture resulted in a reduction of the tension-compression asymmetry [40]. Mirza et.al. found that the tension-compression asymmetry was reduced and fatigue strength was improved in the RE containing alloy, GW103K when compared to AM30 [54]. A comparison of the loop shapes is shown in Figure 2.3, where in AM30 the loop resembles the shape associated with twinning and detwinning while the loop for GW103K is stable or the stresses reached in tension and compression are the same [54].

2.3.1 The Influence of Alloying

It is well known that basal <a> slip is the most common deformation mode in Mg due to its low CRSS [1-2]. As a consequence, a strong basal texture generally develops during deformation processes such as extrusion and rolling [57-59]. As stated earlier, this leads to a strong in plane tension-compression asymmetry as well as low formability. In order to increase the use of Mg alloys in structural applications alloying elements are added to weaken the basal texture and improve both strength and ductility [60-64]. Aluminum is one of the most commonly used alloying elements in Mg due to its favorable effects on solid solution strengthening and precipitate hardening [57,65]. Aluminum increases the CRSS for basal slip while also lowering that needed for prismatic slip resulting in a weakened basal texture and an improvement in the both strength and ductility when compared to unalloyed Mg [66]. A study by Akhtar et al found that as the Al concentration increased the yield strength was increased but at the same time the strain hardening rate was reduced [66]. Caceres et al found that the yield strength, hardness and flow strength increased with increasing Al concentrations

between 1-8% (Figure 2.7) [67]. The increase in strength and hardness in solution treated Mg-Al alloys arises from interactions between solute atoms and dislocations where they reduce the mobility of dislocations during deformation [67].

Alloying elements including Al and Zn impact twinning mechanisms in Mg by promoting twin nucleation but preventing it from further growth [48]. Aluminum increases the c/a ratio allowing for easy formation of extension twins but Al atoms suppress twin boundary mobility preventing further growth [48]. Christian et al and Han et al found that the twinning shear stress decreased as the Al content increases and related the observed behavior to an increase in the c/a ratio allowing for easy formation {10-12} extension twins [68-69]. Other studies have found similar behavior in Mg-Zn alloys where the growth of twins was significantly restrained when compared to unalloyed Mg [48,70]. Al also impacts the mechanisms of detwinning by stabilizing twin boundaries [71]. A cyclic compression study on extruded unalloyed Mg and AZ31 by Li et al found that twinning was more stable in AZ31 and the inelastic recovery during detwinning was lowered when compared to unalloyed Mg due to Al and Zn suppressing the mobility of extension twin boundaries [71].

Precipitates can also affect twinning in Mg alloys because it is difficult for a twin boundary to migrate through a high density of precipitates [72-73]. In AZ80, the presence of $Mg_{17}Al_{12}$ precipitates decreased the tension-compression asymmetry when compared to the solution treated condition, shown in Figure 2.8 [72]. Stanford and Barnett found in aged Mg-5%Zn alloy, the twin size and volume fraction were reduced which decreased the tension-compression yield asymmetry [74].

L. Rettberg found that a T6 heat treatment improved the cyclic yield strength of an AZ91 alloy [75]. HCF Studies in AZ80 revealed that a T6 heat treatment decreased the fatigue strength of the material [72,76]. Uematsu et. al found that AZ80 had higher fatigue strength than AZ61 due to the higher Al content allowing precipitation of more $Mg_{17}Al_{12}$ particles [76]. Sajuri et. al found that the addition of Mn to AZ61 at low concentrations improved the fatigue strength, but at high concentrations, the Al-Mn intermetallic served as crack initiation sites decreasing the fatigue strength of the alloy [77].

2.3.2 The Influence of Grain Size

It is well understood that grain size influences the mechanical behavior of materials [78-82]. The well-known Hall-Petch relationship is widely used to relate the grain size to the yield strength of a material [82]. The relationship shows that as the grain size decreases the yield strength of the material increases [82]. Grain size also has an effect on twinning behavior in Mg alloys [20-21,23,24,60,83]. Two studies found that the energy required to form twin interfaces was higher in a fine-grained Mg alloy and the tension-compression yield asymmetry decreased with degreasing grain size [60,83]. Mirza et.al. found that slip was the dominant deformation mode in a fine-grained GW103K due to suppression of twinning resulting in a near-symmetric hysteresis loop [41]. Stanford and Barnett found that during compression tests of unalloyed Mg and Mg-Zn alloys the twin activation stress increases with decreasing grain size [84]. Therefore, grain size effects on deformation in Mg has been studied extensively [20-21,23,24,60,83].

Studies involving molecular dynamics (MD) simulations and experimental techniques including EBSD and optical analysis have shown that grain size has an effect on the number of twins produced within an individual grain [20-21,23,78-82] and hypothesize that as the surface area of the grain boundary increases the likeliness that grain boundary dislocations will encounter a high stress state needed to cause disassociation into twinning dislocations, form a stable twin nucleus, and cause initial expansion increases [20]. In a study by Beyerlein et al using both MD simulations and EBSD (Figure 2.9) it was found that the number of twins nucleated per grain in unalloyed Mg increases with grain size where it increased from 5 for a grain area of 100μm^2 to 17 for a grain area of 500μm^2 [20]. Capuolongo showed similar results for another hcp metal, Zr [85]. Another study by Beyerlein et al showed that smaller grains were just as likely to form at least one twin as large grains [23]. It has also been shown that the twin thickness is independent of grain size [20]. Dislocation slip is also influenced by grain size [20,23]. As the grain size increases the free mean path for dislocation pile ups becomes larger [86]. Therefore, the deformation due to dislocation slip is more likely as the grain size increases [86].

In terms of cyclic loading, understanding how twinning and dislocation slip change with grain size helps understand how the cyclic stress-strain response varies with grain size. Twins contribute to hardening by providing obstacles to dislocation motion [12,82]. This arises since twinning reorients the lattice to a hard-crystallographic orientation that inhibits dislocations from passing through the twin front which can lead to high hardening rates within the twin matrix [82]. Therefore, coarse grain materials may experience higher stress amplitudes or more pronounced hardening than fine grain

materials since the twin boundary surface area is higher. Two studies found that the energy required to form twin interfaces was higher in a fine-grained Mg alloy and the tension-compression yield asymmetry decreased with degreasing grain size [60,83]. Li et al found that during fatigue of both a coarse grained NZ30 Mg alloy and fine grained NZ30K Mg alloy, the stress amplitude of the coarse grain sample increased significantly while that of the fine-grained specimen remained constant with cycling [87]. Mirza et.al. found that slip was the dominant deformation mode in a fine-grained GW103K due to suppression of twinning resulting in a near-symmetric hysteresis loop [41]. This is also shown in other metals. Mahato et al found during LCF of pure copper that the saturated mean stress was higher in the coarse grain condition when compared to the fine grain condition and related the observed behavior to an increase in twin density in the coarse grain condition [88].

2.3.3 In-Situ Fatigue Using Synchrotron Diffraction and Neutron Irradiation

In recent years, neutron scattering has been used to study the twinning-detwinning behavior of wrought Mg alloys during cyclic loading [12,43,81,89-93] while few studies have used high energy x-ray diffraction (HEXD) using synchrotron diffraction [46,51] to study this behavior. Neutron irradiation has relatively low fluxes and intensities and therefore, has many limitations when studying rapid time-dependent processes such as fatigue [94]. Due to these limitations, in practice, many in-situ fatigue experiments involving neutron scattering are paused in order to measure a diffraction pattern [94]. In contrast, HEXD of Mg sample in a transmission geometry may be conducted with relatively short collection times, which allows for studying phenomena in-situ (i.e. fatigue). In fatigue, HEXD provides a means of understanding the behavior

of the bulk material throughout an entire cycle in real time under realistic conditions without pausing the cyclic loading [94].

Both neutron scattering diffraction and HEXD are superior to surface techniques such as electron back scatter diffraction (EBSD) because they allow for the entire volume of a material to be examined in order to understand phase transitions and texture evolutions [94-95]. Behavior may be assessed with minimal impact of the relaxation of kinematics present at the surface. Gharghourri et al used neutron diffraction and found that during cyclic loading, twinning occurred during compression followed by detwinning during the reversal [89]. An in-situ neutron scatter study by Wu et al also found that twinning-detwinning alternates during cyclic loading in ZK60A magnesium alloy [12]. Studies of AZ31 using synchrotron radiation have addressed the texture evolution of samples deformed by ex-situ techniques [43], and the twinning, detwinning, and lattice reorientation within an individual grain during strain reversal of a single cycle. In an in-situ neutron experiment by W. Wu et al, it was found that near the soon before failure extension twinning became less dominant and deformation proceeded by dislocation slip in AZ31B Mg alloy [90].

2.4. Annealing: Recovery, Recrystallization and Grain Growth

Annealing is a heat treatment process used to increase the formability of a deformed material by changing properties such as ductility, toughness, and hardness Annealing is composed of three stages: 1). Recovery, 2). Recrystallization (RX), and 3). Grain Growth (GG) [96]. During recovery, mechanical properties are partially restored to their pre-deformation values by lowering the dislocation density of the material. This occurs through dislocation annihilation where which dislocations of opposite signs on

the same glide plane move towards each other. During recovery dislocations can also rearrange themselves into cell structures of sub grains separated by low angle grain boundaries to reduce the stored energy in the material. Factors such strain (deformation), temperature, solute concentration, and stacking fault energy (SFE) influence the kinetics of recovery [96]. Recovery occurs more easily as the annealing temperature increases. As with recrystallization the driving force for recovery is stored energy and in cases where the material is heavily deformed the driving force for recrystallization is higher and it is harder for recovery to occur [96].

The second stage of annealing is recrystallization. RX occurs when strain energy stored in the form of dislocations is released promoting the nucleation and growth of new strain-free grains into the deformed microstructure. Recrystallization is usually divided into two regimes: nucleation and growth. Nucleation occurs when strain-free nuclei form in a deformed region. Nucleation usually occurs at grain boundaries and triple junctions because strain energy is higher at these locations [96]. Most studies show that nucleation occurs by strain-induced grain boundary migration (SIBM). During SIBM, a pre-existing grain boundary bulges out leaving behind a strain-free region. The driving force for SIBM is the difference in dislocation density on opposite sides of the boundary [96-97].

The third and final stage of annealing is grain growth where larger grains grow at the expense of smaller grains and grain boundaries assume a low energy configuration. The driving force for grain growth is the reduction of energy which is stored in the form of grain boundaries [96]. In the next sections, the concepts of both recrystallization and grain growth will be discussed in detail.

2.4.1 The Concepts of Recrystallization

Recrystallization occurs when strain energy stored in the form of dislocations is released promoting the nucleation and growth of new, strain-free grains [96]. The recrystallization temperature is defined as the temperature at which a material becomes fully-recrystallized. There are two types of recrystallization: Dynamic, which occurs during hot deformation and Static, which occurs during annealing after deformation. In this thesis work, only static recrystallization was studied.

Recrystallization is controlled by five laws [96]:

1. A minimum deformation is needed to initiate RX because the driving force for RX is strain energy;
2. At a certain RX volume fraction the temperature at which RX occurs decreases as the annealing time increases;
3. The RX temperature decreases as strain increases because the driving force for RX increases as the plastic deformation increases. Therefore, nucleation and growth will occur at a lower temperature in heavily deformed material;
4. The RX'd grain size depends on the amount of deformation because in a heavily strained material there will be more nuclei per unit volume producing a finer starting grain size;
5. At a given strain, the RX temperature is affected by the starting grain size and the deformation temperature. This is because in a coarse-grained material there are fewer sites for nucleation leading to a slower RX process, therefore a higher temperature is needed to initiate RX.

Recrystallization is influenced by many factors such as temperature, solute concentration, starting grain size, and deformation mechanisms such as twins and shear bands. Recrystallization is a thermally activated mechanism and as the annealing temperature increases grain boundary migration is increases and therefore, recrystallization occurs more quickly [96]. Chao et al found that for a constant strain, recrystallization increased with temperature in the Mg alloy, AZ31 which is shown Figure 2.10 [98]. Recrystallization kinetics are also influenced by the deformation temperature [96]. An increased deformation temperature increases the driving force for grain boundary migration leading to an increase in dynamic recovery and recrystallization during high temperature deformation. This leads to a smaller driving force for any static recrystallization during post-deformation annealing [96].

The amount of deformation (strain) also influences the recrystallization kinetics during annealing [96,99]. The amount of pre-strain applied to the material before annealing is directly related to the dislocation density. Therefore, a minimum amount of deformation is needed to initiate the nucleus and provided a dislocation density necessary for continuous growth [96]. The effect of pre-strain on recrystallization kinetics is shown in Figure 2.11, where the recrystallization kinetics increases with the amount of pre-strain [96]. The amount of fractional hardening can be related to recrystallization [99]. Dislocations increase the hardness of a material, as RX progresses the material softens decreasing the hardness of the material. As the amount of deformation increases, the recrystallized grain size decreases because at higher strains more nuclei per unit volume are created [100].

The starting grain size is important during recrystallization. It is generally accepted that a fine-grained material will recrystallize more rapidly than a coarse-grained material (Figure 2.12), this is because grain boundaries are favored nucleation sites during recrystallization and their amount is increased in fine grained materials [96]. Inhomogeneity's that form during deformation such as shear bands and twins are more readily formed in coarse grained material [96]. These deformation structures can also serve as nucleation sites during annealing leading to a non-constant nucleation and growth rate [96].

The solute concentration also has an impact on recrystallization kinetics during annealing. It is well understood that solutes can reduce the mobility of grain boundaries during recrystallization [101-107]. This phenomenon is known as solute drag where solute atoms exert a force on grain boundaries as they migrate decreasing their mobility [106]. Kwon et al found that the addition of Nb in C-Mn steels during static recrystallization led to a decrease in recrystallization kinetics when compared to the Nb free material (Figure 2.13) [107].

2.4.2 Constitutive Recrystallization Modeling

Empirical constitutive models have been developed to describe microstructural changes that occur during recrystallization. One of the most widely used models is the Johnson-Mehl-Avrami-Kolmogorov model that is described by equation 5 [96]. The JMAK model can be used to calculate the activation energy for recrystallization and also parameters such as the Zener-Holloman parameter which is used to describe dynamic recrystallization. The JMAK model assumes a random distribution of nucleation sites and that grains grow in 3-dimensions [92, 96,99,108].

$$X = 1 - \exp\left[-0.693\left(\frac{t}{t_{0.5}}\right)^{n}\right] \qquad [5]$$

where X is the fraction recrystallized, β is a material constant, t is the annealing time, $t_{0.5}$ is the time at 50% recrystallization, and n is the Avrami exponent. The Avrami exponent was measured to be three, assuming that nucleation and growth rates remain constant during RX and that all nucleation is complete at the start of recrystallization. In most cases, n is less than the ideal value of three. This reduction in the Avrami exponent is due to a non-constant growth rate during recrystallization. The growth rate can be influenced by recovery, inhomogeneity in deformation, and a non-random distribution of nuclei [96]. The inhomogeneity in stored energy in a material causes nucleation and growth to occur in areas of high stored energy first and then in regions of low stored energy. In regions where the stored energy is low the driving force for RX is reduced which slows down the growth rate [96].

A non-random distribution of nuclei allows for nuclei to cluster in areas of high stored energy and along grain boundaries. During RX, the close proximity causes new grains to impinge on each other as they grow. This impingement slows down the growth rate leading to a lower Avrami exponent [96]. Avrami exponent can be determined by plotting ln[ln(1/1-X)] vs. ln (t) and fitting a straight line to determine the slope, n. The activation energy for recrystallization Q_{REX}, can be determined using an expression developed for $t_{0.5}$ shown in equation 6 [6,23-24].

$$t_{0.5} = A\varepsilon^{p}\dot{\varepsilon}^{q}exp\left(\frac{Q_{REX}}{RT}\right) \qquad [6]$$

The slope of a fit line to the plot for log $t_{0.5}$ vs. 1/RT is equal to the activation energy for RX. The activation energy for RX depends on strain and composition. Using the same

model, Beer. et. al. found the activation energy for recrystallization of AZ31 to be 200 kJ/mol, which is higher than the activation energy for self-diffusion of Mg (135 kJ/mol) [99].

2.4.3 Static Recrystallization In Mg and Mg Alloys

Similar to fatigue, mechanical twinning plays an important role in recrystallization kinetics in Mg and Mg alloys. In addition to grain boundaries, twins and twin boundaries serve as nucleation sites and therefore can have profound effects on the rate of recrystallization. Several studies have shown that twins and twin boundaries serve as dominant nucleation sites during recrystallization of Mg alloys [96,109-117]. Twinning results in highly localized strains which presumably lead to preferential nucleation of recrystallized grains [118]. Once twinning has ceased, the vicinity near the twin is reoriented preventing dislocations from passing through the twin [119]. This leads to build-up of dislocations around twin boundaries causing work hardening as well as a stress concentration along the boundary [119-121]. Guan et al found that double twins and double twin-grain boundary intersections were preferential nucleation sites during static recrystallization of the rare-earth magnesium alloy WE43 (Figure 2.14). They also reported that tension twins did not recrystallize during annealing and were instead consumed by neighboring grains during grain growth [113]. A study by Su et al in AZ31 found that during the initial stages of recrystallization, small, recrystallized grains were found only in the vicinity of twins and shear bands and complete recrystallization of these areas occurred before large, deformed grains began to recrystallize [112].

Inhomogeneous nucleation during recrystallization due to the addition of twins has a significant influence on the JMAK relationship [96, 111-112]. The JMAK

relationship assumes that nucleation sites are randomly distributed and consequently, the rates of nucleation and growth remain constant throughout the entire recrystallization process [96]. Therefore, the entire process can be described by a single Avrami exponent of three [96]. Recrystallization studies in Mg have shown that preferred nucleation at twins leads to an Avrami exponent of less than three and in some cases, a recrystallization process that can be described by two Avrami exponents [111-112]. Nucleation at twins during recrystallization can lead to a two-stage nucleation process where initially nucleation and growth occurs in the vicinity of twinned regions and grain boundaries [112,26]. Once all of those regions are consumed recrystallization proceeds in regions of lower stored energy [122]. One study, in the Mg alloy AZ31 found that heterogeneous distribution of stored energy due to preferred nucleation at twins led to a recrystallization process that could be described by two Avrami exponents, one representing the first stage (recrystallization at twins) and the other representing the second stage (recrystallization at deformed grains) [112]. The two-stage recrystallization process due to inhomogeneous nucleation has also been found in cold-deformed titanium, copper, and carbon steel [122].

2.4.4 Concept of Grain Growth

Once recrystallization is complete, the third and final stage of annealing known as grain growth can proceed [96]. Grain growth (GG) occurs after all deformed regions have been depleted and the driving force for recrystallization is no longer active. After recrystallization is complete, the grain boundary energy results in a microstructure that is not yet energetically stable [96]. In order to decrease the total grain boundary area, grain growth occurs. The kinetics of grain growth were first described by Burke and

Turnbull who assumed that the driving pressure that causes grain boundary motion is derived from the grain boundary curvature which leads to a concentration gradient where the atomic density on the inside of the curve is higher than that on the outside [123]. Therefore, atoms from the higher concentration diffuse across the grain boundary to the area with the low concentration until an equilibrium is reached. This causes the grain from which the atoms diffuse from to shrink as the other grain grows [123].

The kinetics of grain growth can be described and quantified using the parabolic growth law in equation 7,

$$D - D_o = kt^{\frac{1}{n}} \qquad [7]$$

where D is the average grain size, t is the annealing time and n is the grain growth exponent. Assuming that the grain boundary energy for all boundaries is the same, an ideal n-value of 0.5 was calculated. In the next section, factors that influence grain growth such as texture, solute concentration, and annealing temperature will be discussed [96].

2.4.5 Factors That Influence Grain Growth

As stated earlier, grain growth is a diffusion based process and therefore, the annealing temperature will have a significant influence on grain boundary mobility [96]. Since the driving force for GG is usually small, significant grain growth normally occurs at very high temperatures [96]. Therefore, an increased annealing temperature leads to faster grain growth kinetics. Murphy et al found that in unalloyed Mg and Mg-4Al, grain growth increased with annealing temperature [124]. Gil et al found similar behavior during the annealing of pure titanium at temperatures ranging from 700C to 900C [125].

Although grain growth is influenced by many factors, the addition of alloying elements can also have a significant effect on grain growth [96]. Solute atoms can decrease grain boundary mobility through a process known as solute drag [106]. In general, the driving force for GG is small and the grain boundary velocity is low which allows solute atoms to diffuse to catch up to the grain boundary [96,106,126]. As a consequence, the kinetics are governed by solute diffusion near the grain boundary. As grain growth proceeds, the solute atoms gradually reduce the mobility of the grain boundary. The segregation of solute atoms to grain boundaries also lowers the grain boundary energy which results in a decreased driving force for grain growth [126]. Trump et al found that in Ti-Al binary alloys, the grain growth slowed down as the Al concentration increased (Figure 2.15) and related the observed behavior to a reduction in grain boundary mobility due to solute [127]. Texture influences the grain boundary energy of a material and consequently alters the grain growth kinetics during annealing [96]. Strongly textured materials usually contain many low angle boundaries of low energy which leads to a reduced driving force for grain growth during annealing [96].

Figures

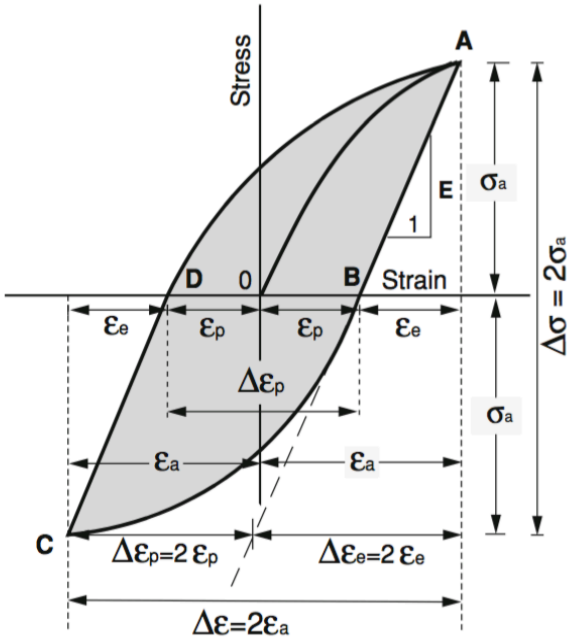

Figure 2.1: Schematic of a stress-strain hysteresis loop from a fatigue experiment detailing the various parameters that can be quantified from the corresponding loop such as plastic strain (ε_p), elastic strain (ε_e), elastic modulus (E), total stress amplitude ($\Delta\sigma$) and total strain amplitude ($\Delta\varepsilon$) [49].

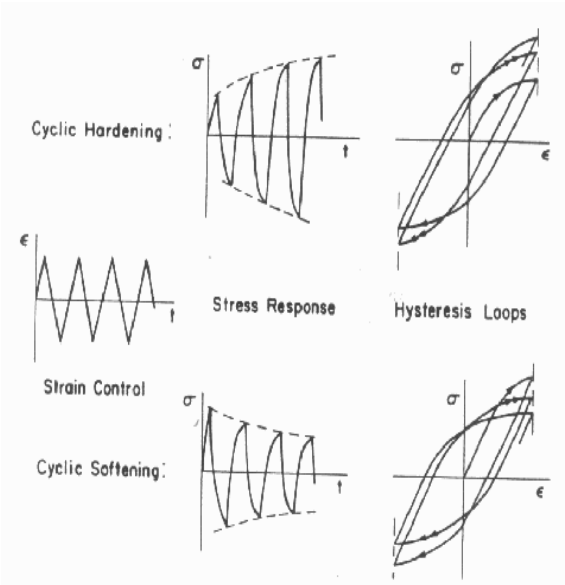

Figure 2.2: A description of cyclic hardening (top) vs. cyclic softening (bottom). During cyclic hardening the total stress amplitude increases from cycle to cycle while during cyclic softening it decreases with cycling [49].

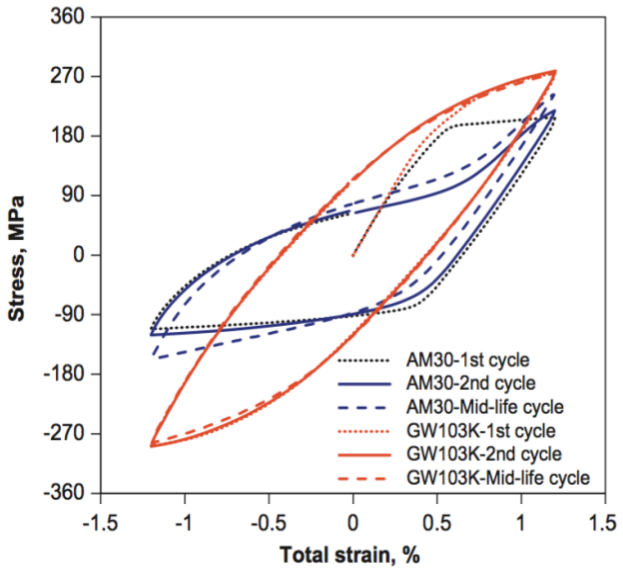

Figure 2.3: Typical stress-strain hysteresis loops of the rare earth Mg alloy, GW103K (red) and the Mg alloy, AM30 (blue) at cycles 1-2 and the mid-life cycle. LCF of GW103K produces a stable, symmetric loop while the loop from AM30 is asymmetric with the abrupt inflection points associated with twinning and detwinning [37].

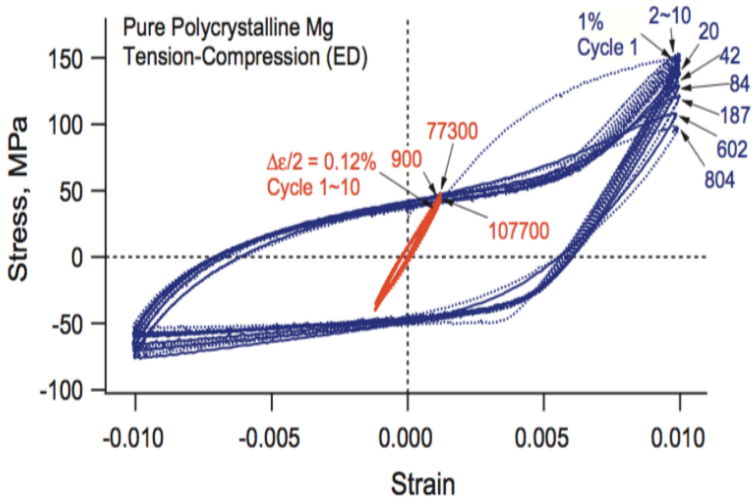

Figure 2.4: Stress-strain hysteresis loops of pure polycrystalline Mg at a low strain amplitude (0.12%) and a high strain amplitude (1.0%). Increased twinning at high strain amplitudes produces an asymmetric loop shape [36].

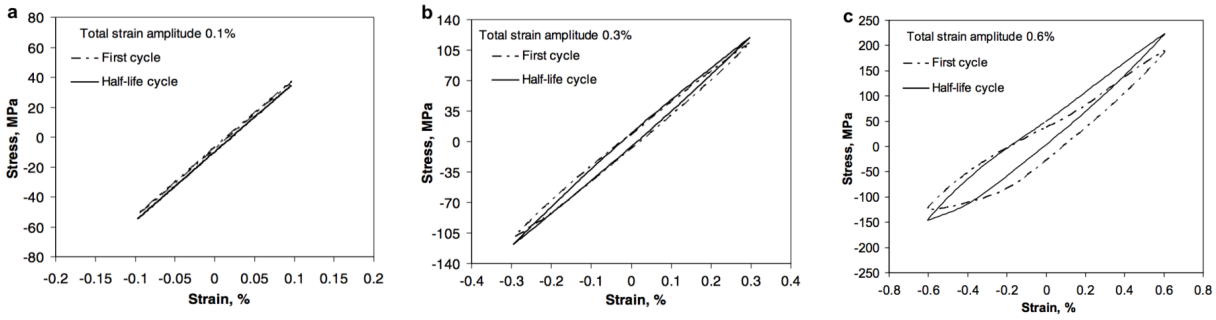

Figure 2.5: A comparison of the tension-compression asymmetry for the Mg alloy, AZ31 at a). 0.1%, b). 0.3%, and c). 0.6%. The tension-compression stress ratio changes with total strain amplitude [39].

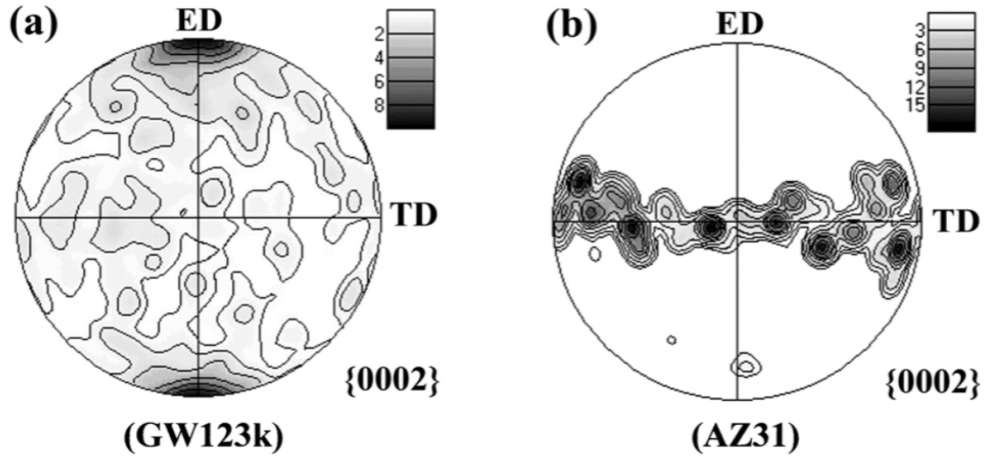

Figure 2.6: Basal pole figures for a a). rare-earth Mg alloy, GW123K and b). AZ31 showing the difference in texture for the two alloys. AZ31 displays a strong basal texture along the transverse direction (TD) while the texture is very weak along that same direction in GW123K [56].

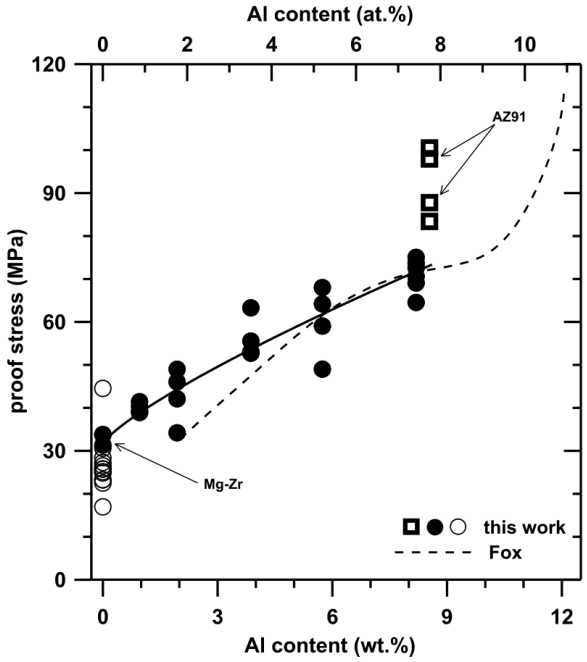

Figure 2.7: The evolution of proof stress in various Mg-Al alloys as a function of Al content. The yield strength increases with an increase in Al concentration [67].

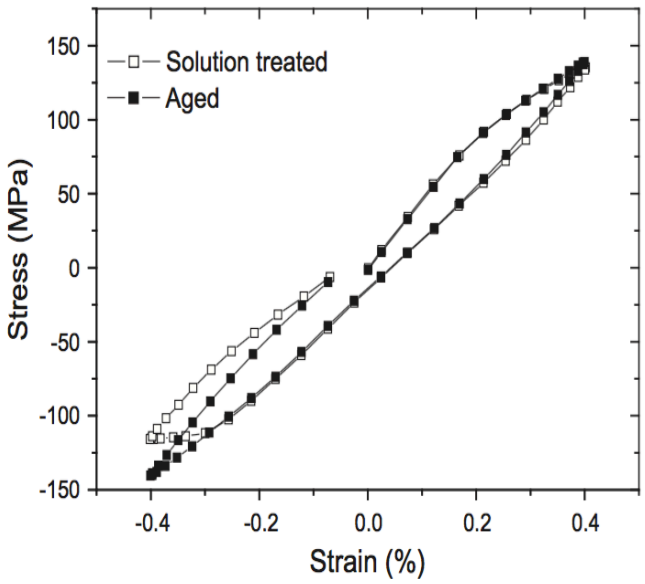

Figure 2.8: The asymmetry in the hysteresis loop is reduced in the aged condition when compared to the solution-treated condition for the Mg alloy, AZ80 [72].

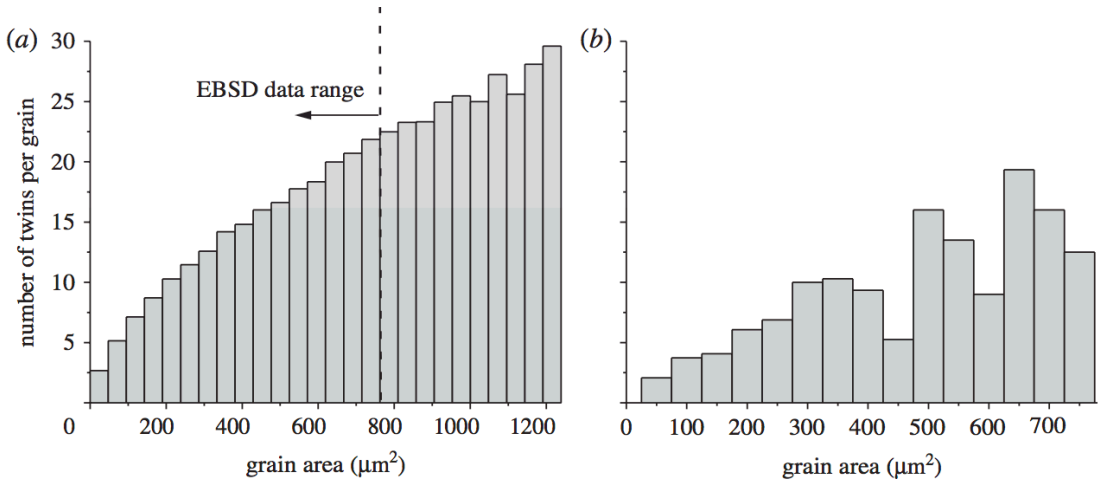

Figure 2.9: Number of twins per grain at 10% strain for unalloyed Mg: a). model prediction and b). EBSD measurements. On average, the number of twins per grain increase with grain area in both cases [20].

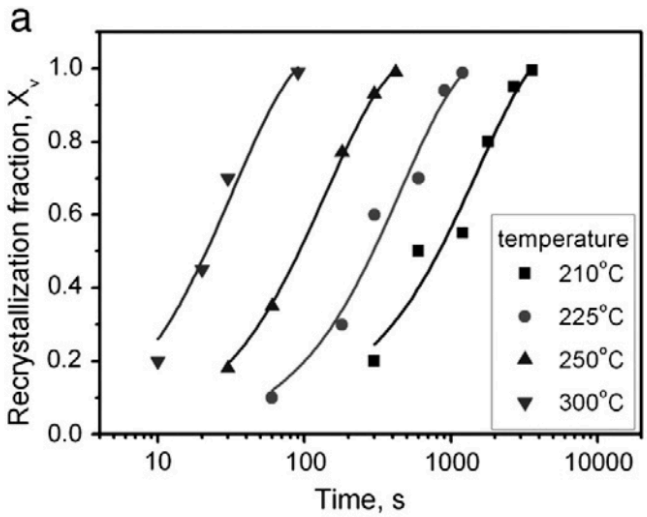

Figure 2.10: The recrystallization fraction as a function of time for annealing temperatures of 210°C, 225°C, 250°C, and 300°C. Recrystallization increases with temperature and time [98].

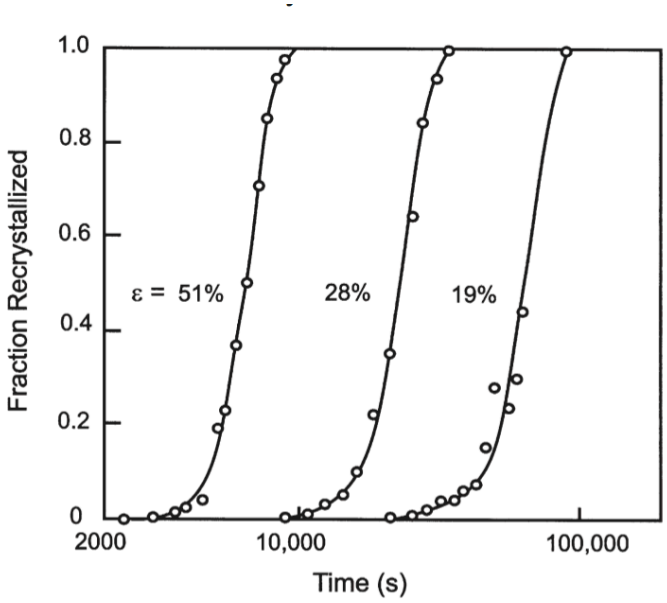

Figure 2.11: The fraction recrystallized as a function of time and strain. As the amount of pre-strain (deformation) increases, recrystallization occurs more rapidly [96].

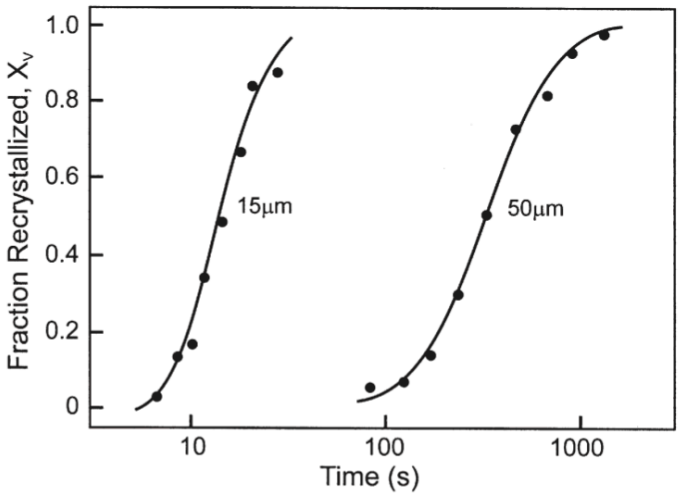

Figure 2.12: The influence of starting grain size on recrystallization kinetics. As the grain size increases recrystallization decreases since there are fewer available nucleation sites [96].

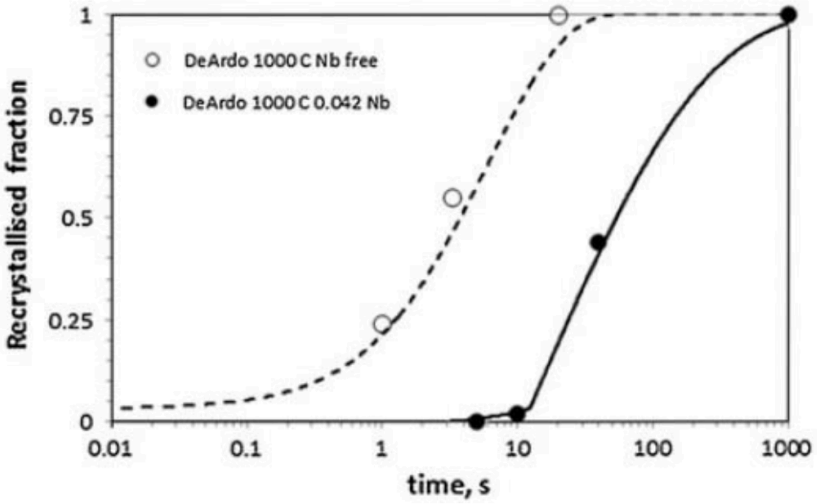

Figure 2.13: The influence of Nb addition on static recrystallization kinetics in a steel. Recrystallization occurs more rapidly in the Nb free alloy [107].

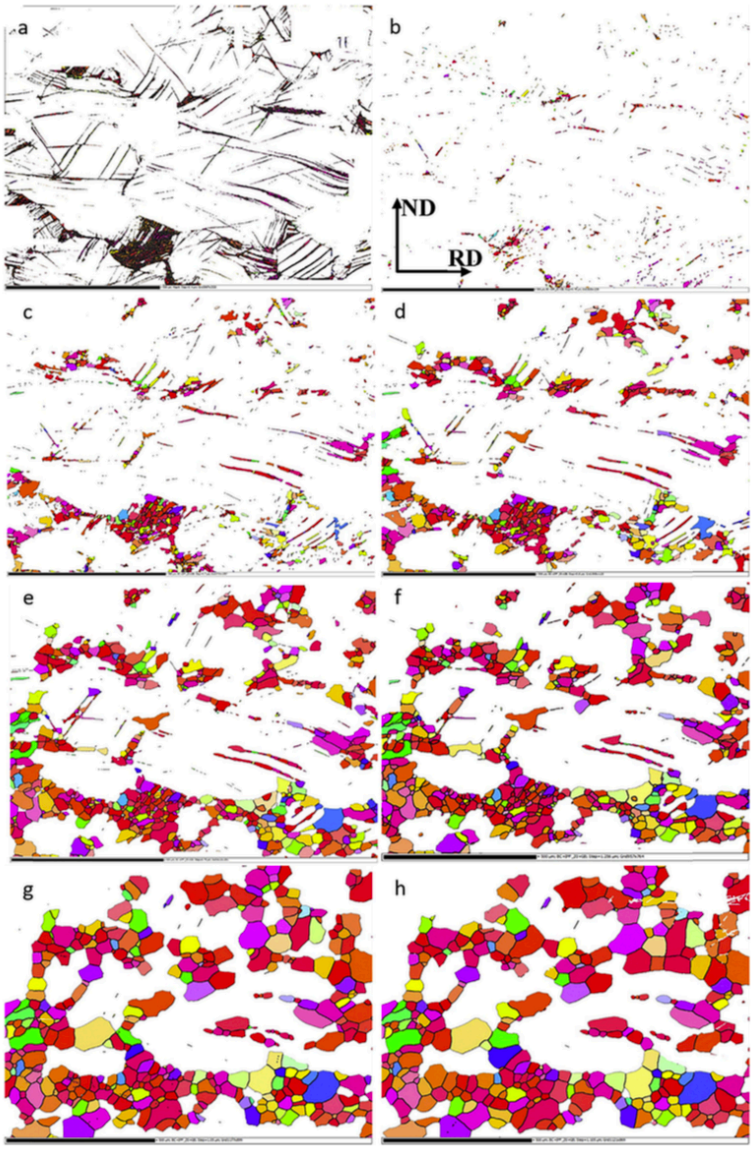

Figure 2.14: EBSD inverse pole figure maps showing the evolution of recrystallization from double twins and double twin-grain boundary intersections for the rare-earth Mg alloy, WE43 at annealing times of a). 0, b). 11, c). 18, d). 28, e). 58, f). 90, g). 198, and h). 378 minutes [113].

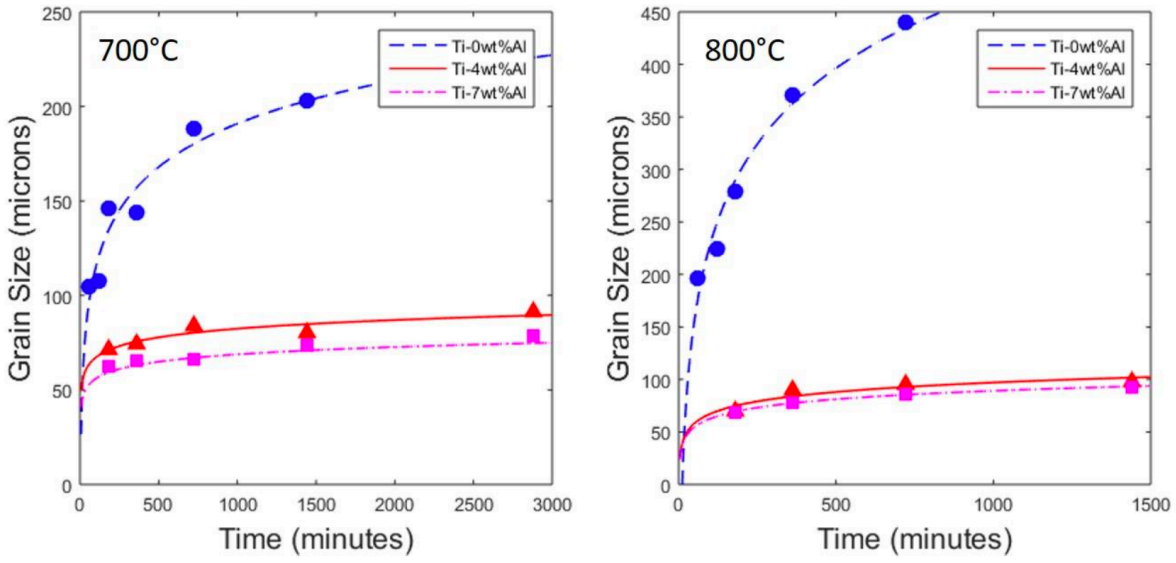

Figure 2.15: At both 700°C and 800°C, grain growth is slowed down as the Al concentration increases in titanium [127].

References

1. X.Y. Lou, M. Li, R.K. Boger, S.R. Agnew, R.H. Wagoner, Hardening evolution of AZ31B Mg sheet, Int. J. Plast. 23 (2007) 44-86
2. C.S. Roberts, Magnesium and its alloys, Wiley, New York/London 1960
3. S. Kleiner, S. Uggowitzer, Mechanical anisotropy of extruded Mg-6%Al-1%Zn alloy, Mater. Sci. Eng. A 379 (2004) 258-263
4. K.Y. Xie, Z. Alam, A. Caffee, K.J. Hemker, Pyramidal I slip in c-axis compressed Mg single crystals, Sripta Mater. 112 (2016) 75-78
5. T. Obara, H. Yoshinga, S. Morozumi, {11-22} <1123> slip system in magnesium, Acta Metall. 21 (1973) 845–853
6. C.M. Byer, B. Li, B. Cao, K. Ramesh, Microcompression study of Mg (0001) single-crystal magnesium, Scr.Mater. 62 (2010) 536–539
7. B. Syed, J. Geng, R. Mishra, K. Kumar, [0001] com- pression response at room temperature of single-crystal magnesium Scr. Mater. 67 (2012) 700–703
8. J.F. Stohr, J.P. Poirier, Electron microscope study of pyramidal slip {1122} <1123> in magnesium, Philos. Mag. 25 (1972) 1313–1329
9. T. Nogaret, W.A. Curtin, J.A. Yasi, L.G. Hector, D.R. Trinkle, Atomistic study of edge and screw <c+a> dislocations in magnesium, Acta Mater. 58 (2010) 4332–4343
10. Y. Tang, J.A. El-Awady, Formation and slip of pyramidal dislocations in hexagonal close-packed magnesium single crystals, Acta Mater. 71 (2014) 319–332
11. A. Singh, J.E. Saal, Dynamic properties of magnesium alloys, J. of Metals 66 (2014) 275-276
12. L.Wu, A. Jain, D.W. Brown, G.M. Stoics, S.R. Agnew, B. Clausen, D.E. Fielden, P.K. Liaw, Twinning-detwinning behavior during the strain controlled low-cycle fatigue testing of a wrought magnesium alloy, ZK60A, Acta. Mater. 56 (2008) 688-695
13. M.H. Yoo, J.R. Morris, K.M. Ho, S.R. Agnew, Nonbasal deformation modes of HCP metals and alloys: role of dislocation source and mobility, Metall. Mater. Trans. A 33 (2002) 813
14. M. Knezevic, A. Levinson, R. Harris, R. Mishra, R. Doherty, S. Kalidindi, Deformation twinning in AZ31: Influence in strain hardening and texture evolution, Acta Mater. 58 (2010) 6230-6242
15. J. Wang, R. Hoagland, J.P. Hirth, L. Capolungo, I.J. Beyerlein, C.N. Tome, Nucleation of (1012) twins in hexagonal close packed crystals, Scripta Mater. 61 (2009) 903–906
16. C.N. Tome´ , P.J. Maudlin, R.A. Lebensohn, G.C. Kaschner, Mechanical response of zirconium—I. Derivation of a polycrystal constitutive law and finite element analysis, Acta Mater. 49 (2001) 3085–3096
17. J. Wang, I.J. Beyerlein, C.N. Tome´, An atomic and probabilistic perspective on twin nucleation in Mg, Scripta Mater. 63 (2010) 741–746
18. L. Wang, P. Eisenlohr, Y. Yang, T.R. Bieler, M.A. Crimp, Nucleation of paired twins at grain boundaries in titanium, Scripta Mater. 63 (2010) 827–830

19. L. Wang, Y. Yang, P. Eisenlohr, T.R. Bieler, M.A. Crimp, D.E. Mason, 2010c. Twin nucleation by slip transfer across grain boundaries in commercial purity titanium, Metall. Mater. Trans. A 41 (2010) 421–430
20. I.J. Beyerlein, C.N. Tome´, A probabilistic twin nucleation model for hcp polycrystalline metals, Proceedings of the Royal Society A 466 (2010) 2517–2544
21. I.J. Beyerlein, L. Capolungo, P.E. Marshall, R.J. McCabe, C.N. Tome´, Statistical analyses of deformation twinning in magnesium, Philosophical Magazine 90 (2010) 2161–2190.
22. R.J. McCabe, G. Proust, E.K. Cerreta, A. Misra, Quantitative analysis of deformation twinning in zirconium, Int. J. Plast. 25 (2009) 454–472
23. I.J. Beyerlein, R.J. McCabe, C.N. Tome, Effect of microstructure on the nucleation of deformation twins in polycrystalline high-purity magnesium: A multi-scale modeling study, J. of the Mechanics and Physics of Solids 59 (2011) 988-1003
24. M.Knezevic, M.R. Daymond, I.J. Beyerlein, Modeling discrete twin lamellae in a microstructural framework, Scr. Mater. 121 (2016) 84-88
25. Serra twins as barriers to basal slip
26. Q. Yu, J. Wang, Y. Jiang, Inverse slip accompanying twinning and detwinning during cyclic loading of magnesium single crystal, J. Mater. 2013 (2013) 1-8
27. A. Serra and D. J. Bacon, “A new model for {1012} twin growth in hcpmetals,” PhilosophicalMagazineA,vol.73, no.2,pp. 333– 343, 1996.
28. J.Wang, I. J. Beyerlein, J. P. Hirth, and C. N. Tom´ e, “Twinning dislocations on {1001} and {1013} planes in hexagonal close- packed crystals,” ActaMaterialia,vol.59, no.10, pp.3990–4001, 2011.
29. J.Wang, J. P. Hirth, and C. N. Tom´ e, “(over(1 0 1 2) Twinning nucleation mechanisms in hexagonal-close-packed crystals,” ActaMaterialia,vol.57, no.18, pp.5521–5530,2009.
30. C. Drouven, I. Basu, T. Al-Samman, and S. Korte-Kerzel: Mater. Sci. Eng. A, 2015, vol. 647, pp. 91-104
31. J. Su, M. Sanjari, A.S.H. Kabir, J.J. Jonas, and S. Yue: Mater. Sci. Eng. A, 2016, vol. 662, pp. 412-425
32. U.F. Kocks et. al. Trans. Metall. Oc. 239 (1967) 1107
33. S.R. Agnew, O. Duygulu, Plastic anisotropy and the role of non-basal slip in magnesium alloy AZ31B, Int. J. Plast. 21 (2005) 1161-1193.
34. Q. Yu, J. Zhang, Y. Jiang, Q. Li, An experimental study on the cyclic deformation and fatigue of extruded ZK60 magnesium alloy, Int. J. Fat. 36 (2012) 47-58
35. Y. N. Wang, J. C. Huang, The role of twinning and untwinning in yielding behavior in hot-extruded Mg-Al-Zn alloy, Acta Mater. 55 (2007) 897–905
36. Q. Yu, Y. Jiang, J. Wang, Cyclic deformation and fatigue damage in single-crystal magnesium under fully reversed strain-controlled tension-compression in the [1010] direction, Scr. Mater. 96 (2015) 41–44.
37. Q. Yu, J. Zhang, Y. Jiang, Fatigue damage development in pure polycrystalline magnesium under cyclic tension-compression loading, Mater. Sci. Eng. A 528 (2011) 7816–7826.

38. S. Begum, D.L. Chen, S. Xu, A. Lou, Low cycle fatigue properties of an extruded AZ31 magnesium alloy, Int. J. of Fat. 31 (2009) 726–735.
39. S. Begum, D.L. Chen, S. Xu, A. Lou, Strain-controlled low-cycle fatigue properties of a newly developed extruded magnesium alloy, Metall. Mater. Trans A 39 (2008) 3014–3026.
40. F. Mokdad, D.L. Chen, Strain-controlled low cycle fatigue properties of a rare-earth containing ZEK100 magnesium alloy, Materials & Design 67 (2015) 436–447.
41. F.A. Mirza, D.L. Chen, D.J. Li, X. Q. Zeng, Low cycle fatigue of a rare-earth containing extruded magnesium alloy, Mater. Sci. Eng. A 575 (2013) 65–73.
42. L. Chen, C. Wang, E.I.W. Wu, Z. Liu, G.M. Stoica, L. Wu, P.K. Liaw, Low-Cycle Fatigue Behavior of an As-Extruded AM50 Magnesium Alloy, Metall. Mater. Trans. A 38 (2007), 2235–2241.
43. L. Wu, S.R. Agnew, Y. Ren, D.W. Brown, B. Clausen, G.M. Stoica, D.R. Wenk, P.K. Liaw, The effects of texture and extension twinning on the low cycle fatigue behavior of a rolled Mg alloy, AZ31B, Mater. Sci. & Eng. A 527 (2010) 7057-7067.
44. F. Wang, J. Dong, Y. Jiang, W. Ding, Cyclic deformation and fatigue of extruded Mg-Gd-Y magnesium alloy, Mater. Sci. Eng. A 561 (2013) 403–410.
45. D. W. Brown, A. Jain, S.R. Agnew, B. Clausen, Twinning and Detwinning During Cyclic Deformation of Mg Alloy AZ31B, Mater. Sci. Forum 539-543 (2007) 3407–3413.
46. W. Wu, Y, Gao, N. Li, C. M. Parish, W. Liu, P.K. Liaw, K. An, Intragranular twinning, detwinning, and twinning-like reorientation in magnesium alloys, Acta. Mater. 121 (2016) 15-23
47. L. Wu, S.R. Agnew, D.W. Brown, G.M. Stoica, B. Clausen, A. Jain, D.E. Fielden, P.K. Liaw, Internal stress relaxation and load redistribution during the twinning-detwinning-dominated cyclic deformation of a wrought magnesium alloy, ZK60A, Acta Mater. 56 (2008) 3699-3707
48. Y. Cui, Y. Li, Z. Wang, X. Ding, Y. Koizumi, H. Bian, L. Lin, A. Chiba, Impact of solute elements on detwinning in magnesium and its alloys, Int. J. of Plast. 91 (2017) 134-159
49. P. Millela. Fatigue and corrosion in metals. Springer. New York (2013)
50. L. Wu, S.R. Agnew, Y. Ren, D.W. Brown, B. Clausen, G.M. Stoica, H.R. Wenk, P. Liaw, The effects of texture and extension twinning on the low cycle fatigue behavior of a rolled magnesium alloy, AZ31, Mater. Sci. Eng. A 527 (2010) 7057-1067
51. S.B. Yi, H.G. Brokmeier, R.E. Bolmaro, K.U. Kainer, T. Lippmann, In-situ measurements of texture variations during a tensile loading of Mg-alloy AM20 using synchrotron x-ray radiation, Scr. Mater. 51 (2004) 455.
52. S.B. Yi, C.H.J. Davies, H.G. Brokmeier, R.E. Bolmaro, K.U. Kainer, J. Homeyer, Deformation and texture evolution in AZ31 magnesium alloy during uniaxial loading, Acta Mater. 54 (2006) 549-562
53. S.B. Yi, H.G. Brokmeier, R. Bolmaro, K.U. Kainer, J. Homeyer, The texture evolutions of Mg alloy, AZ31 under uni-axial loading. Materials Science Forum 495-497 (2005) 1665-1674

54. F.A Mirza, D.L. Chen, Fatigue of rare earth containing Mg alloys: a review, Fat. Fract. Eng. Mater. Struct. 37 (2014) 831-853
55. T.A. Samman, X. Li, Sheet texture modification in magnesium-based alloys by selective rare earth alloying. Mater. Sci. Eng. A 528 (2011) 3809-3822
56. F. Yang, F. Lv, X.M. Yang, S.X. Li, Z.F. Zhang, Q.D. Wang, Enhanced very high cycle fatigue performance of extruded Mg-12Gd-3Y-0.5Zr magnesium alloy, Mater. Sci. Eng. A 528 (2011) 2231-2238
57. M.Z. Bian, A. Tripathi, H. Yu, N.D. Nam, L.M. Yan, Effect of aluminum content on the texture and mechanical behavior of Mg-1wt%Mn wrought magnesium alloys, Mater. Sci. Eng. A 639 (2015) 320-326
58. Y. Chino, K. Sassa, M. Mabuchi. Texture and stretch formability of a rolled Mg-Zn alloy containing dilute content of Y, Mater. Sci. Eng. A 513–514 (2009) 394–400
59. X. Hua, F. Lv, H. Qiao, P. Zhang, Q.Q. Duan, Q. Wang, P.D. Wu, S.X. Li, Z.F. Zhang, The anisotropy and diverse mechanical properties of rolled Mg-3%Al-1%Zn alloy, Mater. Sci. Eng. A 618 (2014) 523–532
60. J. Bohlen, M.R. Nurnberg, J.W. Senn, D. Letzig, S.R. Agnew, On the influence of the grain size and solute content on the AE response of magnesium alloys tested in tension and compression. Mater. Sci. Eng. A, 462 (2007) 302–306
61. N. Stanford, D. Atwell, A. Beer, C. Davies, M.R. Barnett, Effect of microalloying with rare-earth elements on the texture of extruded magnesium-based alloys, Scr. Mater. 59 (2008) 772-775
62. L.W.F. Mackenzie, M. Pekguleryuz, The recrystallization and texture of magnesium-zinc-cerium alloys, Scr. Mater. 59 (2001) 665-668
63. J. Bohlen, S. Yi, D. Letzig, K.U. Kainer, Effect of rare earth elements on the microstructure and texture development in magnesium–manganese alloys during extrusion, Mater. Sci. Eng. A 527 (2010) 7092–7098.
64. D. Griffiths. Explaining texture weakening and improved formability in magnesium rare earth alloys, Mat. Sci. Tech. 31 (2015) 10-24
65. M.M. Avedesian, H. Baker, ASM Specialty Handbook: Magnesium and Magnesium Alloys, ASM International, Materials Park, OH, 1999
66. Akhtar, E. Teghtsoonian, Solid solution hardening in magnesium alloys, Trans. Jpn. Inst. Met. 9 (1968) 692-697
67. C.H. Caceres, D.M. Rovera, Solid solution strengthening in concentrated Mg-Al alloys, J. of Light Metals 1 (2001) 151-156
68. J.W. Christian, S. Mahajan, Deformation twinning, Prog. Mater. Sci. 39 (1995) 1-157
69. J. Han, X.M. Su, Z.H. Jin, Y.T. Zhu, Basal-plane stacking-fault energies of Mg: a first-principles study of Li- and Al-alloying effects, Scr. Mater. 64 (2011) 693-696
70. N. Stanford, M.R. Barnett, Solute strengthening of prismatic slip, basal slip and {10-12} twinning in Mg and Mg-Zn binary alloys, Int. J. Plast. 47 (2013) 165-181
71. Y.P. Li, M. Enoki, Deformation and anelastic recovery of pure magnesium and AZ31B alloy investigated by AE, Mater. Trans. 48 (2007) 2343-2348
72. R. Zhu, J. Wenqing, Y. Wu, X. Cai, Y. Yu, Effect of ageing treatment on low cycle fatigue behavior of extruded Mg-8Al-0.5Zn alloys, Mat. Design 41 (2012) 203-207

73. C.L. Lv, T. Liu, D. Liu, S. Jiang, W. Zeng, Effect of heat treatment on tension-compression yield asymmetry of AZ80 magnesium alloy, Mater. Design 33 (2012) 529-533
74. N. Stanford, M.R. Barnett, Effect of particles on the formation of deformation twins in a magnesium based alloy, Mater. Sci. Eng. A 516 (2009) 226-234
75. L.H. Rettberg, Low cycle fatigue behavior of die cast Mg alloys AZ91 and AM60, Met. Mater. Trans A 43 (2012) 2261-2274
76. Y. Uematsu, K. Tokaji, M. Matsumoto, Effect of aging treatment on fatigue behaviour in extruded AZ61 and AZ80 magnesium alloys, Mater. Sc. Eng. A 517 (2009) 138–145
77. Z. Sajuri, Y. Miyashita, Y. Hosokai, Effects of Mn content and texture on fatigue properties of as-cast and extruded AZ61 Mg alloy, Int. J. Fatigue. 48 (2006) 198-209
78. R. Armstrong, I. Codd, R.M. Douthwaitem N.J. Petch, The plastic deformation of polycrystalline aggregates, Philosophical Magazine 7 (1962) 45–58
79. K. Okazaki, H. Conrad, Effects of interstitial content and grain size of the strength of titanium at low temperatures, Acta Metallurgica 21 (1973) 1117–1129
80. S.G. Song, G.T. Gray, Structural interpretation of the nucleation and growth of deformation twins in Zr and Ti. 1—Application of the coincidence site lattice (CSL) theory to twinning problems in hcp structures, Acta Metallurgica 43 (1995) 2325–2337
81. S.R. Agnew, C.N. Tome, D.W. Brown, S.C. Vogel, Study of slip mechanisms in a magnesium alloy by neutron diffraction and modeling, Scr. Mater. 48 (2003) 1003-1008
82. M.R. Barnett, Z. Keshavarz, A.G. Beer, D. Atwell, Influence of grain size on the compressive deformation of wrought Mg–3Al–1Zn, Acta Mater. 52 (2004) 5093–5103
83. J. Koike, T. Kobayashi, T. Mukai, H. Watanabe, M. Suzuki, K. Maruyama, K. Higashi, The activity of non-basal slip systems and dynamic recovery at room temperature in fine- grained AZ31B magnesium alloys, Acta Mater. 51 (2003) 2055–2065
84. N. Stanford, M.R. Barnett, Solute strengthening of prismatic slip, basal slip, and {10-12} twinning in Mg and Mg-An alloys, Int. J. of Plasticity 47 (2013) 165-181
85. L. Capolungo, P. Marshall, R.J. McCabe, I.J. Beyerlein, C.N. Tome, Nucleation and growth of twins in Zr: a statistical study, Acta Mater. 57 (2009) 6047–6056
86. J.P. Hirth, J. Lothe, Theory of Dislocations, McGraw-Hill, New York, 1968.
87. Z. Li, Q. Wang, A.A. Luo, P. Zhang, L. Peng, Size effect on magnesium alloy castings, Met. Mater. Trans. A. 47 (2016) 2686-2704
88. J.K. Mahato, P.S. De, A. Sarkar, A. Kundu, P.C. Chakraborti, Grain size effect on LCF behavior of two FCC metals, Procedia Eng. 160 (2016) 85-92
89. M.A. Gharghouri, G.C. Weatherly, J.D. Embury, J. & Root, Study of the mechanical properties of Mg-7. 7at. % Al by in-situ neutron diffraction, Philos. Mag. 79 (1999) 1671-1695
90. W. Wu, P.K. Liaw, K. An, Unraveling cyclic deformation mechanisms of a rolled magnesium alloy using in situ neutron diffraction, Acta Mater. 85 (2015) 343-353

91. W. Wu, K. An, L. Huang, S.Y. Lee, P.K. Liaw, Deformation dynamics study of a wrought magnesium alloy by real-time in-situ neutron diffraction, Scripta Mater. 69 (2013) 358-361
92. W. Wu, K. An, Understanding low-cycle fatigue life improvement mechanisms in a pretwinned magnesium alloy. Journal of Alloys and Compounds 656 (2016) 539-550
93. W. Wu, H. Qiao, X. Guo, P. Wu, P.K. Liaw, Investigation of deformation dynamics in a wrought magnesium alloy. Int. Journal of Plasticity 62 (2014) 105-120
94. Y. Ren, High-energy synchrotron x-ray diffraction and its application to in situ structural phase-transition studies in complex sample environments, J. Metals 64 (2012) 140-149
95. B.L. Wu, G.S. Duan, X.H. Du, L.H. Song, Y.D. Zhang, M.J. Philip, C. Esling, In situ investigation of extension twinning-detwinning and its effect on the mechanical behavior of AZ31B magnesium alloy. Mater. Des. 132 (2017) 57-65
96. F.J. Humphreys , M. Hatherlys. Recrystallization and Related Annealing Phenomena. Pergman (2004).
97. D. Griffiths, Explaining texture weakening and improved formability in magnesium rare earth alloys. Mat. Sci. Tech. 31 (2015) 10-24
98. H.Y. Chao, H.F. Sun, W.Z. Chen, and E.D. Wang, Static recrystallization kinetics of a heavily cold drawn AZ31 magnesium alloy under annealing treatment, Mater. Characterization 62 (2011) 312-320
99. A.G. Beer, M.R. Barnett, The post deformation recrystallization behavior of magnesium alloy Mg-3Al-1Zn, Scripta Mater. 61 (2009) 1097-1100
100. X. Yang, Y. Okabe, H. Miura, T. Sakai, Effect of prior strain on continuous recrystallization in AZ31 magnesium alloy after hot deformation, Mater. Sci. Eng. A. 535 (2012) 209-215
101. T. Schambron, L. Chen, T. Gooch, A. Dehghan-Manshadi, E. V. Pereloma, Effect of Mo concentration on dynamic recrystallization behavior of low carbon microalloyed steels, Steel Res. Int. 84 (2013) 1191–1195
102. E. I. Galindo-Nava, A. Perlade, P. E. J. Rivera-Díaz-del-Castillo, A thermostatistical theory for solid solution effects in the hot deformation of alloys: an application to low- alloy steels, Model. Simul. Mater. Sci. Eng. 22 (2014)
103. H. S. Zurob, G. Zhu, S. V. Subramanian, G. R. Purdy, C. R. Hutchinson, Y. Bréchet, Analysis of Mn effect on recrystallization kinetics in high Nb steels, Mater. Sci. Forum 500–501 (2005) 123–130
104. M. K. Rehman, H. S. Zurob, A novel approach to model static recrystallization of austenite during hot rolling of Nb microalloyed steel. part I: precipitate-free case, Metall. Mater. Trans. A 44 (2012) 1862–1871
105. Z. Aretxabaleta, B. Pereda, B. López, Analysis of the effect of Al on the static softening kinetics of C-Mn Steels using a physically based model, Metall. Mater. Trans. A 45 (2013) 934–947
106. J. W. Cahn, The impurity-drag effect in grain boundary motion, Acta Mater. 10 (1962) 789–798
107. O. Kwon, A. J. Deardo, Interations between recrystallization and precipitation in hot- deformed microalloyed steels, Acta Metall. 39 (1991) 529–538

108. M.C. Weinberg, D.P. Birnie, V.A. Shneidman, Crystallization kinetics and the JMAK equation, J. of Non-crystalline Solids 219 (1997) 89-99
109. J. Hirsch, T. Al-Samman, Superior light metals by texture engineering: optimized aluminum and magnesium alloys for automotive applications. Acta Materialia 61 (2013) 818-843
110. C. Drouven, I. Basu, T. Al-Samman, S. Korte-Kerzel. Twinning effects in deformed and annealed magnesium-neodymium alloys. Mat. Sci. Eng. A 647 (2015) 91-104
111. C.W. Su, L. Lu, M.O. Lai, Recrystallization and grain growth of deformed magnesium alloy. Philosophical Magazine 88 (2008) 181-200
112. J. Su, M. Sanjari, A.S.H. Kabir, J.J. Jonas, S. Yue, Static recrystallization behavior of magnesium AZ31 alloy subjected to high speed rolling. Mat. Sci. Eng. A 662 (2016) 412-425
113. D. Guan, W.M. Rainforth, L. Ma, B. Wynne, J. Gao, Twin recrystallization mechanisms and exceptional contribution to texture evolution during annealing in magnesium alloy. Acta Materialia 126 (2017) 132-144
114. M.M. Myshlyaev,H,J. McQueen, A. Mwembela, E. Konopleva, Twinning, dynamic recovery and recrystallization in hot worked Mg-Al-Zn alloy. Mat. Sci. Eng. A 337 (2002) 121-133
115. X. Li, P. Yang, L.N. Wang, L. Meng, F. Cui. Orientational analysis of static recrystallization at compression twins in a magnesium alloy AZ31. Mat. Sci. Eng. A 517 (2009) 160-169
116. T. Al-Samman, K.D. Molodov, D.A. Molodov, G. Gottstein, and S. Suwas: Acta Mater., 2012, vol. 60, pp. 537-545
117. I. Basu, T. Al-Samman. Twin recrystallization mechanisms in magnesium-rare earth alloys. Acta Materialia 96 (2015) 111-132
118. E. Martin, R.K. Mishra, J.J. Jonas, Effect of twinning on recrystallization textures on recrystallization textures in deformed magnesium alloy AZ31. Philos. Mag. 91 (2011) 3613-3626
119. Q. Ma, B. Li, W.R. Whittington, A.L. Oppedal, P.T. Wang, M.F. Horstemeyer, Texture evolution during dynamic recrystallization in magnesium alloy at 450C, Acta Materialia 67 (2014) 102-115
120. M. Knezevic, M.R. Daymond, I.J. Beyerlein Modeling discrete twin lamellae in a microstructural framework. Scripta Materialia 121 (2016) 84-88
121. M. Knezevic, A. Levinson, R. Harris, R.K. Mishra, R.D. Doherty, S.R. Kalidindi, Deformation twinning in AZ31: Influence on strain hardening and texture evolution. Acta Mater. 58 (2010) 6230-6242
122. M. Oyarz'abal, A Martinez-de-Guerenu, I. Gutierrez. Effect of stored energy and recovery on the overall recrystallization kinetics of a cold rolled low carbon steel. Mat. Sci. Eng. A 485 (2008) 200-209
123. J. E. Burke and D. Turnbull, Recrystallization and grain growth, Prog. Met. Phys. 3 (1952) 220–292
124. A.D. Murphy, C. Huber, J.E. Allison, Grain growth behavior of unalloyed Mg and Mg-4Al, 11th Int. Conf. Magnesium Alloys and Their Applications Proceedings (2018)

125. F. J. Gil, J. A. Picas, J. M. Manero, A. Forn, J. A. Planell, Effect of the addition of palladium on grain growth kinetics of pure titanium, J. Alloys Compounds 260 (1997) 147–152
126. J. R. Trelewicz, C. A. Schuh, Grain boundary segregation and thermodynamically stable binary nanocrystalline alloys, Phys. Rev. B 79 (2009)
127. A. Trump and J. Allison, University of Michigan, Ann Arbor, MI, unpublished research, 2016

CHAPTER 3
QUANTIFICATION OF TWINNING-DETWINNING BEHAVIOR DURING LOW-CYCLE FATIGUE OF UNALLOYED MG USING HIGH ENERGY X-RAY DIFFRACTION

3.1. Introduction

Mechanical twinning plays an important and well documented role during the plastic deformation of Mg and its alloys [1-8]. In hexagonal close packed (HCP) Mg alloys, the dominant deformation mode at room temperature is generally <a> slip on the basal (0001) plane. In unalloyed Mg, the critical resolved shear stress (CRSS) to activate basal slip can be as low as 0.5-1 MPa [9-10]. The other slip systems -- prismatic <a> slip, pyramidal <a> slip, and pyramidal <c+a> slip -- require much higher stresses to activate during deformation [11]. Pyramidal <c+a> slip is difficult to activate at room temperature leaving only four independent slip systems available for room temperature deformation in these materials [12]. Therefore, another deformation mode is necessary to accommodate arbitrary isochoric deformations (the Von Mises criterion). In many Mg alloys, this role is served by mechanical twinning which allows grains to deform along their c-axis [9]. Crystal plasticity simulations by Knezevic et al found that the CRSS for twinning was double that for basal slip but three times less than that for prismatic and pyramidal slip [13]. Due to its importance, twinning has been the focus of significant, active research [e.g.,13-23]. In this work, twinning in unalloyed Mg is studied during fully reversed low cycle fatigue (LCF) tests. The formation of deformation twins is probed in-

situ using high-energy X-ray diffraction (HEXD) by monitoring the evolution of specific texture components, uninterrupted, as fully reversed cyclic loads are applied. The points in time / applied strain when twinning begins and ends during loading are identified with high fidelity, made possible by rapid X-ray exposure times. The evolution of the character of twinning and detwinning during the presented experiments provide crucial new information for the development of accurate models to predict the influence of microstructure, texture and alloying on low cycle fatigue for future alloy and process design.

In unalloyed Mg and Mg alloys, with a c/a ratio less than the ideal value of 1.633, $\{10\acute{1}2\}\langle 10\acute{1}1\rangle$ extension twinning is a dominant deformation mode that accommodates extension along the c-axis, but not contractions along that same direction [16, 24]. In textured materials, this can cause the tensile yield strength to be significantly higher than the compressive yield strength [25] and can also produce a Bauschinger effect [2-8,14-15,26]. In wrought Mg alloys where the dominant basal texture component is normal to the loading direction, the Bauschinger effect during cyclic loading is particularly pronounced [3,5, 14-15]. Begum et al. found that the tensile yield strength was much higher than the compressive yield strength during low cycle fatigue of an AM30 extruded Mg alloy and related this to twinning that occurs during compression and detwinning that occurs during tension [5]. During compression, twins form causing an 86.3° reorientation of the basal pole [9,11,15,22]. During reversed (tensile) unloading these twinned regions can become narrower and/or disappear in a process known as detwinning [11,25,27]. Detwinning causes a reorientation of the c-axis from

the twin back to the matrix or parent grain [9, 25, 27-28]. Twins can reappear upon reloading and thus, the twinning-detwinning behavior continues until the end of life [29]. During cyclic loading of Mg alloys, three regions exist with different dominant deformation mechanisms occurring in each region. First, during tensile loading, deformation is dominated by slip, [17-18,30-31]. Second, during compression loading, twinning dominated deformation occurs and the flow curve displays a relatively lower maximum stress [15]. Finally, during the reversed tensile loading portion of a fatigue cycle, dislocation slip occurs simultaneously with detwinning or narrowing of twins [14]. A study by Yu et al. found that the tension-compression yield asymmetry was reduced at low strain amplitudes during LCF of pure polycrystalline magnesium due to a reduction in twinning [3].

The stress-strain response of a material is different when both slip and twinning work together to accommodate deformation than when slip acts alone, since the stresses needed to activate twinning and slip are different [32]. This behavior during cyclic loading leads to an abnormally shaped hysteresis loop with inflections representing the onset of twinning and exhaustion of detwinning [2-8,14-15]. Wu et al reported an abnormal sigmoidal shaped hysteresis loop during LCF of the Mg alloy AZ31, where the stress in tension was much higher than that in compression [33]. Begum et al reported similar behavior for the Mg alloy AM30 [5].

In recent years, neutron scattering has been used to study the twinning-detwinning behavior of wrought Mg alloys during cyclic loading [14-15,17,20,34-37] while few studies have used high energy x-ray diffraction (HEXD) using synchrotron diffraction [30,38] to study this behavior. Both neutron scattering diffraction and HEXD

allow for the bulk response to be examined in order to understand phase transitions and texture evolution [33, 39]. Using these techniques, behavior may be assessed with minimal impact of the free surface. Neutron irradiation has relatively low fluxes and intensities and therefore, has many limitations when studying rapid time-dependent processes such as fatigue [38]. Due to these limitations, in practice, many in-situ fatigue experiments involving neutron scattering are paused in order to measure a diffraction pattern. In contrast, HEXD of an Mg sample in a transmission geometry may be conducted with relatively short collection times, which allows for studying phenomena in-situ. In in-situ fatigue studies, HEXD provides a means of understanding the behavior of the bulk material throughout an entire cycle in real time under realistic conditions without pausing the cyclic loading [39].

Despite the complexities of neutron diffraction, Gharghourri et al used this technique and found that, during cyclic loading, twinning occurred during compression followed by detwinning during the reversal [20]. An in-situ neutron scatter study by Wu et al also found that twinning-detwinning alternates during cyclic loading in ZK60A magnesium alloy [15]. Studies of AZ31 using synchrotron radiation have addressed the texture evolution of samples deformed by ex-situ techniques [14], and the twinning, detwinning, and lattice reorientation within an individual grain during strain reversal of a single cycle. In an in-situ neutron experiment by Wu et al, it was found that during the final stages of fatigue life immediately before failure, twinning became less dominant and deformation proceeded by dislocation slip in AZ31B Mg alloy [34].

In the current work, the twinning-detwinning behavior of extruded, polycrystalline unalloyed magnesium under cyclic loading was investigated at the Cornell High Energy

Synchrotron Source (CHESS) using in-situ HEXD. The purpose of this study is to quantify the twinning and detwinning that occurs during cyclic deformation and to understand the influence of twinning and detwinning on cyclic stress-strain response of unalloyed Mg. It is anticipated that this quantitative information will provide important baseline information for developing physically-based models for predicting the influence of microstructure and alloying on cyclic stress-strain response and low cycle fatigue.

3.2. Experimental Procedure

3.2.1 Material Characteristics and Sample Preparation

The unalloyed Mg used in this study was provided by CanMET Materials in the form of extruded bar. The bar was extruded from an 85mm diameter cast billet at 300°C to a final diameter of 15mm. The as-extruded texture was measured using EBSD with the results shown in Figure 3.1. The initial texture shows that the basal poles are oriented in the radial direction (RD) and are therefore aligned normal to the extrusion direction and the loading direction (LD) [40] In the in-situ experiment described below, the loading direction (LD) is parallel to the extrusion direction and the normal direction (ND) Is equivalent to the radial direction (RD). The microstructure consisted of equiaxed grains with an average grain diameter of 50 μm. The microstructure was 95 percent recrystallized. The details of this microstructural characterization have been reported elsewhere [41].

For the in-situ synchrotron diffraction experiments, cylindrical fatigue specimens were machined by Westmoreland Mechanical Testing and Research, Inc. using low stress turning to ensure a low residual stress, scratch free surface. The final surface was prepared by standard metallographic techniques ending with a 1200 μm grit finish.

The geometry was consistent with the ASTM E606 standard and the samples had a diameter of 6.35mm and a gage length of 19.05mm.

To characterize twinning and detwinning using electron back scatter diffraction (EBSD), flat, rectangular fatigue specimens were inserted in a Tescan Mira 3 scanning electron microscope equipped with an EDAX Hikari XP EBSD detector. Each EBSD scan was taken at a voltage of 30kV and a beam intensity between 18-20 with an average step size of 1.0±0.2μm. TSL OIM software was used to characterize EBSD data and an average confidence index of 0.67±0.1 was obtained. No additional confidence index cleaning was applied to the data. A grain tolerance angle of 5° was used for grain recognition. These were also machined by Westmoreland using low stress turning where the final surface was produced with 1200 μm grit finish. The samples were then electro-polished using a phosphoric acid-ethanol solution at 24V for 2 hours prior to testing. An acetic-picral solution (4.2 g picric acid, 10mL acetic acid, 10 mL water, and 70 mL ethanol) was used to etch the specimens for 3-5 seconds, which revealed grains and twins under scanning electron microscopy.

3.2.2 Cyclic Loading and X-ray Diffraction Measurements

HEXD experiments were performed during in-situ cyclic mechanical loading at the F2 Station at the Cornell High Energy Synchrotron Source (CHESS). Figure 3.2 shows an illustration of the experimental geometry which will be referred to throughout this section. Within the diffraction volume, every grain satisfying Bragg's Law (Equation 1) will diffract producing a peak of diffracted intensity on the detector. Bragg's Law relates the x-ray wavelength, λ to the lattice spacing for a unique family of planes, d_{hkl} and the diffracted angle, θ_{hkl} [42].

$$\lambda = 2d_{hkl} \sin \theta_{hkl} \quad (1)$$

The cyclic loads were applied by a Bose Electroforce 3200 Series III load frame that was mounted on a series of translation and rotation stages for sample manipulation. The macroscopic load was measured on a 5kN load cell located below the sample. The macroscopic strain was measured using an extensometer attached to the sample. Two samples per condition were tested at both 0.52% and 0.75% total strain amplitudes while only one sample was tested at 0.4% total strain amplitude.

During the test, the sample was illuminated by a 61.332 keV X-ray beam that travelled parallel to the -Z direction. The size of the beam illuminating the sample was 1.25 mm (width, X) by 1.25 mm (height, Y). Diffracted intensity was measured in transmission on a wide panel area detector that was placed with face normal to the incoming beam, 859 mm behind the specimen. On the detector, a sufficient number of grains were illuminated such that nearly complete Debye-Scherer powder rings were captured. To maximize the number of crystals illuminated, the sample was continuously rocked about the rotation axis from 0-5°. The timing of the rocking was synced such that a rotation from 0° to 5° and back to 0° degrees was completed during a single exposure. Diffracted intensity was measured at an angle 2θ from the incoming X-ray beam and the angle η defined the azimuthal position along the Debye-Scherer ring at which the diffracted intensity was measured. The area detector employed was a GE41RT+ amorphous silicon area with 2048 x 2048 pixels and 200 μm x 200 μm pixel size.

The cyclic loading was performed in displacement control with displacement end points. A triangular displacement waveform was applied to the specimens. Three different specimens were tested with displacement endpoints of 0.205mm (ε_A =0.75%), 0.192mm (ε_A =0.52%), and 0.135mm (ε_A =0.4%). When not collecting diffraction data,

the sample was loaded at a frequency of 0.25Hz. The loading direction was perpendicular to the incoming X-ray beam. In this geometry, the normals of diffracting lattice planes lie at an angle, θ, away from the loading axis. To observe the twinning process in-situ, a cycle was applied to the specimen and diffraction measurements were continuously made throughout the cycle. During these cycles, the loading rate was reduced such that an entire cycle was completed in 480s. Throughout the cycle, 240 images were collected with exposure times of 2s. Each image number corresponds to a diffraction measurement.

3.3. Results

In this section, the experimental results provided by in-situ HEXD techniques are reported. First the macroscopic stress-strain response showing the variation of tensile and compressive stresses with cycles will be presented. The loading axes of all fatigue specimens were parallel to the extrusion direction. Thus, the c-axis of the majority of grains was normal to the loading direction and it was possible to activate $\{10\acute{1}2\}\langle 10\acute{1}1\rangle$twinning during compression in these grains. This twinning was characterized using HEXD which allowed quantification of the relationship between twinning-detwinning and the intensity evolution of the basal {0002} peak during cyclic loading. This allowed for investigation of the influence of twinning-detwinning behavior on the observed tension-compression asymmetry.

3.3.1 Macroscopic Stress-Strain Response

The twinning-detwinning behavior of unalloyed Mg was characterized using HEXD at three different total strain amplitudes: 0.75%, 0.52%, and 0.4%. Figure 3.3 shows the evolution of maximum stress in compression and tension for each strain amplitude as a function of cycles. The maximum tensile stress was higher at the higher

strain amplitudes (0.75% & 0.52%) compared with the lower strain amplitude (0.4%), where the maximum tensile stresses at the half-life were 63MPa, 62MPa, and 50MPa, respectively. The maximum compressive stresses were approximately the same for all levels of applied stress and at the half-life was -52 MPa, -53 MPa and -47 MPa, respectively. At both 0.75% and 0.52% total strain amplitude, a tension-compression strength asymmetry exists where the stresses reached in tension are higher than those reached in compression. The asymmetry is reduced at the lower strain amplitude of 0.4%. At a total strain amplitude of 0.52% and 0.75%, slight hardening was observed during the first ten cycles and from there a hardening plateau existed until cycle 400 or 500, respectively, after which softening occurred until failure. This strain hardening plateau has also been observed in other alloys that deform by twinning including HCP Mg alloys [11,19,42], Zr alloys [44-45], and the shape memory alloy, NiTi [46]. The diffraction data suggests that hardening during the first ten cycles at 0.75% and 0.52% total strain amplitudes is due to the increasing volume of fraction twins forming, which will be discussed later. At a total strain amplitude of 0.4%, cyclic stability was observed and the maximum tensile and compressive stresses did not significantly vary with cycles until cycle 3000 at which point softening occurred until failure. The diffraction data at 0.4% total strain amplitude suggested that the material was not deforming by mechanical twinning and deformation is likely due to formation and motion of dislocations.

3.3.2 In-Situ HEXD Measurements

Figures 3.4, 3.5 and 3.6 shows the hysteresis loops for total strain amplitudes of 0.75%, 0.52%, and 0.4%, respectively and the evolution of the basal {0002} peak intensity. Peak intensity evolution is shown from scattering in both the loading direction

and the direction normal to the loading direction, i.e., normal to the extrusion direction, as a function of cycles for each strain amplitude. In each HEXD intensity figure, the different stages of loading are indicated, i.e., tensile loading until the maximum tensile strain is reached at A, after which tensile unloading occurs until zero strain is reached; this is followed by compressive loading until the compressive maximum strain is reached at B and ending with compressive unloading back to a strain of zero. For each cycle, the maximum tensile strain is indicated by the letter A and the maximum compressive strain is denoted by B. The stars on each figure (e.g., C1 in Figure 3.4a) represent points of interest and will be discussed throughout the paper.

The initial intensity of the basal {0002} peak in the loading direction is zero. As stated in the previous section, a majority of the parent grains have their c-axis oriented normal to the loading direction, therefore when parent grains undergo twinning, their c-axis is reoriented 86.3° towards the loading direction as outlined in Figure 3.7. In Figure 3.7a, the initial orientation of the {0002} basal pole (c-axis) is normal to the loading direction; in Figure 3.7b as twins are formed during compression the c-axis is reoriented by 86.3° toward the loading direction, and finally during the removal of those twins or detwinning the orientation is returned to its initial orientation (Figure 3.7c). This reorientation can be related to changes in the {0002} peak intensities in the loading and normal directions and is directly related to the degree of twinning and detwinning that occurs during loading. The initial high peak intensity in the normal direction is related to the volume fraction of parent grains with their c-axis perpendicular to the loading direction. These grains are favorably oriented for twinning during compression. The peak intensity data in Figures 3.4-3.6 is plotted as a function of image number (e.g., in

Figure 3.4b, c, e and f). The image number corresponds to the diffraction measurement and 240 diffraction measurements were taken throughout each cycle. An increase in the intensity in the loading direction indicates an increase in twinning while a decrease is related to the degree of detwinning, that is, the removal and/or narrowing of those twinned regions. Concurrently a decrease or increase in intensity in the normal direction is indicative of the volume fraction of regions that have reoriented their c-axis due to twinning or detwinning. Thus, the maximum in the intensity for the {0002} x-ray peak in the loading direction (as shown in Fig 3.4b) corresponds to a minimum in the intensity for the {0002} x-ray peak in the normal direction (as shown in Fig 3.4c).

At 0.75% total strain amplitude (Figure 3.4a-c), during Cycle 1 the intensity of the basal {0002} peak in the loading direction remains zero until the applied stress reaches a value of -52 MPa (indicated by C-1) at which point the x-ray peak intensity begins to increase until it reaches the maximum compressive strain (indicated by B). Immediately during compressive unloading the x-ray peak intensity decreases until the end of cycle 1. This increase in intensity in the loading direction during compressive loading is tied to the onset of twinning, that is, the regions of the parent grains that are reorienting by 86.3° and that the decrease in intensity during the load reversal is caused by detwinning. This detwinning process is also reflected by the intensity changes in the normal direction where, during compressive loading, the intensity begins decreasing at C-1 and continues to decrease until the maximum compressive strain is reached at which point the x-ray peak intensity begins to increase until the end of the first cycle. The intensity does not return to zero or the background intensity at the end of Cycle 1 indicating that all of the twins were not removed during compressive unloading.

During the initial tensile loading of the following cycle (Cycle 2) the intensity in the loading direction immediately returns to zero (indicated by T-2), marking the exhaustion of detwinning at 20 MPa. After that the intensity remains zero until the applied stress reached a value of -44 MPa (C-2). At C-2 the intensity begins increasing and continues until it reaches the maximum compressive strain indicating that twinning begins at the compressive stress, C-2, in the second cycle. As the compressive unloading of Cycle 2 begins, the x-ray peak intensity immediately begins decreasing showing that detwinning is occurring until the end the cycle. By Cycle 200 (Fig. 4.4g, h, i), the detwinning behavior begins to change; detwinning occurs until the maximum tensile strain is reached indicated by the decrease in intensity in the loading direction to its minimum at Point A and the x-ray peak intensity in the loading direction does not return to zero indicating that a certain volume fraction of residual twins remains in the material throughout the cycle. During compressive loading, the intensity increases indicating the onset of twinning. The behavior during Cycle 500 is similar to that of Cycle 200, where the intensity does not return to zero during tensile loading, but detwinning does occur until the maximum tensile strain is reached. The intensity at the maximum tensile strain of Cycle 500 is higher than that of Cycle 200 indicating that the volume fraction of residual twins increases with increasing cycles.

To quantify the volume fraction of twins, ϕ, formed as a function of cycles, the apparent twin volume fraction was characterized using the relationship:

$$\phi = \frac{I_{LD}}{I_{ND}^{0}} (2)$$

where I_{ND}^{0} is the initial basal {0002} x-ray peak intensity of the parent grains in the normal direction and I_{LD} is the basal {0002} x-ray peak intensity in the loading direction at the maximum compressive strain. The value I_{LD} is termed the twin x-ray peak intensity and taken to be a measure of the maximum twin volume fraction during the cycle. The azimuthal data was averaged over an azimuthal length of 5 degrees. The twin x-ray peak intensity and the twin volume fraction are plotted as a function of number of fatigue cycles in Figure 3.8. The twin volume fraction more than doubles in the first five cycles and then gradually increases indicating that the most significant twinning occurs very early during cyclic loading. For the first 100 cycles, near-complete twinning and detwinning occurs, where the majority of the twins formed under compression are removed under the tensile loading of the following cycle. The stress at the initiation of twinning during the first 100 cycles is plotted as a function of cycles in Figure 3.9a. It was found that the twin initiation stress gradually increases with cycles. For example, in the sample fatigued at a total strain amplitude of 0.75%, in the first compression cycle, twinning initiated at -52 MPa but this stress decreases to -44 MPa in Cycle 2, indicating that additional plastic deformation occurred in the second cycle, resulting in the earlier formation of twins as the second cycle progressed. For the detwinning process, the stress at the exhaustion of detwinning during tensile loading was characterized and is shown in Figure 3.9b. This stress also gradually increased throughout the first 100 cycles indicating that more twins are formed during the previous cycle and therefore a higher stress is required to complete detwinning during the tensile loading of the following cycle.

Similar behavior was also observed in the sample cycled at 0.52% total strain amplitude (Figure 3.5). Figure 3.5 shows the hysteresis loops for cycles 1,2, 200 and 500 (at the fatigue half-life). As compressive load was applied in Cycle 1, twinning begins at a stress of -52 MPa (indicated by C-1). The intensity at this point for the basal {0002} peak in the loading direction increases as the intensity in the normal direction decreases confirming the beginning of twin formation as portions of some grains are reorienting their c-axis due to twinning. During tensile loading of the next cycle, the intensity returns to zero at 15 MPa (T-1) and remains zero until compressive loading commences. The diffraction data suggests that the exhaustion of detwinning occurs at this point, indicated by the decreasing intensity of the basal {0002} peak in the loading direction up until this point and the increasing intensity in the normal direction until the maximum tensile strain is reached. The detwinning behavior immediately begins to evolve in Cycle 2, twinning now begins at a stress of -46 MPa (C-2) which is indicated by the increase intensity from this point until the maximum compressive strain is reached. Similar to the specimen deformed to 0.75% strain, as tensile load is applied in Cycle 200, the x-ray peak intensity in the loading direction decreases until the maximum tensile strain is reached but never returns to zero due to the presence of residual twins. The stress at which twins were initiated also gradually increased with cycles as well as the stress at the exhaustion of detwinning (Figure 3.9a-b). The twin intensity and the twin volume fraction at 0.52% total strain amplitude significantly increases during the first five cycles (Figure 3.8a-b).

At 0.4% total strain amplitude, during cyclic loading up to 2000 cycles, no diffracted intensities in the loading direction were detected. Thus, only the intensity of

the {0002} basal peak in the normal direction is reported in Figure 3.6. The diffraction data suggests that the initiation of extension twins did not occur during cyclic loading at this strain amplitude and that plastic deformation occurred by crystallographic slip.

3.3.3 Internal Elastic Lattice Strain Evolution

Each family of planes has a unique lattice spacing that can be used to calculate the internal elastic lattice strains ϵ_{hkl} using the change in lattice spacing between the loaded and un-loaded patterns (Equation 3).

$$\epsilon_{hkl} = \frac{d_{hkl} - d^o_{hkl}}{d^o_{hkl}} (3)$$

where d_{hkl} and d^0_{hkl} are the lattice spacing's in the loaded and unloaded conditions, respectively. The relationship between the internal elastic lattice strain evolution and applied stress in the loading and normal directions for the 0.52% total strain amplitude sample can be found in Figure 3.10. Figure 3.10a shows the initial tensile loading for Cycle 1. During this initial loading, the ease for basal slip influences the internal elastic strain behavior for both the $(10\acute{1}1)$ and $(10\acute{1}0)$ grains. In the loading direction (Figure 3.10a) the $(10\acute{1}1)$ grains plastically yield at ~45MPa while the elastic strains for the $(10\acute{1}0)$ grains continue to increase until the maximum tensile stress is reached indicating that $(10\acute{1}1)$ grains are favorably oriented for basal slip while the latter are not. This observation is also supported by the higher internal elastic strain in the $(10\acute{1}0)$ grains during tensile loading. In the normal direction, the internal lattice strain due to Poisson's contraction for the (0002) and $(10\acute{1}1)$ grains are the same while the $(10\acute{1}0)$ grains had the highest internal lattice strain when compared to the other orientations. The curves in the normal direction are also steeper than those in the loading direction which is explained in the discussion section.

As the sample is unloaded and compressed (Figure 3.10b and Figure 3.10c), in the LD direction, the internal lattice strain of the $(10\acute{1}1)$ grains decreases until -35MPa where it then plateaus until the compressive yield strength is reached. Concurrently, the slope of the stress-internal strain curve in the $(10\acute{1}0)$ also decrease slightly. It should be noted in Figure 3.10C that, due to the Poisson's effect, in the ND direction the (0002) grains are placed in a tensile strain state along their c-axis which is necessary for "extension" twinning to occur. When the sample starts to plastically deform by twinning at -52 MPa, the (0002) grains in the normal direction are relaxed relative to the stress field in the neighboring grains (Figure 3.10c). At the same time, the LD curves for the $(10\acute{1}1)$ and $(10\acute{1}0)$ grains deviate from linearity suggesting that twinning is also causing plastic relaxation in those grains during compressive loading (Figure 3.10c).

In contrast, while the compressive load is removed (Figure 3.10d), the internal elastic strain decreases at the same pace for all of the orientations due to the elastically isotropic behavior of Mg. The $(10\acute{1}0)$ and $(10\acute{1}1)$ grains contain a very small residual compressive strain at ~0MPa. At -6MPa the internal strain in the (0002) grains in the loading direction changes sign and beyond this point the (0002) grains are placed in a tensile stress state along their c-axis (ND direction) which is important for promoting detwinning during reloading.

In the final portion of a cycle (Figure 3.10e), plastic deformation is dominated by detwinning. At the transition to dislocation-slip-dominated deformation the (0002) grains disappear since detwinning is complete. The $(10\acute{1}1)$ grains are favorably oriented for basal slip and near 50 MPa the grains plastically yield and slow down their elastic loading. At the same time, the elastic loading continues in the $(10\acute{1}0)$ oriented grains.

3.3.4 In-plane Tension-Compression Asymmetry

The twinning in compression and detwinning during reversed loading observed in unalloyed Mg is responsible for the tension-compression stress asymmetry normally seen in wrought Mg alloys. The maximum tensile and compressive stresses at Cycle 2 are listed in Table 3.1. Note: two samples were tested at 0.52% and 0.75% total strain amplitudes while only one sample was tested at 0.4% total strain amplitude. The anisotropic behavior was more significant at higher strain amplitudes (0.52% and 0.75%) when compared to the lower strain amplitude of 0.4%. The maximum tensile stress at 0.75% strain amplitude was 16 MPa more than the compressive maximum stress of -52 MPa. At 0.4% strain amplitude, the differences in the tensile and compressive maximum stress at Cycle 2 are negligible which also confirms that the deformation was slip-dominated at this strain level.

The diffraction results suggest that twinning and detwinning occur alternately during cyclic loading. To image this mechanism during cyclic deformation, strain-controlled, ex-situ, monotonic tension and compression experiments were performed at 0.6% total strain amplitude on rectangular flat specimens. The samples were polished prior to loading and periodically characterized using electron back scatter diffraction. Samples were examined at zero load after straining in a servo-hydraulic test machine. Figure 3.11 shows the evolution of microstructure during loading. The initial microstructure is shown in Figure 3.11a. The black circles on each image outline areas of interest. After the initial compressive loading to -0.6% strain, twins were formed in the grains outlined by the black circles (Figure 3.11b). During tensile loading to +0.6% strain, in those same grains the twins were no longer observed indicating that the twins

formed during compression were removed during the tensile loading stage of the following cycle (Figure 3.11c).

3.4. Discussion

In this study, the twinning-detwinning behavior observed during low cycle fatigue of unalloyed Mg was characterized using in-situ HEXD. The intensity of the {0002} basal peak was monitored throughout each cycle and was used to characterize twinning and detwinning. Moreover, the stress at which twinning initiates and detwinning is exhausted was quantified using this technique. In addition, evolution of the twinning and detwinning behavior with increasing number of cycles applied was monitored. The cyclic fluctuations in twinning and detwinning that were measured in this paper are critical for accurate modeling of cyclic deformation in Mg alloys.

In Mg alloys, straining along the HCP c-axis can only occur by pyramidal <c+a> slip or deformation twinning [47-51]. In many Mg alloys, the CRSS for <c+a> slip is substantially higher than that for twinning and thus twinning is the preferred and dominant mode of non-basal deformation. Of the many HCP twin modes, the $\{10\acute{1}2\}\langle 10\acute{1}1\rangle$ extension twins are the most common [49-50]. These extension twins create a strong asymmetry between the in-plane tension and compression yielding behavior. In samples with a basal texture commonly found in extrusions and rolled sheet materials, these so-called "extension" twins form perpendicular to the loading axes during compression of samples loaded along the extrusion or rolling direction. Upon their formation, twins introduce a new orientation into the grain and within twins, slip systems can be preferred that are different from those of the parent grain and thus influence the macroscopic stress-strain response of the material during loading [32]. A model by Knezevic et al found that during reversed tensile loading, twins developed

during compression can impede slip that is non-coplanar to the twin boundaries; they can also provide domains for new slip modes or they can de-twin [32].

3.4.1 In-Situ HEXD characterization of twin evolution

It was determined that the onset of twinning could be related to the increase in the basal {0002} peak intensity in the loading direction. At strain amplitudes 0.52% or greater, the initiation of twinning occurs at lower stresses as cycling continues (Figure 4.9) which suggests that twinning becomes easier as cycling continues. Both the maximum compressive strain and maximum x-ray peak intensity in the loading direction also increases (Figure 3.8) indicating that the number of twins formed also increases. This was confirmed using a normalized peak intensity given by Equation 2, and it was observed that the apparent twin volume fraction more than doubles in the first five cycles at both strain amplitudes. A diffraction study by Wu et al found similar results for the Mg alloy, ZK60A, where compressive yielding occurred at lower stresses during the second cycle and the intensity of the basal {0002} peak was increased for Cycle 2 which indicated that an increase in twinning occurred during the second cycle [15].

In Mg alloys, twins created during previous compressive loading gradually disappear during compressive unloading and/or tensile reloading. This detwinning has a significant effect on the stress-strain response of the material since it requires reorientation of portions of the grain back to the original orientation (prior to twinning) via a change in the size of the twin or complete removal of twin boundaries [44,52]. The occurrence of detwinning during strain path changes has also been observed in HCP zirconium and hcp beryllium [44]. A detwinning model by Proust found that in Zr detwinning occurred due to internal twinning within the primary twin [44]. In the current study at both strain amplitudes, the detwinning occurred immediately upon reversal of

the maximum compressive strain. This was evident as the twin intensity continually decreases from the compressive peak until the end of the cycle. The reorientation of twinned regions to their original orientation during detwinning was confirmed by the increase in the normal direction intensity during compressive unloading until the end of each cycle. The intensity at the end of each of cycle never returns to zero indicating that twins are not completely removed during compressive unloading and that there are twins left to be removed during tensile straining in the following cycle. Within the first 100 cycles at 0.75% strain amplitude and 200 cycles at 0.52% strain amplitude complete twinning-detwinning occurs in which the twins that formed during compressive loading appear to be fully removed during reverse loading in tension. This is indicated in the diffraction data at the point where the twin intensity returns to zero during reverse loading. During these early cycles, as cycling increases the tensile stress at which detwinning is complete (the twin exhaustion stress) more than doubles, because a larger volume fraction of twins is available to be detwinned and consequently a higher tensile stress is needed to remove twins (Figure 3.9b). This is confirmed by the observation that the twin intensity increases with increasing cycles indicating that the twin volume fraction is also increasing. Similar behavior has been reported in literature. Wu et al showed that, in ZK60A, as the volume fraction of twins increased with cycles, additional tensile strain was needed to detwin the material on the following cycle. Muransky et al found that in AZ31 the driving force for detwinning comes from the high tensile stresses produced in favorably oriented grains prior to tensile unloading [51].

After a number of cycles, some twins are not fully detwinned and thus "residual" twins remain in the material throughout each cycle. As a result, the twin intensity never

returns to zero during tensile loading and increases from cycle to cycle indicating that, after a certain incubation time, the residual twin content increases with increasing numbers of cycles (Figure 3.12). This behavior has been observed in several other studies [7,15,22]. A diffraction study by Brown et al showed that the residual twin content increased with cycling in the Mg AZ31B alloy [22]. Mirza et al found residual twins in regions near the fracture surface after low cycle fatigue in the Mg alloys, GW103K and AM30 [7]. Wu et al also determined that the residual twin content in ZK60A made twinning-detwinning more difficult, contributing to hardening during compression and softening during tension [15]. The residual twin content contributes to the hardening of the material as twin boundaries can act as barriers to dislocation motion. It has been proposed that residual twins may also "retwin" in situations in which there is repeated growth of the residual twin as cycling continues [29]. This retwinning is the repeated cyclic growth of a residual twin that has not been completely detwinned [53]. This repeated growth of residual twins may also cause an increase in the basal peak intensity in the loading direction during compressive loading since such twins would be increasing in size. A study by Q. Yu et al found that retwinning of residual twins occurred during compression of a unalloyed Mg single crystal [29].

3.4.2 In-Situ Measurements of Internal Elastic Strain Evolution

Although elastic grain strains are linearly related to individual grain stresses [17,54-55], they are not necessarily linearly related to the applied stress due to stress redistribution at the grain level. Deviations from linearity (vs applied stress) indicate that stress has been redistributed between different grains in the material [17, 54-55] because of the differences in their propensity for yielding due to differences in orientation, size, or neighborhood. Once grains yield macroscopically, soft-oriented

grains begin to plastically deform and the change in elastic strain with applied stress abruptly decreases resulting in a near vertical line [17, 54-55]. At the same time, grains in a hard orientation begin to accept more of the applied stress leading to a rapid increase in their elastic loading [17,54]. The load redistribution between hard and soft oriented grains has also been observed in composite materials [56-57].

In this study, the $(10\acute{1}1)$ grains were favorably oriented for basal slip and therefore yield more easily during tensile loading causing their internal elastic strains to accumulate at a slower rate as the applied stress increases (Figure 3.10a). The $(10\acute{1}0)$ grains must then accept a higher amount of the applied stress leading to an increase in the elastic loading of these grains (Figure 3.10a). Once twinning is activated during compression, the internal strains of the $(10\acute{1}0)$ and $(10\acute{1}1)$ grains are relaxed as more grains are becoming basal oriented (Figure 3.10c) and decrease more slowly with applied stress. Also, the internal strain accumulation in the (0002) grains in the normal direction decrease due to stress relaxation. The slight yielding observed in the $(10\acute{1}0)$ during compressive loading suggests that <c+a> pyramidal dislocations may play a small role plastic deformation. Xie et al found that pyramidal I slip was the dominant non-basal slip mode during compressive loading of unalloyed Mg single crystals and that these sources generated a small amount of plastic strain when compared to basal sources [58]. When the twinned grains are exhausted during tensile reloading (Figure 3.10e), the (0002) grains are hard with respect to deformation by basal slip and therefore, plastic deformation continues through activation of harder, non-basal slip systems or $\{10\acute{1}1\}\langle 10\acute{1}2\rangle$ compression twinning and the internal strain in these grains increases with stress [17]. However, grains in a soft orientation such as the $(10\acute{1}1)$

grains yield and slow down their elastic loading while the hard oriented $(10\acute{1}0)$ grains accept more of the applied stress and their internal strain accumulates at a higher rate [17]. Agnew et al found similar behavior in the Mg alloy AZ31B, where during micro-yielding the internal strains in all of the grain orientations deviated from linear elastic loading [17]. Wu et al also found that during compressive loading of AZ31, the internal strain rapidly transferred to the (0002) twin grains during macroscopic yielding while the internal elastic strain $(10\acute{1}1)$ grains increased slowly until it saturated [37]. In this work, the internal lattice strains of the observed grain orientations decrease at the same pace due to the near-elastic isotropic behavior of Mg (Figures 3.10d) during compressive loading, suggesting that little plastic deformation is occurring during unloading and that the internal strain is mainly controlled by detwinning. Wu et al found similar behavior during compressive unloading of the Mg alloy, ZK60A [55].

The slopes of the internal elastic strains versus applied stress in the normal direction are much steeper than those in the loading direction since they are mainly produced by Poisson constraint effects. A normal Poisson strain produces a tensile strain perpendicular to an applied compressive strain [17,55,59]. This has also been shown in Mg alloys and steels. Lorentzen et al found that internal strains in the transverse direction in a stainless steel were smaller than in the longitudinal direction [59]. Wu et al also found that in AZ31 the slopes in the transverse direction were steeper and that the strains were much smaller when compared to the strains in the longitudinal direction [55].

3.4.3 The Influence of Twinning-Detwinning on the Tension-Compression Asymmetry

The alternating occurrence of twinning and detwinning during cyclic loading of unalloyed Mg results in the tension-compression strength asymmetry that was found at 0.52% and 0.75% total strain amplitudes. The maximum tensile stress was more than 10 MPa higher than the maximum compressive stress at both strain amplitudes (Table 3.1) Many studies have related the asymmetry to the different deformation mechanisms occurring during tension and compression. The flow stress in compression is related to the stress required to activate twinning (and possibly retwinning) while the flow stress during tension is controlled by detwinning and crystallographic slip. This is corroborated by the findings of Begum et al who found that the tensile yield strength was much higher than the compressive yield strength during low cycle fatigue of an AM30 extruded Mg alloy due to twinning during compression and detwinning during tension [5].

Table 3.1: Maximum cyclic compressive and tensile stress at Cycle 2 for 0.40%, 0.52%, and 0.75% total strain amplitudes.

Total Strain Amplitude (%)	Maximum Tensile Stress (MPa)	Maximum Compressive Stress (MPa)
0.40	50	-47
0.52	65±0.7	-51±3
0.75	68±2	-52±0.0

The tension-compression asymmetry found at the higher strain amplitudes was not observed in samples strained at 0.4% total strain amplitude and is related to the absence of twinning as evidenced by the absence of diffracted intensity appearing in the loading direction during cyclic loading. The lack of extension twinning in this condition also resulted in equivalent maximum tensile and compressive stresses. Similar results were reported by Yu et al, who conducted tests at low strain amplitudes in unalloyed Mg and observed that deformation was dominated by slip on basal and non-basal planes

rather than twinning and detwinning [3]. A study by Begum et al found that the asymmetry was increased at higher strain amplitudes due to increased twinning during compression in the Mg alloy, AZ31 [5].

3.5. Conclusions

The twinning-detwinning behavior in unalloyed Mg extrusions during cyclic deformation was studied using in-situ high energy x-ray diffraction techniques. The major conclusions are as follows:

1. An increase or decrease in the {0002} basal x-ray peak intensity in the loading direction was observed during cyclic loading and can be directly related to $\{10\acute{1}2\}\langle 10\acute{1}1\rangle$ extension twinning and detwinning.
2. The twin volume fraction and twin intensity doubles in the first five cycles, then gradually increases until failure. This finding indicates that twin evolution is more active earlier during cyclic loading.
3. The compressive stress at which twinning initiates decreases with cycling, indicating that twin-associated plastic flow is increasing on every cycle with twins forming earlier in the cycle.
4. A detwinning exhaustion stress under reversed tensile loading, at which detwinning is completed, was characterized using HEXD. This stress increases with cycling; as the twin volume fraction increases, a higher tensile stress is needed to detwin the material during the following cycle.
5. Near-complete twinning and detwinning occurred for the first few hundred cycles where all twins formed during compressive loading appear to be removed during reverse loading.

6. At higher numbers of cycles, complete detwinning was not observed and HEXD results indicated that residual twins remain in the material throughout each cycle and the amount of these residual twins increased with increasing cycles.
7. The above conclusions were for applied strains of 0.52% and above. At an applied strain of 0.4% no indication of twinning was observed in either the stress-strain loop behavior or in the HEXD measurements.

Figures

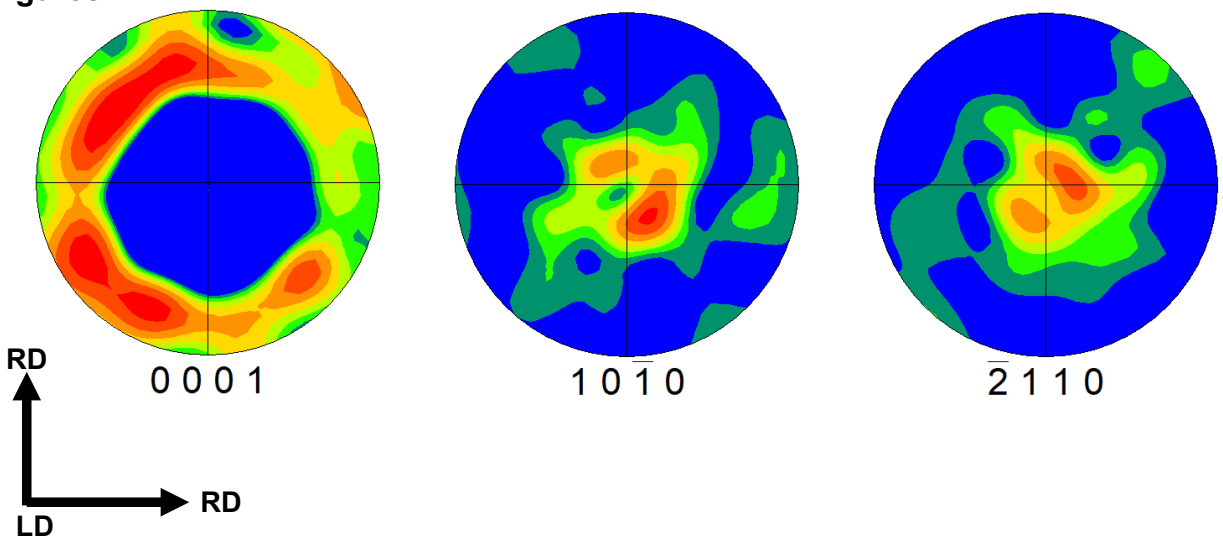

Figure 3.1: Pole figures showing the initial texture with the basal poles aligned perpendicular to the loading direction. LD: Loading Direction (Extrusion Direction); RD: Radial Direction (normal to the loading direction).

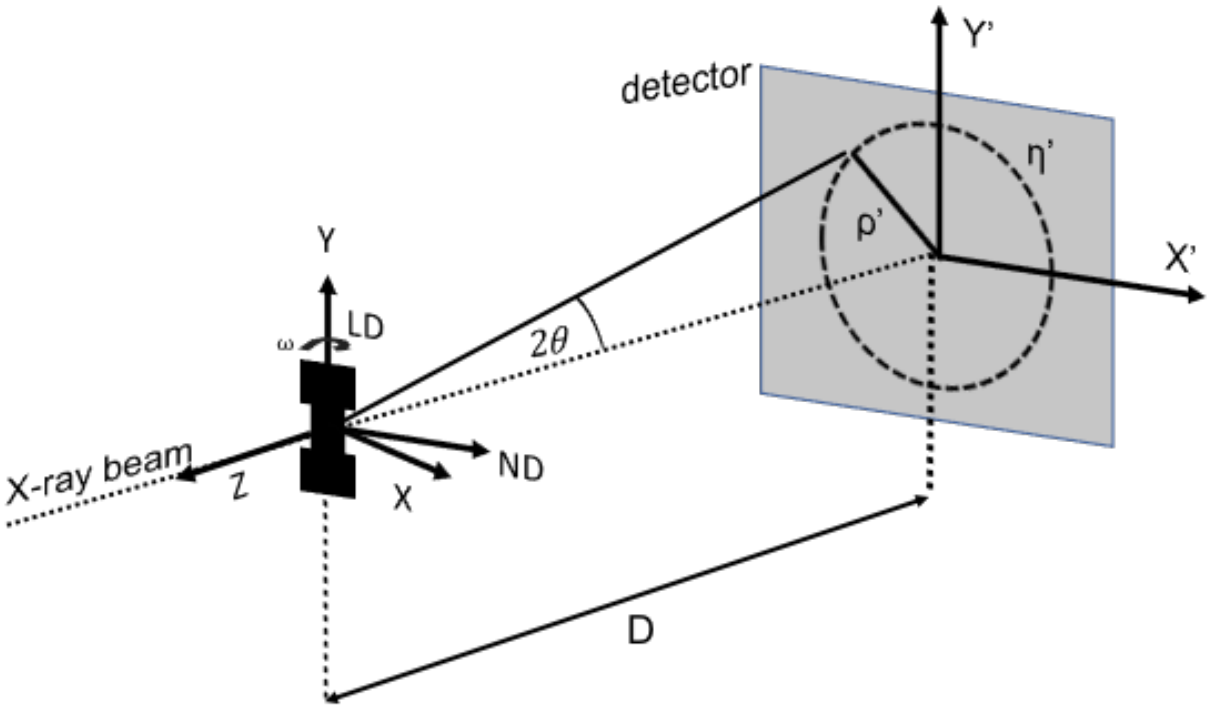

Figure 3.2: Schematic of the diffraction experiment detailing the specimen geometry in relation to the detector as well as the coordinate systems. The detector coordinate system can either be described using the rectangular coordinate system [X,Y,Z] or a polar coordinate system [2θ,η], where 2θ is the Bragg angle, η is the azimuthal angle, and D is the distance from the sample to the detector. During the experiment the

laboratory system is fixed while the sample is free to rotate about the loading axis defined by angle, ω [42].

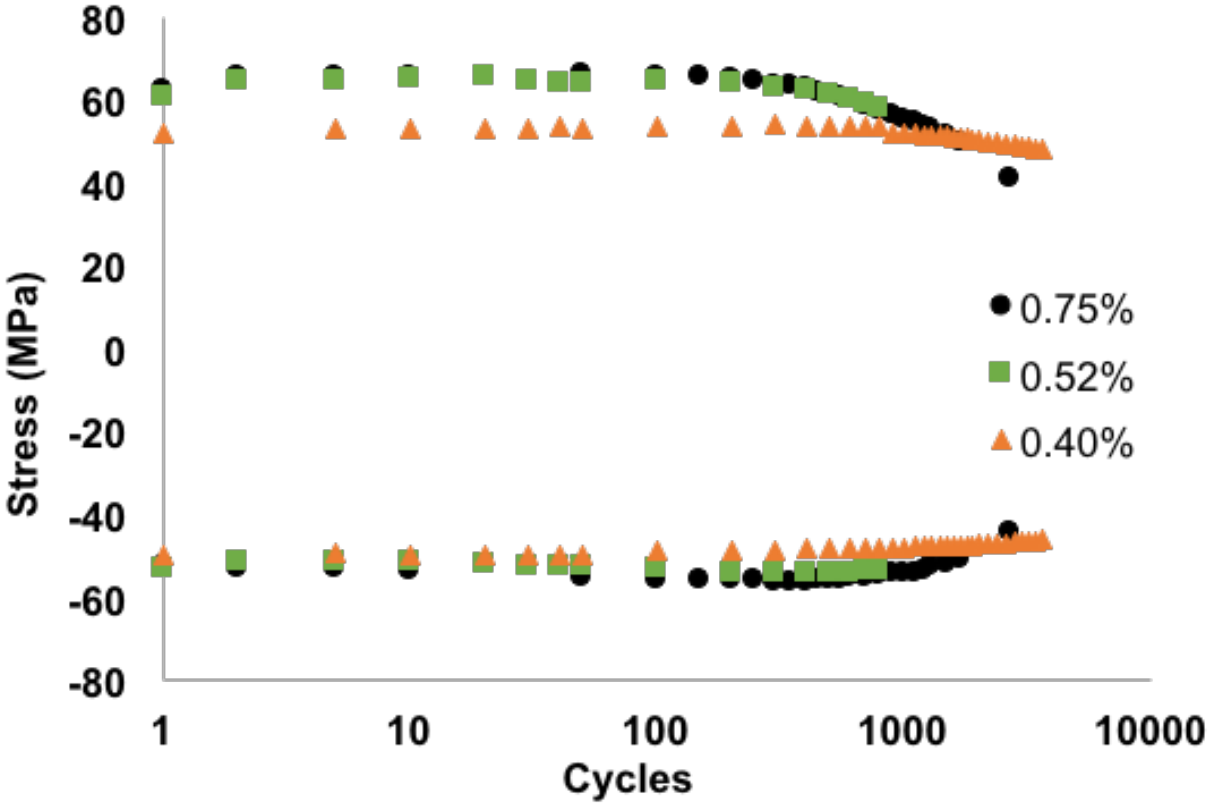

Figure 3.3: The cyclic stress response in tension and compression as a function of fatigue cycles at the total strain amplitudes of 0.4%, 0.52%, and 0.75%.

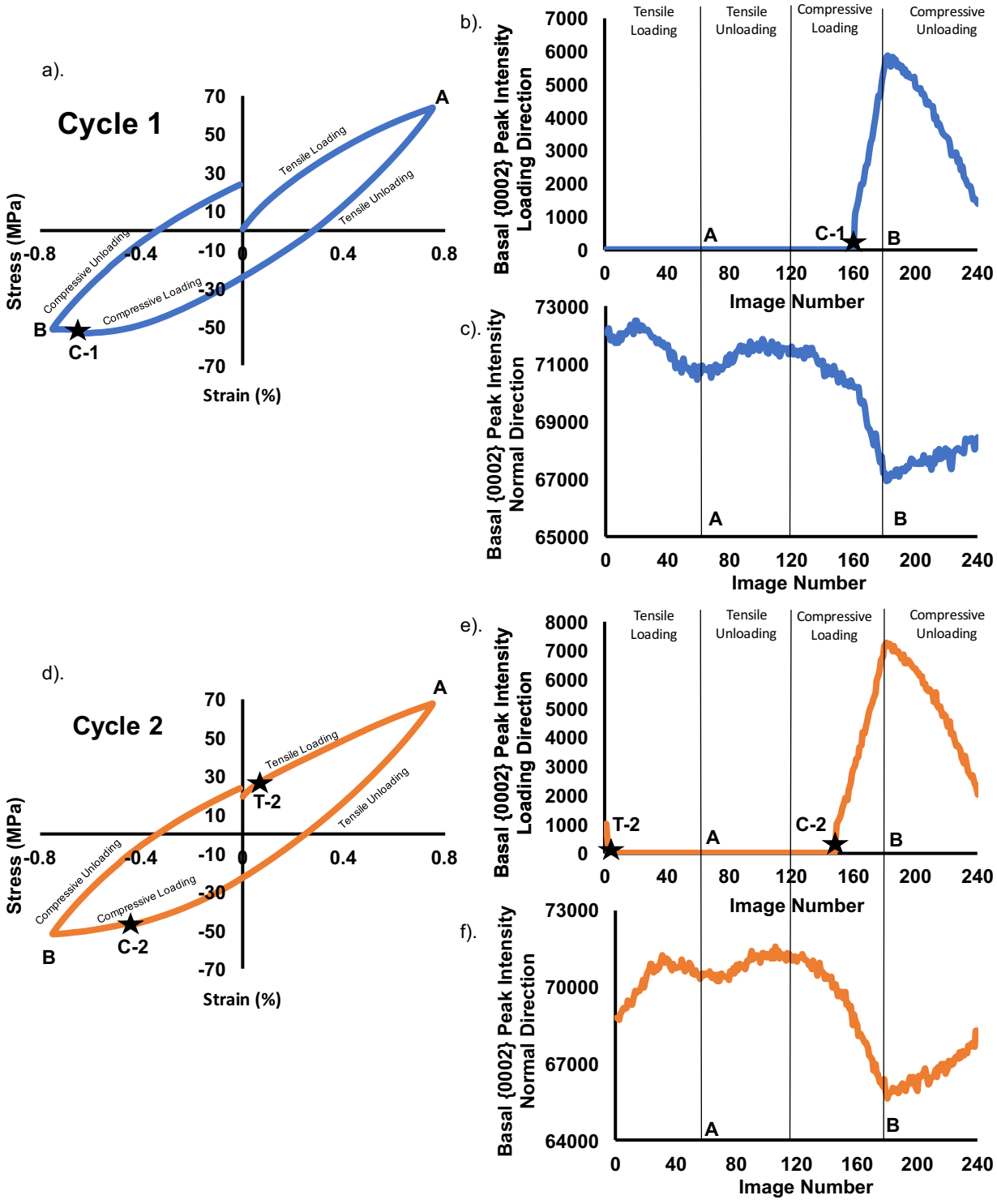
a).
Cycle 1
Stress (MPa)
Strain (%)
Tensile Loading
Tensile Unloading
Compressive Unloading
Compressive Loading
A
B
C-1
b).
Basal {0002} Peak Intensity Loading Direction
Tensile Loading
Tensile Unloading
Compressive Loading
Compressive Unloading
Image Number
c).
Basal {0002} Peak Intensity Normal Direction
d).
Cycle 2
T-2
C-2
e).
f).

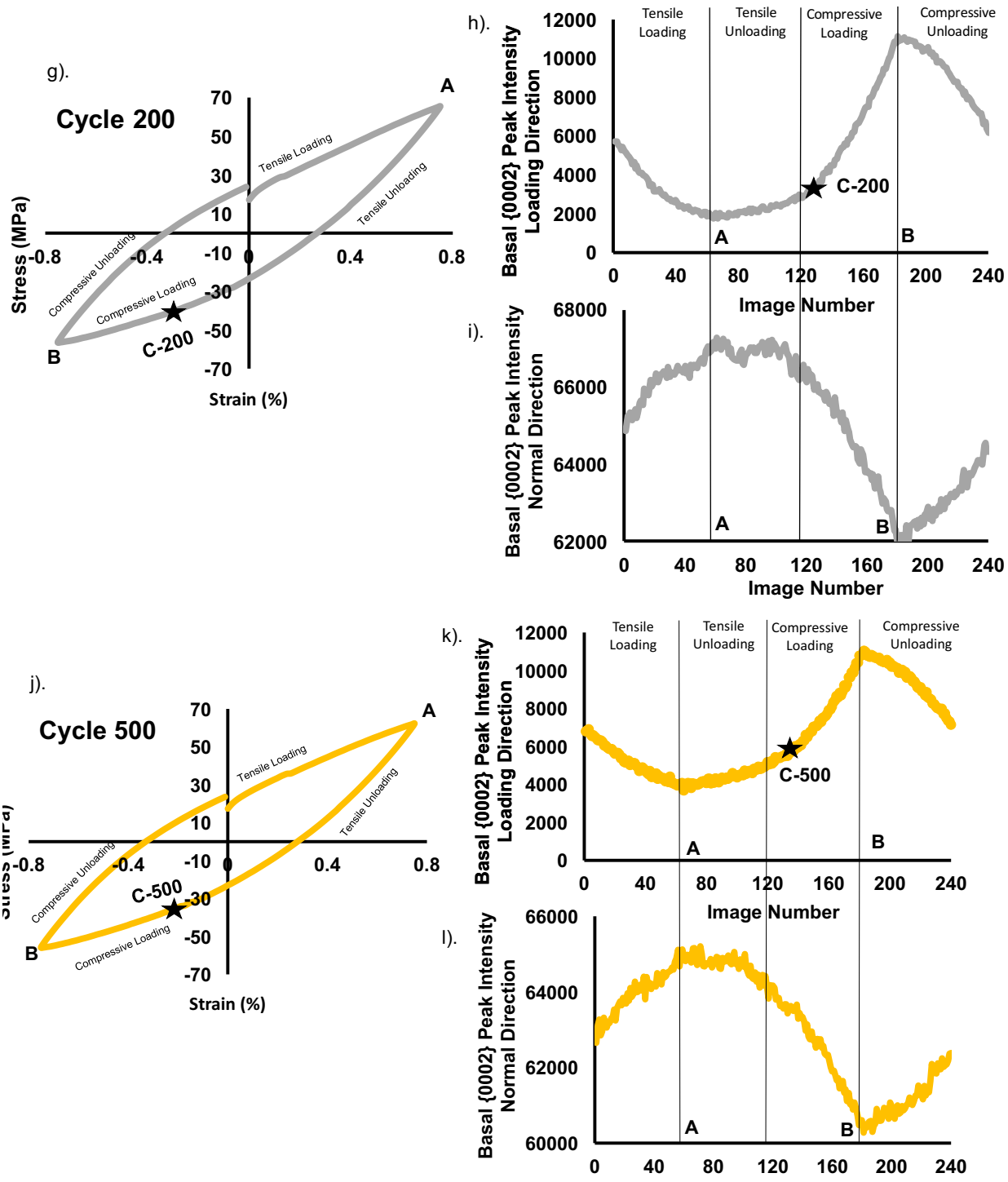

Figure 3.4: Cyclic stress-strain loops and corresponding x-ray peak intensity of the basal {0002} peak for tests conducted at a total strain amplitude of 0.75% a-c) Cycle 1,

d-f) Cycle 2, g-i) Cycle 200, & j-l) Cycle 500. HEXD peak intensities in the Loading Direction (Figure 4b,e,h,k) indicate the onset of twinning and detwinning; HEXD peak intensities in the Normal Direction (Figure 4b c, f, i, l) indicate the activation of other slip systems. Note: Vertical lines at Image 0 and Image 120 are at zero strain. Vertical lines at Image 60 and 180 are at peak tensile strain and peak compressive strain, respectively.

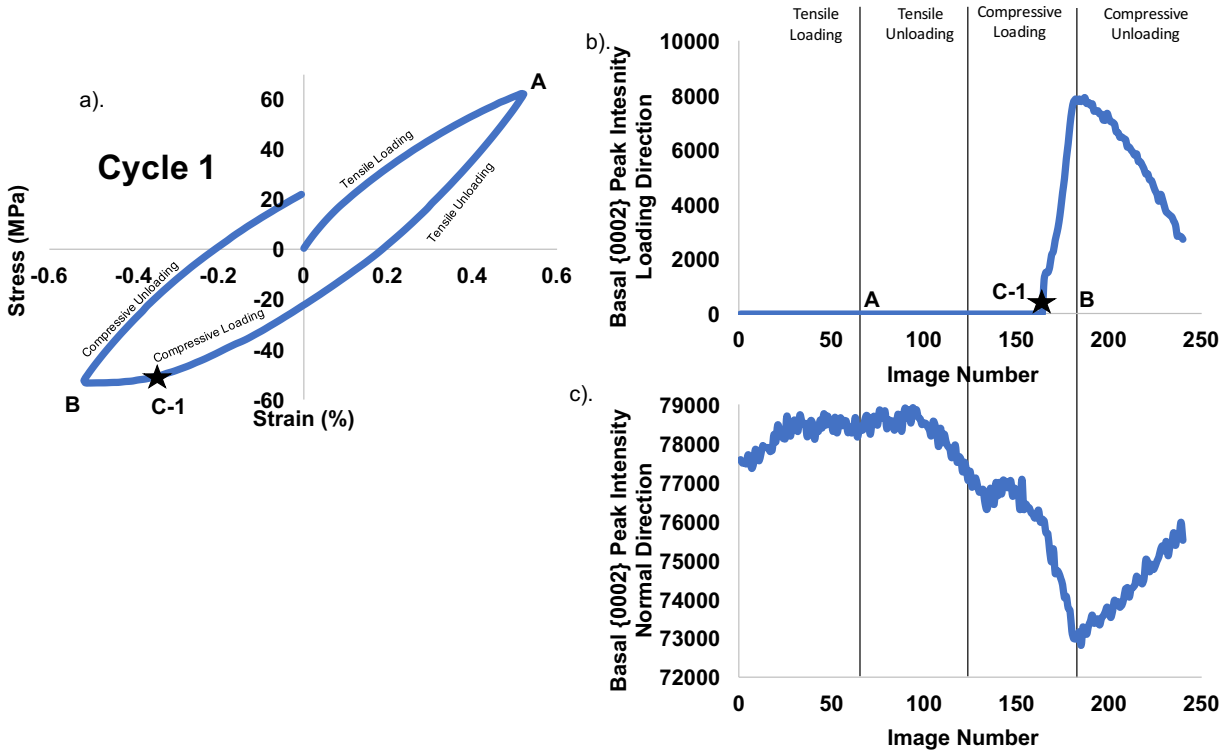

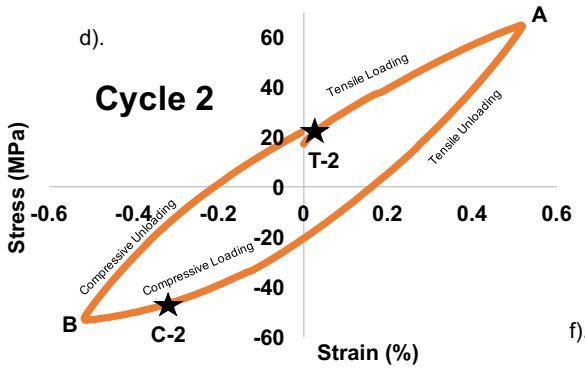
d).
Cycle 2
Stress (MPa)
Strain (%)
Tensile Loading
Tensile Unloading
Compressive Unloading
Compressive Loading
T-2
C-2
A
B

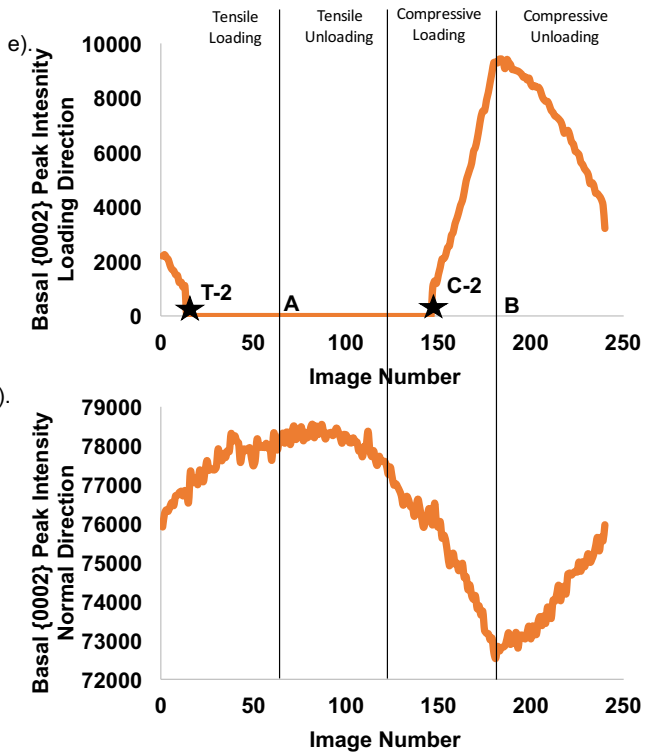
e).
Tensile Loading
Tensile Unloading
Compressive Loading
Compressive Unloading
Basal {0002} Peak Intesnity Loading Direction
Image Number
T-2
C-2
A
B
f).
Basal {0002} Peak Intensity Normal Direction
Image Number

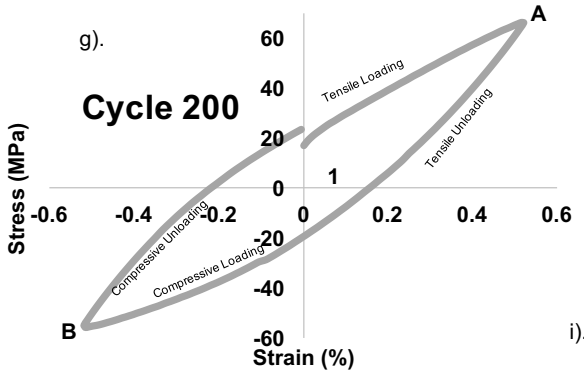
g).
Cycle 200
Stress (MPa)
Strain (%)
Tensile Loading
Tensile Unloading
Compressive Unloading
Compressive Loading
1
A
B

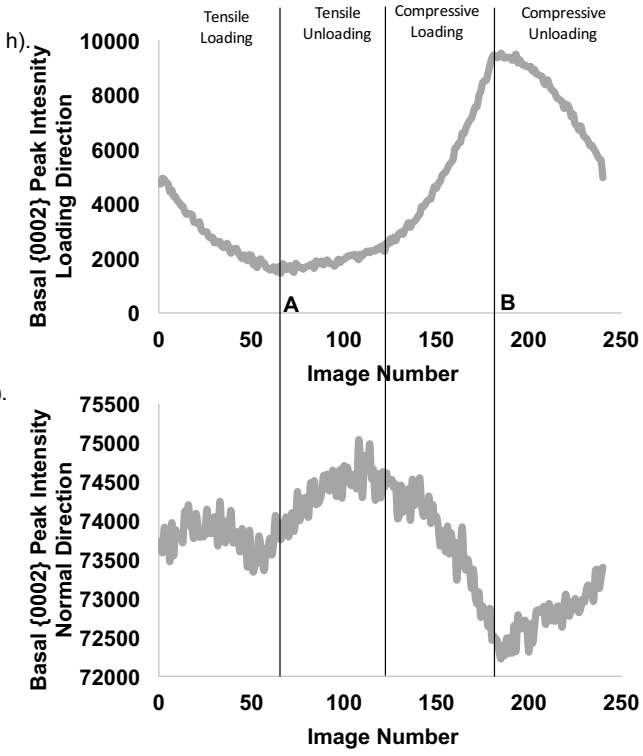
h).
Tensile Loading
Tensile Unloading
Compressive Loading
Compressive Unloading
Basal {0002} Peak Intesnity Loading Direction
Image Number
A
B
i).
Basal {0002} Peak Intensity Normal Direction
Image Number

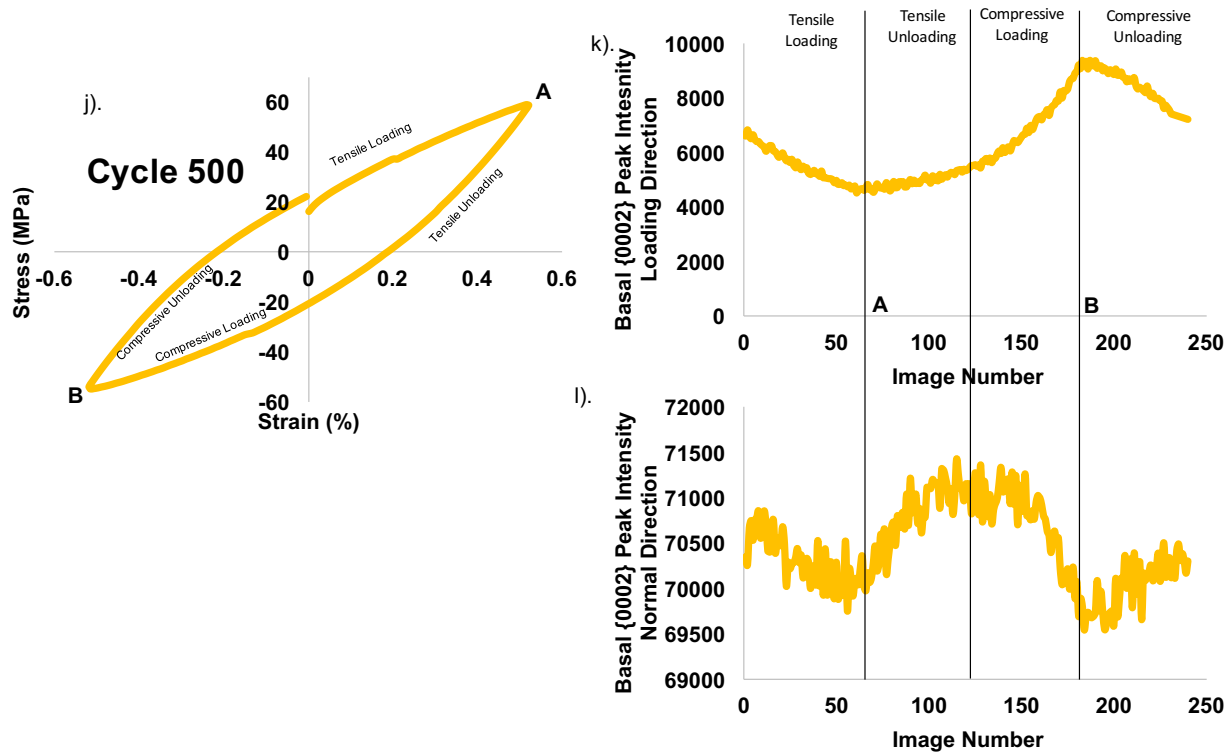

Figure 3.5: Cyclic stress-strain loops and corresponding x-ray peak intensity of the basal {0002} peak for tests conducted at a total strain amplitude of 0.52% a-c) Cycle 1, d-f) Cycle 2, g-i) Cycle 200, & j-l) Cycle 500 HEXD peak intensities in the Loading Direction (Figure 5 b, e, h, k) indicate the onset of twinning and detwinning; HEXD peak intensities in the Normal Direction (Figure 5c, f, i, l) indicate the activation of other slip systems. Note: Vertical lines at Image 0 and Image 120 are at zero strain. Vertical lines at Image 60 and 180 are at peak tensile strain and peak compressive strain, respectively.

.

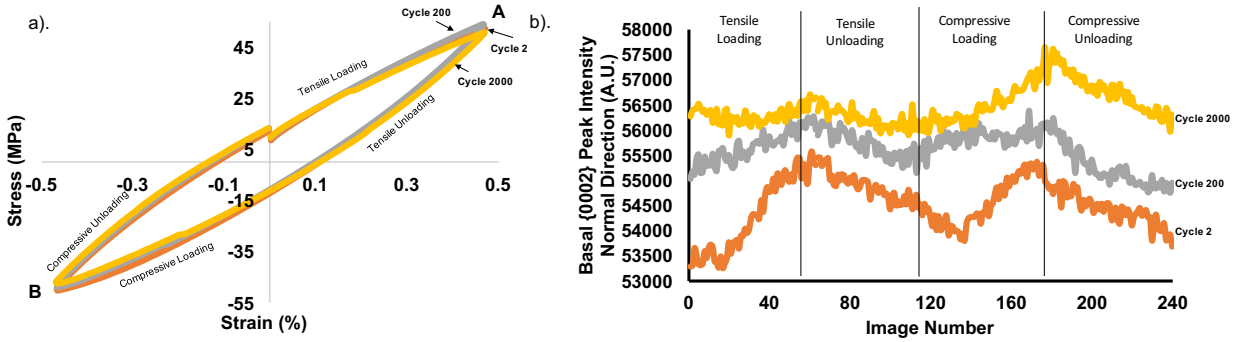

Figure 3.6: Cyclic stress-strain loops and corresponding x-ray peak intensity of the basal {0002} peak for tests conducted at a total strain amplitude of 0.4%. a) Stress-strain loops for Cycles 2, 200, & cycle 2000; b) HEXD of the x-ray peak intensity for the basal {0002} planes in the normal direction. Note: HEXD measurements in the loading directions indicated intensities of zero, indicating no twinning. Note: Vertical lines at Image 0 and Image 120 are at zero strain. Vertical lines at Image 60 and 180 are at peak tensile strain and peak compressive strain, respectively.

.

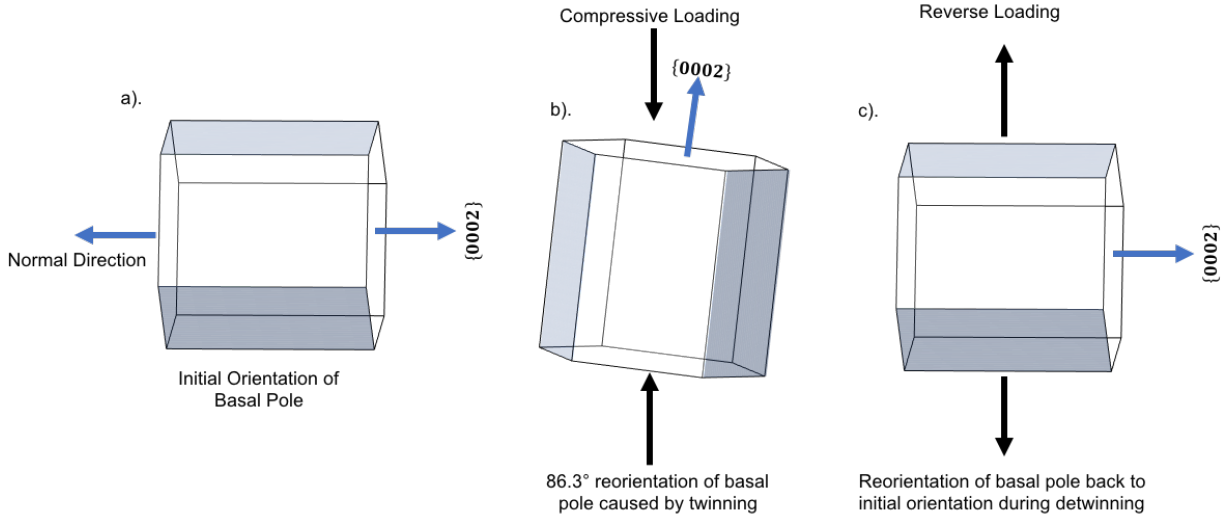

Figure 3.7: Orientation changes between parent grains and twinned regions for compression and reverse tensile loading: a) the initial orientation of the {0002} basal pole (c-axis) for the parent grain is normal to the loading direction, b) during compressive loading as the twins form the c-axis is reoriented 86.3° toward the loading direction in the twins and c). during reverse tensile loading as twins are removed (detwinning) the c-axis is returned to the initial orientation of the parent grain.

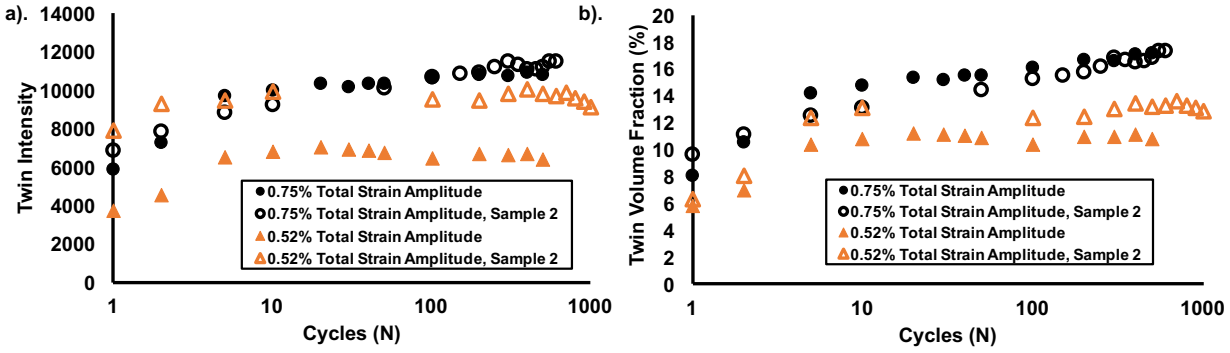

Figure 3.8: The a) twin x-ray peak intensity (at the maximum compressive strain) and b) apparent twin volume fraction (at the maximum compressive strain) calculated using equation 1 at both 0.75% and 0.52% total strain amplitudes.

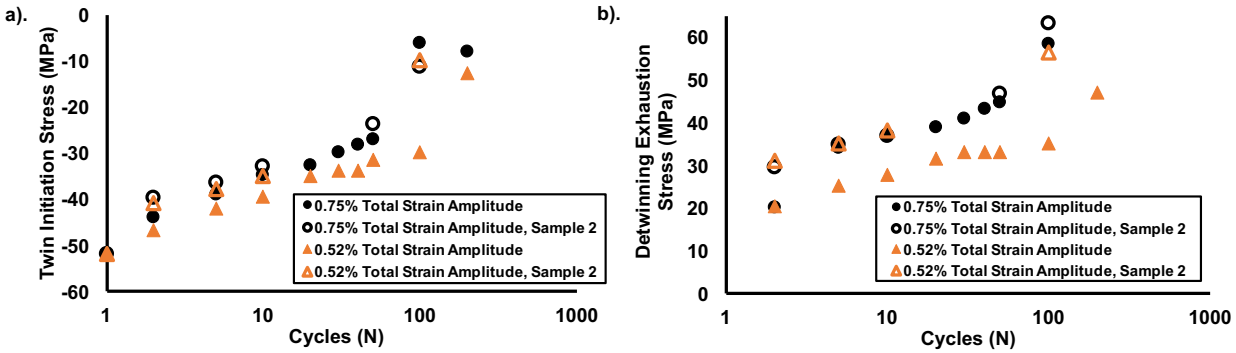

Figure 3.9: a)The stress at the initiation of twinning and b) the stress at the completion of detwinning for both 0.75% and 0.52% total strain amplitudes.

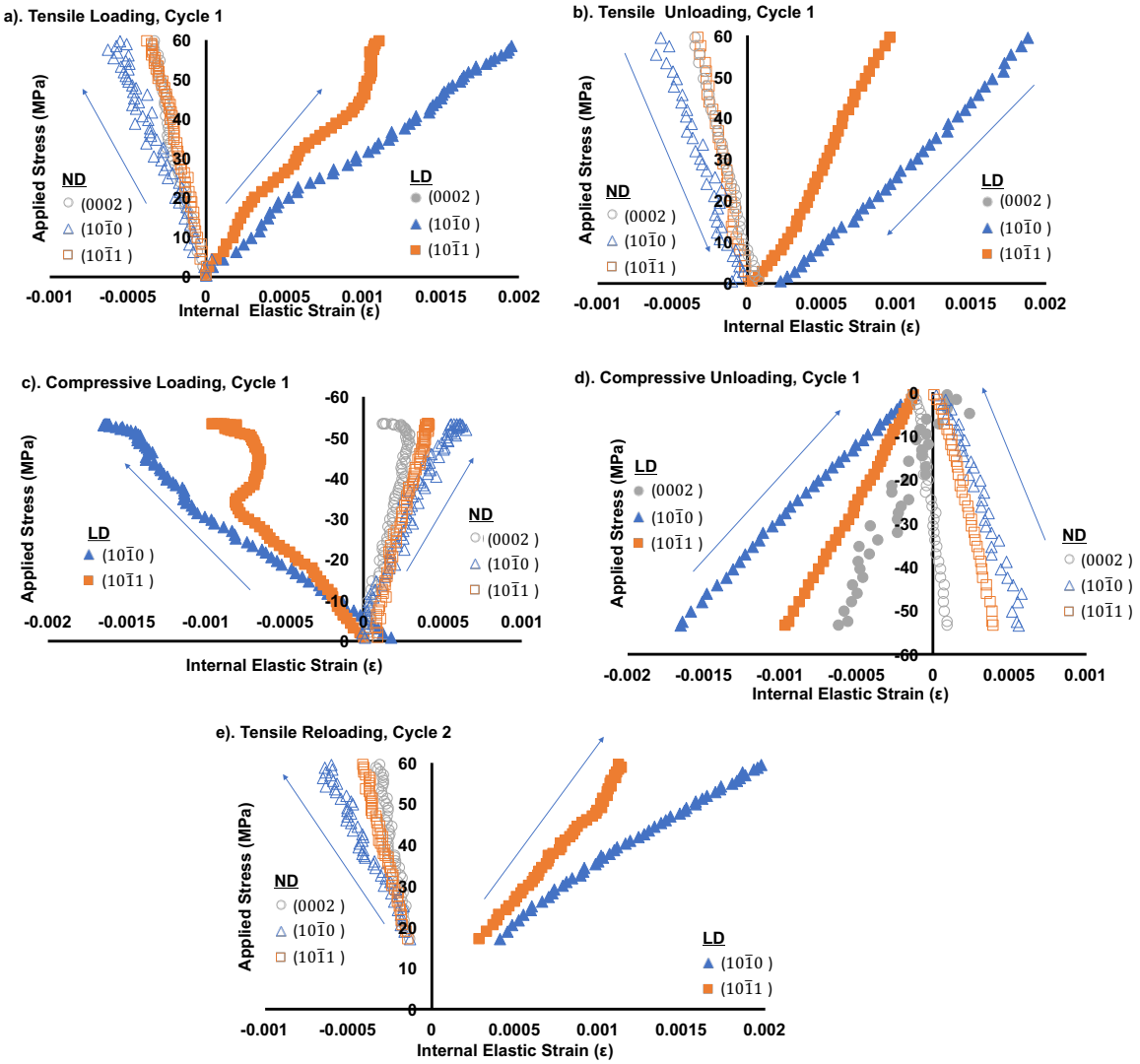

Figure 3.10: The internal elastic lattice strain evolution at 0.52% total strain amplitude during a) tensile loading, b) tensile unloading, c) compressive loading, d) compressive unloading and e) tensile reloading. ND: Normal Direction and LD: Loading Direction

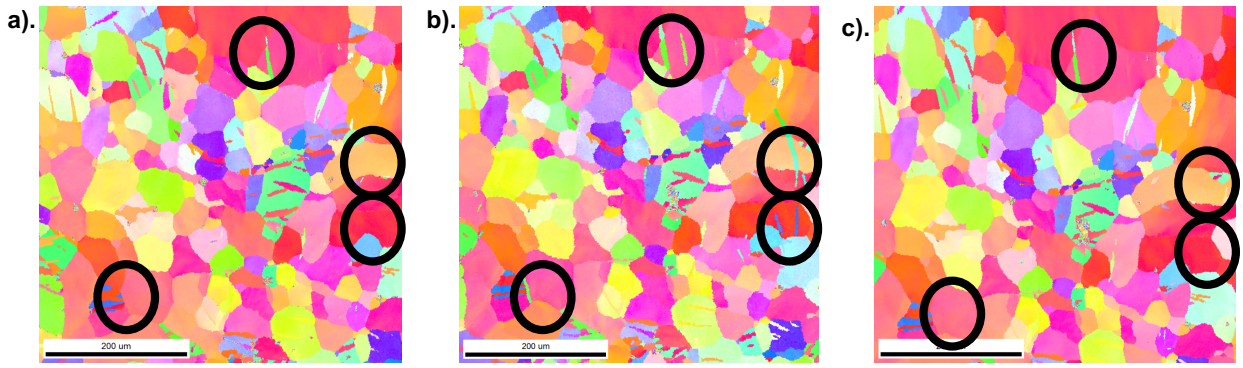

Figure 3.11: Electron back scatter diffraction patterns showing evolution of twinning and detwinning: a) as electro-polished condition (black circles denote areas of interest), b) twins form in grains outlined in black circles after compression to -0.6% strain and c) those same twins are removed after tension to +0.6% strain. All EBSD measurements were in the unloaded condition.

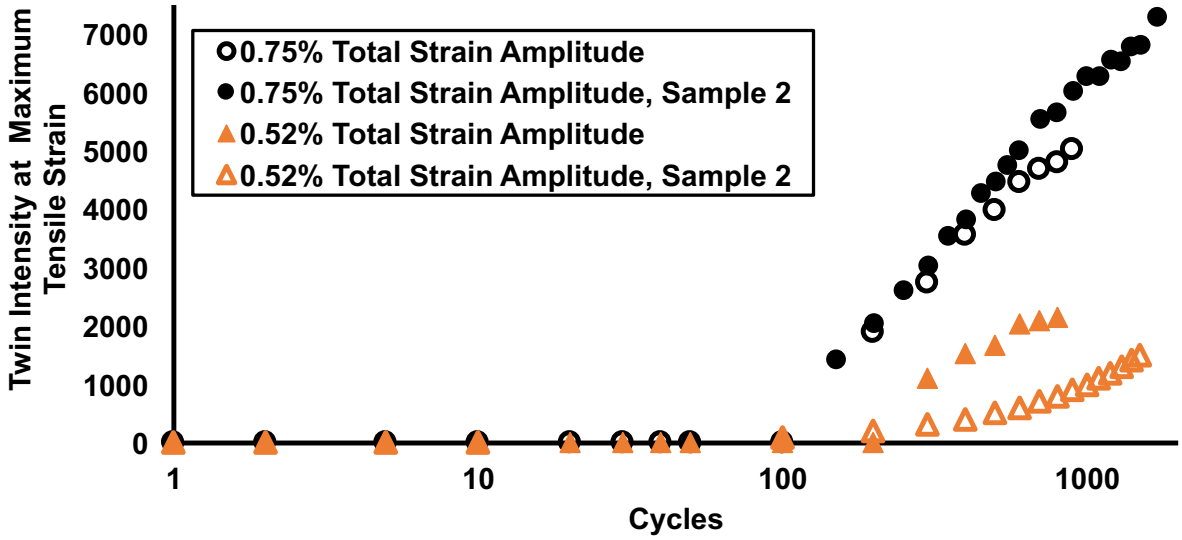

Figure 3.12: The twin intensity (intensity of the [0002] basal peak) at the maximum tensile strain for both 0.75% and 0.52% total strain amplitudes.

References

1. C. Bettles, M. Gibson, Current wrought magnesium alloys: strengths and weaknesses, J. Metals 57(2005) 46–49. https://doi.org/10.1007/s11837-005-0095-0
2. Q. Yu, Y. Jiang, J. Wang, Cyclic deformation and fatigue damage in single-crystal magnesium under fully reversed strain-controlled tension-compression in the [1010] direction, Scr. Mater. 96 (2015) 41–44. https://doi.org/10.1016/j.scriptamat.2014.10.020
3. Q. Yu, J. Zhang, Y. Jiang, Fatigue damage development in pure polycrystalline magnesium under cyclic tension-compression loading, Mater. Sci. Eng. A 528 (2011) 7816–7826. http://dx.doi.org/10.1016/j.msea.2011.06.064
4. S. Begum, D.L. Chen, S. Xu, A. Lou, Low cycle fatigue properties of an extruded AZ31 magnesium alloy, Int. J. of Fat. 31 (2009) 726–735. http://dx.doi.org/10.1016/j.ijfatigue.2008.03.009
5. S. Begum, D.L. Chen, S. Xu, A. Lou, Strain-controlled low-cycle fatigue properties of a newly developed extruded magnesium alloy, Metall. Mater. Trans A 39 (2008) 3014–3026. 10.1007/s11661-008-9677-0
6. F. Mokdad, D.L. Chen, Strain-controlled low cycle fatigue properties of a rare-earth containing ZEK100 magnesium alloy, Materials & Design 67 (2015) 436–447. https://doi.org/10.1016/j.matdes.2014.11.058
7. F.A. Mirza, D.L. Chen, D.J. Li, X. Q. Zeng, Low cycle fatigue of a rare-earth containing extruded magnesium alloy, Mater. Sci. Eng. A 575 (2013) 65–73. https://doi.org/10.1016/j.msea.2013.03.041
8. L. Chen, C. Wang, E.I.W. Wu, Z. Liu, G.M. Stoica, L. Wu, P.K. Liaw, Low-Cycle Fatigue Behavior of an As-Extruded AM50 Magnesium Alloy, Metall. Mater. Trans. A 38 (2007), 2235–2241. https://doi.org/10.1007/s11661-007-9181-y
9. X.Y. Lou, M. Li, R.K. Boger, S.R. Agnew, R.H. Wagoner. Hardening evolution of AZ31B Mg sheet, Int. J. Plast. 23 (2007) 44-86. doi:10.1016/j.ijplas.2006.03.005
10. C.S. Roberts, Magnesium and its alloys, Wiley, New York/London 1960
11. S. Kleiner, S. Uggowitzer, Mechanical anisotropy of extruded Mg-6%Al-1%Zn alloy, Mater. Sci. Eng. A 379 (2004) 258-263. https://doi.org/10.1016/j.msea.2004.02.020
12. M.H. Yoo, J.R. Morris, K.M. Ho, S.R. Agnew, Nonbasal deformation modes of HCP metals and alloys: role of dislocation source and mobility, Metall. Mater. Trans. A 33 (2002) 813. https://doi.org/10.1007/s11661-002-0150-1
13. M. Knezevic, A. Levinson, R. Harris, R. Mishra, R. Doherty, S. Kalidindi, Deformation twinning in AZ31: Influence in strain hardening and texture evolution, Acta Mater. 58 (2010) 6230-6242. http://dx.doi.org/10.1016/j.actamat.2010.07.041
14. L. Wu, S.R. Agnew, Y. Ren, D.W. Brown, B. Clausen, G.M. Stoica, D.R. Wenk, P.K. Liaw, The effects of texture and extension twinning on the low cycle fatigue behavior of a rolled Mg alloy, AZ31B, Mater. Sci. & Eng. A 527 (2010) 7057-7067. https://doi.org/10.1016/j.msea.2010.07.047

15. L.Wu, A. Jain, D.W. Brown, G.M. Stoics, S.R. Agnew, B. Clausen, D.E. Fielden, P.K. Liaw, Twinning-detwinning behavior during the strain controlled low-cycle fatigue testing of a wrought magnesium alloy, ZK60A, Acta. Mater. 56 (2008) 688-695. https://doi.org/10.1016/j.actamat.2007.10.030
16. S.R. Agnew, O. Duygulu, Plastic anisotropy and the role of non-basal slip in magnesium alloy AZ31B, Int. J. Plast. 21 (2005) 1161-1193. https://doi.org/10.1016/j.ijplas.2004.05.018
17. S.R. Agnew, C.N. Tome, D.W. Brown, S.C. Vogel, Study of slip mechanisms in a magnesium alloy by neutron diffraction and modeling, Scr. Mater. 48 (2003) 1003-1008. https://doi.org/10.1016/S1359-6462(02)00591-2
18. S.B. Yi, H.G. Brokmeier, R. Bolmaro, K.U. Kainer, J. Homeyer, The texture evolutions of Mg alloy, AZ31 under uni-axial loading. Materials Science Forum
19. 495-497 (2005) 1665-1674. https://doi.org/10.4028/www.scientific.net/MSF.495-497.1585
20. D.W. Brown, S.R. Agnew, M.A.M. Bourke, T.M. Holden, S.C. Vogel, C.N. Tome, Internal strain and texture evolution during deformation twinning in magnesium, Mater. Sci. Eng. A 399 (2005) 1–12. https://doi.org/10.1016/j.msea.2005.02.016
21. M.A. Gharghouri, G.C. Weatherly, J.D. Embury, J. & Root, Study of the mechanical properties of Mg-7. 7at. % Al by in-situ neutron diffraction, Philos. Mag. 79 (1999) 1671-1695. https://doi.org/10.1080/01418619908210386
22. C.H. Caceres, T. Sumitomo, M. Veidt, Pseudoelastic behaviour of cast magnesium AZ91 alloy under cyclic loading – unloading, Acta. Mater. 51 (2003) 6211–6218. https://doi.org/10.1016/S1359-6454(03)00444-0
23. D. W. Brown, A. Jain, S.R. Agnew, B. Clausen, Twinning and Detwinning During Cyclic Deformation of Mg Alloy AZ31B, Mater. Sci. Forum 539-543 (2007) 3407–3413. https://doi.org/10.4028/www.scientific.net/MSF.539-543.347
24. A. Jain, S.R. Agnew, Modeling the temperature dependent effect of twinning on the behavior of magnesium alloy AZ31B sheet, Mater. Sci. Eng. A 462 (2007) 29-36. https://doi.org/10.1016/j.msea.2006.03.160
25. Q. Yu, J. Zhang, Y. Jiang, Q. Li, An experimental study on the cyclic deformation and fatigue of extruded ZK60 magnesium alloy, Int. J. Fat. 36 (2012) 47-58. https://doi.org/10.1016/j.ijfatigue.2011.08.016
26. Y. N. Wang, J. C. Huang, The role of twinning and untwinning in yielding behavior in hot-extruded Mg-Al-Zn alloy, Acta Mater. 55 (2007) 897–905. https://doi.org/10.1016/j.actamat.2006.09.010
27. F. Wang, J. Dong, Y. Jiang, W. Ding, Cyclic deformation and fatigue of extruded Mg-Gd-Y magnesium alloy, Mater. Sci. Eng. A 561 (2013) 403–410. https://doi.org/10.1016/j.msea.2012.10.048
28. J. W. Christian, S. Mahajan, Deformation twinning, Prog. Mater. Sci. 39 (1995) 1-157. https://doi.org/10.1016/0079-6425(94)00007-7
29. J. Wang, I. J. Beyerlein, and C.N. Tome, An atomic and probabilistic perspective on twin nucleation in Mg, Scr. Mater. 63 (2010) 741–746. https://doi.org/10.1016/j.scriptamat.2010.01.047
30. Q. Yu, J. Wang, Y. Jiang, Inverse slip accompanying twinning and detwinning during cyclic loading of magnesium single crystal, J. Mater. 2013 (2013) 1-8. http://dx.doi.org/10.1155/2013/903786

31. S.B. Yi, H.G. Brokmeier, R.E. Bolmaro, K.U. Kainer, T. Lippmann, In-situ measurements of texture variations during a tensile loading of Mg-alloy AM20 using synchrotron x-ray radiation, Scr. Mater. 51 (2004) 455. https://doi.org/10.1016/j.scriptamat.2003.12.034
32. S.B. Yi, C.H.J. Davies, H.G. Brokmeier, R.E. Bolmaro, K.U. Kainer, J. Homeyer, Deformation and texture evolution in AZ31 magnesium alloy during uniaxial loading, Acta Mater. 54 (2006) 549-562. https://doi.org/10.1016/j.actamat.2005.09.024
33. M.Knezevic, M.R. Daymond, I.J. Beyerlein, Modeling discrete twin lamellae in a microstructural framework, Scr. Mater. 121 (2016) 84-88. https://doi.org/10.1016/j.scriptamat.2016.04.026
34. B.L. Wu, G.S. Duan, X.H. Du, L.H. Song, Y.D. Zhang, M.J. Philip, C. Esling, In situ investigation of extension twinning-detwinning and its effect on the mechanical behavior of AZ31B magnesium alloy. Mater. Des. 132 (2017) 57-65. https://doi.org/10.1016/j.matdes.2017.06.023
35. W. Wu, P.K. Liaw, K. An, Unraveling cyclic deformation mechanisms of a rolled magnesium alloy using in situ neutron diffraction, Acta Mater. 85 (2015) 343-353. https://doi.org/10.1016/j.actamat.2014.11.030
36. W. Wu, K. An, L. Huang, S.Y. Lee, P.K. Liaw, Deformation dynamics study of a wrought magnesium alloy by real-time in-situ neutron diffraction, Scripta Mater. 69 (2013) 358-361. https://doi.org/10.1016/j.scriptamat.2013.05.008
37. W. Wu, K. An, Understanding low-cycle fatigue life improvement mechanisms in a pretwinned magnesium alloy. Journal of Alloys and Compounds 656 (2016) 539-550. https://doi.org/10.1016/j.jallcom.2015.09.247
38. W. Wu, H. Qiao, X. Guo, P. Wu, P.K. Liaw, Investigation of deformation dynamics in a wrought magnesium alloy. Int. Journal of Plasticity 62 (2014) 105-120. https://doi.org/10.1016/j.ijplas.2014.07.005
39. W. Wu, Y, Gao, N. Li, C. M. Parish, W. Liu, P.K. Liaw, K. An, Intragranular twinning, detwinning, and twinning-like reorientation in magnesium alloys, Acta. Mater. 121 (2016) 15-23. https://doi.org/10.1016/j.actamat.2016.08.058
40. Y. Ren, High-energy synchrotron x-ray diffraction and its application to in situ structural phase-transition studies in complex sample environments, J. Metals 64 (2012) 140-149. https://doi.org/10.1007/s11837-011-0218-
41. Y.N. Wang, J.C. Huang, Texture analysis in hexagonal materials, Mat. Chemistry and Physics 81 (2003) 11-26. https://doi.org/10.1016/S0254-0584(03)00168-8
42. A. Murphy, J. Allison, The recrystallization behavior of unalloyed Mg and a Mg-Al alloy, Met. Trans. A 49 (2018) 1492-1508. https://doi.org/10.1007/s11661-018-4494-6
43. M. Obstalecki, S.L. Wong, P.R. Dawson, M.P. Miller, Quantitative analysis of a crystal scale deformation heterogeneity during cyclic plasticity using high-energy x-ray diffraction and finite-element simulation, Acta Mater. 75 (2014) 259-272. https://doi.org/10.1016/j.actamat.2014.04.059
44. S.R. Agnew, M.H. Yoo, C.N. Tome, Application of texture simulation to understanding mechanical behavior of Mg and solid solution alloys containing Li or Y, Acta Mater. 49 (2001) 4277-4289. https://doi.org/10.1016/S1359-6454(01)00297-X

45. G. Proust, C.N. Tome, G.C. Kaschner, Modeling texture, twinning and hardening evolution during deformation of hexagonal materials, Acta Mater. 55 (2007) 2137-2148. https://doi.org/10.1016/j.actamat.2006.11.017
46. C.N. Tome, P.J. Maudlin, R.A. Lebensohn, G.C. Kaschner, Mechanical response of zirconium-I Derivation of a polycrystal constitutive law and finite element analysis, Acta Mater. 49 (2001) 3085-3096. https://doi.org/10.1016/S1359-6454(01)00190-2
47. Y. Liu, Y. Li, K.T. Ramesh, Rate dependence of deformation mechanisms in a shape memory alloy, Philosophical Magazine A 82 (2002) 2461-2473. https://doi.org/10.1080/01418610208240046
48. M. Matsuzuki, S. Horibe, Analysis of fatigue damage process in magnesium alloy AZ31, Mater. Sci. Eng. A 504 (2009) 169-174. https://doi.org/10.1016/j.msea.2008.10.034
49. Q. Li, Q. Yu, J, Zhang, Y. Jiang, Effect of strain amplitude on tension-compression fatigue behavior of extruded Mg6Al1ZnA magnesium alloy, Scripta Mater. 62 (2010) 778-781. https://doi.org/10.1016/j.scriptamat.2010.01.052
50. I.J. Beyerlein, R.J. McCabe, C.N. Tome, Effect of microstructure on the nucleation of deformation twins in polycrystalline high-purity magnesium: A multi-scale modeling study, J. of the Mechanics and Physics of Solids 59 (2011) 988-1003. https://doi.org/10.1016/j.jmps.2011.02.007
51. I.J. Beyerlein, C.N. Tome, A probabilistic twin nucleation model for HCP polycrystalline metals, Proceedings of The Society A 466 (2010) 2517-2544. 10.1098/rspa.2009.0661
52. O. Muransky, D.G. Carr, P. Sittner, E.C. Oliver, In situ neutron diffraction investigation of deformation twinning and pseudoelastic-like behavior of extruded AZ31 magnesium alloy, Int. J. of Plast. 25 (2009) 1107-1127. https://doi.org/10.1016/j.ijplas.2008.08.002
53. G. Proust, C.N. Tome, A. Jain, S. Agnew, Modeling the effect of twinning and detwinning during strain path changes of magnesium alloy AZ31, Inter. J. of Plast., 25 (2009) 861-880. https://doi.org/10.1016/j.ijplas.2008.05.005
54. Q. Yu, J. Zhang, Y. Jiang, Direct observation of twinning-detwinning-retwinning on magnesium single crystal subjected to strain-controlled cyclic tension-compression in [0001] direction, Philosophical Magazine Letters 91 (2011) 757-765. https://doi.org/10.1080/09500839.2011.617713
55. S. R. Agnew, D.W. Brown, C.N. Tome, Validating a polycrystal model for the elastoplastic response of magnesium alloy AZ31 using in situ neutron diffraction, Acta Mater., 54 (2006) 4841-4852. https://doi.org/10.1016/j.actamat.2006.06.020
56. L. Wu, S.R. Agnew, D.W. Brown, G.M. Stoica, B. Clausen, A. Jain, D.E. Fielden, P.K. Liaw, Internal stress relaxation and load redistribution during the twinning-detwinning-dominated cyclic deformation of a wrought magnesium alloy, ZK60A, Acta Mater. 56 (2008) 3699-3707. https://doi.org/10.1016/j.actamat.2008.04.006
57. A.J. Allen, M. Bourke, S. Dawes, M.T. Hutchings, P.J. Withers, The analysis of internal strains measured by neutron diffraction in Al/SiC MMCs, Acta Metall. 40 (1992) 2361-2373. https://doi.org/10.1016/0956-7151(92)90155-8

58. N. Shi, M.A.M. Bourke, J.A. Roberts, J.E. Allison, Phase-stress partition during uniaxial tensile loading of a TiC-particulate-reinforced Al composite, Metall. Mater. Trans. A 28 (1997) 2741-2753. https://doi.org/10.1007/s11661-997-0031-8
59. K.Y. Xie, Z. Alam, A. Caffee, K.J. Hemker, Pyramidal I slip in c-axis compressed Mg single crystals, Sripta Mater. 112 (2016) 75-78. https://doi.org/10.1016/j.scriptamat.2015.09.016
60. T. Lorentzen, M.R. Daymond, B. Clausen, C.N. Tome, Lattice strain evolution during cyclic loading of stainless steel, Acta Mater. 50 (2002) 1627-1638. https://doi.org/10.1016/S1359-6454(02)00029-0

CHAPTER 4
A STUDY ON THE INFLUENCE OF AL ON TWINNING-DETWINNING BEHAVIOR IN MAGNESIUM DURING LOW CYCLE FATIGUE USING HIGH ENERGY X-RAY DIFFRACTION

4.1. Introduction

Mechanical twinning is an important deformation mechanism in hexagonal close packed (hcp) metals since it helps satisfy the Von Mises criterion as the fifth independent deformation system and allows for straining along the hcp c-axis [1-4]. It is well understood that the tension-compression asymmetry observed during cyclic loading of wrought Mg alloys is due to twin nucleation and growth which occurs during compression and the narrowing and/or removal of those twinned regions (detwinning) upon load reversal [1,4]. Twinning and detwinning as well as dislocation slip mechanisms has been studied extensively using advanced techniques such as synchrotron diffraction and neutron irradiation [1,5-12]. However, a comparative study involving the influence of Al on this behavior as it relates to the stresses needed to initiate twinning and exhaust detwinning as well as the evolution of twin volume fraction has not been reported in literature between solute-free Mg and binary Mg-Al alloys. Since Al is a common alloying element in Mg alloys, due to its enhancement of strength, understanding its influence on loop shape and the tension-compression strength asymmetry is important for designing Mg alloys for structural applications and for developing predictive models that accurately simulate cyclic stress-strain behavior and low cycle fatigue.

The propensity for this twinning behavior in hcp Mg alloys is dependent on the initial texture present. In wrought Mg alloys the majority of the grains generally have their c-axis oriented normal to the prior working direction [1] and this texture allows for twinning during compression and detwinning upon unloading and/or tensile loading [1]. This texture also enables the quantitative study of this twinning behavior using advance in-situ techniques involving electron back scatter diffraction (EBSD) and synchrotron diffraction. The mechanism of twin nucleation and growth in hcp metals has been studied using both experimental and computational techniques [13-23]. Several studies on Mg, Zr, and Ti have found that twins generally nucleate from grain boundaries [14,16,18] since grain boundaries, including triple and quadruple joints, produce large internal stresses that can support the nucleation and expansion of twins [21]. Other studies have found that both twin growth and detwinning are driven by the mobility of twinning dislocations [24-26]. A DFT study by Ghaziseidi et al found that CRSS for twin dislocation mobility increased with Al concentration [24].

In the present work, we have characterized the cyclic twinning-detwinning behavior of an extruded, Mg-4Al alloy using in-situ high energy x-ray diffraction (HEXD). These results are compared with the behavior of unalloyed Mg from Chapter x [27]. The quantitative information provided will be used in future work to develop physically based models for predicting the effect of alloying on cyclic stress-strain behavior and fatigue lifetime.

4.2. Experimental Procedure

4.2.1 Material and sample preparation

Mg-4Al was provided by CanMET Materials in the form of extruded bar. The bar was extruded from an 85mm diameter cast billet at 413°C to a final diameter of 15mm. Prior to extrusion, the cast billet was homogenized at 413°C for 15 hours. The as-extruded texture was measured using EBSD with the results shown in Figure 4.1. The initial texture shows that the basal poles are oriented in the radial direction (RD) and normal to the extrusion direction (ED). In the in-situ experiment described below, the loading direction (LD) is parallel to the extrusion direction and the normal direction (ND) Is equivalent to the radial direction (RD). The microstructure consisted of equiaxed, recrystallized grains with an average grain diameter of 55 μm. Based on EBSD Grain Orientation Spread measurements the amount of recrystallized was determined to be 95 percent.

For the in-situ synchrotron diffraction experiments, cylindrical fatigue specimens were machined by Westmoreland Mechanical Testing and Research, Inc. using low stress turning to ensure a low residual stress, scratch free surface. The final surface was prepared by standard metallographic techniques with a final step using a 1200 μm grit finish. The geometry was consistent with the ASTM E606 standard and the samples had a diameter of 6.35mm and a gage length of 19.05mm.

Images of twinning and detwinning during cyclic deformation were obtained using electron back scatter diffraction (EBSD) of flat, rectangular fatigue specimens in a Tescan Mira 3 scanning electron microscope equipped with an EDAX Hikari XP EBSD detector. Each EBSD scan was taken at a voltage of 30kV and a beam intensity

between 18-20 with an average step size of 1.0μm. TSL OIM software was used to characterize EBSD data and an average confidence index of 0.62±0.2 was obtained. No additional confidence index cleaning was applied to the data. A grain tolerance angle of 5° was used for grain recognition. These flat samples were also machined by Westmoreland using low stress grinding. The samples were then polished using standard metallographic techniques finishing with a 0.05μm polycrystalline diamond solution prior to testing. An acetic-nitric solution (5mL nitric acid, 15mL acetic acid, 20 mL water, and 60 mL ethanol) was used to etch the specimens for 3 seconds, which revealed grains and twins under scanning electron microscopy.

4.2.2 In-situ HEXD Measurements and Cyclic Experiments

HEXD experiments were performed during in-situ cyclic loading at three different strain amplitudes: 0.65%, 0.75%, and 0.85%. The tests were conducted at the F2 station at the Cornell High Energy Synchrotron Source (CHESS). The experimental geometry has been described elsewhere [42]. A Bose Electroforce 3200 series III load frame equipped with a 5kN load cell was employed to apply cyclic loads to each sample. The macroscopic strain was measured using an 8mm gage length extensometer which was attached to the sample. Cyclic experiments were performed under full-reversed, displacement controlled conditions using a triangular displacement waveform with continuous monitoring of the strain using the extensometer. The displacement endpoints were: 0.154mm (0.65% strain), 0.164mm (0.75% strain), and 0.174mm (0.85% strain). Specific details on the cyclic experiment can be found elsewhere [27].

During each experiment, the sample was illuminated by a 61.332keV x-ray beam where the beam size was 1.25mm (width) by 1.25mm (height). The area detector employed was a 2x Dexela 2923 amorphous silicone detector with 3888x3072 pixels each and a 72μm pixel size. On the detector, a sufficient number of grains were illuminated such that nearly complete Debye-Scherer powder rings were captured. When not collecting diffraction data, the sample was loaded at a frequency of 0.25Hz. The loading direction was perpendicular to the incoming X-ray beam. To observe the twinning process in-situ, a cycle was applied to the specimen and diffraction measurements were continuously made throughout the cycle. Periodically the loading rate was reduced such that an entire cycle was completed in 480s during which HEXD data was taken. Throughout the cycle, 240 images were collected with exposure times of 2s. Each image number corresponds to a diffraction measurement.

4.3. Results

4.3.1 Stress-Strain Response

In this study, cyclic experiments were performed at three different total strain amplitudes: 0.65%, 0.75%, and 0.85%, to study twinning-detwinning behavior using HEXD. Figure 4.2 shows the evolution of the maximum tensile and compressive stresses as a function of cycles for each strain amplitude. At each strain amplitude, the maximum tensile stress was observed to increase until the end of the test while, the maximum compressive stress increased slightly until approximately cycle 100 after which cyclic softening was observed. The maximum tensile and compressive stress for cycle 100 are shown in Table 4.1 and it was shown that a tension-compression asymmetry exists at all three strain amplitudes. For example, at 0.65% total the tensile

stress is 95 MPa higher than the maximum compressive stress value. As stated earlier, inflection points associated with twinning and detwinning are normally seen on stress-strain hysteresis loops during cyclic loading. An example of this is shown in Figure 4.3, where the hysteresis loops for Cycles 1 and 2 for 0.85% total strain amplitude is displayed. During compressive loading of cycle 1, a pronounced yielding behavior (the sharp change in the slope of that stress-strain curve that occurs at the yield point of -90 MPa) associated with twinning was observed. During tension in the following cycle (cycle 2) a small inflection point was observed at 84 MPa which is related to the point of complete detwinning. At higher tensile stresses deformation is dominated by dislocation slip. In cycle 2, the pronounced yield point associated with the re-initiation of twins is reduced. As cycling continues to cycle 150, the inflection points related to twinning and detwinning have become less pronounced as shown in Figure 4.4. The diffraction data described below indicates that the cyclic stress strain response is directly related to twinning during compression and detwinning and dislocation slip during tension.

Table 4.1: The maximum tensile and compressive stresses for cycle 100 at the total strain amplitudes of 0.65%, 0.75%, and 0.85%

Total Strain Amplitude (%)	Maximum Tensile Stress (MPa)	Maximum Compressive Stress (MPa)
0.65	194	-99.4
0.75	200	-122
0.85	205	-103

4.3.2 In-situ HEXD Measurements

Figures 4.4-4.6 show the stress-strain hysteresis loops for each total strain amplitude: 0.85%, 0.75%, and 0.65%, respectively along with the evolution of the basal {0002} peak intensity. It should be noted that the load drop at 0%strain at the beginning of each cycle is due to stress relaxation, where the test was paused to collect a pole

figure after each cycle. The peak intensity evolution is shown from scattering in the loading direction (LD) and the normal direction (ND) as a function of cycles for each strain amplitude. In each figure, the different stages of loading are indicated i.e. compressive loading until the maximum compressive strain is reached at B after which compressive unloading occurs until zero strain. In each figure, the maximum tensile strain is indicated by the letter A and the maximum compressive strain is denoted by the letter B. The stars on each figure represent points of interest that will be discussed throughout the paper.

The initial intensity of the basal {0002} peak in the loading direction is zero (Figures 4.4b, 4.5b & 4.6b). As shown in Figure 4.1, in the extruded bar the majority of grains have an initial texture in which the basal pole is normal to the loading direction. Therefore, when twinning is initiated, the c-axis in these grains is reoriented by 86.3 º, toward the loading direction.

At 0.85% total strain amplitude, during tensile loading of cycle 1 (Figure 4.4) the basal {0002} peak intensity in the loading direction remains zero until an applied stress of -80MPa (indicated by C-1) at which point the diffraction peak intensity continuously increases until the maximum compressive strain (indicated by B). At the same time, the basal {0002} peak intensity in the normal direction decreases. Once the load is reversed the diffraction peak intensity in the loading direction immediately decreases until the end of the cycle. The decrease in intensity during compressive unloading is related to detwinning, that is, the narrowing or complete removal of the twinned regions that formed during compressive loading. The detwinning process is also reflected by the change in diffraction peak intensity in the normal direction in which, during compressive

unloading, the intensity increases as detwinned grains are reorienting back to their initial orientation. At the end of cycle 1, the intensity does not return to zero (the background intensity) indicating that all of the twins were not removed during compressive unloading and that residual twins remain in the material at zero strain. During the initial tensile loading of the following cycle (cycle 2) the intensity in the loading direction returns to zero (marked as T-2 in Figure 4.4d), indicating that complete detwinning has occurred at 120 MPa. In cycle 2, as the load increases, the intensity in the loading direction remains zero until the applied stress has reversed to compression and reaches -66 MPa (indicated by C-2). At this point, the intensity again begins to increase indicating that the initiation of twins occurs at the compressive stress, C-2, in cycle 2. As cycling continues (Cycle 150), similar behavior is observed, as twinning and detwinning continue to occur alternately during cyclic loading. Similar behavior was observed at 0.65% total strain amplitude and 0.75% total strain amplitude and the results are summarized in Figure 4.5 and 4.6.

The diffraction data can be used to characterize the change in volume fraction of twins as a function of cycles at each strain amplitude. An apparent twin volume fraction was calculated using the following relationship:

$$\phi = \frac{I_{LD}}{I_{ND}^{0}} (2)$$

where I_{ND}^{0} is the initial basal {0002} x-ray peak intensity of the parent grains in the normal direction and $I_{\square D}$ is the basal {0002} x-ray peak intensity in the loading direction at the maximum compressive strain. The value I_{LD} is termed the twin x-ray peak intensity and taken to be a measure of the maximum twin volume fraction during the

cycle. The azimuthal data was averaged over an azimuthal length of 5 degrees. The twin volume fraction and twin x-ray peak intensity evolution as a function of cycles is shown in Figure 4.7. At each strain amplitude, the twin volume fraction is slightly higher in the initial cycle. After that it decreases and remains stable until near failure. It should be noted that near the end of life, the twin intensity fluctuates due to the initiation of fatigue cracks.

The stress at the onset of twinning during the first 100 cycles is shown in Figure 4.8a for all three cyclic strain amplitudes. This twin initiation stress gradually decreases during the early stages of cycling after which it remains stable until the end of the test. For example, in the sample fatigued at 0.75% total strain amplitude, in the first compression cycle, twinning initiates at -90MPa, but the stress decreases to -66MPa in cycle 2, indicating that twins formed earlier during the second cycle. The stress at the completion of detwinning is also plotted as a function of cycles in Figure 4.8b. The stress is highest in cycle 2 and then slightly decreases and remaining stable until the end of the test. Since the twin volume fraction is slightly higher in cycle 1, a higher stress is required to detwin the material during tensile loading of the following cycle. As the twin volume fraction stabilizes, the stress needed to remove those twins is nearly the same on every cycle.

During the test at total strain amplitude of 0.75%, after 175 cycles the twin intensity never returns to zero and increases with increasing cycles and indicates that "residual twins" begin to form at later cycles. Residual twins are regions in which detwinning is not complete during the cycle. At 0.65% and 0.85% the sample failed before the point at which residual twins remain in the material. In this situation in which

residual twins are formed, detwinning starts immediately after unloading from the maximum compressive strain and continues until the maximum tensile strain is reached. An apparent residual twin volume fraction (α) can be calculated using equation 3 and multiplying the result by the twin volume fraction calculated in equation 2,

$$\alpha = \frac{I_T}{I_C} (3)$$

where I_C is the basal peak intensity at the maximum compressive strain in the loading direction and I_T is the basal peak intensity at the maximum tensile strain in the loading direction. The results are shown in Figure 4.9.

4.4.4 EBSD Characterization

To provide images of twins, the surface of flat fatigue samples was characterized using EBSD after each load step. Figure 4.10 shows the microstructural evolution during loading at 0.6% total strain amplitude (black circles outline areas of interest). It was observed that with successive cycling twins form in the same location within these grains. After the initial compressive loading to -0.6% strain twins formed in grains outlined in black circles (Figure 4.10a). In the second compression cycle, the majority of the twins return to those same grains (outlined in black) while some new additional twins are formed (outlined by white circles) which is shown in Figure 4.10b. Red circles indicate twins that do not return on the following cycle. As cycling to continues to cycle 4 (Figure 4.10c), twins continue to initiate in the same grains as cycle 1 (outline by black circles).

4.4. Discussion

In this study, the twinning-detwinning behavior observed during low cycle fatigue of Mg-4Al was characterized using in-situ HEXD. The intensity of the basal {0002} peak was monitored throughout each cycle and was used to characterize the alternate occurrence of twinning and detwinning. HEXD enables quantification of the twin volume fraction and the evolution of twins during cyclic loading. In addition, we quantify the cyclic stress at which twins are initiated and the stress at which detwinning is completed. This is similar to a previous investigation of cyclic deformation and twinning in unalloyed Mg described in Chapter 3 and in a submitted paper [42] and the results of the two studies will be compared here.

It was determined that the initiation of twinning was related to an increase in the basal {0002} peak intensity in the loading direction during compressive loading. This was also evident in the stress-strain hysteresis loop where the increase in intensity coincides with the pronounced yielding caused by twinning. This is similar to results from previous neutron scattering and synchrotron diffraction studies for AZ31 and ZK60A [1,5-6,8,11-12]. For each strain amplitude, the twin initiation stress was the highest in cycle 1 when compared to the following cycles suggesting that twinning becomes easier after the first cycle (Figure 4.9a). Similar results were found in unalloyed Mg, where the twin initiation stress increased with cycling as a result of increasing plastic deformation with successive cycling. A comparison of the twin initiation stress for unalloyed Mg and Mg-4Al is shown in Figure 4.11a. As can be observed, the twin initiation stress for both materials is similar which suggests that the

addition of Al solute does not have a significant effect on the stress needed to initiate a twin.

However, the twin volume fraction (Figure 4.12) is strongly influenced by the addition of solute and the addition of Al to Mg substantially increases the twin volume fraction at a constant maximum compressive strain level. At a compressive strain of 0.75%, the unalloyed Mg had a twin volume fraction of approximately 7% while the Mg-4Al has a twin volume fraction of approximately 32%. Observation of the hysteresis loops indicate that at the compressive strain of 0.75% the Mg-4Al exhibited a much higher stress compared to the unalloyed Mg. This indicates that although the solute did not affect the CRSS for twin initiation, the presence of Al solute did increase the hardening rate leading to more twin formation as the stress increased. It is well understood that twins nucleate from local stresses at grain boundaries including triple and quadruple points [13-16] and the stress state around these nucleation sites influences twin nucleation during loading. In Mg-4Al, solute hinders the mobility of twin dislocations and other dislocations. A DFT study by Ghazaseidi et al showed that the critical resolved shear stress (CRSS) for twin growth, referred to as the twinning yield stress, increased with increasing Al content and that the values for twinning yield stress were for 14MPa, 23MPA, and 28MPa for AZ31, AZ61, and AZ80, respectively [24]. In a material that contains solute, once a twin is nucleated a higher stress is needed to grow the twin due to solute-dislocation interactions, as a result the macroscopic compressive stresses are also increased (Figure 4.13). This increase in the compressive stresses may also increase the number of twin nucleation sites or the number of sites with a high local stress concentration needed for twin initiation in Mg-4Al. A study by Wang et al

combining MD simulations, EBSD, and a nucleation model suggested that when grain boundary defects needed for twin nucleation did not exist, local stress concentrations at grain boundaries could provide the energy needed to overcome energetic barriers needed to produce these defect sources and thus, allow for twin nucleation [15]. We speculate that the internal stresses surrounding nucleation sites such as grain boundaries also increases with increasing stress allowing for twin nucleation from these regions resulting in a higher twin volume fraction in Mg-4Al when compared to unalloyed Mg. There are a limited number of studies on the influence of solute on twin nucleation in Mg and the available studies focus on the influence of precipitates on twin nucleation [28-30]. In this study, the material is solution treated and no evidence of precipitates were observed during microstructural characterization of the Mg-4Al alloy.

The stress at the exhaustion of detwinning was also measured in Mg-4Al (Figure 4.11b). Significantly, the detwinning exhaustion stress in the Mg-4Al is ~100 MPa higher than that in the unalloyed Mg. Detwinning is mainly controlled by the migration of twin boundaries into the twins via glide of twinning dislocations resulting in the propagation of the parent grains into the twinned regions [31]. In a synchrotron diffraction study by Wu et al, it was found that during detwinning the parent grain was completely removed through the migration of twinning dislocations from an untwinned region into a twinned region [31]. It is proposed that the increased twin volume fraction and the addition of Al solute in Mg-4Al both contribute to the increase in this twin exhaustion stress since they both influence the mobility of twin dislocations. This occurs in two different ways, that is, 1) as the twin volume fraction increases a higher tensile stress is needed to detwin the material during reloading since there is an increase in the

amount of twin dislocations that need to migrate for detwinning and hence a higher stress is needed to drive this migration, and 2) the addition of Al solute decreases the mobility of twin dislocations and as a result a higher stress is needed to drive the migration of twin boundaries. As a result of these two mechanisms the stress at the exhaustion of detwinning will also be increased. However, we believe that the increasing twin volume fraction is the dominant mechanism. To show this, the twin volume fraction as a function of the detwinning stress at each strain amplitude for both unalloyed Mg and Mg-4Al was compared in Figure 4.14 and revealed that independent of solute content, as the twin volume fraction increases the stress needed to detwin the material was also increased. This suggests that of the two mechanisms, the higher twin volume fraction observed in the Mg-4Al had the predominant effect on the detwinning exhaustion stress.

In Mg-4Al, at 0.75% total strain amplitude after approximately 175 cycles twins are not fully removed even at the highest tensile stress and residual twins remain in the material. Residual twins were also observed in unalloyed Mg [42], and in both unalloyed Mg and Mg-4Al the fraction of residual twins increases with increasing cycles but is slightly higher in unalloyed Mg (Figure 5.15). The reduction in the fraction of residual twins in Mg-4Al may also be related to the addition of solute. In both Mg-4Al and unalloyed Mg, the macroscopic stress is increased to drive detwinning during tension. However, in Mg-4Al solute-dislocation interactions also contribute to the increased stress. As a result, the tensile stresses in Mg-4Al are higher than those for unalloyed Mg and thus more twins can be detwinned during reloading.

The twinning and detwinning phenomena was also investigated using surface EBSD of cycled samples. This indicated that the twins that disappeared during detwinning reappeared in the same grains and at nominally the same locations. Persistent twin formation was also observed during cyclic loading of unalloyed Mg using EBSD [27]. These can be termed "persistent twins" and may be similar to persistent slip band (PSB) formation during cyclic loading [32]. A PSB is defined as a region in which a cyclic strain concentration exists and where the dislocation structure is different from that of the surrounding matrix [32]. Persistent twin formation suggests that the grain boundary defects needed for twin nucleation already exists at the initiation site and therefore twinning is favored at that site.

It is well understood that PSB's are favorable sites for crack initiation. Although this was not the subject of the current work we may anticipate that persistent twins may play a similar role. Yu et al found that during cyclic loading of unalloyed Mg twin tips were the sites of dominant crack initiation and related this behavior to a stress concentration in these initiation zones [33]. Future studies are warranted to elucidate the role of alloying on persistent twin formation and fatigue crack initiation. Fatigue damage development studies using in-situ EBSD techniques may provide correlations between microstructural features such as grain orientation and local grain boundary conditions and twin nucleation and growth and how this behavior relates to crack initiation and growth during LCF.

4.5. Conclusions

The twinning-detwinning behavior in Mg-4Al extrusions during cyclic deformation was studied using in-situ high energy x-ray diffraction techniques and compared to that of unalloyed Mg. The major conclusions are as follows:

1. An increase or decrease in the {0002} basal x-ray peak intensity in the loading direction was observed during cyclic loading and can be directly related to $\{10\acute{1}2\}\langle 10\acute{1}1\rangle$ extension twinning and detwinning.
2. In-situ HEXD confirmed that the compressive stress at which twinning initiates is similar in Mg-4Al and unalloyed Mg which suggests that the CRSS for twin nucleation is not affected by solute.
3. The twin volume fraction is higher in Mg-4Al when compared to unalloyed Mg and is related to an increase in the internal stresses at nucleation sites in Mg-4Al as a result of the higher compressive stresses needed to produce twin growth. We suggest that this is related to the substantial influence of Al on the CRSS for motion of twinning dislocation predicted by DFT.
4. The stress at which complete detwinning occurs can be characterized using HEXD. There is a substantial difference in the stress at which complete detwinning occurs in Mg-4Al and unalloyed Mg, and interestingly, the stress in Mg-4Al is substantially higher than that in unalloyed Mg. We suggest that this is predominately due to the higher volume fraction present in the Mg-4Al, however the solute also increases CRSS for twin dislocation motion in the Mg-4Al alloy and thus plays a role.
5. As cycling continues, at a certain point, complete detwinning is no longer observed and residual twins remain even at the highest tensile stress. In Mg-4Al,

residual twins begin to form after 175 cycles and the amount increases throughout the fatigue test. The fraction of residual twins is lower in Mg-4Al than in the unalloyed Mg and is related to an increase in the tensile stresses needed to produce detwinning in Mg-4Al due to solute-dislocation interactions during tensile loading.

Figures

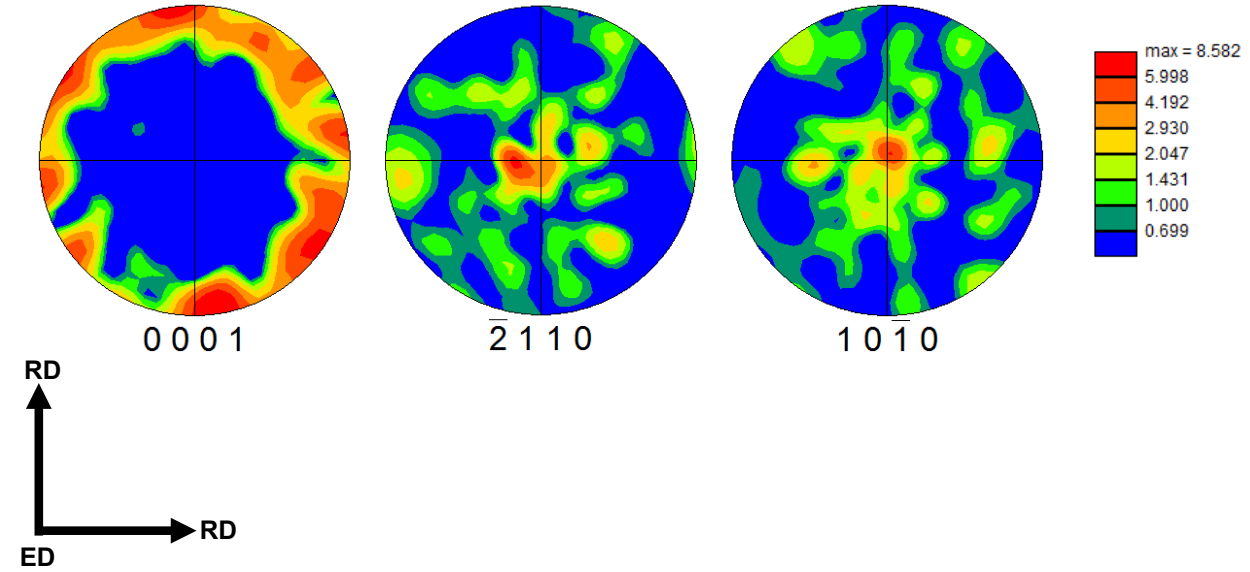

Figure 4.1: Pole figures showing the initial texture with the basal poles aligned normal to the loading extrusion direction (loading direction). ED: Extrusion Direction (Loading Direction); RD: Radial Direction (perpendicular to the extrusion direction)

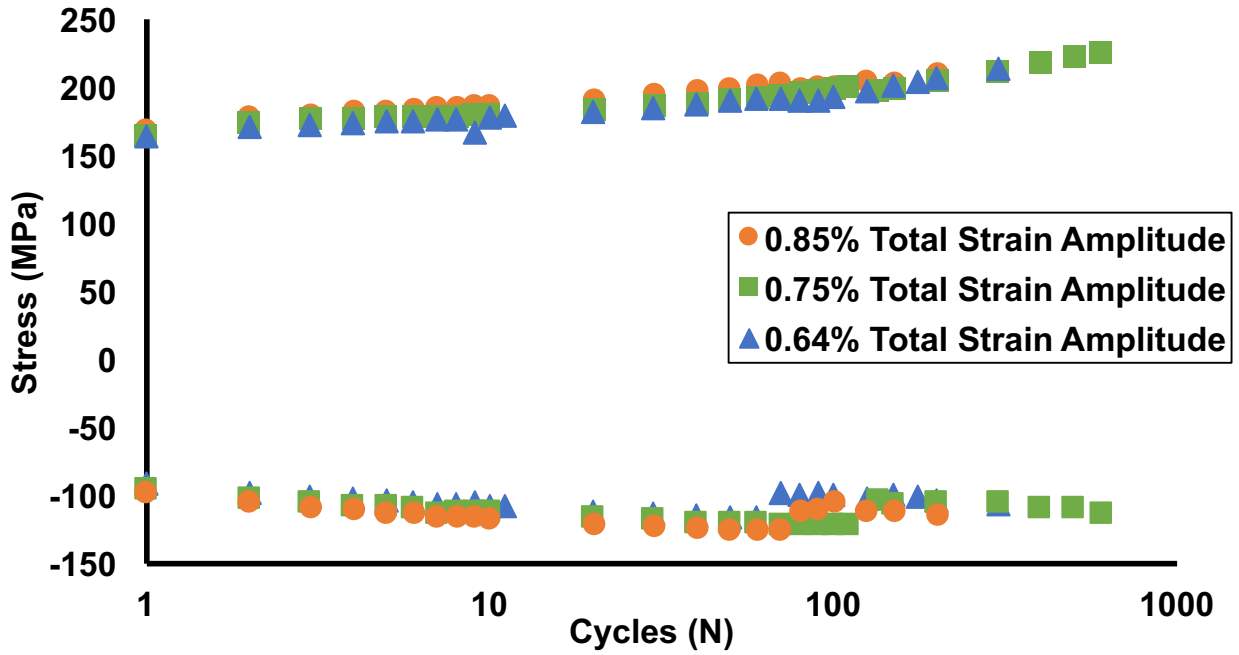

Figure 4.2: The cyclic stress-strain response as a function of cycles showing the maximum tensile and compressive stresses for each cycle at the total strain amplitudes of 0.65%, 0.75%, and 0.85%

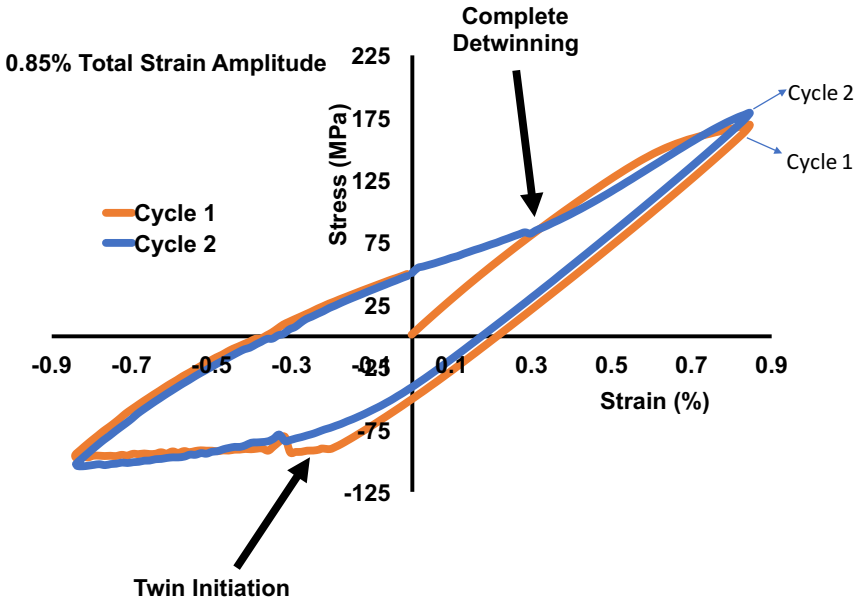

Figure 4.3: Loop shape for cycles 1 and 2 at 0.85% total strain amplitude. The inflection points associated with the initiation of twinning is more pronounced in cycle 1 than cycle 2 and the inflection point associated with complete detwinning is shown during tensile reloading of cycle 2.

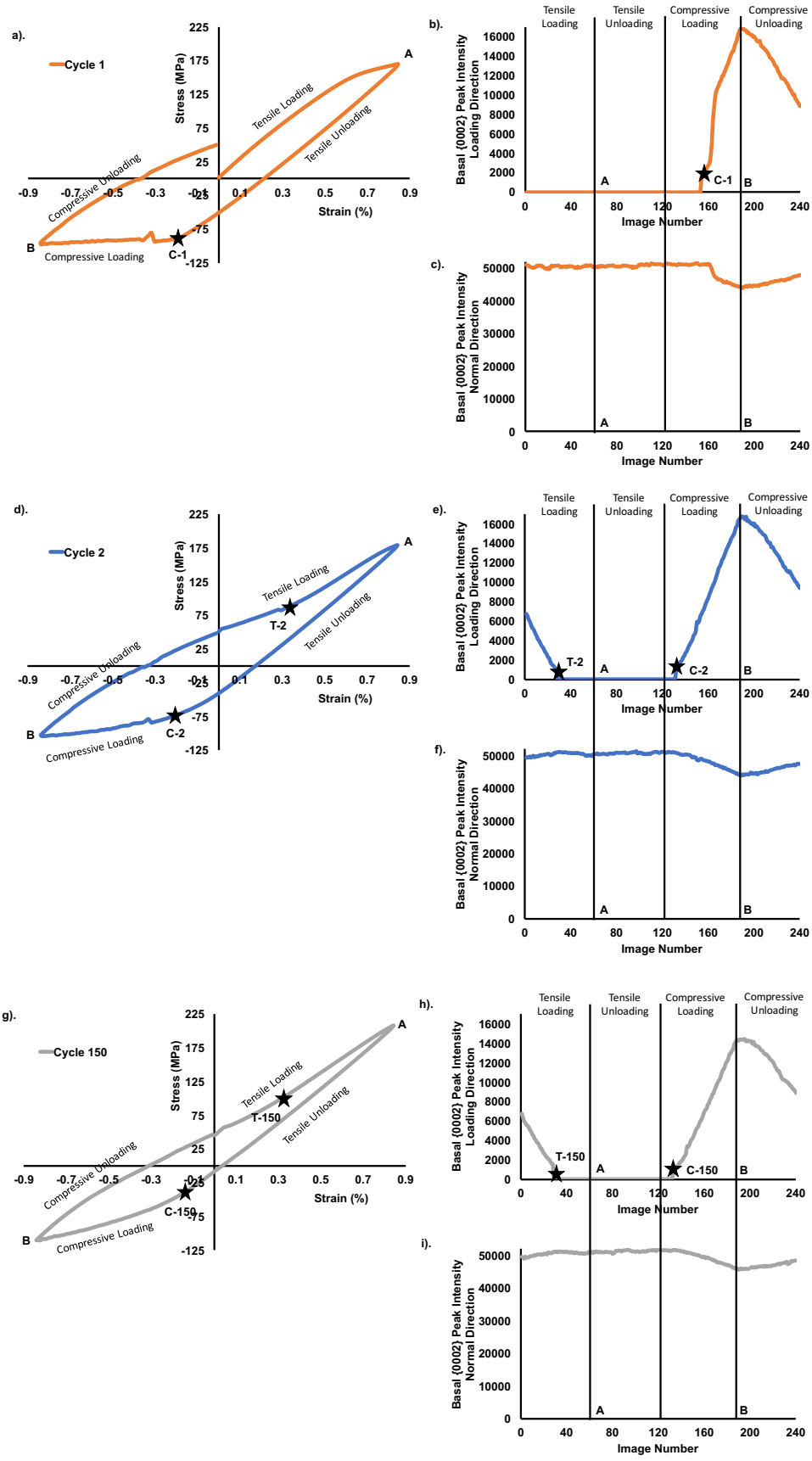
a).
Cycle 1
Stress (MPa)
Strain (%)
Tensile Loading
Tensile Unloading
Compressive Unloading
Compressive Loading
A
B
C-1
b).
Tensile Loading
Tensile Unloading
Compressive Loading
Compressive Unloading
Basal {0002} Peak Intensity Loading Direction
Image Number
C-1
c).
Basal {0002} Peak Intensity Normal Direction
Image Number
d).
Cycle 2
T-2
C-2
e).
T-2
C-2
f).
g).
Cycle 150
T-150
C-150
h).
T-150
C-150
i).

Figure 4.4: Cyclic stress-strain loops and corresponding x-ray peak intensity of the basal {0002} peak for tests conducted at a total strain amplitude of 0.85% a-c) Cycle 1, d-f) Cycle 2, g-i) Cycle 150. HEXD peak intensities in the Loading Direction (Figure 4b,e,h) indicate the onset of twinning and detwinning; HEXD peak intensities in the Normal Direction (Figure 4c, f,i) indicate the activation of other slip systems. Note: Vertical lines at Image 0 and Image 122 are at zero strain. Vertical lines at Image 62 and 186 are at peak tensile strain and peak compressive strain, respectively.

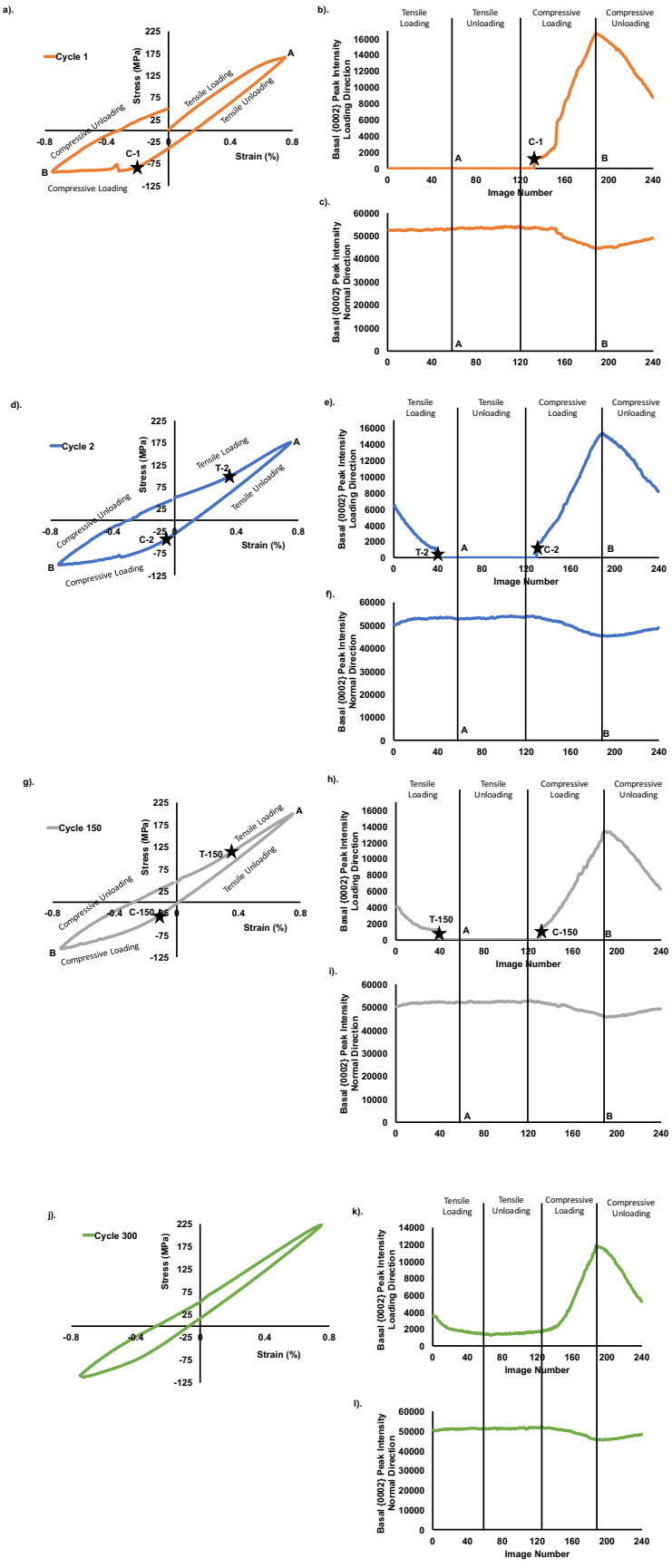
a).
Cycle 1
Stress (MPa)
Strain (%)
Tensile Loading
Tensile Unloading
Compressive Unloading
Compressive Loading
C-1
A
B
b).
Tensile Loading
Tensile Unloading
Compressive Loading
Compressive Unloading
Basal (0002) Peak Intensity Loading Direction
Image Number
c).
Basal (0002) Peak Intensity Normal Direction
d).
Cycle 2
T-2
C-2
e).
f).
g).
Cycle 150
T-150
C-150
h).
i).
j).
Cycle 300
k).
l).

Figure 4.5: Cyclic stress-strain loops and corresponding x-ray peak intensity of the basal {0002} peak for tests conducted at a total strain amplitude of 0.75% a-c) Cycle 1, d-f) Cycle 2, g-i) Cycle 150, j-l) Cycle 300. HEXD peak intensities in the Loading Direction (Figure 4b,e,h,k) indicate the onset of twinning and detwinning; HEXD peak intensities in the Normal Direction (Figure 4c, f,i,l) indicate the activation of other slip systems. Note: Vertical lines at Image 0 and Image 122 are at zero strain. Vertical lines at Image 62 and 186 are at peak tensile strain and peak compressive strain, respectively.

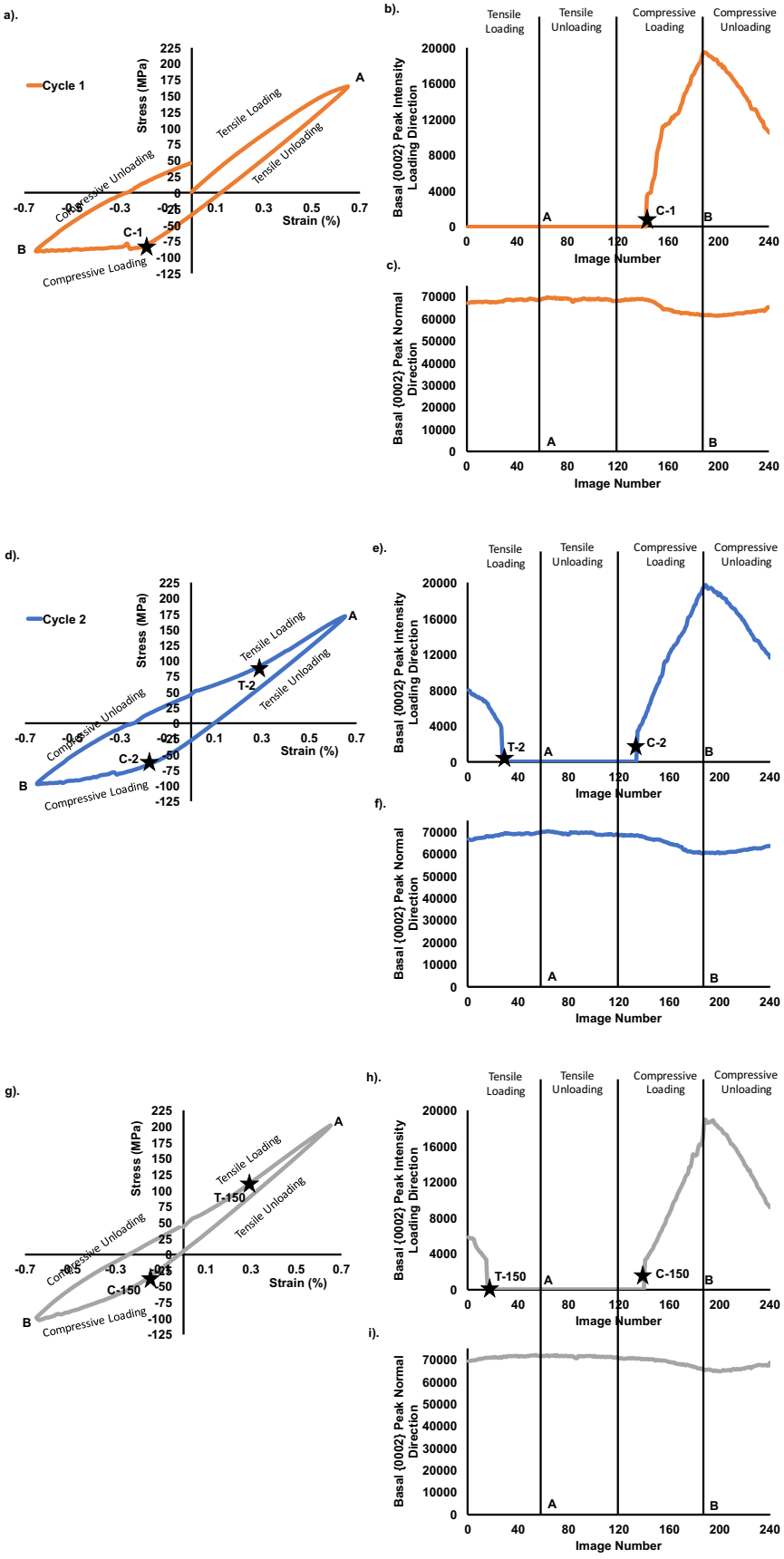
a).
Cycle 1
Stress (MPa)
Strain (%)
Tensile Loading
Tensile Unloading
Compressive Unloading
Compressive Loading
A
B
C-1
b).
Tensile Loading
Tensile Unloading
Compressive Loading
Compressive Unloading
Basal {0002} Peak Intensity Loading Direction
Image Number
C-1
c).
Basal {0002} Peak Normal Direction
Image Number
d).
Cycle 2
T-2
C-2
e).
f).
g).
T-150
C-150
h).
i).

Figure 4.6: Cyclic stress-strain loops and corresponding x-ray peak intensity of the basal {0002} peak for tests conducted at a total strain amplitude of 0.65% a-c) Cycle 1, d-f) Cycle 2, g-i) Cycle 150. HEXD peak intensities in the Loading Direction (Figure 4b,e,h) indicate the onset of twinning and detwinning; HEXD peak intensities in the Normal Direction (Figure 4c, f,i) indicate the activation of other slip systems. Note: Vertical lines at Image 0 and Image 122 are at zero strain. Vertical lines at Image 62 and 186 are at peak tensile strain and peak compressive strain, respectively.

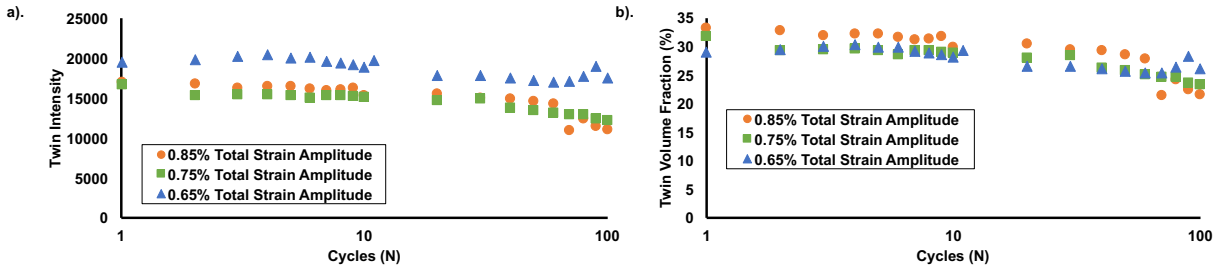

Figure 4.7: The a) twin x-ray peak intensity (at the maximum compressive strain) and b) apparent twin volume fraction (at the maximum compressive strain) calculated using equation 1 at 0.85%, 0.75% and 0.65% total strain amplitudes.

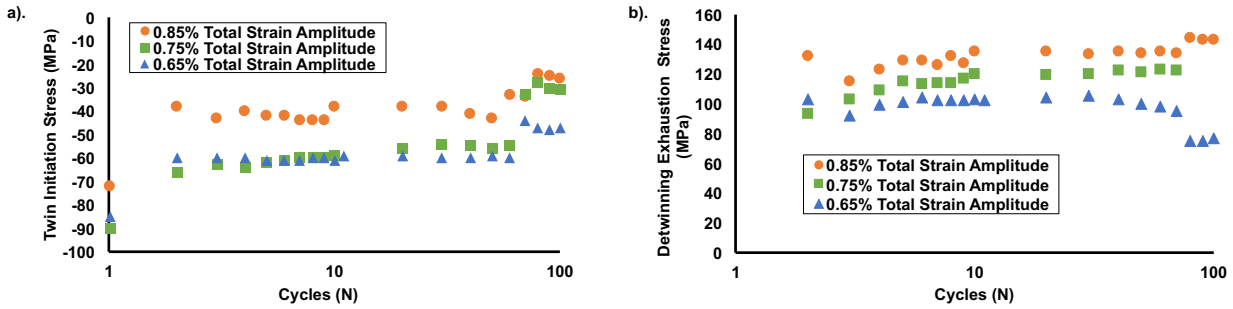

Figure 4.8: a) The stress at the initiation of twinning and b) the stress at the completion of detwinning (detwinning exhaustion stress) for 0.85%, 0.75% and 0.65% total strain amplitudes.

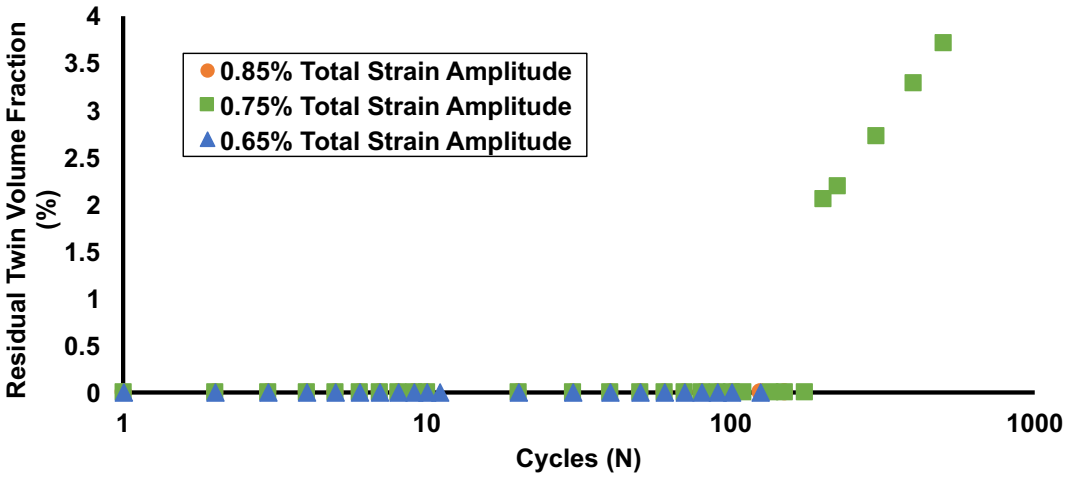

Figure 4.9: The fraction of residual twins at the maximum tensile strain for 0.85%, 0.75% and 0.65% total strain amplitudes.

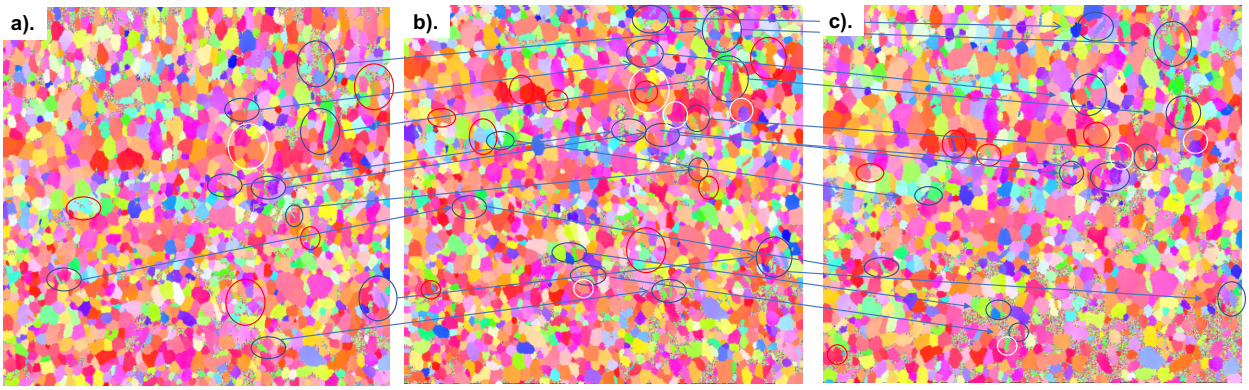

Figure 4.10: Electron back scatter diffraction patterns showing persistent twin formation, a) twins form in grains after compression to -0.6% strain in cycle 1 in regions outlined in black circles, b) those same twins are formed during the second compressive cycle to -0.6% strain at the same locations which is outlined in black circles (white circles outline regions with new twin activity and red circle outline regions where twins did not return), c) the same twins return to the same grains after the 4^{th} compression cycle to -0.6% strain. All EBSD measurements were in the unloaded condition.

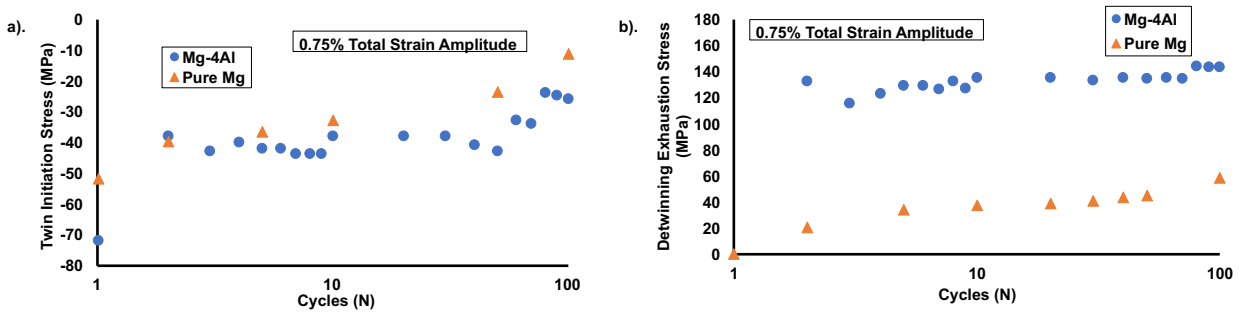

Figure 4.11: A comparison of the a) the stress at the initiation of twinning and b) the stress at the completion of detwinning (detwinning exhaustion stress) for both unalloyed Mg and Mg-4Al at 0.75% total strain amplitude

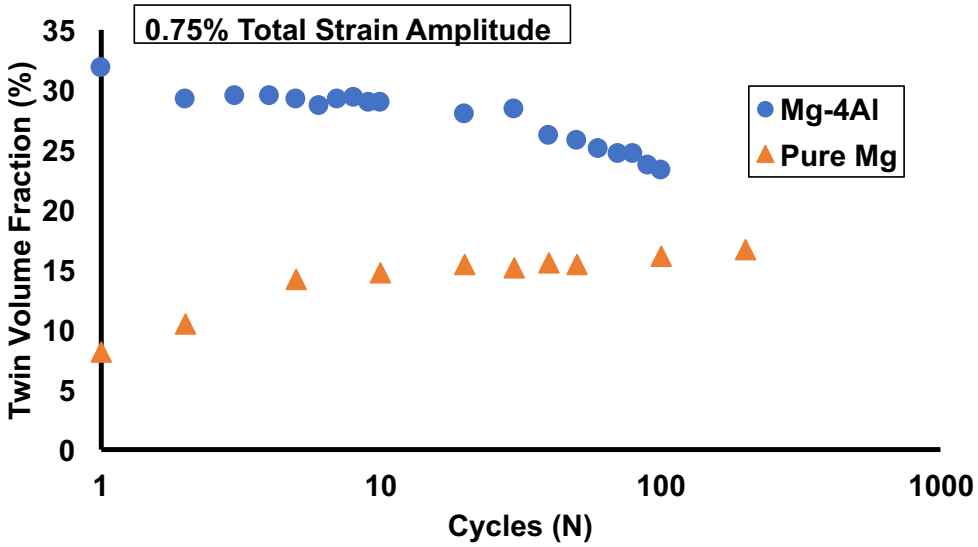

Figure 4.12: A comparison of the twin volume fraction at the peak compressive stress as a function of cycles for both unalloyed Mg and Mg-4Al at 0.75% total strain amplitude

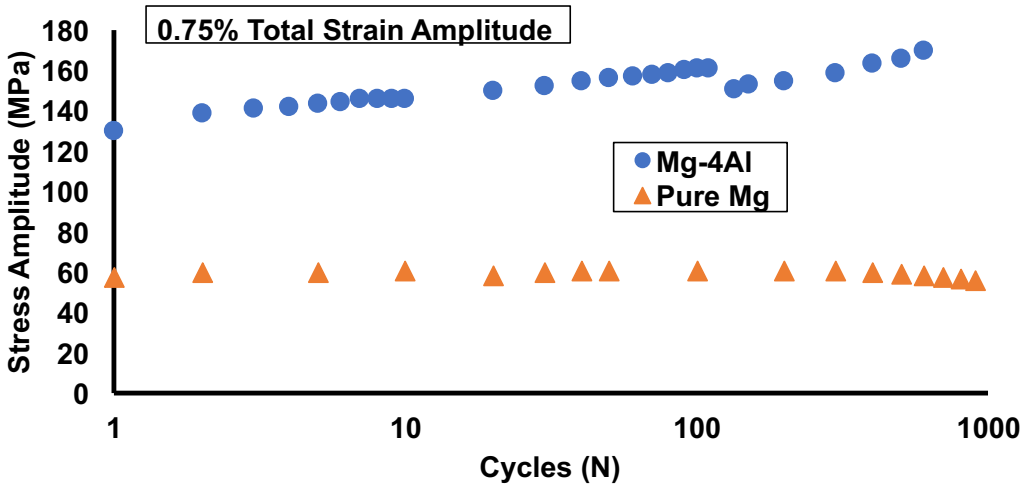

Figure 4.13: A comparison of the stress amplitude as a function of cycles for both unalloyed Mg and Mg-4Al at 0.75% total strain amplitude

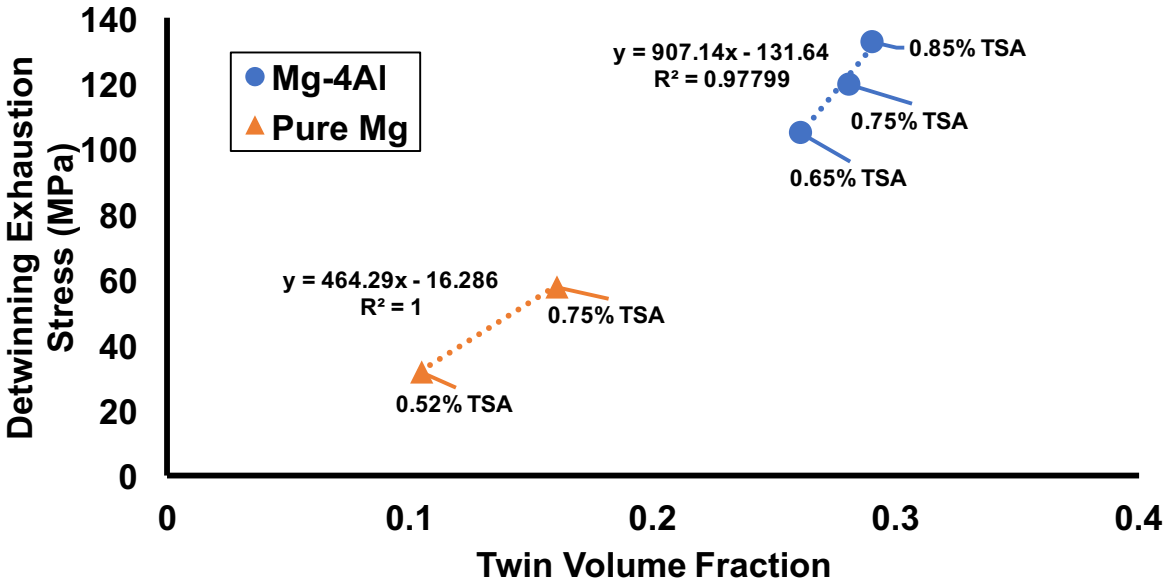

Figure 4.14: The relationship between detwinning exhaustion stress and the twin volume fraction at each strain amplitude for unalloyed Mg and Mg-4Al

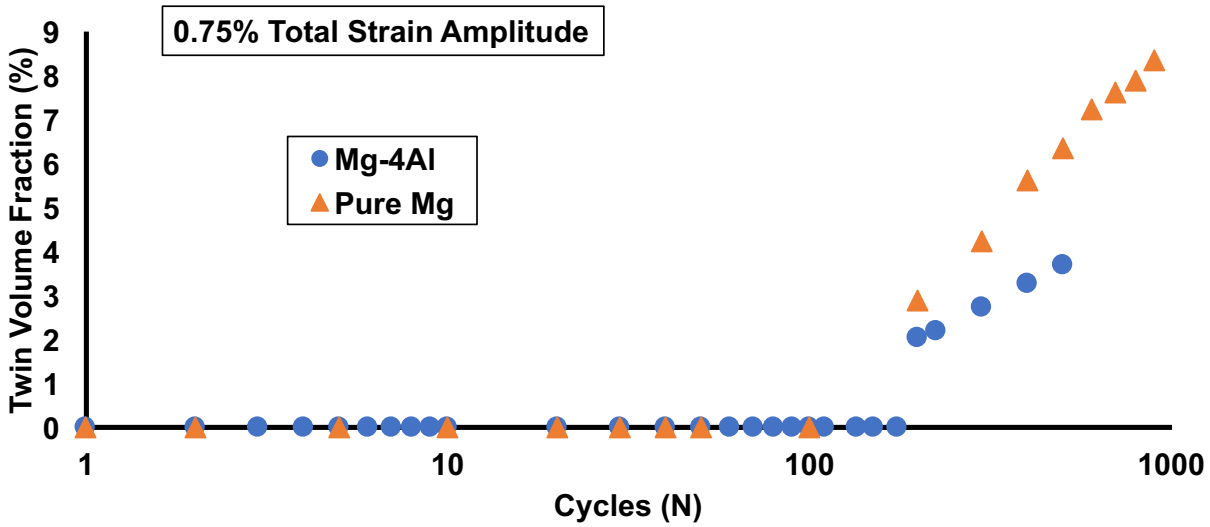

Figure 4.15: A comparison of the residual twin volume fraction as a function of cycles for both unalloyed Mg and Mg-4Al at 0.75% total strain amplitude

References

1. L.Wu, A. Jain, D.W. Brown, G.M. Stoics, S.R. Agnew, B. Clausen, D.E. Fielden, P.K. Liaw, Twinning-detwinning behavior during the strain controlled low-cycle fatigue testing of a wrought magnesium alloy, ZK60A, Acta. Mater. 56 (2008) 688-695
2. M.H. Yoo, J.R. Morris, K.M. Ho, S.R. Agnew, Nonbasal deformation modes of HCP metals and alloys: role of dislocation source and mobility, Metall. Mater. Trans. A 33 (2002) 813
3. A. Singh, J.E. Saal, Dynamic properties of magnesium alloys, J. of Metals 66 (2014) 275-276
4. M. Knezevic, A. Levinson, R. Harris, R. Mishra, R. Doherty, S. Kalidindi, Deformation twinning in AZ31: Influence in strain hardening and texture evolution, Acta Mater. 58 (2010) 6230-6242
5. L. Wu, S.R. Agnew, Y. Ren, D.W. Brown, B. Clausen, G.M. Stoica, D.R. Wenk, P.K. Liaw, The effects of texture and extension twinning on the low cycle fatigue behavior of a rolled Mg alloy, AZ31B, Mater. Sci. & Eng. A 527 (2010) 7057-7067.
6. W. Wu, K. An, L. Huang, S.Y. Lee, P.K. Liaw, Deformation dynamics study of a wrought magnesium alloy by real-time in-situ neutron diffraction, Scripta Mater. 69 (2013) 358-361
7. W. Wu, K. An, Understanding low-cycle fatigue life improvement mechanisms in a pretwinned magnesium alloy. Journal of Alloys and Compounds 656 (2016) 539-550.
8. W. Wu, H. Qiao, X. Guo, P. Wu, P.K. Liaw, Investigation of deformation dynamics in a wrought magnesium alloy. Int. Journal of Plasticity 62 (2014) 105-120
9. W. Wu, P.K. Liaw, K. An, Unraveling cyclic deformation mechanisms of a rolled magnesium alloy using in situ neutron diffraction, Acta Mater. 85 (2015) 343-353.
10. S.R. Agnew, C.N. Tome, D.W. Brown, S.C. Vogel, Study of slip mechanisms in a magnesium alloy by neutron diffraction and modeling, Scr. Mater. 48 (2003)
11. M.A. Gharghouri, G.C. Weatherly, J.D. Embury, J. & Root, Study of the mechanical properties of Mg-7.7at. % Al by in-situ neutron diffraction, Philos. Mag. 79 (1999) 1671-1695.
12. D. W. Brown, A. Jain, S.R. Agnew, B. Clausen, Twinning and Detwinning During Cyclic Deformation of Mg Alloy AZ31B, Mater. Sci. Forum 539-543 (2007) 3407–3413
13. J. Wang, R. Hoagland, J.P. Hirth, L. Capolungo, I.J. Beyerlein, C.N. Tome, Nucleation of (1012) twins in hexagonal close packed crystals, Scripta Mater. 61 (2009) 903–906
14. C.N. Tome´ , P.J. Maudlin, R.A. Lebensohn, G.C. Kaschner, Mechanical response of zirconium—I. Derivation of a polycrystal constitutive law and finite element analysis, Acta Mater. 49 (2001) 3085–3096
15. J. Wang, I.J. Beyerlein, C.N. Tome´, An atomic and probabilistic perspective on twin nucleation in Mg, Scripta Mater. 63 (2010) 741–746

16. L. Wang, P. Eisenlohr, Y. Yang, T.R. Bieler, M.A. Crimp, Nucleation of paired twins at grain boundaries in titanium, Scripta Mater. 63 (2010) 827–830
17. L. Wang, Y. Yang, P. Eisenlohr, T.R. Bieler, M.A. Crimp, D.E. Mason, 2010c. Twin nucleation by slip transfer across grain boundaries in commercial purity titanium, Metall. Mater. Trans. A 41 (2010) 421–430
18. I.J. Beyerlein, C.N. Tome´, A probabilistic twin nucleation model for hcp polycrystalline metals, Proceedings of the Royal Society A 466 (2010) 2517–2544
19. I.J. Beyerlein, L. Capolungo, P.E. Marshall, R.J. McCabe, C.N. Tome´, Statistical analyses of deformation twinning in magnesium, Philosophical Magazine 90 (2010) 2161–2190.
20. R.J. McCabe, G. Proust, E.K. Cerreta, A. Misra, Quantitative analysis of deformation twinning in zirconium, Int. J. Plast. 25 (2009) 454–472
21. I.J. Beyerlein, R.J. McCabe, C.N. Tome, Effect of microstructure on the nucleation of deformation twins in polycrystalline high-purity magnesium: A multi-scale modeling study, J. of the Mechanics and Physics of Solids 59 (2011) 988-1003
22. M. Knezevic, M.R. Daymond, I.J. Beyerlein, Modeling discrete twin lamellae in a microstructural framework, Scr. Mater. 121 (2016) 84-88
23. A. Serra, D.J. Bacon, R.C. Pond, Twins as barriers to basal slip in hexagonal close packed metals, Met. Mater. Trans. A 33 (2002) 809-812
24. M. Ghazisaeidi, L.G. Hector Jr., W.A. Curtin, Solute strengthening of twinning dislocations in Mg alloys, Acta Mater. 80 (2014) 278-287
25. Y. Cui, Y. Li, Z. Wang, X. Ding, Y. Koizumi, H. Bian, L. Lin, A. Chiba, Impact of solute elements on detwinning in magnesium and its alloys, Int. J. of Plast. 91 (2017) 134-159
26. J. Xu, B. Guan, H. Yu, X. Cao, Y. Xin, Q. Liu, Effect of twin boundary-dislocation-solute interaction on detwinning in a Mg-3Al-1Zn alloy, J. Mater. Sci. Tech. 32 (2016) 1239-1244
27. A. Murphy, D. Pagan, A. Beaudoin, M. Miller, J. Allison, Quantification of Twinning-Detwinning Behavior During Low-Cycle Fatigue of Pure Magnesium Using High Energy X-Ray Diffraction, Int. J. Fat. (2018) Under Review
28. J.D. Robson, N. Stanford, M.R. Barnett, Effect of particles in promoting twin nucleation in a Mg-5wt % Zn alloy, Scripta Mater. 63 (2010) 823-826
29. S. Kada, P.A. Lynch, J.A. Kimpton, M.R. Barnett, In-situ x-ray diffraction studies of slip and twinning in the presence of precipitates in AZ91 alloy, Acta Mater. 119 (2016) 145-156
30. P. Lukas, L. Kunz, Role of persistent slip bands in fatigue, Phil. Magazine, 84 (2004) 317-330
31. W. Wu, Y, Gao, N. Li, C. M. Parish, W. Liu, P.K. Liaw, K. An, Intragranular twinning, detwinning, and twinning-like reorientation in magnesium alloys, Acta. Mater. 121 (2016) 15-23
32. P. Lukas, L. Kunz, Role of persistent slip bands in fatigue, Phil. Magazine, 84
33. Q. Yu, J. Zhang, Y. Jiang, Fatigue damage development in pure polycrystalline magnesium under cyclic tension-compression loading, Mater. Sci. Eng. A 528 (2011) 7816–782

CHAPTER 5
THE INFLUENCE OF GRAIN SIZE AND ALLOYING ON CYCLIC STRESS-STRAIN AND LOW-CYCLE FATIGUE BEHAVIOR IN UNALLOYED MG

5.1. Introduction

Understanding the influence of grain size and alloying on low-cycle fatigue (LCF) and cyclic stress-strain (CSS) behavior is important for rapid development of new Mg alloys for engineering applications [1]. During room temperature deformation, mechanical twinning helps Mg satisfy the Von Mises criterion which requires five independent deformation systems and results in a unique hysteresis loop during fatigue [2,5-6,10-20]. It is well established that wrought Mg alloys show a strong initial basal texture, where the c-axis in most grains is aligned normal to the working direction [15-18,20-23]. During cyclic loading the grains with this initial texture, favor twinning during compression, where the c-axis is rotated 86.3 toward the working direction and subsequent detwinning when the load is reversed [20]. Detwinning is the removal and/or narrowing of twinned regions, which causes an 86.3 reorientation of the c-axis to its initial position or that prior to twinning [20].

Several studies have shown that the twinning-detwinning mechanism observed during LCF produces an abnormal hysteresis loop where the stresses in tension are much higher than those in compression [5-7,12,14, 20-25]. Begum et al found that during LCF of the Mg alloy AZ31, the tensile yield stress was much higher than the compressive yield stress and related the observed behavior to twinning in compression

and subsequent detwinning during tension [6]. Q. Yu et al showed that in unalloyed Mg, at high strain amplitudes (1.0%) twinning-detwinning produced an abnormal hysteresis loop while at lower strain amplitudes (0.2%) the lack of twinning led to a symmetric loop where the stresses in tension and compression were the same [12]. Other LCF studies have shown that when no twinning is observed, the resultant hysteresis loop is symmetric [13,26]. Mirza et al found that the rare-earth (RE) Mg alloy, GW103K exhibited a symmetric hysteresis loop and related the behavior to a weaker basal texture and lack of twinning-detwinning during cyclic loading [13].

During LCF the cyclic stress-strain response is greatly influenced by the stresses needed to activate dislocation slip, deformation twinning, and/or interactions between dislocations and other dislocations, twins, solute atoms, precipitates. The ease of these deformation mechanisms is closely linked to the grain size and alloying since both influence dislocation motion and twin propagation. However, prior research on the role of grain size and Al addition on mechanical behavior in Mg is mainly focused on monotonic experiments [27-34] and not low cycle fatigue. There is limited literature on LCF and cyclic stress strain behavior in unalloyed Mg [11-12] and Mg-4Al and most studies have focused on Mg-rare-earth, Mg-Al-Zn, and Mg-Al-Mn alloys [2, 5-7, 9, 13-14, 26, 35-49].

In the current investigation, the low cycle fatigue and cyclic stress-strain behavior of unalloyed Mg in two different grain size conditions, 45μm and 350μm and a Mg-4Al binary alloy was examined. This study emphasizes the effect of grain size and Al addition on the fatigue lifetime and macroscopic stress-strain response during room temperature cyclic loading. The experimental results were modeled using the Coffin-

Manson [50] and Basquin [51] relationships to characterize the effect of plastic strain and stress amplitude on low cycle fatigue parameters.

5.2. Experimental Procedure

5.2.1 Materials and Microstructural Characterization

Cylindrical extruded bars of unalloyed Mg and Mg-4Al bars were the starting materials for this study and provided by CanMet Materials. These bars were also used in a previous study and the details of the microstructural characterization have been reported elsewhere [66]. The initial texture of both materials was characterized using Electron Back Scatter Diffraction (EBSD) and it was found that the basal poles are aligned normal to both the loading and extrusion direction (Figure 5.1). In unalloyed Mg, the microstructure consisted of equiaxed grains with an average diameter of 45 μm and was 95 percent recrystallized (Figure 5.1a). In order to characterize the influence of grain size on LCF in unalloyed Mg, the as-extruded bar was heat-treated at 525°C for 3 hours in a Carbolite box furnace. This resulted in a grain size of 350 μm, which allowed comparison with the 45 μm condition. In Mg-4Al the average grain diameter was 52 μm and was 93 percent recrystallized (Figure 5.1b).

For the cyclic experiments, cylindrical fatigue specimens were machined by Westmoreland Mechanical Testing and Research Inc. (WMTR), using low stress turning to ensure a smooth, low residual stress surface condition. The surface was further prepared using standard metallographic techniques ending with a 1200 μm grit finish and polishing such that any fine scratches were parallel to the loading conditions. The sample geometry was consistent with the ASTM E606 standard with a diameter of 6.35 mm and a gage length of 19.05 mm. In the fine-grained (FG) unalloyed Mg and Mg-4Al,

the fatigue specimens were machined from the as-extruded bar and for the coarse-grained (CG) unalloyed Mg condition, the samples were machined from the solution-treated bar.

To characterize the alternate occurrence of twinning and detwinning using electron back scatter diffraction (EBSD), flat, rectangular fatigue specimens were prepared in a similar manner, fatigued and periodically examined in a Tescan Mira 3 scanning electron microscope equipped with an EDAX Hikari XP EBSD detector. Each EBSD scan was taken at a voltage of 30kV and a beam intensity of 20 with an average step size of 1.0 μm. TSL OIM software was used to characterize EBSD data and an average confidence index of 0.7±0.1 was obtained. No additional confidence index cleaning was applied to the data. A grain tolerance angle of 5° was used for grain recognition. These samples were also machined by WMTR using low stress grinding where the final surface was produced with 1200 μm grit finish. The samples were then prepared using standard using standard metallographic techniques, finishing with a 0.05μm polycrystalline diamond solution. Care was taken to minimize polishing-induced deformation twins. An acetic-nitric solution (10mL nitric acid, 5mL acetic acid, 20 mL water, and 60 mL ethanol) was used to etch the specimens for 5 seconds, which revealed grains and twins under scanning electron microscopy. These samples were then subjected to cyclic deformation and periodically examined using EBSD with no further surface preparation.

5.2.2 Low-Cycle Fatigue and Monotonic Tensile Experiments

Strain-controlled, fully-reversed (R=-1) cyclic experiments were performed using an MTS servohydraulic load frame equipped with a 150kN load cell. All of the cyclic

experiments were conducted at room temperature at a frequency of 0.5Hz. The gripping system was accurately aligned using the MTS 709 Alignment System to eliminate buckling of the testing specimen. A triangular waveform was applied during loading and five strain amplitudes, 0.2%, 0.4%, 0.6%, 0.8%, and 1.0% were employed in the experimental investigation. An extensometer with a gage length of 8mm was used to control strain during testing.

Displacement-controlled tensile experiments were performed on unalloyed Mg and Mg-4Al using the same MTS load frame discussed above. An extensometer with a gage length of 25.4mm was used to measure the strain during each test. The sample geometry was consistent with the ASTM E8 standard with a diameter of 6 mm and a gage length of 24 mm. Two samples were tested for each alloy.

5.3. Results

5.3.1 Cyclic Stress Response

The evolution of the stress amplitude as a function of cycles for the different strain amplitudes for the coarse grained unalloyed Mg, fine-grained unalloyed Mg and Mg-4Al are shown in Figures 5.2, 5.3, and 5.4 respectively. A direct comparison between both unalloyed Mg and Mg-4Al at 0.4% total strain amplitude is shown in Figure 5.5. It should be noted that similar behavior was observed for every strain amplitude and the data for each strain amplitude can be found in Appendix B (Figure B.1). Tables 5.1 and 5.2 show the maximum tensile and compressive stresses at the half-life for the fine grain and coarse grain condition, respectively while the results for Mg-4Al are shown in Table 5.3. At the half-life in the fine-grained unalloyed Mg condition, the maximum tensile and compressive stresses are similar at each strain

amplitude while in the coarse-grained unalloyed Mg and Mg-4Al, the stress in tension is much higher than that in compression. For example, in the coarse grained unalloyed Mg condition at 1.0% total strain amplitude, the maximum tensile stress is 21 MPa more than the absolute value of the maximum compressive stress.

For both unalloyed Mg and Mg-4Al, the stress amplitude increases as the strain amplitude increases. In the fine-grained unalloyed Mg condition, at higher strain amplitudes (0.6-1.0%), cyclic hardening was observed for up to ~120 cycles which was followed by a constant stress amplitude. After this period, cyclic softening was observed until fracture. The significant increase in cyclic softening at approximately 75-85% of life is likely due to crack growth until final fracture. Numerous cracks were observed on the sample surface after final fracture. At the lower strain amplitude (0.2%) the stress amplitude remained constant for up to 20,000 cycles after which point cyclic softening was observed until final fracture. In the coarse-grained condition, significant cyclic hardening was observed for the majority of life followed by end-of-life cyclic softening due to crack initiation and growth. Using Figure 5.5 it is obvious that cyclic hardening was more pronounced in the coarse grain condition and continued for more cycles when compared to the fine-grained condition. At 0.4% total strain amplitude, in the coarse-grained condition the highest strain amplitude achieved was 37 MPa more than that of cycle 1, while it was only 7 MPa for that of the fine-grained condition.

In Mg-4Al at high strain amplitudes (0.8% and 1.0%) continuous cyclic hardening was observed until failure while at intermediate strain amplitudes (0.6%) very little hardening was observed for up to ten cycles which was followed by an increase in hardening until failure. During loading at lower strain amplitudes (0.4%) the alloy

exhibited a small amount of hardening for up to 10 cycles after which the alloy exhibited cyclic hardening until ~1400 cycles followed by a region of stable stress amplitude until failure. The rapid stress drop near the end of life is related to the formation and growth of microscopic cracks causing a reduction in the load carrying ability of the sample. At 0.4% total strain amplitude, the stress amplitude in Mg-4Al was higher than that observed in both unalloyed Mg conditions. Similarly, to the coarse-grained condition, cyclic hardening occurred for most of life.

Table 5.1: The maximum tensile and compressive stresses at the half-life for different strain amplitudes for the unalloyed Mg, 45μm condition. ± refers to the standard deviation between the 7-8 samples that were tested per condition or total strain amplitude

Total Strain Amplitude (%)	Maximum Tensile Stress (MPa)	Maximum Compressive Stress (MPa)
1.0	66±5	-60±3
0.8	70±6	-69±2.2
0.6	57±0.7	-56±1.2
0.4	54±0.2	-54±0.3

Table 5.2: The maximum tensile and compressive stresses at the half-life for different strain amplitudes for the unalloyed Mg, 350μm condition. ± refers to the standard deviation between the 7-8 samples that were tested per condition or total strain amplitude

Total Strain Amplitude (%)	Maximum Tensile Stress (MPa)	Maximum Compressive Stress (MPa)
1.0	96±2.3	-75±2
0.8	96±3	-71±1.9
0.6	95±1.2	-66±1.7
0.4	91±4	-52±1.1

Table 5.3: The maximum tensile and compressive stresses at the half-life for different strain amplitudes for the Mg-4Al. ± refers to the standard deviation between the 7-8 samples that were tested per condition or total strain amplitude

Total Strain Amplitude (%)	Maximum Tensile Stress (MPa)	Maximum Compressive Stress (MPa)
1.0	294±4	-145±1.1
0.8	271±2	-124±2.3
0.6	252±1.4	-115±3
0.4	214±3	-111±2.5

5.3.2 Cyclic Strain Response

The evolution of plastic strain amplitude as a function of cycles for the fine-grained unalloyed Mg, coarse-grained unalloyed Mg, and Mg-4Al is shown in Figures 5.6, 5.7, and 5.8 respectively. A comparison, between the plastic strain amplitude for both unalloyed Mg and Mg-4Al at 0.4% total strain amplitude is shown in Figure 5.9. It should be noted that similar behavior was observed for every strain amplitude and the data for each strain amplitude can be found in Appendix B (Figure B.2). In both unalloyed Mg conditions and Mg-4Al, as the total strain amplitude increases the plastic strain amplitude also increased. In the fine-grained condition, the plastic strain amplitude was nearly constant for the first ~1000 cycles at which point it then increased somewhat until failure. At the end of life, the abrupt increase in the plastic strain amplitude is due to crack induced softening. When a fatigue crack forms in the material, the hysteresis loop expansion is small. After the crack begins to propagate through the specimen, the hysteresis loop expands gradually leading to an apparent increase in the plastic strain due to the increasing compliance of the sample in tension. Xiong et al found similar results during load controlled fatigue of a structural steel, where the hysteresis loop continued to expand as the crack propagated through the sample [52]. In the coarse-grained unalloyed Mg condition, the plastic strain amplitude remains near constant for the first ~100 cycles, where after it gradually decreases until near the failure cycle as a result of cyclic hardening, which was discussed in the previous section. In Mg-4Al at higher strain amplitudes (0.6-1.0%) the plastic strain amplitude gradually decreased up until ~25 cycles where after the slope of the curve decreased abruptly as the plastic strain amplitude significantly decreased with increasing cycles due to cyclic

hardening. Begum et al proposed the following relationship to describe the change in slope and how it relates to hardening [6],

$$\frac{\Delta\varepsilon_p}{2} = \alpha + \beta \log N \quad (1)$$

where N is the number of cycles, α is the initial plastic strain amplitude at the 25th cycle (cycle where the slope changes), and β is the hardening coefficient which is a negative value as a result of the decreasing slope. Table 5.4-5.6 shows the β values for the fine-grained unalloyed Mg, coarse-grained unalloyed Mg, and Mg-4Al for each total strain amplitude, respectively. For Mg-4Al, it was found that the hardening coefficient increased with total strain amplitude and the value at 1.0% was more than double that at 0.4% total strain amplitude. The behavior is consistent with the stress amplitude results in Figure 5.4 where significant cyclic hardening was observed at higher strain amplitudes when compared to lower strain amplitudes. In the coarse-grained unalloyed Mg material, the β-value is similar for each strain amplitude indicating that the hardening rate is independent of strain amplitude in this material. However, the values are much lower than observed in Mg-4Al which is consistent with the observation that hardening was more pronounced in the Mg-4Al alloy (Figure 5.5). For example, at 1.0% total strain amplitude the hardening coefficient in Mg-4Al is three times larger than that in the coarse-grained unalloyed Mg condition. Even though softening was observed in the fine-grained unalloyed Mg material the relationship can still be used to described this behavior. In this case, the β-value is positive since the plastic strain amplitude is increasing with cycles. In the fine-grained condition the β-value increases with total strain amplitude suggesting that the rate of softening is higher at higher strain amplitudes, which is consistent with the experimental data in Figures 5.2 and 5.6.

Table 5.4: The effect of total strain amplitude on the hardening coefficient, β for fine-grained unalloyed Mg. ± refers to the standard deviation between the 7-8 samples that were tested per condition or total strain amplitude

$\Delta\varepsilon_T$ (%)	β
1.0	+0.19±0.001
0.8	+0.17±0.004
0.6	+0.10±0.0012
0.4	+0.063±0.0001

Table 5.5: The effect of total strain amplitude on the hardening coefficient, β for coarse-grained unalloyed Mg. ± refers to the standard deviation between the 7-8 samples that were tested per condition or total strain amplitude

$\Delta\varepsilon_T$ (%)	β
1.0	-0.04±0.0014
0.8	-0.055±0.0011
0.6	-0.055±0.003
0.4	-0.052±0.0001

Table 5.6: The effect of total strain amplitude on the hardening coefficient, β for Mg-4Al. ± refers to the standard deviation between the 7-8 samples that were tested per condition or total strain amplitude

$\Delta\varepsilon_T$ (%)	β
1.0	-0.12±0.003
0.8	-0.10±0.0013
0.6	-0.09±0.005
0.4	-0.05±0.0002

5.3.3 Loop Shape Asymmetry

Figure 5.10a-c shows a comparison of the hysteresis loops at 0.2% and 1.0% total strain amplitudes at cycle 2 for the fine-grained unalloyed Mg, coarse-grained unalloyed Mg, and Mg-4Al, respectively. The maximum tensile and compressive stresses at 0.2% and 1.0% total strain amplitudes for cycle 2 are shown in Tables 5.7-

5.9 along with the ratio between the maximum tensile and compressive stresses. A stress ratio of one indicates that the peak tensile and compressive stresses are the same while a ratio greater than one indicates that the tensile stress is higher than the compressive stress. A distinct difference is observed in the shape of the hysteresis loop for the two strain amplitudes. At 1% strain amplitude, the hysteresis loop displayed the abnormal shape due to twinning in which the maximum tensile stress reached was much higher than that in compression. For example, in the fine-grained unalloyed Mg condition, during compression once the stress reached -45 MPa the material exhibited the pronounced yielding point associated with the initiation of twins (as noted in Figure 5.10) followed by a low hardening rate as twin nucleation and growth continues. During the initial tensile portion, the stress-strain curve displays a low hardening rate as twins previously formed in compression shrink and/or disappear i.e. detwinning occurs. Once detwinning is complete, the hardening rate is increased as plastic deformation continues through dislocation slip. This abrupt increase in the hardening rate leads to a distinct inflection point. At 0.2% total strain amplitude, in both the fine-grained and coarse-grained unalloyed Mg conditions and Mg-4Al, both the abrupt yielding in compression and the inflection point in tension were not observed. In addition, the maximum tensile and compressive stresses are similar (Table 5.6), showing that the T/C asymmetry normally seen in wrought Mg alloys is non-existent at the lower strain amplitudes. In previous work on the same fine-grained unalloyed Mg material used in this study, in-situ high energy x-ray diffraction confirmed that at low strain amplitudes, diffracted basal peak intensities associated with twinning during compression were not detected and that the resulting loop shape was symmetric suggesting that plastic deformation is

dominated by dislocation slip [30]. Therefore, in this study, at 0.2% total strain amplitude, plastic deformation is occurring through dislocation slip and not twinning-detwinning.

Table 5.7: Peak tensile and compressive stresses at 1.0% and 0.2% total strain amplitude as well as the ration between the both stresses for unalloyed Mg in the 45μm condition

Total Strain Amplitude (%)	Peak Tensile Stress (MPa)	Peak Compressive Stress (MPa)	Ratio
1.0	96	-57	1.68
0.2	44	-45	0.98

Table 5.8: Peak tensile and compressive stresses at 1.0% and 0.2% total strain amplitude as well as the ration between the both stresses for unalloyed Mg in the 350μm condition

Total Strain Amplitude (%)	Peak Tensile Stress (MPa)	Peak Compressive Stress (MPa)	Ratio
1.0	100	-54	1.85
0.2	45	-40	1.12

Table 5.9: Peak tensile and compressive stresses at 1.0% and 0.2% total strain amplitude as well as the ration between the both stresses for Mg-4Al

Total Strain Amplitude (%)	Peak Tensile Stress (MPa)	Peak Compressive Stress (MPa)	Ratio
1.0	198	-104	1.90
0.2	60	-60	1

The asymmetry observed in both unalloyed Mg and Mg-4Al also changes with successive cycling. Figures 5.11a-c shows the hysteresis loop for cycles 2 and the half-life cycle for the fine-grained unalloyed Mg, coarse-grained unalloyed Mg, and Mg-4Al, respectively. In both the unalloyed Mg and the Mg-4Al the inflection points associated with twinning and detwinning are greatly reduced. However, in Mg-4Al the T/C stress asymmetry is not reduced as it is in both unalloyed Mg conditions. In Mg-4Al, solute-dislocation interactions must also be considered as solute atoms act as barriers to dislocation motion and also contribute to hardening.

Experiments involving EBSD tracing confirmed that twinning and detwinning occurred alternately during cyclic loading in the fine-grained unalloyed Mg, coarse-grained unalloyed Mg and Mg-4Al which is shown in Figures 5.12-14, respectively. To observe this behavior during cyclic loading, strain-controlled, ex-situ monotonic tension and compression experiments were performed at 0.6% total strain amplitude on rectangular flat specimens. The specimen surface was polished prior to loading and characterized after each loading step using EBSD. It should be noted that the twins shown prior to loading are induced during mechanical polishing. It should be noted that Figure 5.12a shows the initial microstructure for the fine-grained unalloyed Mg specimen and the black circles outline regions of interest. After the initial compressive loading to -0.6% strain, twins were formed in the areas outlined by the white circles (Figure 5.12b). During tensile loading to +0.6% strain, the twins previously formed in compression were no longer observed (Figure 5.12c). The alternate occurrence of twinning and detwinning using EBSD in coarse-grained unalloyed Mg and Mg-4Al can be seen in Figures 5.13 and 5.14 respectively.

EBSD analysis was also used to show that residual twins remain in the material after a number of cycles and that twin activity reoccurs in the same locations as cycling proceeds which will be referred to as “persistent twin formation”. The results for the fine-grained unalloyed Mg condition are shown in Figure 5.15. In Figure 5.15a, twins form in regions outlined by black circles after compression to -0.6% strain. After tensile loading to +0.6% strain those same twins are removed. Once an additional 103 cycles are applied to the sample, twinning reoccurs in the same locations as cycle 1, while no new twin activity was observed in the region characterized (Figure 5.15c). Finally, after an

additional quarter tension (+0.6% strain) cycle is applied to the sample (Figure 5.15d), the twins are not completely removed indicating that residual twins remain in the material after 104.25 cycles are applied to the sample. There was also low indexing of Kikuchi patterns in the twinned regions in Figure 5.15d which will be discussed in more detail in section 4.

5.3.4 Low Cycle Fatigue Behavior in unalloyed Mg and Mg-4Al

The total, plastic, and elastic strain amplitudes plotted as a function of cycles to failure is shown in Figure 5.16 for fine-grained unalloyed Mg, coarse-grained unalloyed Mg, and Mg-4Al. The total strain amplitude can be expressed in terms of the elastic strain amplitude $\left(\frac{\Delta\varepsilon_e}{2}\right)$ and plastic strain amplitude $\left(\frac{\Delta\varepsilon_p}{2}\right)$.

$$\left(\frac{\Delta\varepsilon_t}{2}\right) = \left(\frac{\Delta\varepsilon_e}{2}\right) + \left(\frac{\Delta\varepsilon_p}{2}\right) \quad (2)$$

The elastic strain amplitude can be expressed as the Basquin equation

$$\left(\frac{\Delta\varepsilon_e}{2}\right) = \frac{\Delta\sigma}{2E} = \frac{\sigma_f'\left(2N_f\right)^b}{E} \quad (3)$$

and the second term of equation 2 is the well-known Coffin-Manson (CM) equation

$$\left(\frac{\Delta\varepsilon_p}{2}\right) = \varepsilon_f'\left(2N_f\right)^c \quad (4)$$

Equation 2 can be rewritten as a function of both of these relationships.

$$\left(\frac{\Delta\varepsilon_t}{2}\right) = \frac{\sigma_f'\left(2N_f\right)^b}{E} + \varepsilon_f'\left(2N_f\right)^c \quad (5)$$

where σ_f' is the fatigue strength coefficient, N_f is the fatigue life, b is the fatigue strength exponent, E is the Young's Modulus, which is approximately 45 GPa [6], ε_f' is the fatigue ductility coefficient and c is the fatigue ductility exponent. Experimental data was taken

from the half-life cycle. A comparison of the Coffin-Manson, Basquin, and total life relationships for both unalloyed Mg and Mg-4Al are shown in Figure 5.17 and the corresponding LCF parameter values are reported in Table 5.10. The fatigue strength exponent was determined by plotting $\log\frac{\Delta\varepsilon_e}{2}$ vs. $\log N_f$ and measuring the slope of the line. The fatigue strength exponent (b) in both unalloyed Mg, grain size conditions were similar while that of Mg-4Al was much lower. The b value for Mg-4Al was consistent with values found in other Mg alloys. Begum et al [6] measured a value of -0.15 for the Mg alloy, AZ31 while Mokdad et al [2] reported a value of -0.14 for ZEK100. The fatigue ductility exponent was calculated by plotting the $\log\frac{\Delta\varepsilon_p}{2}$ vs. $\log N_f$ and measuring the slope of the line. In general, the fatigue ductility exponent (c) was similar for unalloyed Mg and Mg-4Al and is within the range (-0.40 to -0.68) of what has been reported in other Mg alloys. Begum et al reported values of -0.40 and -0.44 for AZ31 [6] and AM30 [5], respectively. Monotonic, strain-controlled tension tests were also performed and the values for ultimate tensile strength, yield strength, and %elongation are reported in Table 5.10.

Table 5.10: LCF parameters and tensile properties for both the 45μm and 350μm unalloyed Mg conditions and Mg-4Al

LCF & Tension Parameters	Pure Mg, 45µm	Pure Mg, 350µm	Mg-4Al
Fatigue strength coefficient σ_f' (MPa)	591	572	615
Fatigue strength exponent *b*	-0.22	-0.27	-0.10
Fatigue ductility coefficient ε_f' (%)	1.74	1.07	1.16
Fatigue ductility exponent *c*	-0.57	-0.47	-0.42
Ultimate tensile strength (MPa)	160	147*	239
Yield Strength (MPa)	43	28	155
% Elongation	10.8	2.6	11.2

*fracture stress

Energy based models have also been used to describe LCF behavior [53-56]. These models consider the entire hysteresis loop area and may be more appropriate in materials were twinning-detwinning and solute interactions need to be considered [55-56] since the hysteresis area in compression is usually larger than that in tension due to twinning. The hysteresis loop energy or hysteresis loop area is defined as the amount of energy loss or dissipated as plastic work within a cycle [53-56]. Therefore, in cases where the amount of plastic work is high, the area will be large. The hysteresis loop area (energy) was measured from the hysteresis loops produced from the LCF experiments and the corresponding values at half-life for unalloyed Mg and Mg-4al are reported in Table 5.11. To develop an analytical relationship for life, the hysteresis loop energy (ΔW) can be written as a function of the stress and plastic strain amplitude which is given by equation 6 [55].

$$\Delta W = \frac{1-n'}{1+n'}\Delta\sigma\Delta\varepsilon^p \quad (6)$$

Substituting in equations 3 and 4, the hysteresis loop energy can be related to the fatigue life (N_f) using equation 7 [55],

$$\Delta W = \frac{4(1-\square')}{(1+n')}\sigma_f'\varepsilon_f'\left(2N_f\right)^{b+c} \quad (7)$$

Analysis showed that the energy is the highest for Mg-4Al when compared to unalloyed Mg. A comparison of the hysteresis loop energy as a function of cycles at 0.8% total strain amplitude for both unalloyed Mg and Mg-4Al is shown in Figure 5.17. It should be noted that this behavior was exhibited at all strain amplitudes. During cyclic loading in the fine-grained and coarse-grained unalloyed Mg, the energy gradually increases for majority of life which is consistent with data reported in a recent synchrotron study on the same fine-grained unalloyed Mg extruded bar where it was found that the twin volume fraction gradually increased with cycling [24]. In Mg-4Al the loop energy is highest during the first cycle. After that, it slightly decreases and remains near stable for majority of life. The behavior in Mg-4Al is also consistent with twin volume fraction data reported on the same Mg-4Al material here [25], where it was found that the twin volume fraction was the highest during cycle 1 where after it remained stable.

Table 5.11: Hysteresis loop energy values for Mg-4Al, coarse-grained unalloyed Mg and fine-grained unalloyed Mg at each strain amplitude. $\pm$ refers to the standard deviation between the 7-8 samples that were tested per condition or total strain amplitude

Total Strain Amplitude (%)	Mg-4Al (kJ/m^3)	Unalloyed Mg 350μm (kJ/m^3)	Unalloyed Mg 45μm (kJ/m^3)
1.0	1.76$\pm$0.006	1.38$\pm$0.05	1.18$\pm$0.01
0.8	1.08$\pm$0.009	0.916$\pm$0.05	0.808$\pm$0.002
0.6	0.573$\pm$0.0010	0.574$\pm$0.007	0.515$\pm$0.016
0.4	0.08$\pm$0.000	0.246$\pm$0.000	0.213$\pm$0.007

5.4. Discussion

The cyclic stress-strain response of a material is heavily influenced by interactions between dislocations and barriers such as, solute atoms and/or twin boundaries as well as dislocation mobility [1]. In the current work the influence of grain

size and alloying on both the plastic strain and stress amplitude as well as the tension-compression asymmetry were investigated under strain-controlled LCF conditions. The stresses needed to activate twinning and exhaust detwinning will also be discussed in detail and related to previous work involving in-situ high energy x-ray diffraction of the unalloyed Mg [24] and Mg-4Al [25] alloy used in this study. EBSD was also used to characterize residual twins and persistent twin formation.

5.4.1 The influence of grain size on cyclic stress-strain response in unalloyed Mg

In this study, it was determined that of the two grain sizes investigated, the twin initiation stress is independent of grain size in unalloyed Mg. During compressive loading, twin-induced yielding occurs at ~-45MPa followed by a low hardening rate as twins continue to nucleate and expand for both materials during cycle 2 (Figure 5.19). Other studies involving synchrotron diffraction and neutron irradiation have shown that this observed compressive yield behavior is characteristic of mechanical twinning [20,22]. The synchrotron diffraction study described in Chapter 3, on the fine-grained unalloyed Mg material found that the point at which the material yields during compression coincides with twin nucleation [24]. The influence of grain size on twin initiation in unalloyed Mg has not been studied extensively and the available literature provides data from monotonic compression tests and not cyclic experiments where twinning, detwinning, and dislocation slip need to be considered. Raeisinia at al showed that in as-cast unalloyed Mg for various grain sizes (40, 91, 670, 474, 1440μm) the CRSS for twinning increased with a decreasing grain size [29]. However, the data is limited and for grain sizes of 91 and 40μm the CRSS only decreased from 24MPa to 21MPa and at larger grains sizes the values (~10MPa) were approximately the same

[29]. It should also be noted that the scatter in the data in the coarser grains was related to a weakened texture due to the columnar casting grain structure [29]. Stanford and Barnett showed similar results for a rolled unalloyed Mg sheet where for grain sizes from 64 to 250μm the CRSS for twinning only decreased by ~7MPa [28]. Even though literature shows that the CRSS increases slightly with a decreasing grain size, the stresses needed to activate twinning does not appear to be influenced by grain size in the current study.

It was also observed that of the two grain sizes investigated, the stress at the point at which detwinning is complete (referred to as the detwinning exhaustion stress) is independent of grain size. Synchrotron diffraction and neutron irradiation studies have shown that for a given total strain amplitude the detwinning exhaustion stress may be related to the volume fraction of twins initiated during the previous cycle i.e. as the twin volume fraction increases the tensile stress needed to detwin the material also increases, and thus the stress at the completion of detwinning also increases [20,24-25]. In this study, during tensile reloading, the tensile stress (inflection point) at which detwinning is complete (+60MPa) and deformation continues through dislocation slip is the same for both grain sizes. This suggests that the volume fraction of twins produced during compression of the previous cycle is also the same for both materials and therefore not a function of grain size within the range investigated here. The role of grain size on twin volume fraction was examined by Beyerlein et al in unalloyed Mg, who determined that the number of twins per grain increased with grain size [57-58]. However, there was no evidence in that study that the overall twin volume fraction increased with increasing grain size. It was also determined that twin thickness was

independent of grain size [57-58]. In the current study, EBSD analysis also confirmed that for the grains in which twins were observed, the grains in the coarse-grained condition contained more twins than those in the fine-grained condition.

In terms of cyclic loading, understanding how twinning is influenced by grain size helps understand its effect on cyclic stress-strain behavior. Twin boundaries contribute to strengthening by providing obstacles to dislocation motion [27,59-60]. $\{10\bar{1}2\}\langle 10\bar{1}1\rangle$ extension twinning reorients the lattice to a hard-crystallographic orientation which can inhibit dislocation motion within twin and leading to high hardening rates within the twin [27]. In this study, the stress amplitude of the coarse-grained condition increases significantly as a result of cyclic hardening while that of the fine-grained condition remains near constant. This may be due to the longer free mean path for dislocation pile-ups in the coarse-grained material which can produce a back stress that further impedes the movement of dislocations resulting in strain hardening [6]. Residual twins also influence the hardening behavior since twin boundaries provide obstacles to dislocation motion. A neutron irradiation study on the Mg alloy, ZK60A, by Wu et al found that after a number of cycles residual twins remain in the material [20]. In the results described in Chapter 4, we found that in unalloyed Mg and Mg-4Al, the residual twin volume fraction increased with increasing cycles [25]. This behavior was confirmed in the present work using EBSD analysis, where after a 104 cycles residual twins remained in the material and twin activity reoccurred at the same location (Figure 5.15). The Kikuchi patterns in the twinned regions in Figure 5.15d indexed poorly which is presumably an indication of dislocation accumulation in twinned regions due to successive cycling. We suggest that at a certain point in cycling, the accumulation of

dislocations in the twin regions inhibits complete detwinning and "locks" in the residual twin structure.

The grain size effect on twinning behavior also influences the loop shape asymmetry usually found in wrought Mg alloys. The asymmetric hysteresis loop shape arises from the pronounced yielding that occurs during compression and is associated with the initiation and expansion of new twins while the inflection point in tension occurs due to the complete removal of those twinned regions. When complete detwinning ceases and if no new twins are nucleated, the inflection points disappear and the tension-compression strength asymmetry is reduced. An example of this is shown in Figure 5.11a for the fine-grained condition where after 500 cycles the inflection points seen in cycle 2 disappear and the peak tensile and compressive stresses are the same resulting in a symmetric loop. The opposite effect was observed in the coarse-grained condition where the loop shape asymmetry remained for the majority of life suggesting that complete twinning-detwinning continues for longer in this condition and that the twin volume fraction has not yet stabilized (Figure 5.11b).

In the previously described HEXD study (Chapter 4) [30] it was determined that at low strain amplitudes (0.4%), the diffraction peaks associated with twinning were not detected and the hysteresis loop remained symmetric for the entire fatigue life. In these ex-situ LCF tests, the loop shape asymmetry was also found to be dependent on total strain amplitude (Figure 5.12) and at 0.2% total strain amplitude a symmetric loop shape was produced. The results from previous work suggest that in conditions where the tension-compression asymmetry is observed, e.g. at high strain amplitudes and during the early stages of fatigue, twinning and detwinning occur. In contrast, at low

strain amplitudes below the stress at which twins are formed or at longer lives where residual twins are formed, deformation is dominated by dislocation slip and a stable symmetric stress-strain loop is produced.

5.4.2 The influence of aluminum on stress-strain response in Mg

In this study, it was found that the addition of Al doesn't have a significant effect on the twin initiation stress (Figure 5.19). The compressive yield behavior associated with twinning occurred at slightly higher stress in the Mg-4Al alloy when compared to unalloyed Mg where it was 12MPa more than that of unalloyed Mg. This was also confirmed in in-situ HEXD experiments on both materials described in Chapter 3 and 4. Similar to unalloyed Mg, the detwinning exhaustion stress is also influenced by the twin volume fraction. During the tensile reversal, the inflection point related to the exhaustion of detwinning is increased by 30 MPa in the Mg-4Al alloy. Results from the synchrotron study (Chapter 5) confirmed that the twin volume fraction in Mg-4Al was ~7% higher than that of unalloyed Mg [25]. Therefore, a higher tensile stress is required for complete detwinning during reloading. Even though a study by Ghazasedi et al found that the addition of solute increases the CRSS for twin dislocation motion [61], the analysis described in Chapter 4 indicated that that the impact of solute on the detwinning exhaustion stress appeared to be negligible. The hardening rate following detwinning is also dramatically increased in the Mg-4Al alloy when compared to unalloyed Mg. It is well understood that much lower activation stresses are needed to initiate detwinning than twinning since no nucleation is required [19,62]. The transition from detwinning which requires low activation stresses to slip which requires much higher stresses leads to an increased hardening rate in both materials. However, in the

Mg-Al alloy, solute-dislocation slip interactions must also be considered since solute atoms reduce dislocation mobility and may also contribute to the high hardening rate displayed in Mg-Al. Caceres et al found that the yield strength, hardness and flow strength increased with increasing Al concentrations between 1-8% during tensile loading [63].

In this study, significant cyclic hardening behavior was observed in Mg-4Al when compared to unalloyed Mg. The increase in strength in solution treated Mg-Al alloys arises from interactions between solute atoms and dislocations including the twinning-type where they reduce the mobility of dislocations during deformation [63]. The increase in CRSS for twin dislocation motion with aluminum concentration [61] suggests that in order to drive twin growth of new twins and/or residual twins during compression or the shrinking of twins during detwinning, the macroscopic stress must be increased. This results in higher stresses during tension and compression in Mg-4Al when compared to solute-free unalloyed Mg. Begum et al found that significant cyclic hardening was dominant at high strain amplitudes in AZ31 and related this behavior to the formation and interactions with twins [7].

5.4.3 Low Cycle Fatigue Behavior

In this study, for a given plastic strain amplitude (Figure 5.17b) fatigue life was independent of grain size (for the two grain sizes investigated) in unalloyed Mg and shorter in Mg-4Al samples even though the plastic strain amplitude was significantly lower in Mg-4Al. In LCF studies, the Coffin-Manson relationship is normally used to relate plastic strain amplitude to fatigue life, where the plastic strain amplitude, is measured as the width of the hysteresis loop at zero stress. In Mg alloys, where the

hysteresis loop is asymmetric and the area in compression is larger than that in tension due to twinning, the plastic strain amplitude may be insufficient to explain the fatigue damage during LCF, since the entire hysteresis loop area is not considered. However, plastic strain energy based models may be more appropriate to understand the relationship between plastic strain and fatigue life since the entire area within the hysteresis loop is considered [55-56]. The plastic strain energy is measured as the hysteresis loop area and is defined as the amount of energy loss as plastic work during a fatigue cycle [53-56]. In this study, at each strain amplitude, the energy is higher in the Mg-4Al alloy (Table 5.11) when compared to unalloyed Mg which may be a direct result of the increased twin volume fraction in this alloy which was discussed in the previous section. This increase in twin volume fraction causes the area within the loop during compression to be much larger than that of unalloyed Mg. The hysteresis loop energy vs. $2N_f$ is shown in Figure 17d, where it was found that for a given plastic strain energy the life is the shortest in Mg-4Al and the longest in fine-grained unalloyed Mg which was consistent with the measured values in Table 5.11. The longer fatigue life in fine-grained unalloyed Mg can be attributed to a lower plastic strain energy.

Even though there was no evidence that the twin volume fraction was increased in coarse grained unalloyed Mg, for a given plastic strain energy (Figure 5.17d) the fatigue life was generally shorter when compared to the fine-grained unalloyed Mg condition which may be related to the longer free mean path for dislocation pile ups in the coarse grain condition[6,57]. Dislocation pile-ups produce a forward/back stress against the grain boundary and when that stress is greater than the critical obstacle strength of the grain boundary, dislocations can pass through the boundary resulting in

slip of the neighboring grain [65]. Inherently, in the coarse-grained condition since there is a longer path for dislocation pile-ups the likelihood of such a pile-up resulting in plastic deformation of neighboring grains is higher and may explain why the plastic strain energy is higher in this condition when compared to the fine-grained condition.

It was determined that for a given total strain amplitude the fatigue life in the coarse-grained unalloyed Mg and Mg-4Al was similar while that of the fine-grained unalloyed Mg was slightly increased. The increased twin volume fraction in Mg-4Al and longer path for dislocation pile ups in the coarse grained unalloyed Mg may explain why (Figure 5.17c), the fatigue life is generally shorter than the fine-grained unalloyed Mg since stress concentrations at twin tips and the tips of pile-ups can serve as crack initiation sites. A fatigue damage study in unalloyed Mg by Yu et al found that at high strain amplitudes twin tips were dominant crack initiation sites due to an increase in twinning during compression [12]. However, crack initiation and growth were not the focus of this study and future experiments examining this behavior are needed to confirm this hypothesis.

The LCF parameters were also calculated and it was found that in all three conditions, the fatigue ductility exponent was similar and within the range (-0.40 to -0.68) of what has been reported in other Mg alloys. Begum et al reported values of -0.40 and -0.44 for AZ31 [6] and AM30 [5], respectively. Figure 5.20 shows a comparison of the total and plastic strain amplitudes for other aluminum containing wrought Mg alloys reported in literature and Mg-Al and fine-grained unalloyed Mg. The Mg-4Al shows a relatively enhanced fatigue life at high strain amplitudes but in general is similar to values reported in literature. The same was found for the plastic strain

amplitude, where for a given amplitude the fatigue life is similar to that of AZ31 and AM30. However, for unalloyed Mg at a given total and plastic strain amplitude the fatigue life is longer than that reported for aluminum containing Mg alloys but not much different than that reported for unalloyed Mg [12]. In a LCF study by Yu et al in unalloyed Mg (grain size =120μm) at 1.0% total strain amplitude it was reported that the sample separated into two pieces after 1110 cycles [12]. This value is slightly lower that the fatigue life (1133-1762) for the fine-grained unalloyed Mg sample tested at the same strain amplitude which may be a result of the grain size difference since the grain size is almost three times higher than that of the unalloyed Mg used in the present study. However, the fatigue life for the fine-grained unalloyed Mg is comparable to the value reported by Yu et al [12].

5.5. Conclusions

In the current study, strain-controlled low cycle fatigue experiments were conducted on unalloyed Mg in two different grain size conditions and a Mg-Al alloys. All studies were performed on extruded materials with a weak basal texture normal to the extrusion (loading) direction. The following conclusions were drawn from this work:

1. For the two grain sizes investigated, the twin initiation stress is independent of grain size in unalloyed Mg. In both the 45 and 350 μm condition the pronounced yielding in compression related to twinning occurred at the same stress.
2. The stress at the completion of detwinning for the two grain sizes investigated is independent of grain size in unalloyed Mg suggesting that the number of twins initiated during the following cycle was the same for both conditions.

3. The twin initiation stress in Mg-4Al is slightly higher than that in both unalloyed Mg conditions suggesting that the addition of Al may not play a large role in the stress needed to initiate twins.
4. The addition of aluminum significantly increases the stress at the exhaustion of detwinning and may be related to the increased twin volume fraction produced by compressive loading in the Mg-Al alloy.
5. The increased hardening rate after the completion of detwinning in the Mg-4Al alloy is closely related to solute-dislocation interactions since solute atoms can reduce dislocation mobility
6. For a given plastic strain amplitude, the fatigue life was independent of grain size in unalloyed Mg (for the two grain sizes investigated) and was reduced in Mg-4Al
7. Analysis of the hysteresis loop area found that the plastic strain energy was the highest in Mg-4Al and may explain the reduced fatigue life in this alloy

Figures

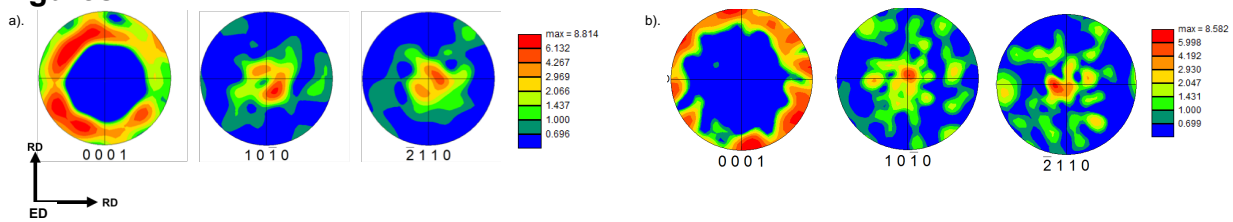

Figure 5.1: Pole figures showing the initial texture for a) unalloyed Mg and b) Mg-4Al with the basal poles aligned perpendicular to the extrusion direction. ED: Extrusion direction (parallel to loading direction); RD: Radial direction (normal to the extrusion direction)

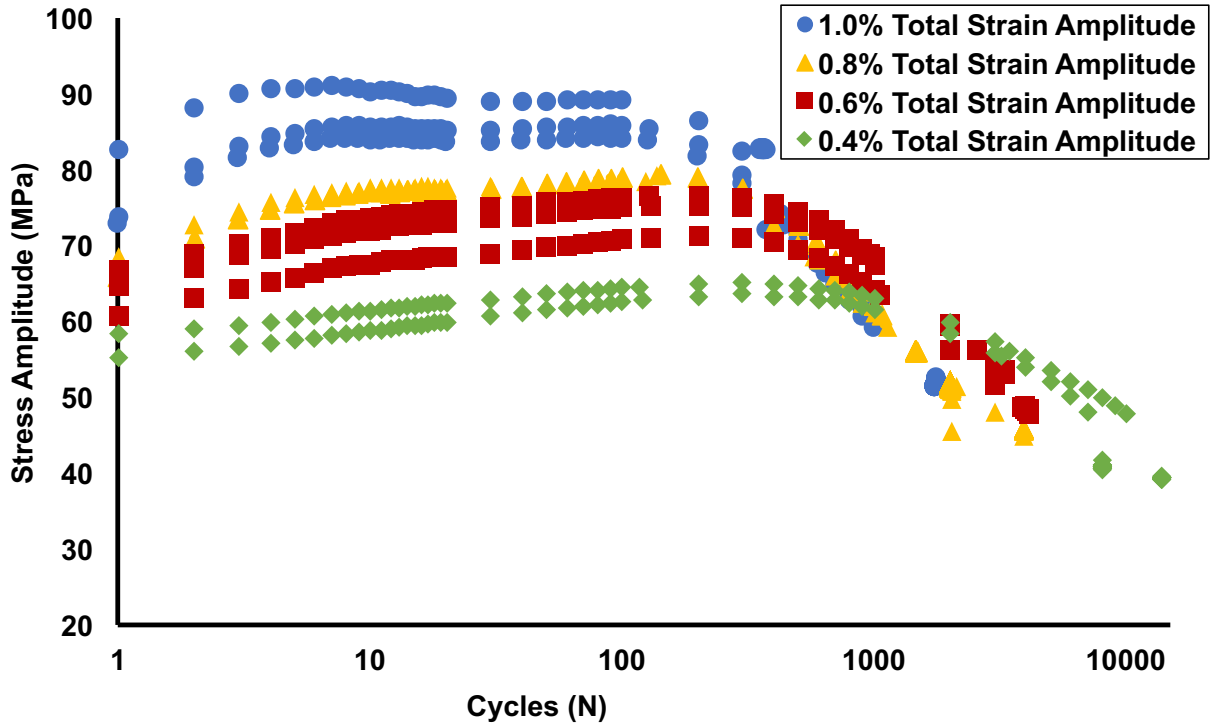

Figure 5.2: Stress Amplitude vs. the number of cycles at different strain amplitudes for unalloyed Mg in the 45μm fine grain condition

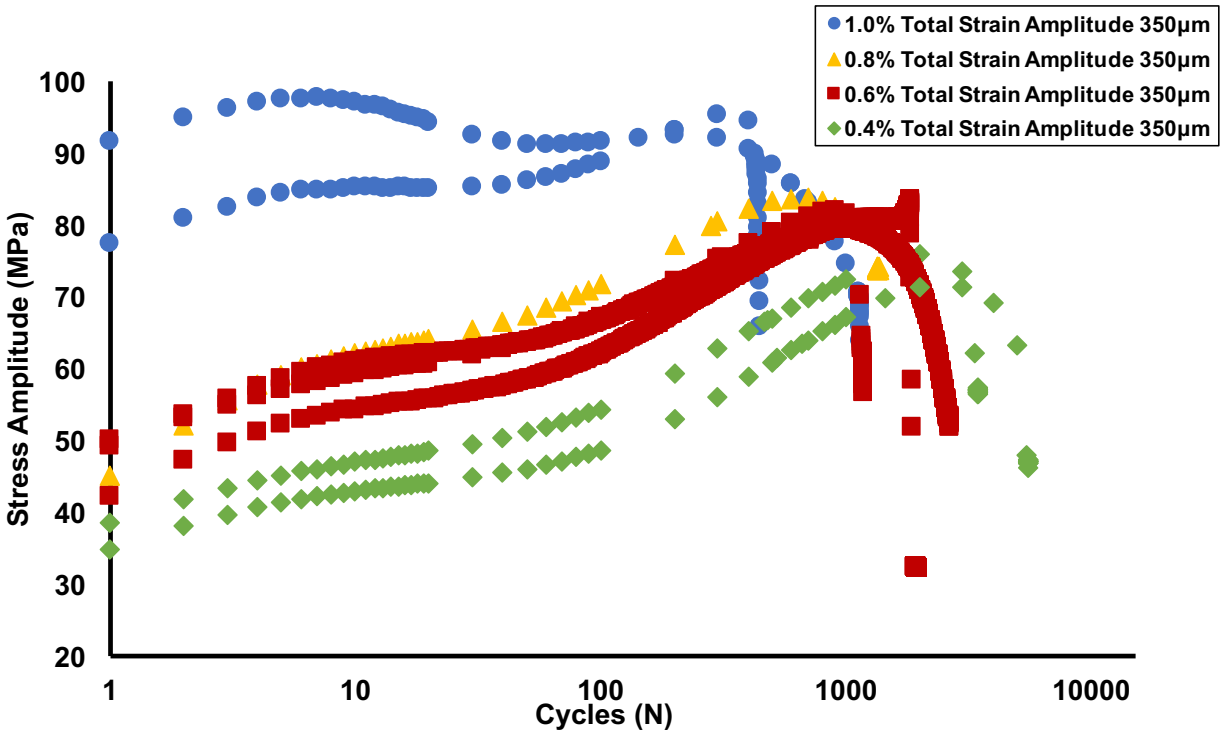

Figure 5.3: Stress Amplitude vs. the number of cycles at different strain amplitudes for unalloyed Mg in the 350µm fine grain condition

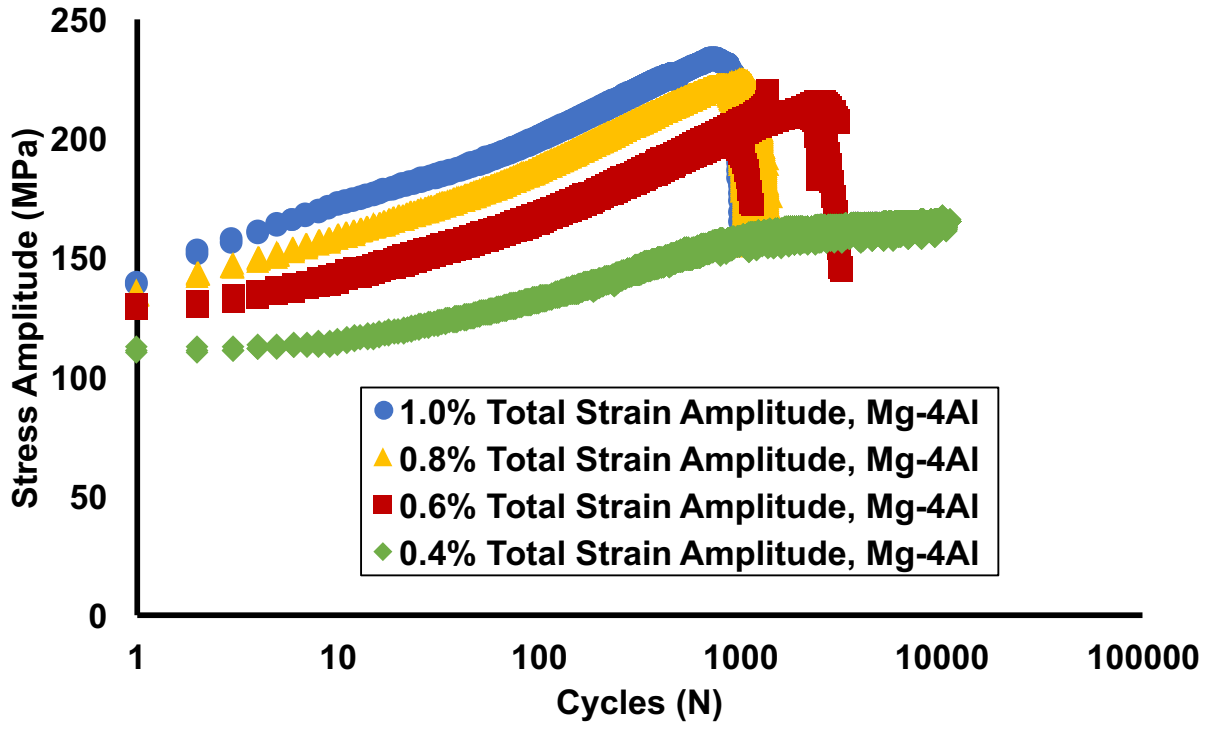

Figure 5.4: Stress Amplitude vs. the number of cycles at different strain amplitudes for Mg-4Al

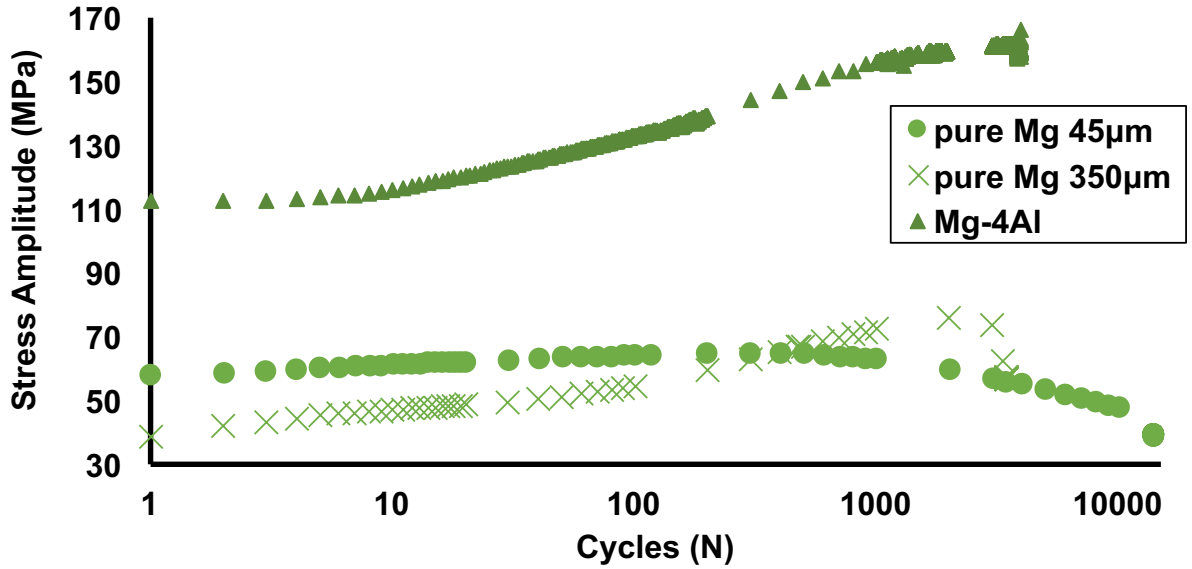

Figure 5.5: A comparison of stress amplitude vs number of cycles for the 45µm and 350µm unalloyed Mg conditions and Mg-4Al showing the difference in hardening behavior between the two conditions at 0.4% total strain amplitude

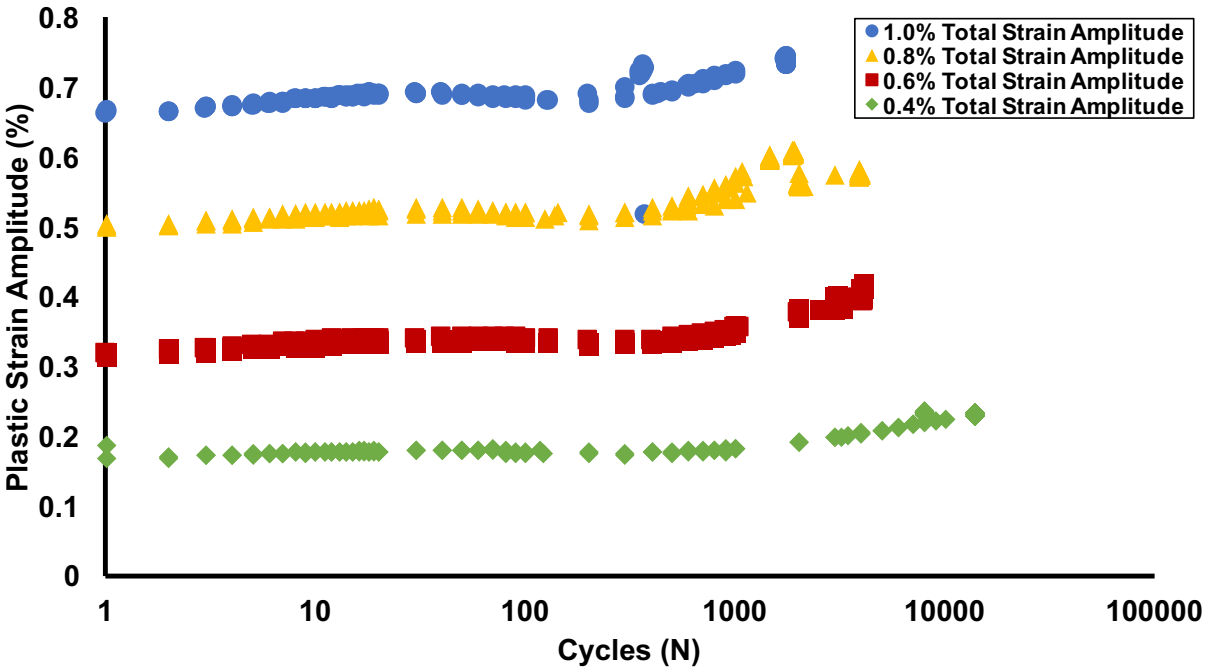

Figure 5.6: The evolution of plastic strain amplitude vs. number of cycles at 0.4%, 0.6%, 0.8%, and 1.0% total strain amplitudes for the unalloyed Mg, 45µm condition

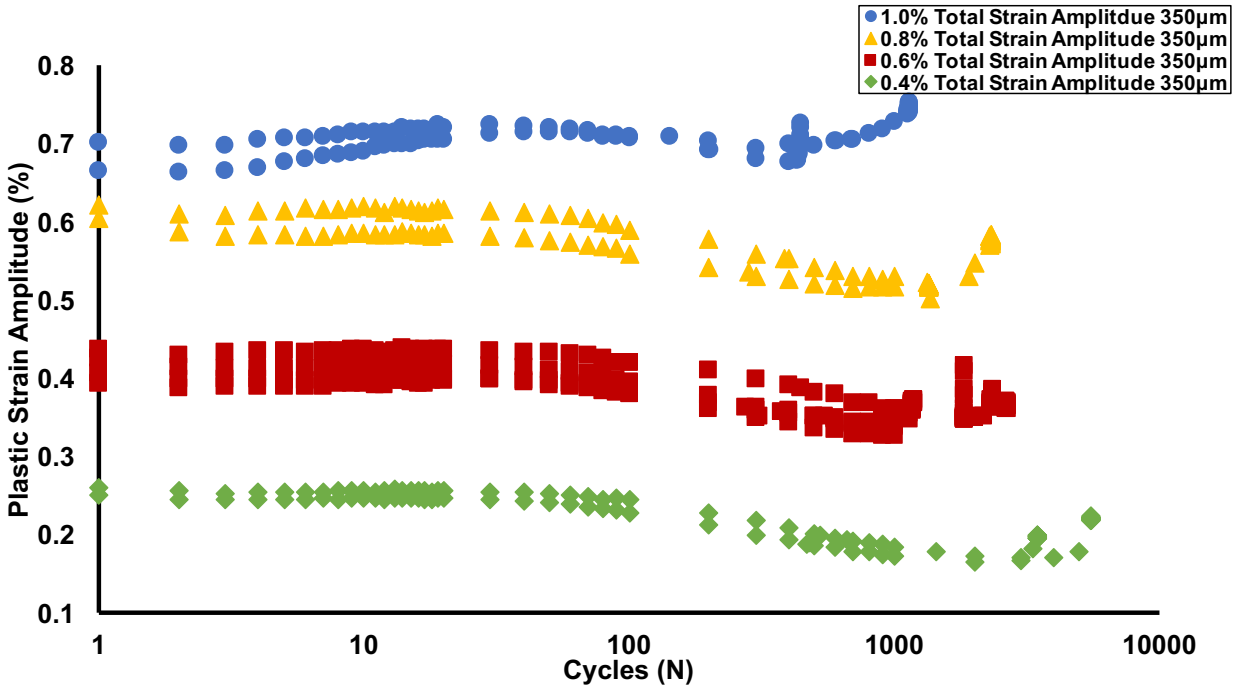

Figure 5.7: The evolution of plastic strain amplitude vs. number of cycles at 0.4%, 0.6%, 0.8%, and 1.0% total strain amplitudes for the unalloyed Mg, 350µm condition

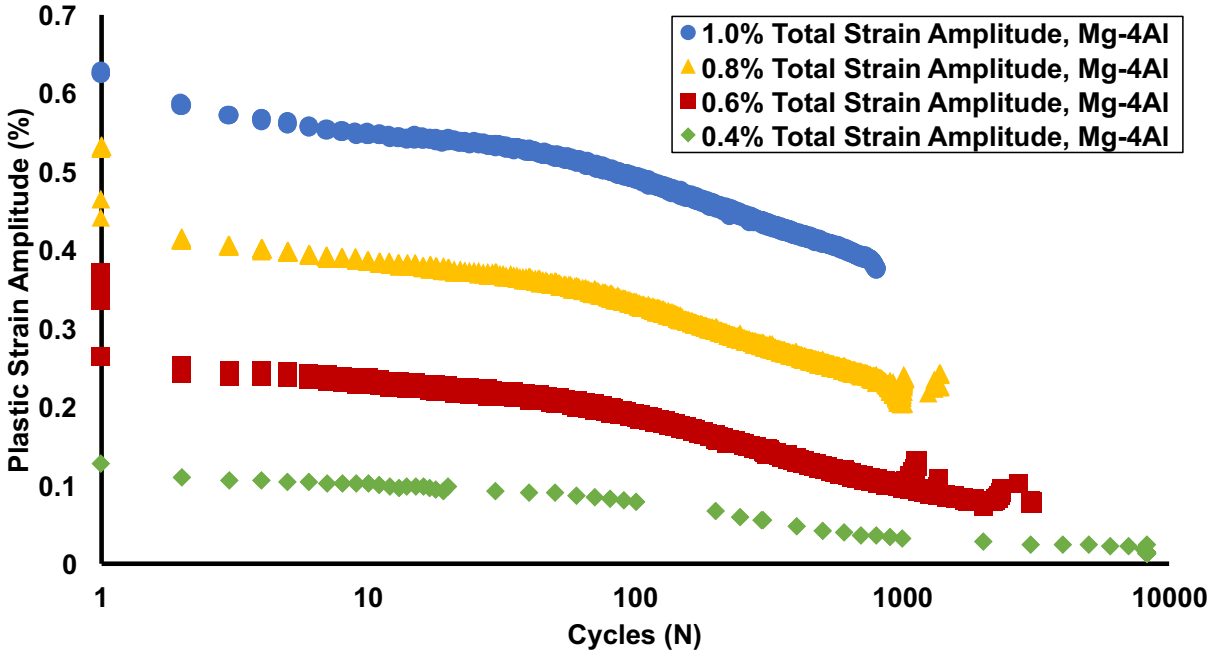

Figure 5.8: The evolution of plastic strain amplitude vs. number of cycles at 0.4%, 0.6%, 0.8%, and 1.0% total strain amplitudes for Mg-4Al

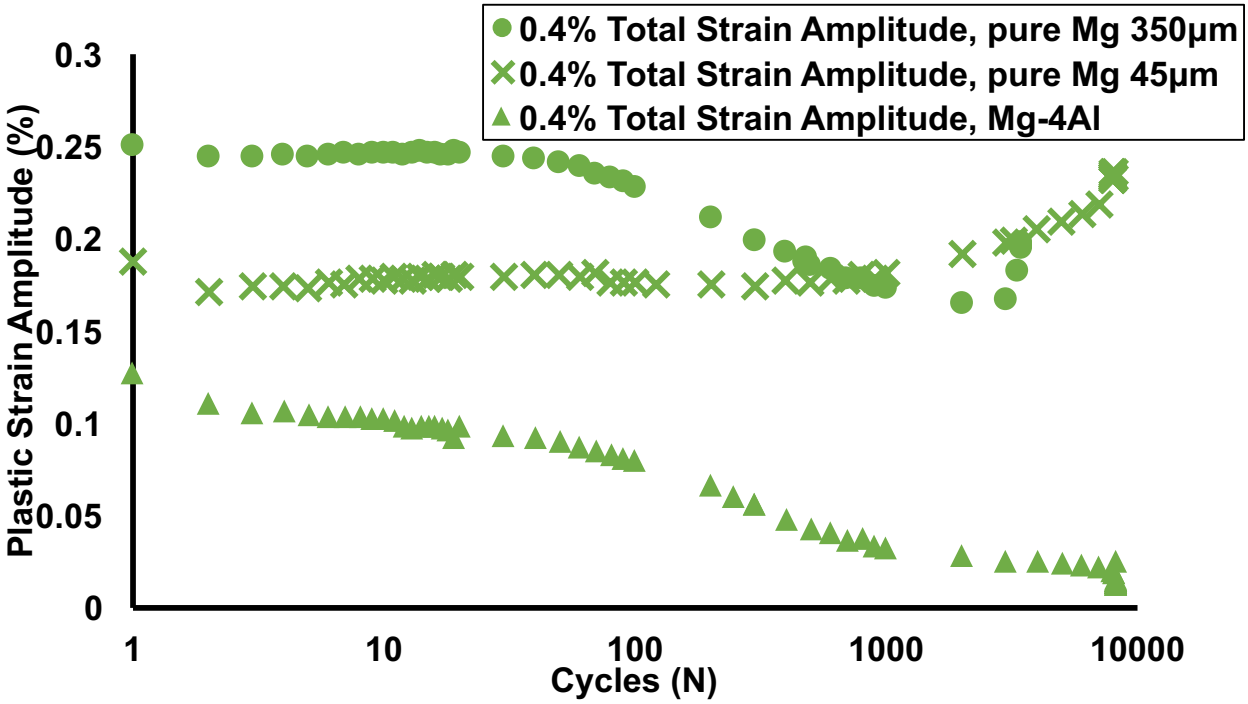

Figure 5.9: A comparison between the evolution of plastic strain amplitude as a function of cycles for the 45μm unalloyed Mg, 350 μm unalloyed Mg, and Mg-4Al

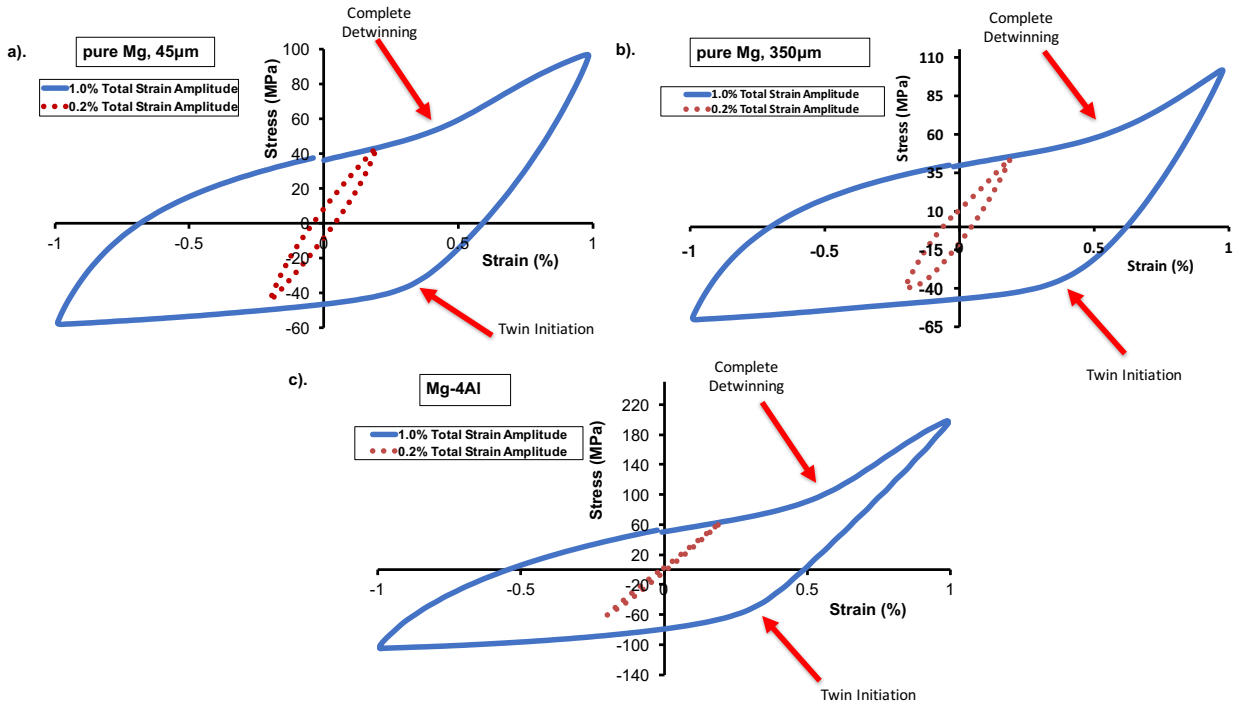

Figure 5.10: Loop shape comparison at 1.0% and 0.2% total strain amplitudes for a). fine-grained unalloyed Mg (45μm) b). coarse-grained unalloyed Mg (350μm) and c). Mg-4Al. The loop shape asymmetry is more pronounced at high strain amplitudes when compared to low strain amplitudes. It should be noted that the stress scales are different for each condition so that the stress-strain loop shape can be more fully visualized.

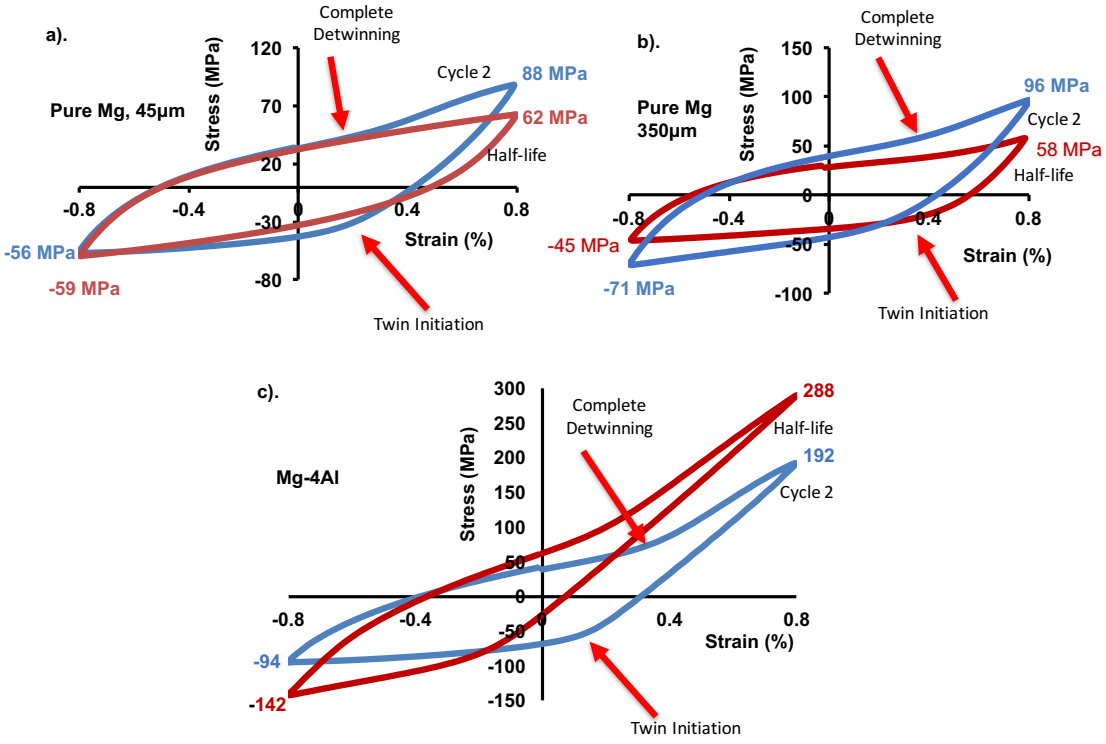

Figure 5.11: Comparison between the loop shape for cycle 2 and the half-life cycle for a). fine-grained unalloyed Mg (45μm), b). coarse-grained unalloyed Mg (350μm), and c). Mg-4Al. With successive cycling the tension-compression asymmetry is reduced in both unalloyed Mg and Mg-4Al

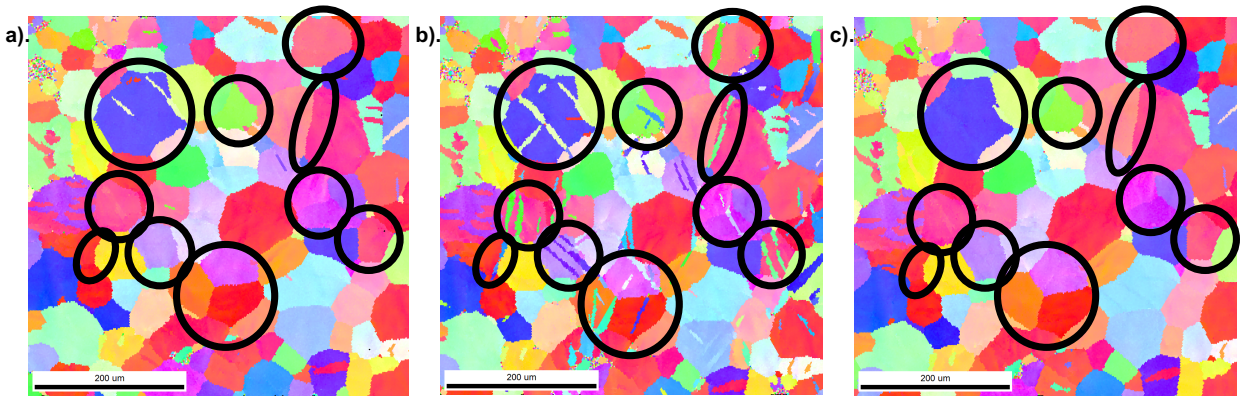

Figure 5.12: Electron back scatter diffraction patterns showing evolution of twinning and detwinning in fine-grained unalloyed Mg (45μm): a) as electro-polished condition (black

circles denote areas of interest), b) twins form in grains outlined in black circles after compression to -0.6% strain and c) those same twins are removed after tension to +0.6% strain. All EBSD measurements were in the unloaded condition.

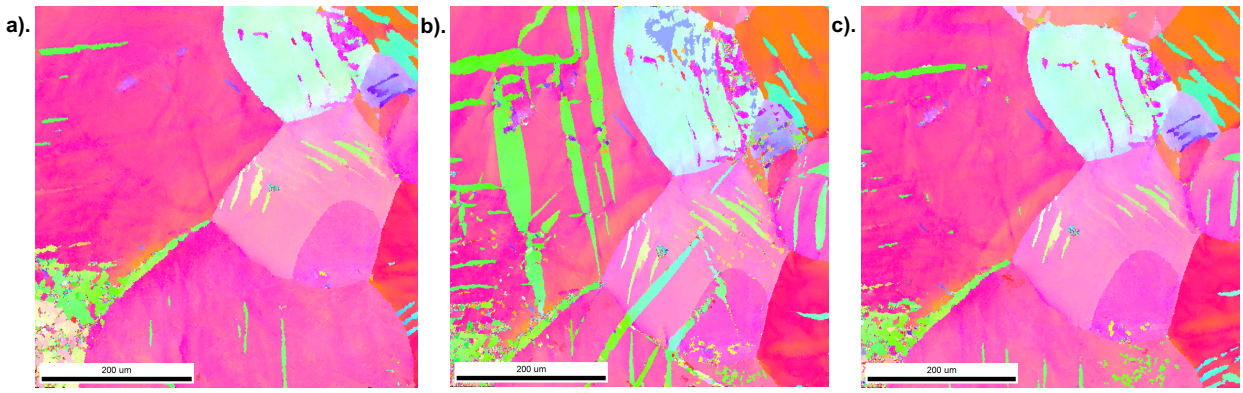

Figure 5.13: Electron back scatter diffraction patterns showing evolution of twinning and detwinning in the coarse-grained unalloyed Mg (350μm): a) as electro-polished condition b) twins form in some grains after compression to -0.6% strain and c) those same twins are removed after tension to +0.6% strain. All EBSD measurements were in the unloaded condition.

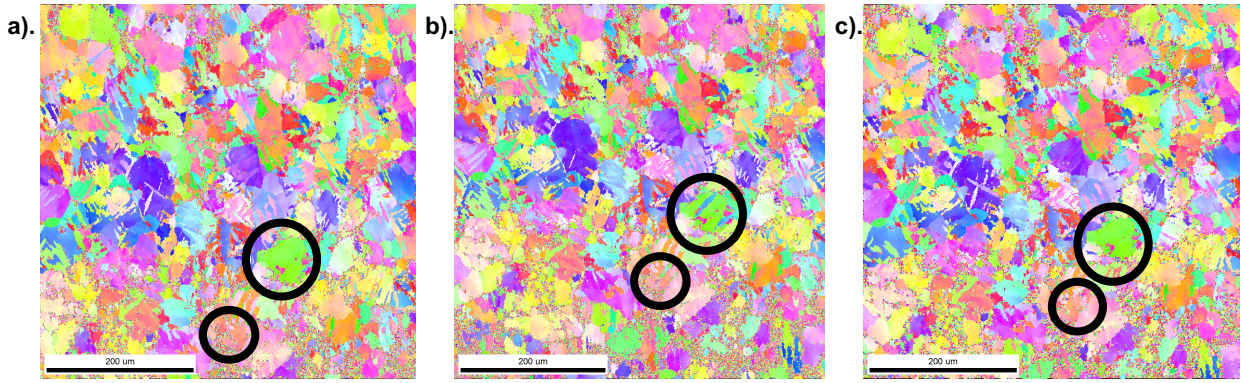

Figure 5.14: Electron back scatter diffraction patterns showing evolution of twinning and detwinning in Mg-4Al: a) as electro-polished condition (black circles denote areas of interest), b) twins form in grains outlined in black circles after compression to -0.6% strain and c) those same twins are removed after tension to +0.6% strain. All EBSD measurements were in the unloaded condition.

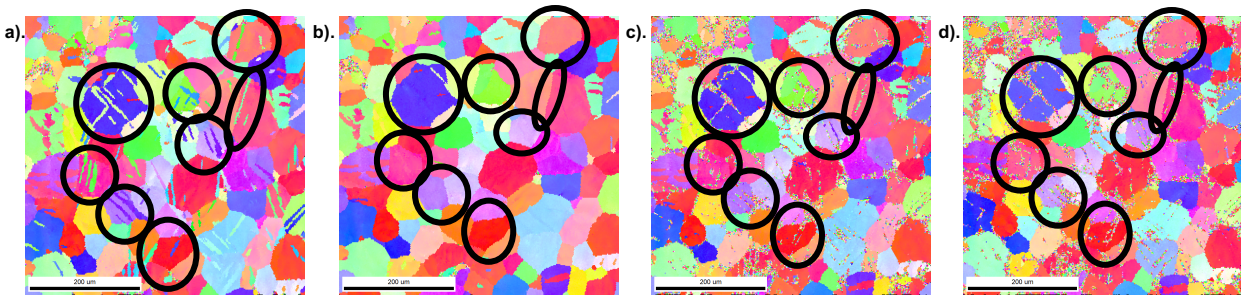

Figure 5.15: Electron back scatter diffraction patterns showing residual twins in fine-grained unalloyed Mg (45μm): a) twins form in grains after compression to -0.6% strain (black circles denote areas of interest), b) those same twins are removed after tension to +0.6% strain in areas outlined in black circles strain, c) the same twins return to the same grains after 104 cycles are applied to the sample, and d). when a quarter tension (+0.6% strain) cycle is applied after 104 cycles the twins are not completely removed confirming that residual twins remain in the material. All EBSD measurements were in the unloaded condition.

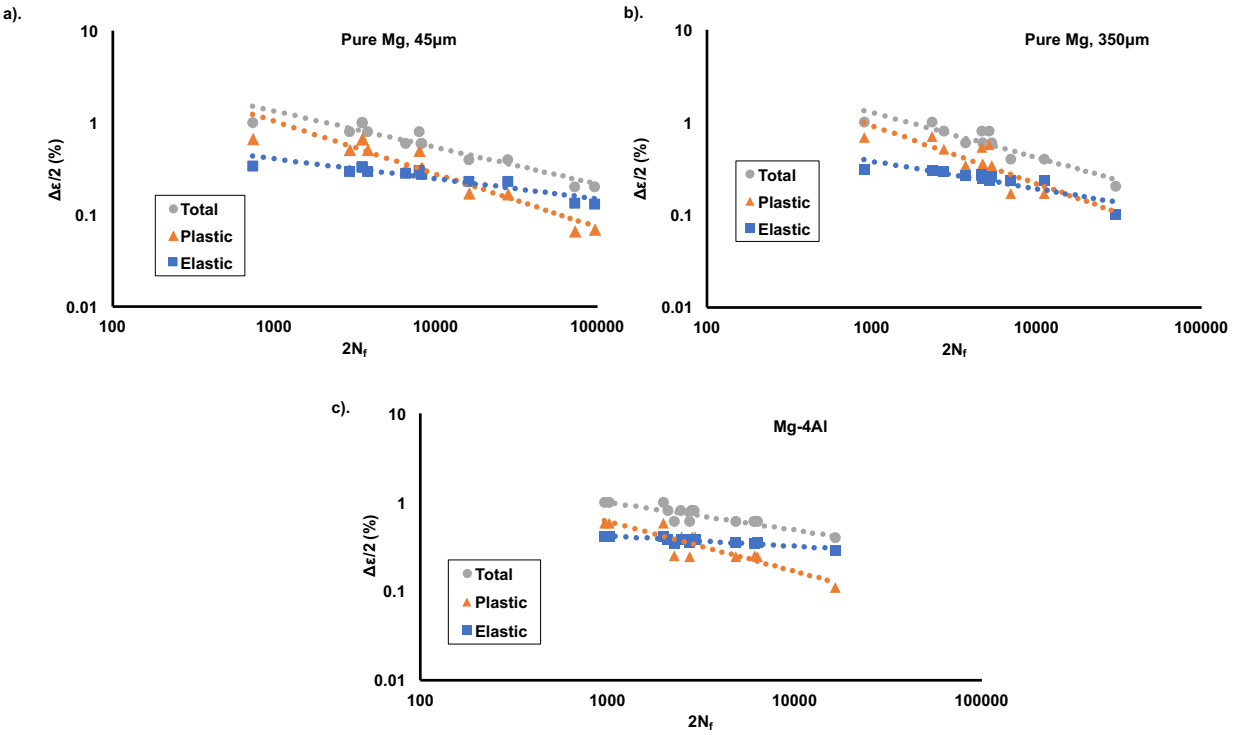

Figure 5.16: The total (grey circles), plastic (orange triangles), and elastic (blue squares) strain amplitudes as a function of cycles for a). fine-grained unalloyed Mg (45μm), b). coarse-grained unalloyed Mg (350μm), and Mg-4Al.

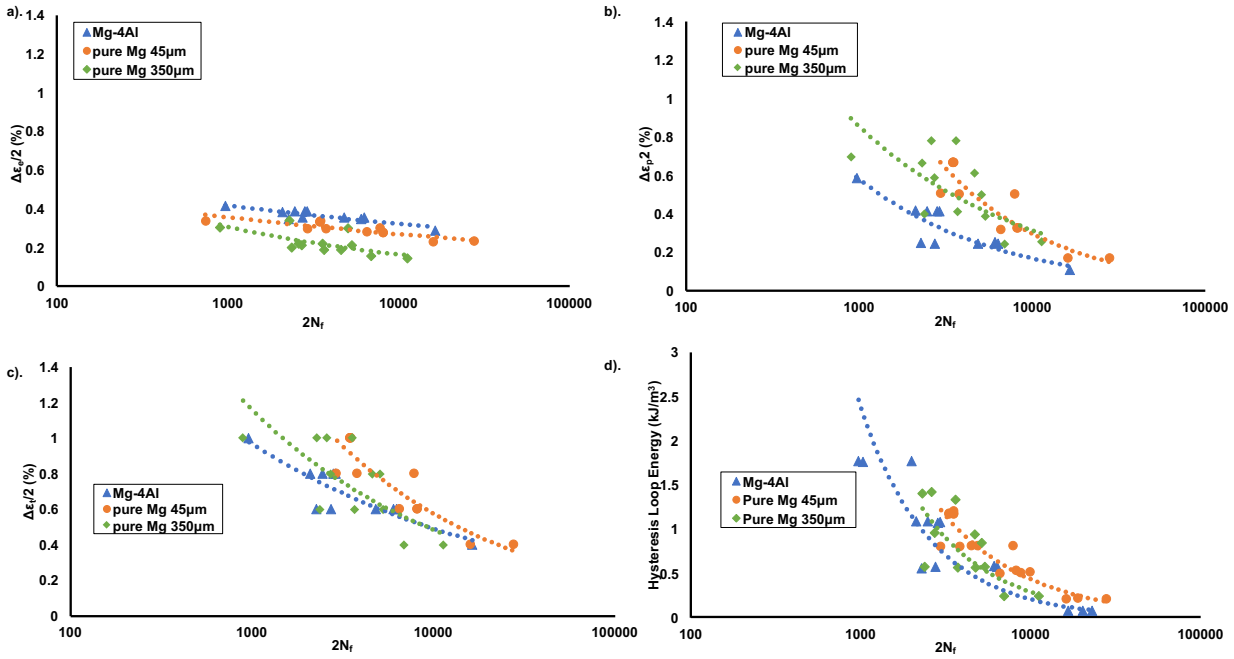

Figure 5.17: A comparison of the a). Basquin (elastic) b). Coffin-Manson (plastic) c). total strain-life and d). hysteresis loop energy relationships for unalloyed Mg and Mg-4Al

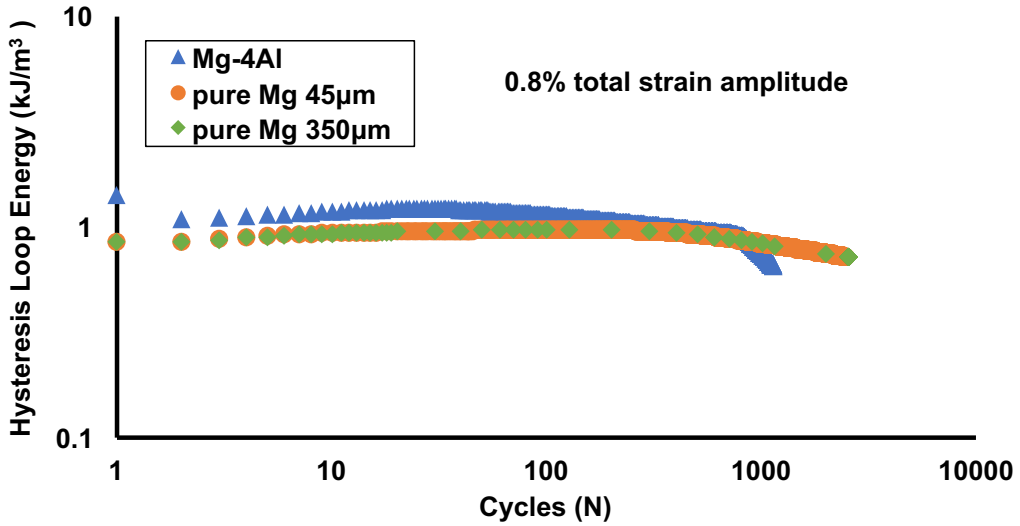

Figure 5.18: A comparison of the hysteresis loop energy as function of cycles for the fine-grained unalloyed Mg, coarse-grained unalloyed Mg, and Mg-4Al at 0.8% total strain amplitude

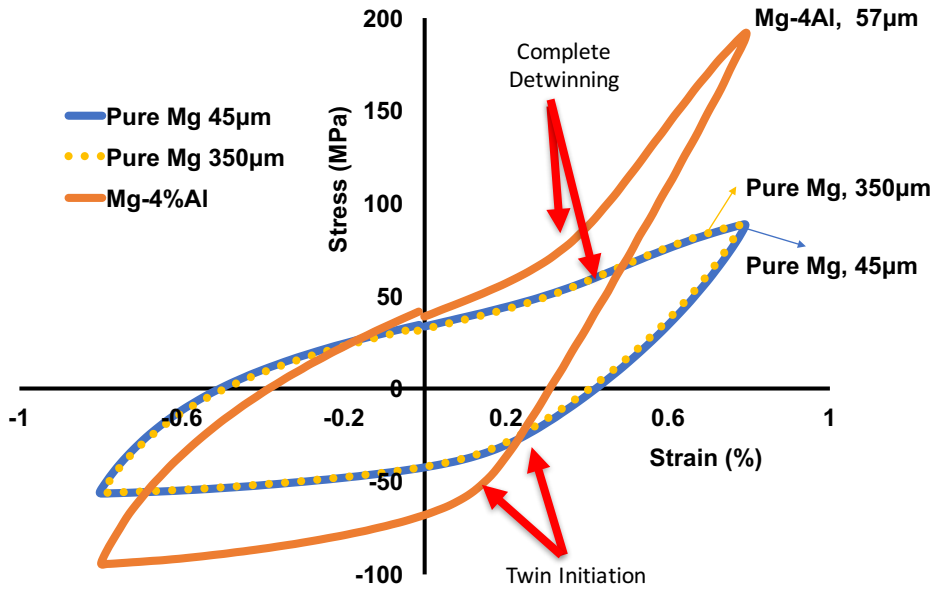

Figure 5.19: A comparison of the loop shape for cycle 2 of fine-grained unalloyed Mg (45µm) and Mg-4Al (52µm) showing the inflection points associated with twinning and detwinning

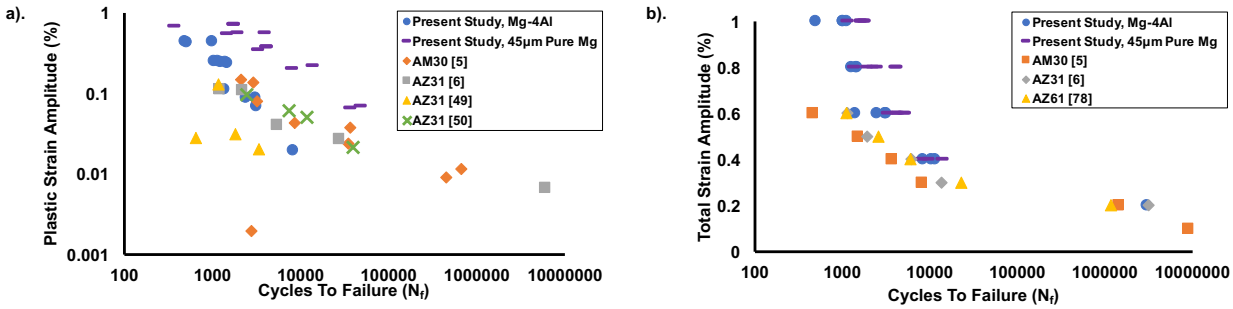

Figure 5.20: a). plastic and b). total strain amplitudes as a function of cycles to failure for Mg-4Al alloy and the fine-grained unalloyed Mg condition, in comparison with data reported in literature for other aluminum containing wrought Mg alloys

References

1. J.K. Mahato, P.S. De, A. Sarkar, A. Kundu, P.C. Chakraborti, Grain size effect on LCF behavior of two FCC metals, Procedia Eng. 160 (2016) 85-92
2. F. Mokdad, D.L. Chen, Strain-controlled low cycle fatigue properties of a rare-earth containing ZEK100 magnesium alloy, Materials & Design 67 (2015) 436–447
3. N. Stanford, D. Atwell, M.R. Barnett, The effect of Gd on the recrystallization, texture and deformation behavior of magnesium-based alloys. Acta Mater. 58 (2010) 6773-6783
4. X.Z. Lin, D.L. Chen, Strain hardening and strain-rate sensitivity of an extruded magnesium alloy. J Mater. Eng. Performance 17 (2008) 894-901
5. S. Begum, D.L. Chen, S. Xu, A. Lou, Strain-controlled low-cycle fatigue properties of a newly developed extruded magnesium alloy, Metall. Mater. Trans A 39 (2008) 3014–3026
6. S. Begum, D.L. Chen, S. Xu, A. Lou, Low cycle fatigue properties of an extruded AZ31 magnesium alloy, Int. J. of Fat. 31 (2009) 726-735
7. S. Begum, D.L. Chen, S. Xu, A.A. Luo, Effect of strain ratio and strain rate on low cycle fatigue behavior of AZ31 wrought magnesium alloy, Mater. Sci. Eng. A, 517 (2009) 334-343
8. C.L. Fan, D.L. Chen, and A.A. Luo, Dependence of the distribution of deformation twins on strain amplitudes in an extruded magnesium alloy after cyclic deformation, Mater. Sci. Eng. A 519 (2009) 38–45
9. F. Yang, F. Lv, X.M. Yang, S.X. Li, Z.F. Zhang, and Q.D. Wang, Enhanced very high cycle fatigue performance of extruded Mg-12Gd-3Y-0.5Zr magnesium alloy, Mater. Sci. Eng. A 528 (2011) 2231–2238
10. C. Bettles, M. Gibson, Current wrought magnesium alloys: strengths and weaknesses, J. Metals 57(2005) 46–49
11. Q. Yu, Y. Jiang, J. Wang, Cyclic deformation and fatigue damage in single-crystal magnesium under fully reversed strain-controlled tension-compression in the [1010] direction, Scr. Mater. 96 (2015) 41–44
12. Q. Yu, J. Zhang, Y. Jiang, Fatigue damage development in pure polycrystalline magnesium under cyclic tension-compression loading, Mater. Sci. Eng. A 528 (2011) 7816–7826
13. F.A. Mirza, D.L. Chen, D.J. Li, X. Q. Zeng, Low cycle fatigue of a rare-earth containing extruded magnesium alloy, Mater. Sci. Eng. A 575 (2013) 65–73
14. L. Chen, C. Wang, E.I.W. Wu, Z. Liu, G.M. Stoica, L. Wu, P.K. Liaw, Low-Cycle Fatigue Behavior of an As-Extruded AM50 Magnesium Alloy, Metall. Mater. Trans. A 38 (2007), 2235–2241
15. W. Wu, P.K. Liaw, K. An, Unraveling cyclic deformation mechanisms of a rolled magnesium alloy using in situ neutron diffraction, Acta Mater. 85 (2015) 343-353
16. W. Wu, K. An, L. Huang, S.Y. Lee, P.K. Liaw, Deformation dynamics study of a wrought magnesium alloy by real-time in-situ neutron diffraction, Scripta Mater. 69 (2013) 358-361

17. W. Wu, K. An, Understanding low-cycle fatigue life improvement mechanisms in a pretwinned magnesium alloy. Journal of Alloys and Compounds 656 (2016) 539-550
18. W. Wu, H. Qiao, X. Guo, P. Wu, P.K. Liaw, Investigation of deformation dynamics in a wrought magnesium alloy. Int. Journal of Plasticity 62 (2014) 105-120
19. W. Wu, Y, Gao, N. Li, C. M. Parish, W. Liu, P.K. Liaw, K. An, Intergranular twinning, detwinning, and twinning-like reorientation in magnesium alloys, Acta. Mater. 121 (2016) 15-23
20. L. Wu, A. Jain, D.W. Brown, G.M. Stoics, S.R. Agnew, B. Clausen, D.E. Fielden, P.K. Liaw, Twinning-detwinning behavior during the strain controlled low-cycle fatigue testing of a wrought magnesium alloy, ZK60A, Acta. Mater. 56 (2008) 688-695
21. D. W. Brown, A. Jain, S.R. Agnew, B. Clausen, Twinning and Detwinning During Cyclic Deformation of Mg Alloy AZ31B, Mater. Sci. Forum 539-543 (2007) 3407–3413
22. L. Wu, S.R. Agnew, Y. Ren, D.W. Brown, B. Clausen, G.M. Stoica, D.R. Wenk, P.K. Liaw, The effects of texture and extension twinning on the low cycle fatigue behavior of a rolled Mg alloy, AZ31B, Mater. Sci. & Eng. A 527 (2010) 7057-7067
23. L. Wu, S.R. Agnew, D.W. Brown, G.M. Stoica, B. Clausen, A. Jain, D.E. Fielden, P.K. Liaw, Internal stress relaxation and load redistribution during the twinning-detwinning-dominated cyclic deformation of a wrought magnesium alloy, ZK60A, Acta Mater. 56 (2008) 3699-3707
24. A. Murphy, D. Pagan, A. Beaudoin, M. Miller, J. Allison, Quantification of Twinning-Detwinning Behavior During Low-Cycle Fatigue of Pure Magnesium Using High Energy X-Ray Diffraction, Int. J. Fatigue (2018) Submitted
25. A. Murphy, D. Pagan, M. Miller, J. Allison, A Study On The Influence of Al on Twinning-Detwinning Behavior In Magnesium During Low Cycle Fatigue Using High Energy X-Ray Diffraction, In Preparation
26. F. Wang, J. Dong, Y. Jiang, W. Ding, Cyclic deformation and fatigue of extruded Mg-Gd-Y magnesium alloy, Mater. Sci. Eng. A 561 (2013) 403–410
27. M.R. Barnett, Z. Keshavarz, A.G. Beer, D. Atwell, Influence of grain size on the compressive deformation of wrought Mg–3Al–1Zn. Acta Materialia 52 (2004) 5093–5103
28. N. Stanford, M.R. Barnett, Solute strengthening of prismatic slip, basal slip and {10-12} twinning in Mg and Mg-Zn binary alloys, Int. J. Plast. 47 (2013) 165-181
29. B. Raeisinia, S.R. Agnew, Using polycrystal plasticity modeling to determine the effects of grain size and solid solution additions on individual deformation mechanisms in cast Mg alloys, Scripta Mater. 63 (2010) 731–736
30. Y. Cui, Y. Li, Z. Wang, X. Ding, Y. Koizumi, H. Bian, L. Lin, A. Chiba, Impact of solute elements on detwinning in magnesium and its alloys, Int. J. of Plast. 91 (2017) 134-159
31. S. Kada, P.A. Lynch, J.A. Kimpton, M.R. Barnett, In-situ x-ray diffraction studies of slip and twinning in the presence of precipitates in AZ91 alloy, Acta Mater. 119 (2016) 145-156

32. M.Z. Bian, A. Tripathi, H. Yu, N.D. Nam, L.M. Yan, Effect of aluminum content on the texture and mechanical behavior of Mg-1wt%Mn wrought magnesium alloys, Mater. Sci. Eng. A 639 (2015) 320-326
33. J.D. Robson, N. Stanford, M.R. Barnett, Effect of particles in promoting twin nucleation 27-34in a Mg-5wt % Zn alloy, Scripta Mater. 63 (2010) 823-826
34. N. Stanford, M.R. Barnett, Effect of particles on the formation of deformation twins in a magnesium based alloy, Mater. Sci. Eng. A 516 (2009) 226-234
35. U. Noster U, B. Scholtes, Isothermal strain-controlled quasi-static and cyclic deformation behavior of magnesium wrought alloy AZ31. Z Metallkd 2003;94(5):559–63.
36. S, Hasegawa, Y. Tsuchida Y, H. Yano, M. Matsui, Evaluation of low cycle fatigue life in AZ31 magnesium alloy, Int. J. Fatigue 29 (2007) 1839-1845
37. C. Wang, T. Luo, Y. Yang, Low cycle fatigue behavior of the extruded AZ80 magnesium alloy under different strain amplitudes, J. Mag. Alloys 4 (2016) 181-187
38. M. Canadija, X. Guo, D. Lanc, W. Yang, J. Brnic, Low cycle fatigue and mechanical properties of magnesium alloy Mg-6Zn-1Y-0.6Ce-0.6Zr
39. P. L. Mao, Z. Liu, Y. Li, L.J. Chen, "Low Cycle Fatigue Behavior of As-Extruded AZ31 Magnesium Alloy", Materials Science Forum, Vol. 686, pp. 202-207, 2011
40. S.H. Park, S. Hong, W. Bang, C.S. Lee, Effect of anisotropy on the low cycle fatigue behavior of rolled AZ31 magnesium alloy, Mat. Sci. Eng. A 527 (2010) 417-423
41. R.E. Sanders, E.A. Starke, The effect of grain refinement on the low cycle fatigue behavior of an Aluminum-Zinc-Magnesium-Zirconium alloy, 28 (1977) 53-68
42. Y.C. Lin, X.M. Chen, Z.H. Liu, J. Chen, Investigation of uniaxial low-cycle fatigue failure behavior of hot-rolled AZ91 magnesium alloy, Int. J. Fatigue 48 (2013) 122-132
43. Y.C. Lin, X.M. Chen, Z.H. Liu, J. Chen, Uniaxial ratcheting and low cycle fatigue failure behavior of AZ91D magnesium alloy under cyclic tension deformation, J. Alloys Compounds 509 (2011) 6838-6843
44. K. Gall, G. Biallas, H.J. Maier, P. Gullett, M.F. Horstemeyer, D.L. McDowell, In-situ observations of low cycle fatigue damage in cast AM60B magnesium in an environmental scanning electron microscope 35 (2004) 321-331
45. X.Z. Lin, D.L. Chen, Strain controlled cyclic deformation behavior of an extruded magnesium alloy, Mater. Sci. Eng A (2008) 106-113
46. S.H. Park, S. Hong, B.H. Lee, W. Bang, C.S. Lee, Low cycle fatigue characteristics of rolled Mg-3Al-1Zn alloy, Int. J. Fatigue (2010) 1835-1842
47. F.A. Mirza, D.L. Chen, D.J. Li, X. Q. Zeng, Low cycle fatigue of an extruded Mg-3Nd-0.2Zn-0.5Zr magnesium alloy, Mater. Design 64 (2014) 63–73
48. K. Shiozawa, J. Kitajima, T. Kaminashi, T. Murai, T. Takahashi, Low cycle fatigue deformation behavior and evaluation of fatigue life on extruded magnesium alloys, Proc. Eng 20 (2011) 1244-1249
49. J. Zhang, Q. Yu, Y. Jiang, Q. Li, An experimental study of cyclic deformation of extruded AZ61A magnesium alloy, Int. J. Fatigue 27 (2011) 768-787
50. D. Sornette, T. Magnin, Y. Brechet, The physical origin of the coffin-manson law in low-cycle fatigue, Europhysics Letters 20 (1992) 433-438

51. G.E. Dieter, (2013) Mechanical Metallurgy. McGraw-Hill
52. Y. Xiong, J. Katsuta, K. Kawano, T. Sakiyama, Characteristics of fatigue crack propagation behavior as identified by hysteresis loop at the crack tip, Fatigue Fract. Eng. Mater. Struct. 29 (2006) 454-463
53. J.D. Morrow, Cyclic plastic strain energy and fatigue of metals, Internal Friction, Dampling, and Cyclic Plasticity, ASTM (1965) 45-84
54. G.R. Halford, The energy required for fatigue, J. Mater. 1 (1966) 3-18
55. F. Ellyin, D. Kujawski, Plastic strain energy in fatigue failure, J. Pressure Vessel Technol. 106 (1984) 342-347
56. S.H. Kwon, K.S. Song, K.S. Shin, S.I. Kwun, Low cycle fatigue properties and an energy-based approach for as-extruded AZ31 magnesium alloy, Met. Mater. Int. 17 (2011) 207-213
57. I.J. Beyerlein, R.J. McCabe, C.N. Tome, Effect of microstructure on the nucleation of deformation twins in polycrystalline high-purity magnesium: A multi-scale modeling study, J. of the Mechanics and Physics of Solids 59 (2011) 988-1003
58. I.J. Beyerlein, C.N. Tome, A probabilistic twin nucleation model for HCP polycrystalline metals, Proceedings of The Society A 466 (2010) 2517-2544
59. A. Serra, D.J. Bacon, R.C. Pond, Twins as barriers to basal slip in hexagonal close packed metals, Met. Mater. Trans. A 33 (2002) 809-812
60. S.R. Agnew, C.N. Tome, D.W. Brown, S.C. Vogel, Study of slip mechanisms in a magnesium alloy by neutron diffraction and modeling, Scr. Mater. 48 (2003) 1003-1008
61. M. Ghazisaeidi, L.G. Hector Jr., W.A. Curtin, Solute strengthening of twinning dislocations in Mg alloys, Acta Mater. 80 (2014) 278-287
62. L. Wang, G. Huang, Z. Shi, H. Zhang, P. Bassani, M. Vedani, F. Pan, The effects of detwinning on the mechanical properties of AZ31B magnesium alloy with different strain rates at 423K, Mater. Sci. Eng. A 612 (2014) 423-430
63. C.H. Caceres, D.M. Rovera, Solid solution strengthening in concentrated Mg-Al alloys, J. of Light Metals 1 (2001) 151-156
64. J.B. Jordon, J.B. Gibson, M.F. Horstmeyer, H.E. Kadiri, A.A Luo, Effect of twinning, slip, and inclusions on the fatigue anisotropy of extrusion-textured AZ61 magnesium alloy. Mater Sci Eng, A 528 (2011) 528 6860–6871
65. M. Hamid, H. Lyu, B.J. Schuessler, P.C. Woo, H.M. Zbib, Modeling and characterization of grain boundary and slip transmission in dislocation density-based crystal plasticity, Crystals 152 (2017) 1-20

CHAPTER 6
THE RECRYSTALLIZATION BEHAVIOR OF UNALLOYED MG AND A MG-AL ALLOY

6.1. Introduction

Magnesium alloys are important materials due to their attractive properties including low density and an excellent strength-to-weight ratio [1-3]. One study found that the fuel efficiency of vehicles can be increased by 6-8% for each 10% in weight reduction [4]. Despite the advantages Mg alloys offer, they can have poor ductility and can be difficult to form at room temperature due in part to the limited number of independent slip systems available in hcp Mg and a tendency to form a strong deformation texture [1-2,5-9]. Grain refinement achieved via recrystallization is a technique for improving the strength and ductility of Mg alloys and to weaken the strong basal texture formed during deformation, and thus should be studied more extensively [7-10].

Deformation during processing leads to a buildup of dislocations and this increases the amount of strain energy stored in the material. During subsequent annealing reducing this stored energy drives the nucleation and growth of new, strain-free grains [11]. The formation of twins plays an important role in static recrystallization (SRX) of Mg alloys. Under certain conditions, Mg and Mg alloys have a tendency to form twins during deformation [12-16]. Several studies have shown that twins and twin boundaries serve as dominant nucleation sites during recrystallization of Mg alloys [9,12-19]. Dislocations cannot penetrate through twin boundaries leading to a build-up

of stored energy in their vicinity [13,17, 20-22]. There are three common twinning modes in Mg alloys: the primary $\{10\bar{1}2\}\langle 10\bar{1}1\rangle$ tension twins with an 86° lattice rotation about the $\langle 11\bar{2}0\rangle$ axis, $\{10\bar{1}1\}\langle 10\bar{1}2\rangle$ compression twins that have a 56° rotation around the $\langle 11\bar{2}0\rangle$ axis, and double twins that form when compression twins undergo tension twinning [12,14]. Guan et al found that double twins and double twin-grain boundary intersections were preferential nucleation sites during static recrystallization of the rare-earth magnesium alloy WE43. They also reported that tension twins did not recrystallize during annealing and were instead consumed by neighboring grains during grain growth [15].

Other studies have found that shear bands serve as nucleation sites in addition to twins and grain boundaries [23-25]. Shear band boundaries have a high angular misorientation which can accommodate dislocation cells and entanglements, increasing their stored energy [13]. A study by Su et al in AZ31 found that during the initial stages of recrystallization, small, recrystallized grains were found only in the vicinity of twins and shear bands and complete recrystallization of these areas occurred before large, deformed grains began to recrystallize [14].

Inhomogeneous nucleation of recrystallized grains due to the addition of twins has a profound effect on recrystallization behavior and differs from the well-known Johnson-Mehl-Avrami-Kolmogorov (JMAK) relationship, which assumes that nucleation sites are randomly distributed leading to a constant growth rate during recrystallization and that recrystallization kinetics can be described by a single Avrami exponent value of three [6,11,13-14]. Several studies have shown that preferred recrystallization at twins leads to Avrami exponent values which are less than three [13-14].

Nucleation at twins during recrystallization can lead to a two-stage nucleation recrystallization process where initially nucleation and growth occurs in the vicinity of twinned regions and grain boundaries [14,26]. Once all of those regions are consumed recrystallization proceeds in regions of lower stored energy. One study, in the Mg alloy AZ31 found that heterogeneous distribution of stored energy due to preferred nucleation at twins led to a recrystallization process that could be described by two Avrami exponents, one representing the first stage (recrystallization at twins) and the other representing the second stage (recrystallization at deformed grains) [14]. The two-stage recrystallization process due to inhomogeneous nucleation has also been found in cold-deformed titanium, copper, and carbon steel [26].

Many previous recrystallization studies in magnesium have focused on dynamic recrystallization behavior [13-16,18,20,22,27-29,30] and relatively limited information is available on the static recrystallization behavior of these materials. Studies on static recrystallization in Mg have focused primarily on the Mg-Al-Zn series and Mg-rare-earth alloys [10,12,14,16-17,19,22-23,29].

In the current investigation, the static recrystallization behavior of unalloyed Mg and a binary Mg-4wt%Al alloy was examined. This study emphasizes the effect of solute concentration, temperature, and deformation modes, e.g. twinning, on the recrystallization behavior after room temperature deformation. A limited study was conducted on the influence of starting grain size on recrystallization in the unalloyed Mg condition. The experimental results were modeled using the JMAK relationship [11] to characterize the static recrystallization kinetics of the materials.

6.2. Experimental Procedure

6.2.1 Materials

Unalloyed Mg was provided in the form of extruded bar by CanmetMaterials. The bar was extruded from an 85-mm diameter cast billet at 300°C at a speed of 254 mm/min to a final diameter of 15mm. An 85-mm diameter cast Mg-4Al billet was also used in this work. The as-received cast billet was solution treated at 413°C for 15 hours prior to machining of the cylindrical samples to homogenize the Al concentration. It should be noted that the samples for the recrystallization experiments in Mg-4 weight percent Al (Mg-4Al) were taken from the heat-treated billet due to the γ-$Mg_{17}Al_{12}$ phase precipitation that occurred during the extrusion process. The starting grain size of the unalloyed Mg and Mg-4Al, was 45±15μm and 350±50μm, respectively. In order characterize the influence of starting grain size in unalloyed Mg, cylindrical samples were heat treated at 525°C for 3 hours in a Carbolite box furnace. This produced a starting grain size of 350μm. This also allowed comparison with the Mg-4Al condition.

After annealing the samples were water quenched and sectioned parallel to the compression axis for further examination. Metallographic specimens were prepared using standard techniques, finishing with a 0.05μm polycrystalline diamond solution. An acetic-nitric solution was used to etch the specimens for 3-5 seconds, which revealed grains and twins under microscopy. Electron back scatter diffraction (EBSD) was used to determine the crystallographic orientation of grains in each sample. The fraction of recrystallized grains was measured using OIM Analysis 7 software via the Grain Orientation Spread (GOS) technique [31].

6.2.2 Experimental Methods

6.2.2.1 Room temperature deformation

Cylindrical specimens, 10 mm in diameter and 12 mm in height were machined from the as-received materials using electrical discharge machining (EDM); the specimens were cut so that the compression axis was parallel to the extrusion direction. The cylinders were then compressed to a 20% height reduction at room temperature using an Instron load frame equipped with a 100kN load cell at a constant displacement rate of 0.03mm/min. To reduce the friction between the samples and the compression dies, the ends of the cylindrical samples were hand ground to an 800 SiC grit finish and both Teflon tape and a commercial lubricant were applied between the two surfaces. Previous work had indicated that, due to friction effects, compression of the cylinder lead to non-uniform strains. All recrystallization measurements were taken from a uniform section in the center of the cylindrical compression sample. Global macroscopic strains were calculated from end displacement measurements. To quantify the plastic strain in the central uniform measurement zone of the sample, a finite element analysis simulation of the compression of the cylindrical samples was conducted using the commercial program Abaqus. The purpose of the simulation was to determine the strain distribution in the compressed cylindrical sample. In Abaqus, a 1/8 axi-symmetric model was used with a four-node bilinear axi-symmetric quadrilateral mesh. The upper die was modeled as a rigid body and given properties of a steel. The cylindrical sample was modeled as a deformable body, where input data including the elastic modulus and stress-strain data that had been measured using uniaxial tensile tests performed at room temperature. The stress-strain input data was inserted in tabular form for use by

Abaqus. The simulation boundary conditions were such that the free end of the sample is not free to move along the x and z directions but does move along the y-direction, which is outlined in Figure 6.1. The results of the simulation are shown in Figure 6.1 and the 1mmx1mm region outlined by the black box indicates the area of high and uniform plastic strain. The variation in strain within this region was within 1% of the reported local strain. For the purposes of this study all experimental EBSD characterization was performed within this region. It was determined that after a global macroscopic average strain of 20%, the amount of plastic strain in the central measurement in the fine-grained unalloyed Mg was 32% and 30% in the Mg-4Al.

6.2.2.2 Annealing

The compressed samples were then annealed using the conditions listed in Table 6.1. The annealing heat treatments for unalloyed Mg at all temperatures and for Mg-4Al at 250°C were performed in an oil bath, while a Carbolite box furnace was used to anneal the Mg-4Al samples at both 275°C and 300°C. A different heat-treating method was used for the Mg-4Al at 275°C and 300°C because the maximum temperature limit of the oil bath was 250°C and therefore, could not be used at temperatures above this point. Thermocouples were placed on samples during the annealing processes to ensure that the temperatures were equivalent in both the oil bath and the box furnace. Recrystallization was characterized in both the fine-grained and coarse-grained unalloyed Mg.

Table 6.1: Annealing conditions for unalloyed Mg and Mg-4Al

Material	Temperature (°C)	Time (sec)
unalloyed Mg	150,200, 250	1-604800
Mg-4Al	250, 275, 300	10-604800

At the annealing temperatures of interest some annealing times were relatively short. To ensure that the annealing time represented a nominally isothermal condition, heating experiments were performed on both unalloyed Mg and Mg-4Al in the form of 10mm diameter cylinders and 6-8 mm thick rectangular specimens. A thermocouple was drilled in the center of each sample to measure the temperature transient. A 5 mm x 5 mm x 6 mm rectangular specimen was found to provide a sufficiently short heat up time and were machined from the center of each compressed cylinder prior to annealing. All of the annealing experiments discussed throughout this paper were performed on these rectangular specimens. The heat-up time was 10 seconds for the unalloyed Mg samples in the oil bath and 30 seconds for the Mg-4Al samples in the Carbolite box furnace. The annealing times reported were time at temperature in the bath or furnace. Annealing times of 1 second were used in this study, during these experiments a thermocouple was spot welded to the side of the specimen to monitor the temperature during annealing, once the specimen reached temperature, it was removed and water quenched.

6.2.2.3 Microstructural Characterization

Crystallographic orientation information for each sample was collected using electron back scatter diffraction (EBSD). Scans were performed using a Tescan Mira 3 scanning electron microscope equipped with an EDAX Hikari XP EBSD detector. Each scan was taken at a voltage of 30kV and a beam intensity between 18-20 with an average step size of 1.2±0.1μm. TSL OIM software was used to characterize EBSD data and an average confidence index of 0.7±0.2 was obtained. No additional

confidence index cleaning was applied to the data. A grain tolerance angle of 5° was used for grain recognition and at least 1000 grains were sampled per condition.

The grain orientation spread (GOS) method was employed to measure the fraction recrystallized for each specimen [31]. It is a grain-based approach to measure the local misorientation value for a grain. GOS uses the concept that regions with high amounts of deformation will have a large variation in local crystallographic orientation due to lattice rotations caused by dislocations; in contrast, recrystallized (strain-free) grains will have little or no variation in orientation. The GOS method uses the orientation data provided by EBSD to measure the average orientation of a grain. It then compares each point within the grain to that average orientation to determine a misorientation value for each point. Once that analysis is complete, the misorientation values within a grain are averaged to get a single misorientation value that is assigned to that grain. That final misorientation value is known as the GOS value [31-32]. The TSL-OIM software calculates the GOS value using the formula below, where g_{ave} is the orientation matrix for the average orientation of the grain.

$$GOS = \frac{1}{N}\sum_{A=1}^{N}\left\{min\left[cos^{-1}\left(\frac{trace[g_{ave}(h_i g^A)^{-1}]-1}{2}\right)\right]\right\} \quad (1)$$

In this investigation, any grain with a GOS value of 1° or less is considered recrystallized. This was determined by analyzing the GOS distributions for partially recrystallized unalloyed Mg samples annealed at 200°C shown in Figure 6.2. The sample displays a bimodal distribution in misorientation with one peak at low GOS values representing the strain-free, recrystallized grains and the second peak at high GOS values representing the deformed grains. The GOS distribution in this sample show that the first peak representing the recrystallized grains occurs at 0° to 1°. An

example of the GOS method being used in Mg-4Al sample annealed at 250°C for 2 hours is shown in Figure 6.3, where the recrystallized grains are highlighted in light blue representing the bin of GOS values of 0° to 1°. In this example, the fraction recrystallized was
determined to be 56%.

6.3. Results

6.3.1 Static Recrystallization in Mg-4Al

In the present study, three different annealing temperatures, 300°C, 275°C, & 250°C, were selected to study the effect of temperature on static recrystallization in Mg-4Al. The experimental results for each temperature are shown in Figure 6.4. Each point on the plot represents the recrystallization fraction for a specific condition (time/temperature). Three separate annealing experiments were conducted for each condition. The JMAK relationship was used to model the experimental results at each temperature and is represented by the solid lines in Figure 6.4. The JMAK relationship, which is outlined in Equation 2 relates the fraction of recrystallized grains (X) to the annealing time (t).

$$X = 1 - \exp\left[-0.693\left(\frac{t}{t_{0.5}}\right)^{n}\right] \quad (2)$$

The relationship includes the time required to achieve 50% recrystallization ($t_{0.5}$) and the Avrami exponent (n). The Avrami exponent was determined by plotting ln(ln(1/1-X)) vs. ln(t) and measuring the slope of the line (Figure 6.5). Recrystallization was observed to occur at a slower rate at longer times and that a single Avrami

exponent, n was inadequate to describe the entire recrystallization process. This is highlighted at longer annealing times where the experimental data is not well captured by the JMAK model lines (solid lines) especially at 300°C, which demonstrates that a single Avrami exponent does not represent well this recrystallization process. Rather the recrystallization exponent appeared to be bilinear which is representative of a two-stage recrystallization process [14]. Figure 6.5 shows the two stages of nucleation and growth during the recrystallization process, represented by two different Avrami exponents, n_1 and n_2. Characterization of the microstructure during the annealing process indicates that the two stages are related to recrystallization at microstructural inhomogeneities, specifically, twins that formed during the compressive deformation. The analysis of this recrystallization process will be discussed in Section 3.1.2. The $t_{0.5}$ is interpolated from the experimental data. The JMAK parameters can be found in Table 6.2 and the results will be discussed in later sections.

Table 6.2: Summary of JMAK constants for Mg-4Al at each annealing temperature

Annealing Temperature (°C)	**n_1**	**n_2**	**$t_{0.5}$ (seconds)**
250	0.45	0.08	7200
275	0.51	0.20	2800
300	0.48	0.05	200

As expected, recrystallization slows down as the annealing temperature is decreased as indicated by an increase in $t_{0.5}$: from 200 seconds at 300°C to 7200 seconds at 250°C. The activation energy for recrystallization (Q_{REX}) can be calculated using Equation 3 by plotting $\ln(t_{0.5})$ versus 1000/RT and determining the slope of the linear best fit which is shown in Figure 6.6 [11]. From the results, it was determined that the recrystallization activation energy, $Q_{REX,}$ for Mg-4Al was 177 kJ/mol.

$$t_{0.5} = A\varepsilon^{p}\dot{\varepsilon}^{q}exp\left(\frac{Q_{REX}}{RT}\right) \quad (3)$$

EBSD characterization of the as-compressed state (Figure 7a) of Mg-4Al revealed that twins were formed throughout the microstructure. Twinning is a common deformation mode in magnesium and its alloys and was particularly evident due to the coarse grain size of the starting material. EBSD Kikuchi patterns in regions of high deformation were unable to be indexed and are shown in black on the GOS map. During the early stages of annealing, small, recrystallized grains were found within twins and along grain boundaries. An example of this is outlined in Figure 6.7, where the IPF maps along with the corresponding GOS map are shown for 275°C and 300°C. The light blue regions on the GOS maps represent recrystallized grains in the material. Recrystallization of twins and along grain boundaries occurred as early as 300 seconds at 250°C, 30 seconds at 275°C and 10 seconds at 300°C.

As indicated, twins and grain boundaries were found to be preferential nucleation sites for recrystallization and as the annealing time increased recrystallization continued in those regions indicating that the stored energy was higher in these regions. Once regions of high stored energy were fully recrystallized, recrystallization continued in the lower strained grain interiors. These two stages are described by two different Avrami exponents, which are found in Table 6.2. The Avrami exponent, n, is an indication of recrystallization kinetics during annealing and is strongly influenced by the microstructure of the material. The classic JMAK relationship assumes that the rates of nucleation and growth remain constant during recrystallization due in part to a random distribution of nuclei and therefore can be represented by a single Avrami exponent.

When the mechanisms controlling recrystallization are influenced by a non-random distribution of nuclei or differences in stored energy throughout the material the nucleation and growth rates change over time and more than one Avrami exponent is needed to describe the recrystallization process. The results showed that the n_1 value is much higher than the value of n_2, indicating that recrystallization occurred faster during the first stage where the strain energy is higher and slower during the second stage where the stored energy is lower. An example of the microstructural evolution process during annealing of Mg-4Al at 275°C is shown in Figure 6.7. As shown in Figure 6.7d, after annealing at 275C for 30 seconds small, recrystallized grains formed in the vicinity of twins and along grain boundaries. As time increased to 60 seconds nucleation and growth of new grains continued in those regions (Figure 6.8b). After 4 hours, full recrystallization of twins had occurred and all of the twinned regions were depleted leaving behind only large, deformed grains (Figure 6.8c). Even after annealing for 56 hours some grains had not recrystallized as indicated by the high GOS value. (Figure 6.8d).

6.3.2 Static Recrystallization in Unalloyed Mg

In this section, recrystallization of the coarse-grained (350μm) and the fine-grained (45μm) unalloyed Mg material will be described. The EBSD and GOS maps of the as-compressed state for the coarse-grained unalloyed Mg sample are shown in Figures 6.9a and 9b, respectively. SEM and EBSD analysis revealed the formation of twins and deformed grains throughout the material post compression. As with Mg-4Al, after short annealing times small, recrystallized grains were found at twins and along grain boundaries. This can be seen in the high magnification images which in Figures

6.10a and 6.10b. To study the microstructural evolution during recrystallization the samples were annealed at 250°C for various times (Figures 6.11a-f). After only 1 second of annealing, small, recrystallized grains were observed within twins and along grain boundaries (indicated by white circles in Figures 6.11a-b). Recrystallization continued at these regions of high strain energy. After 86,400 seconds (2 weeks) some deformed, un-recrystallized grains remained in the material revealing that the strain within these grains was insufficient to cause further recrystallization in these regions (Figures 6.11e-f). Similar to the Mg-4Al, the recrystallization behavior showed two stages with two distinctly different Avrami slopes, where the n_1 value was significantly higher than the n_2 value, indicating that at shorter annealing times recrystallization occurs at a fast rate at twins and grain boundaries while at longer annealing times recrystallization occurred at a slower rate in regions with a lower strain energy.

Analysis of the as-compressed state of the fine-grained unalloyed Mg revealed the formation of twins and deformed grains. The EBSD and GOS map of the as-compressed state are shown in Figures 6.12a and 6.12b, respectively. Due to the fine grain size and rapid recrystallization it was more difficult to capture recrystallization in twins in the fine-grained unalloyed Mg compared to the coarse-grained unalloyed Mg and Mg-4Al. The experimental results also showed a change in Avrami slope at the beginning of Stage 2, which can be seen in Figures 6.13 and 6.14. Similar to the Mg-4Al alloy and the coarse-grained unalloyed Mg, the preferential nucleation of recrystallized grains at twins and grain boundaries creates a two-stage recrystallization process described by two different Avrami exponents.

To characterize the effect of temperature on static recrystallization behavior in unalloyed Mg, three annealing temperatures were studied: 150°C, 200°C, and 250°C. The results for each temperature are shown in Figure 6.13. The JMAK relationship described in Equation 2 was used to model the experimental data and is represented by the solid lines in Figure 6.13.

The early stages of recrystallization were difficult to capture at 250°C due to the rapid nature of the process at that temperature. The results for ln(ln(1/1-X)) versus ln (annealing time) shown in Figure 6.14 was used to determine the Avrami exponents, n_1 and n_2, at each annealing temperature. Similar to the Mg-4Al alloy, two different Avrami exponents were apparent indicating that there were two stages of recrystallization during annealing. The $t_{0.5}$ was interpolated from the experimental data. The JMAK constants are reported in Table 6.3. From the experimental results, it was observed that temperature had a significant effect on recrystallization kinetics in unalloyed Mg. As temperature increased from 150°C to 250°C, the recrystallization kinetics increased and $t_{0.5}$ decreased from 1000 seconds at 150°C to 1 second at 250°C.

Table 6.3: Summary of JMAK constants for Unalloyed Mg at each annealing temperature

Annealing Temperature (°C)	**n_1**	**n_2**	**$t_{0.5}$ (seconds)**
150	0.52	0.12	1000
200	0.59	0.02	300
250	0.36	0.05	0.95

The activation energy for recrystallization was determined using Equation 3 by plotting ln($t_{0.5}$) versus 1000/RT and calculating the slope of the line (Figure 6.15). It was

determined that the recrystallization activation energy, $Q_{REX,}$ for unalloyed Mg was 123kJ/mol.

6.4. Discussion

The kinetics of the recrystallization process are generally modeled using a JMAK relationship and can be represented by a single Avrami exponent with a constant exponent. The Avrami exponent, n, is an indication of how quickly recrystallization progresses during annealing. The classic sigmoidal relationship during recrystallization indicates that recrystallization decelerates during the later stages without a change in the Avrami exponent. In the Mg materials investigated here two-stage recrystallization kinetics were observed, with an initial rapid recrystallization phase during the early stages of recrystallization followed by a rather abrupt change in the rate of deceleration of recrystallization as the process continues. It was determined that the Avrami exponent was not constant but exhibited a bi-linear behavior indicating that recrystallization occurs in two stages, which can be described by the two different Avrami exponents, n_1 and n_2. The slope of Stage 2 recrystallization, $n_{2,}$ was to 2-10 times lower than that for Stage 1 recrystallization. The second stage always began well after $t_{0.5}$ and more generally started after 70-80% of the volume was recrystallized, at which point the rate of recrystallization abruptly slowed down and then practically ceased all together, even at times one to two orders of magnitude beyond $t_{0.5}$.

The recrystallization rate during annealing can be affected by many factors including the spatial distribution of stored energy (heterogeneous vs homogeneous distribution) and the non-random distribution of nuclei. For all conditions observed in this study the Stage 1 Avrami exponent varied from 0.35 to 0.6. This is significantly

lower than the "standard" value of three for site saturated nucleation [11] and normally indicates the occurrence of heterogeneous nucleation of strain free grains. An exponent of three indicates that the growth rate of new, strain-free grains remains constant due to site-saturated nucleation and a random distribution of nucleation sites exist throughout the material.

In the current research, we attribute both the low Stage 1 Avrami exponent and the two-stage nature of recrystallization to heterogeneous nucleation of strain free grains at twins and grain boundaries. During Stage 1 nucleation of new, strain-free grains occurred at both twins and grain boundaries. An example of this is shown for the Mg-4Al annealed at 300°C for 10 seconds, where recrystallized grains were observed within twins and along grain boundaries (Figure 6.7e-f). As the annealing time increased, recrystallization continued at twins and grain boundaries until the end of the first stage. The preferential nucleation of recrystallized grains at twins and grain boundaries suggests that the stored energy is higher in these regions. The nucleation of recrystallized grains at twins and grain boundaries shows that nucleation sites are non-randomly distributed throughout the material. When deformed nuclei are clustered together, recrystallized grains nucleating and growing from these regions impinge on each other during growth due to their close proximity. This localized impingement phenomenon hinders the growth of the recrystallized grain boundaries leading to a non-constant growth rate during recrystallization and a low Avrami exponent.

It is generally understood that grain boundaries are preferred nucleation sites, however in Mg alloys, it has also been observed by others that twins play a significant role in recrystallization [6,13]. The relatively low value of the Avrami exponent has also

been observed for other studies of recrystallization in Mg alloys and also attributed to preferred nucleation at twins and grain boundaries [6,13]. Chao et al found that preferred nucleation at twins and grain boundaries during recrystallization in AZ31 led to Avrami exponents of 1.18-1.38 for various temperatures [6]. Su et al also observed an Avrami exponent of 0.7-1.8 during the first stage and 0.4-0.5 for the second stage due to twin recrystallization in AZ31 [13].

Numerous studies have been conducted on twin formation in magnesium and how twins affect microstructure and mechanical properties [12,15-17,19-20,29,33-34]. Twinning results in highly localized strains [29] which presumably lead to preferential nucleation of recrystallized grains. During twinning, the twinned region is reoriented causing twin boundaries to act as barriers to dislocation motion, which leads to work hardening and a stress-concentration along the boundaries [30,33-34]. There are three common twinning modes found in Mg alloys: extension twins, contraction twins, and double twins [30,33-34]. Extension twins form to accommodate the c-axis strain during deformation, which results in reorientation of the c-axis towards the compression direction causing the twin to form a hard orientation. This causes an increase in stress within the twin and along the twin boundary [19]. The formation of contraction twins also creates a stress concentration leading to an increase in strain energy. This is because the formation of contraction twins is energetically unfavorable and the resistance to their growth creates a stress concentration between the twin boundary and the matrix, increasing the strain energy in this region [12,19]. Double twins are created when contraction twins undergo basal slip or extension twinning. Since basal slip is the easiest deformation mode in hcp metals, in many situations the twinned regions

undergo more deformation than the neighboring matrix increasing the stored energy within double twins [15,19]. The formation and growth of twins is also dependent on the starting grain size of the deformed material. Dobron et al found that during compression of AZ31, coarse grains tend to twin preferentially when compared to fine grains [35].

Once recrystallization is exhausted at twins and grain boundaries, strain-free grains impinge and recrystallization slows and is finally terminated leading to the second stage of recrystallization. During Stage 2, the Avrami exponent was up to a factor of ten times lower than that of Stage 1. Analysis revealed that deformed grains remained in the material during this stage, indicating that the stored energy within the remaining grains was insufficient to cause recrystallization. In coarse-grained unalloyed Mg annealed at 250°C, large, deformed grains still remained in the material after up to two weeks of annealing. The recrystallization rate is influenced by the amount of strain (dislocation density) energy in the material. Therefore, when the strain energy in the remaining unrecrystallized regions is relatively low, recrystallization is reduced or does not occur, lowering the Avrami exponent. During Stage 2, recrystallization continues slowly at the lower strain grain interiors, which is represented by n_2. After long annealing times, deformed grains still remain in the material, indicating that the driving force for recrystallization is reduced and the strain energy within these grains is not sufficient to cause nucleation of strain free grains or further growth of existing recrystallized grains into these regions. Similar behavior has been observed by others [14]. Su et.al reported two stages of recrystallization during annealing of AZ31, where small, recrystallized grains were found near twins after 2 minutes at 200°C and after long annealing times in excess of 100 hours, large deformed grains still remained while all twins had been

completely recrystallized [14]. A schematic of the two-stage recrystallization process is outlined in Figure 6.16.

Twinning is normally more pronounced as grain size increases [35] and thus an interesting observation was that the recrystallization kinetics were substantially faster in unalloyed Mg with fine grain size (45μm) compared to the coarse grain size condition (350μm) which is shown in Figure 6.17. The fine grain size unalloyed Mg exhibited a $t_{0.5}$ of 1 second compared to 5000 seconds in the coarse-grain size material. This is consistent with literature for other alloys [11,35-36] but given the importance of twinning on recrystallization of Mg it requires further explanation. Humphreys and Hatherly [11] reported that grain boundaries are common nucleation sites during recrystallization, therefore a larger initial grain size provides fewer nucleation sites, lowers the nucleation rate, and recrystallization is slower for a given temperature. Li et al. found that recrystallization was retarded in a Nb microalloyed steel as the grain size increased from 17 to 83μm [36]. From this we conclude that although twinning plays an important role in nucleation of recrystallization, grain boundaries continue to play the dominant role.

In addition to this study of heterogeneous nucleation and two stage recrystallization, the influence of temperature on static recrystallization was analyzed in Mg-4Al and unalloyed Mg. As expected for this thermally activated process, as temperature increased the recrystallization kinetics were accelerated. Kim et.al also have confirmed that recrystallization increased with increasing temperature in a cold-rolled Mg-3%Al alloy [37]. The activation energy for recrystallization, Q_{REX}, for Mg-4Al and fine-grained unalloyed Mg was 177 kJ/mol and 123 kJ/mol, respectively. This is

similar to findings of others. Beer et. al found the activation energy for recrystallization of AZ31 to be 200 kJ/mol while Yang et.al determined it was 125kJ/mol for the same alloy [10,38]. The Q_{REX} for unalloyed Mg was similar to the activation energy for self-diffusion in Mg of 135 kJ/mol and the Q_{REX} of 92 kJ/mol previously determined for as-cast unalloyed Mg [6,10]. This finding indicates that recrystallization is controlled by the self-diffusion of Mg.

The influence of alloying on recrystallization has received only limited attention in Mg alloys. In the current study, recrystallization was slightly faster in unalloyed Mg when compared to Mg-4Al where the $t_{0.5}$ increased from 5000 seconds in unalloyed Mg to 7200 seconds in Mg-4Al (Figure 6.18). This is consistent with the somewhat limited results from a previous study on Mg-Al alloys [37]. Although alloying elements can have a significant influence on recrystallization in some metal alloys system [38-42] this is not always the case and can be highly system dependent [11]. In other systems, solute effects on recrystallization have been primarily attributed to effects on grain boundary mobility [38 -42] which appears to not be the case for the Mg-Al system since the effect of Al on recrystallization in Mg is minimal.

6.5. Conclusions

The influence of microstructure and temperature on static recrystallization behavior of unalloyed Mg and Mg-4Al was examined in this study. The major conclusions are:

- In both unalloyed Mg and Mg-4Al, a decrease in annealing temperature slows down static recrystallization kinetics. In unalloyed Mg, $t_{0.5}$ decreases from 1000 seconds at 150°C to 1 second at 250°C.

- The activation energy for recrystallization of unalloyed Mg was determined to be 123 kJ/mol, which is consistent with the activation energy for bulk self-diffusion of Mg. The recrystallization activation energy in Mg-4Al was determined to be 177 kJ/mol.
- A two-stage recrystallization process was observed in which rapid initial recrystallization occurred followed by an abrupt retardation of recrystallization occurred at longer annealing times after 65-80% recrystallization.
- The two-stage process was characterized by JMAK exponents in the range of 0.35-0.6 for Stage 1 and a factor of two to ten lower for Stage 2.
- During Stage 1 recrystallization, heterogeneous nucleation of strain-free grains was observed at twins and grain boundaries. The low Stage 1 JMAK exponents and two stage recrystallization process are attributed to these heterogeneous nucleation processes.
- In unalloyed Mg, recrystallization was observed to be significantly enhanced in a fine grain size condition compared to a coarse-grain size condition. This suggests that, although nucleation of recrystallized grains at twins is important, grain boundary nucleation plays a dominant role.
- The addition of Al had a minimal effect on recrystallization at 250°C.

Figures

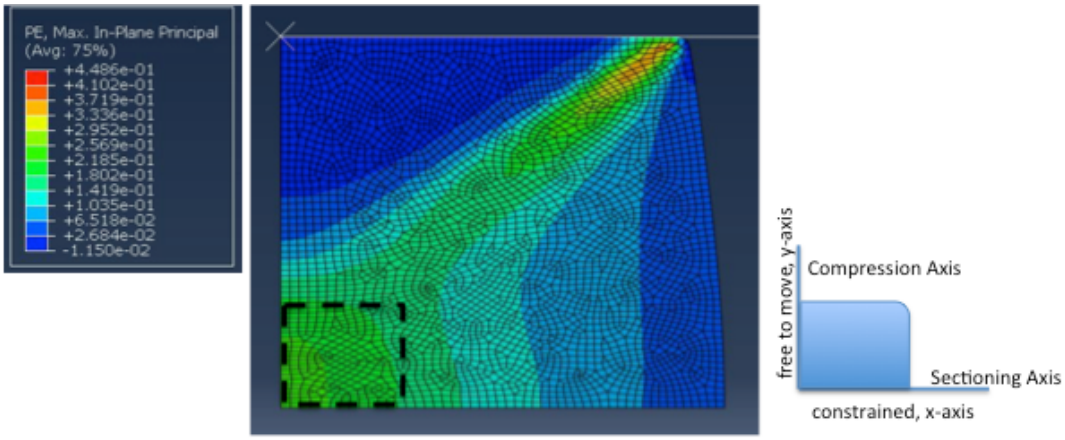

Figure 6.1: Axi-symmetric Abaqus simulation of compression test on unalloyed Mg. Note the dashed box indicating the recrystallization measurement region 1mmx1mm in area.

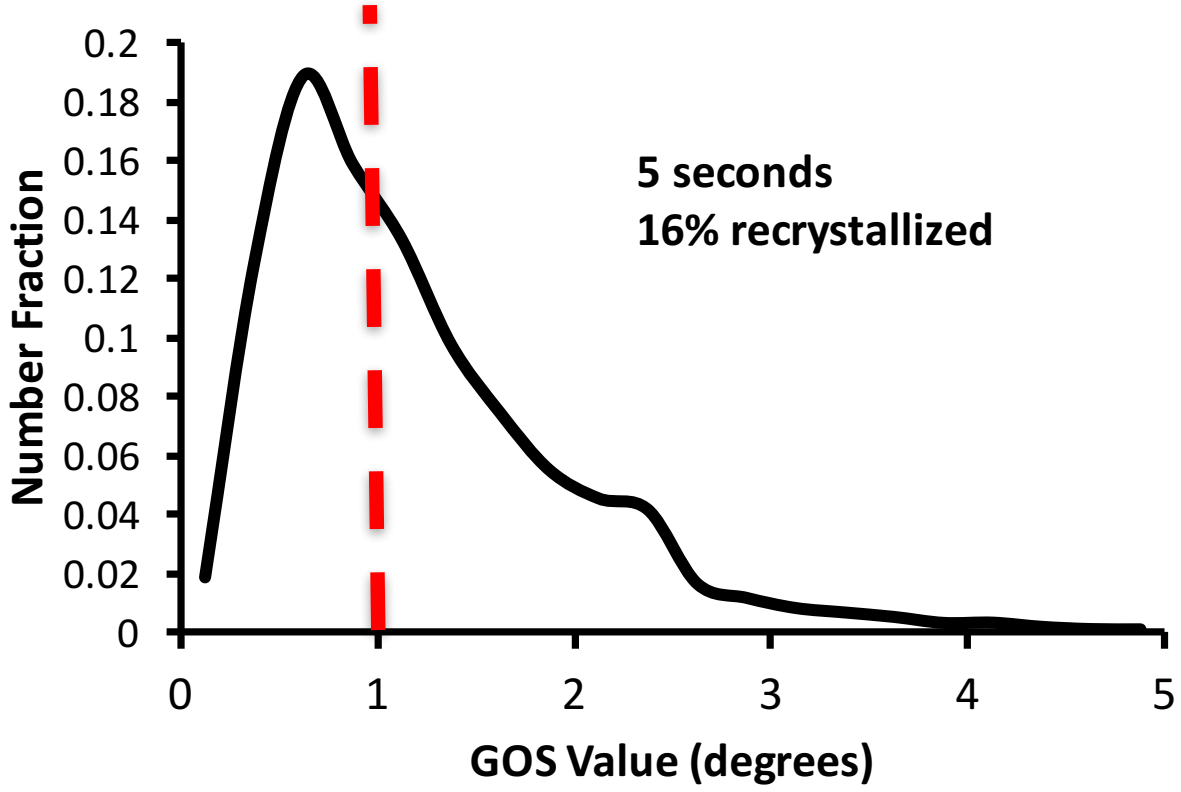

Figure 6.2: Grain Orientation Spread (GOS) distribution for a unalloyed Mg sample annealed at 200°C for 5 seconds

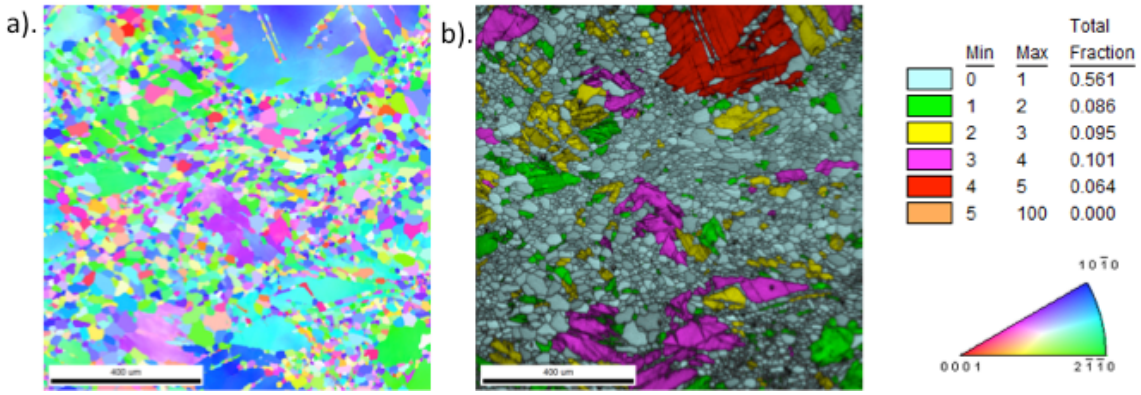

Figure 6.3: a). Inverse pole figure (IPF) map and b). Grain orientation spread (GOS) map of Mg-4%Al sample annealed at 250C for 2 hours.

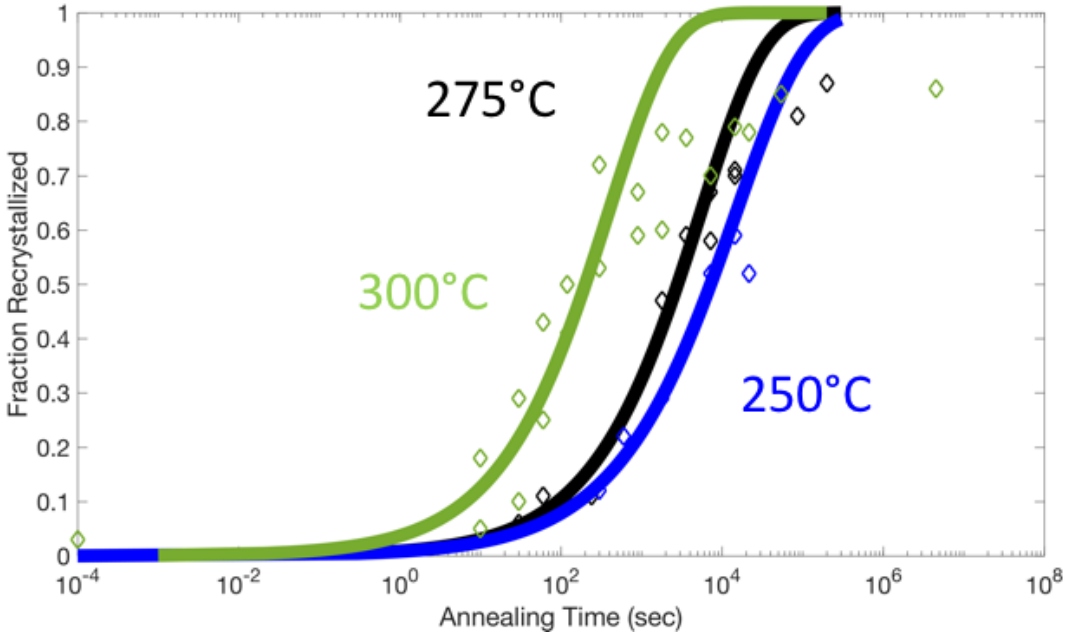

Figure 6.4: The fraction recrystallized versus annealing time for Mg-4%Al at 250°C (blue), 275°C (green), and 300°C (black). The solid lines represent the corresponding JMAK relationships for each condition.

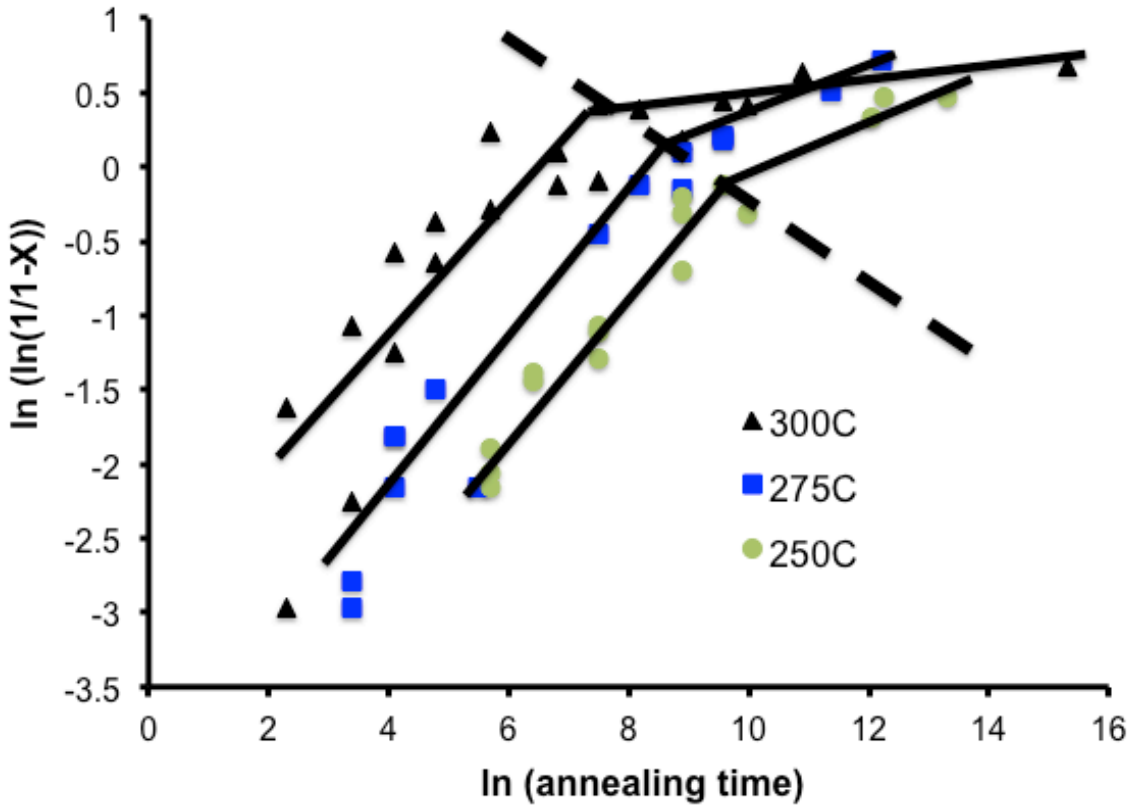

Figure 6.5: A plot of ln(ln(1/1-X)) versus ln(annealing time) used to determine the Avrami exponents at each annealing temperature in Mg-4%Al. X represents the fraction recrystallized. Note the bilinear nature of these results.

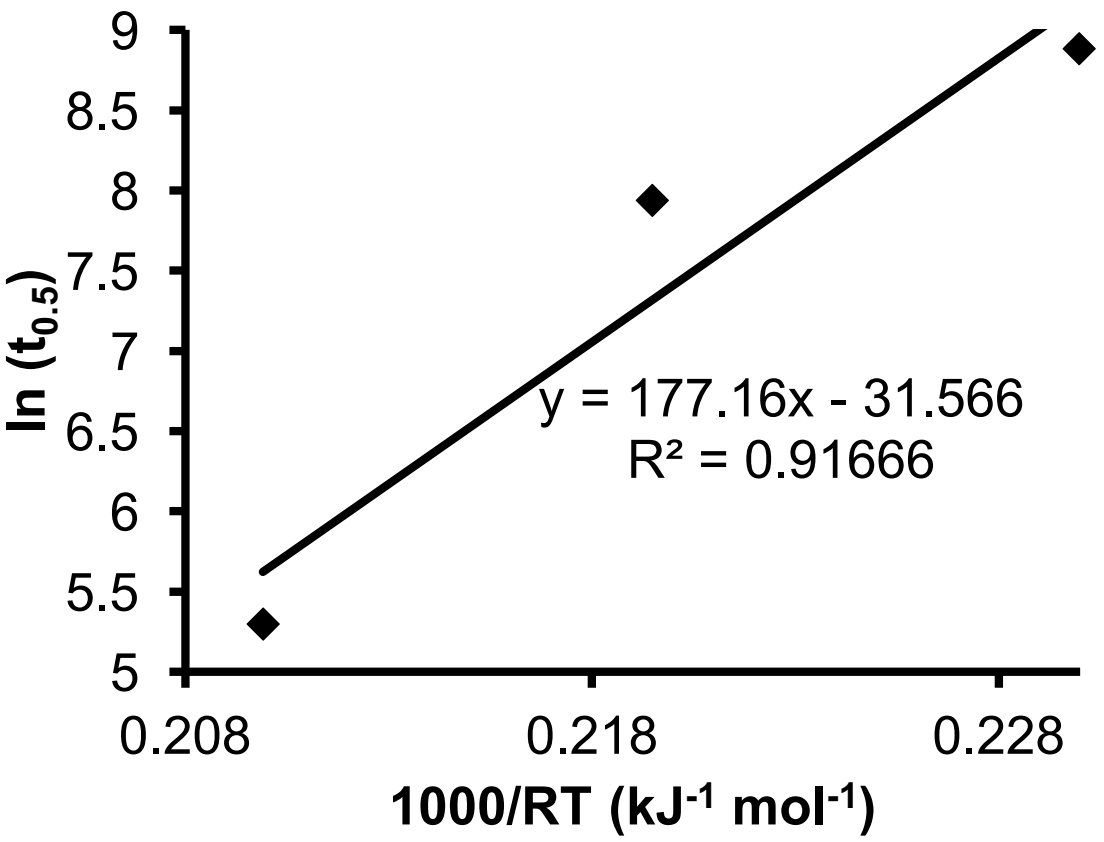

Figure 6.6: A plot of ln($t_{0.5}$) vs. 1000/RT used to determine the activation energy for recrystallization in Mg-4%Al.

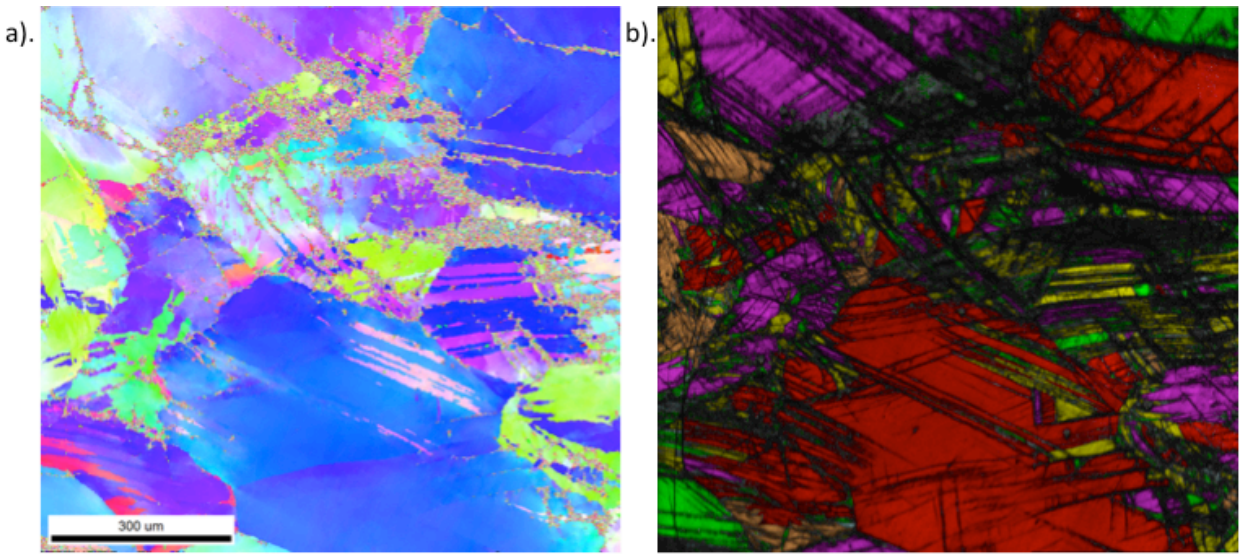

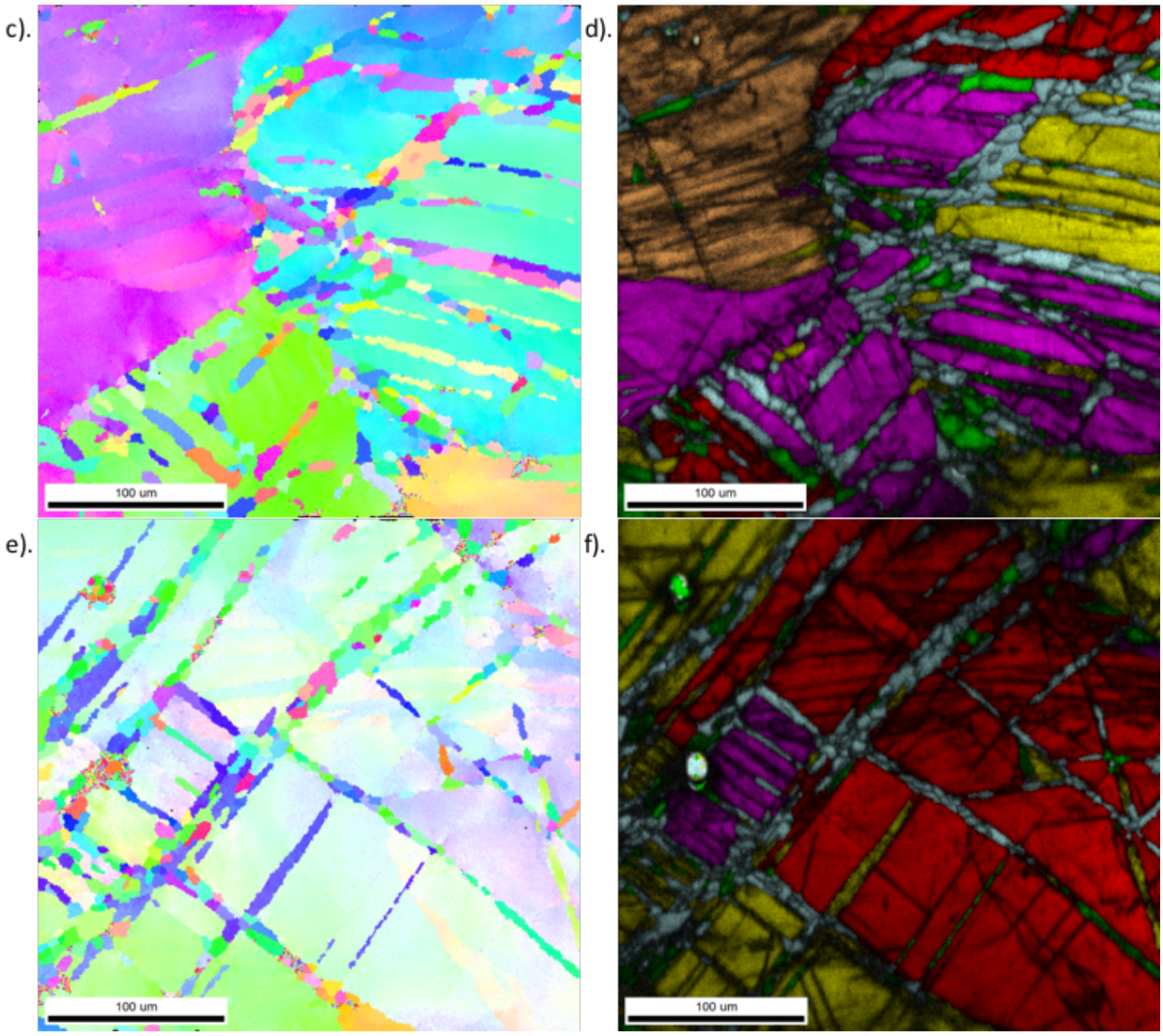

Figure 6.7: IPF and GOS maps for a) and b) as-compressed state, c) and d) 275°C at 30 seconds, e) and f) 300°C at 10 seconds and g) and h) 300°C at 10 seconds showing the early stages of recrystallization at twins and grain boundaries

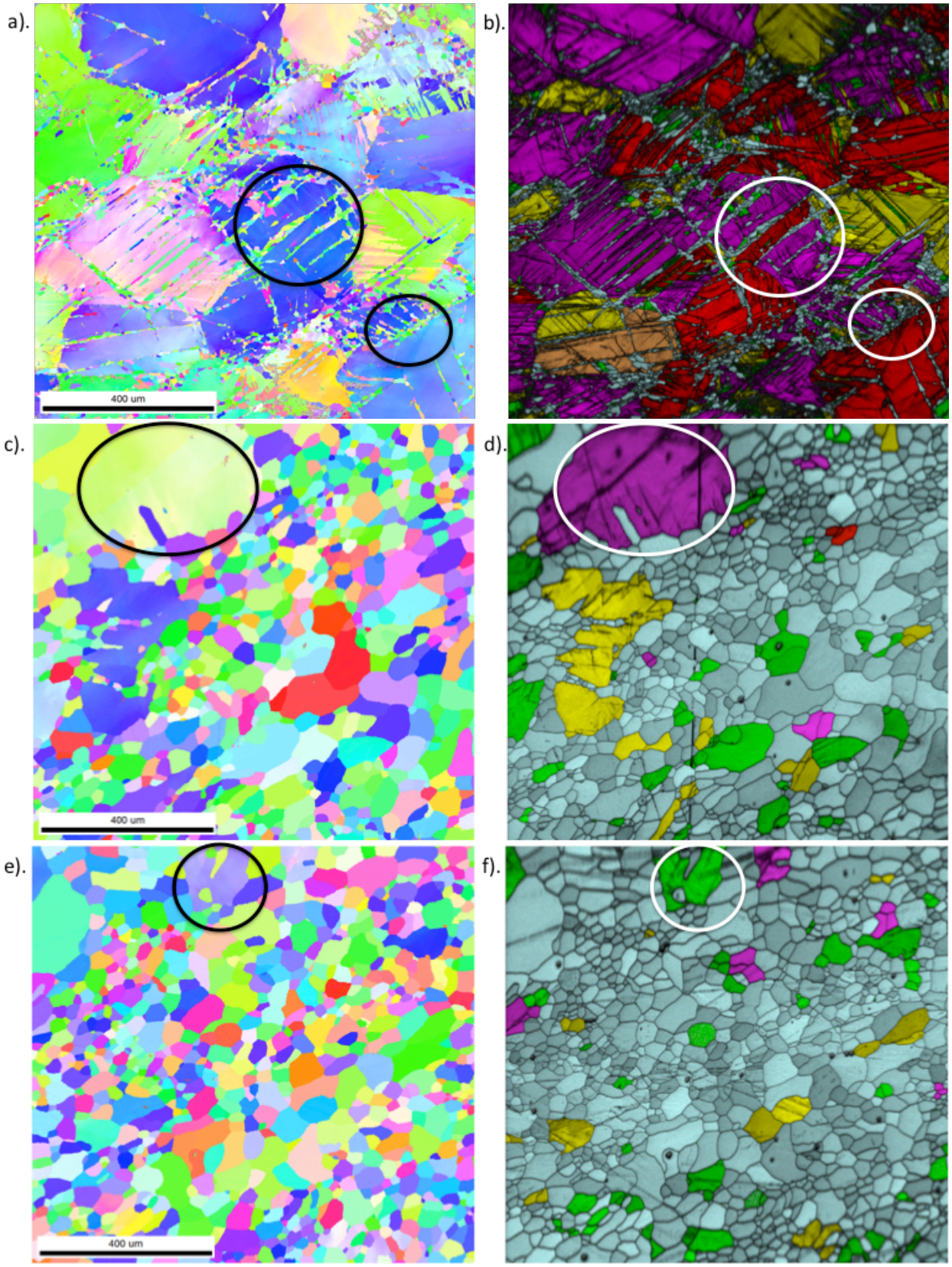
a).
400 um
b).
c).
400 um
d).
e).
400 um
f).

Figure 6.8: IPF and GOS maps detailing the recrystallization process during annealing for Mg-4%Al at 275C a) and b). 60 seconds, c) and d). 4 hours, and e) and f). 56 hours. Full recrystallization of twinned regions occurred after 4 hours.

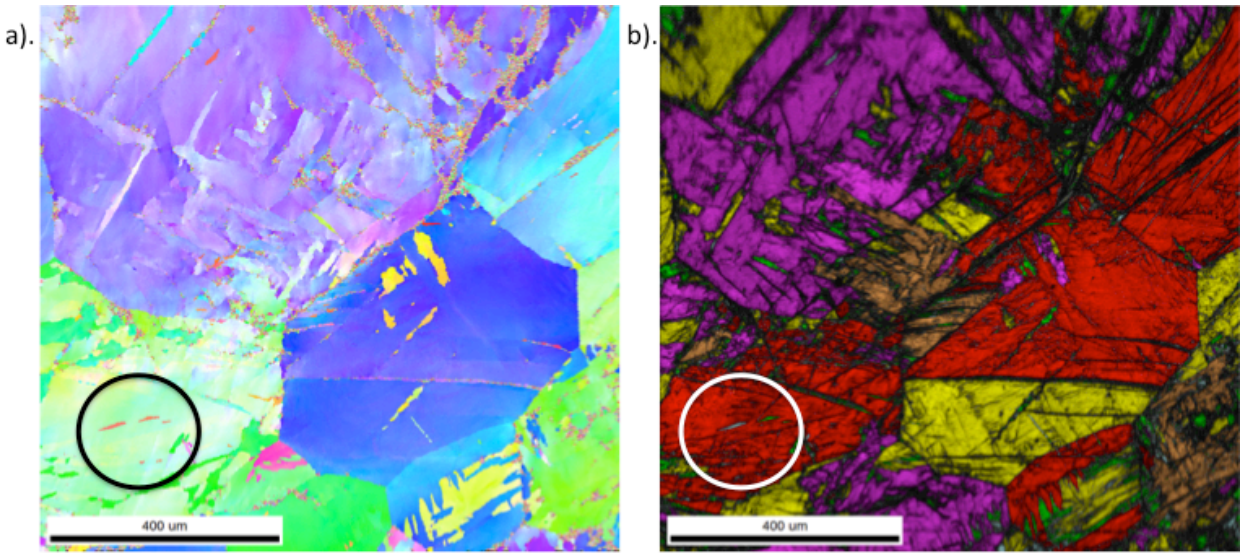

Figure 6.9: IPF and GOS maps for as-compressed state in coarse-grained unalloyed Mg.

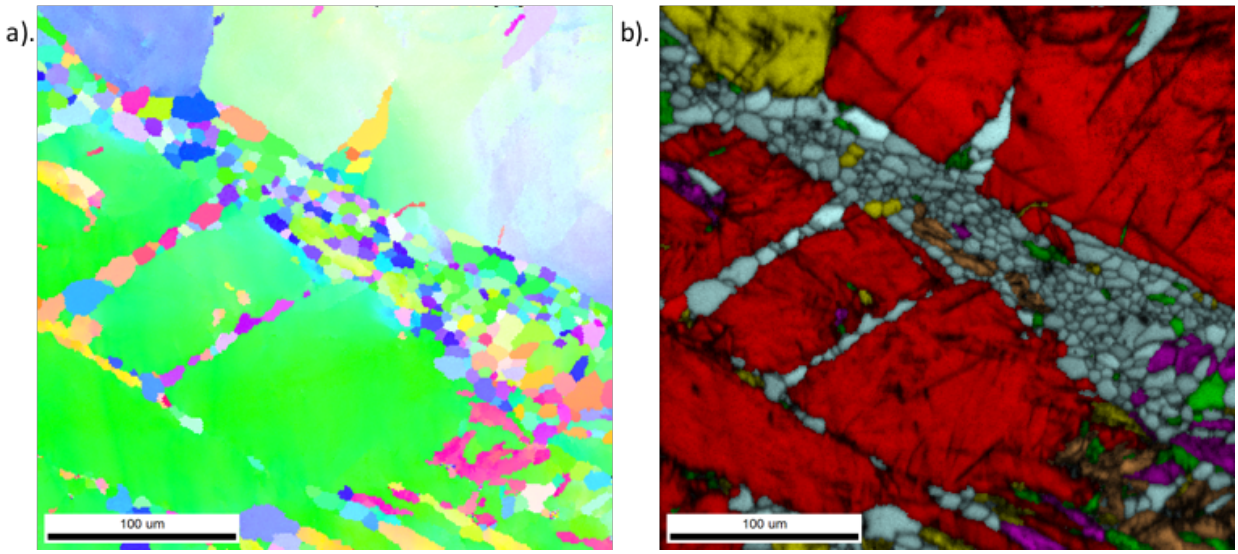

Figure 6.10: A high magnification image detailing recrystallization at twins and grain boundaries in coarse-grained unalloyed Mg.

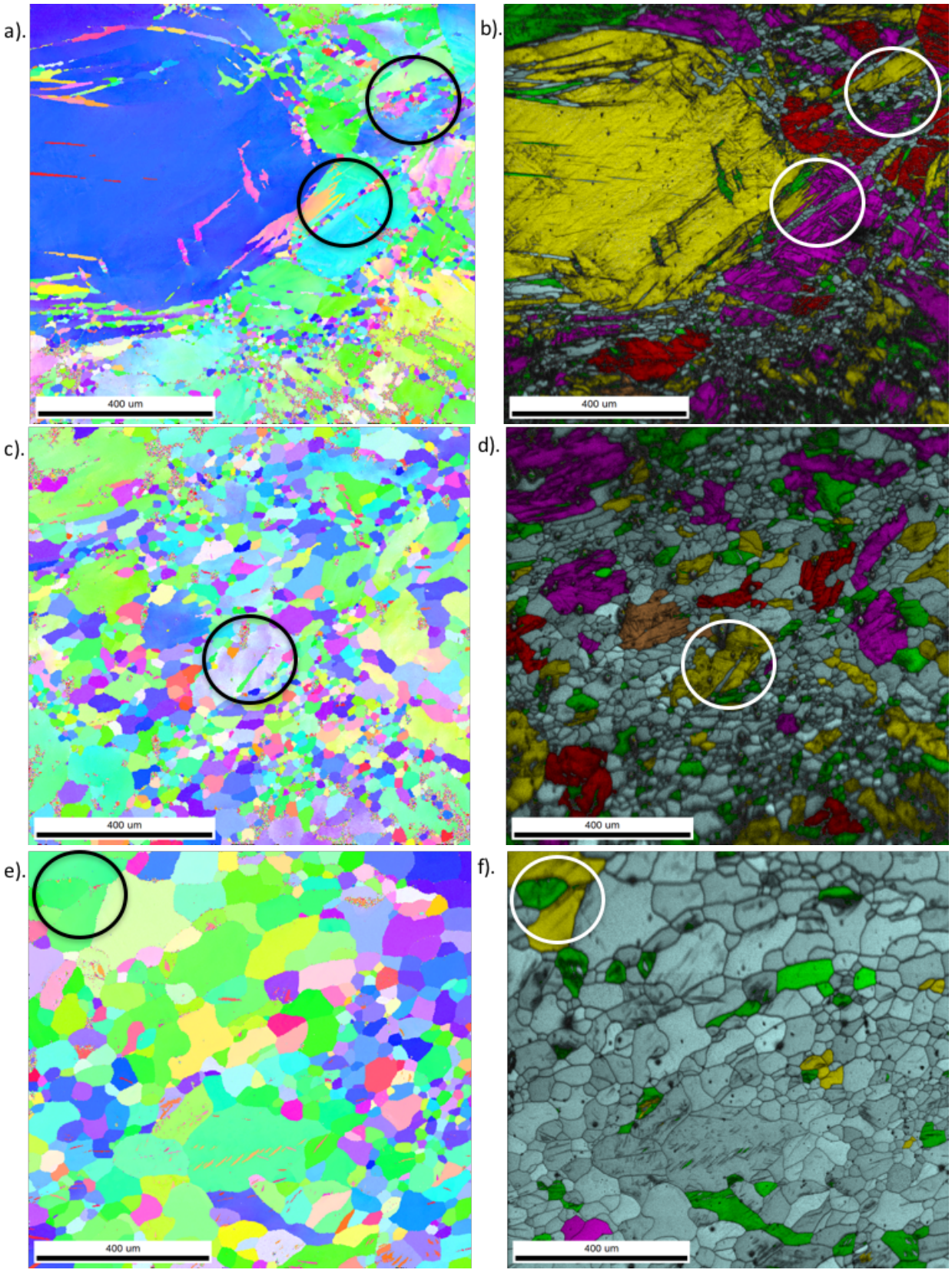
a).
400 um
b).
400 um
c).
400 um
d).
400 um
e).
400 um
f).
400 um

Figure 6.11: IPF and GOS maps detailing the recrystallization process during annealing for unalloyed Mg at 250C, a) and b) 1 second, c) and d) 1800 seconds, e) and f) 86,400 seconds

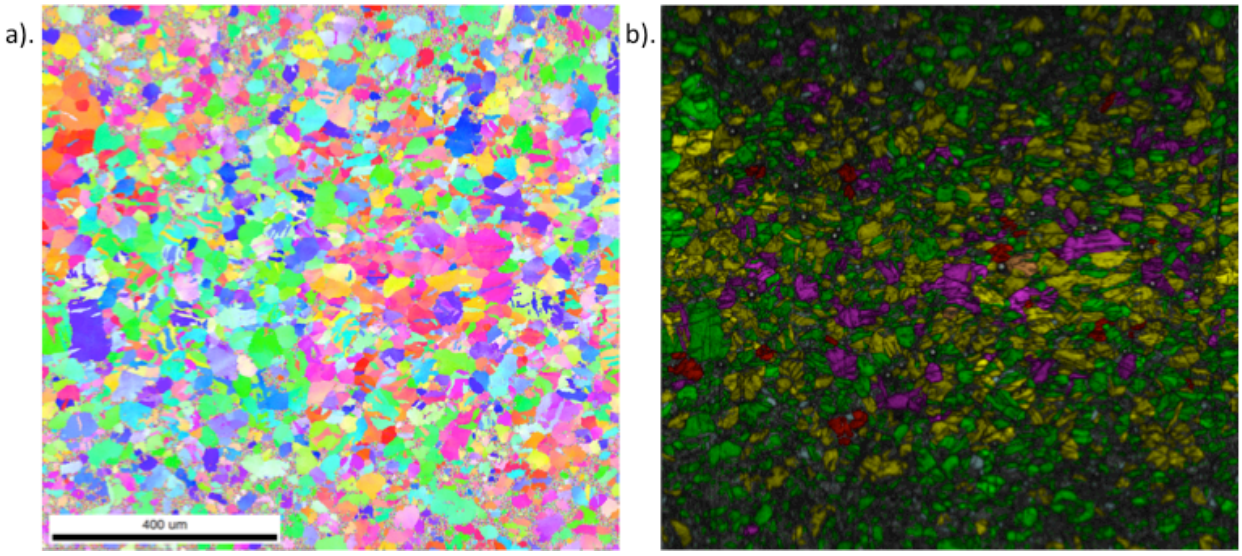

Figure 6.12: The a). IPF and b). GOS maps showing the as-compressed state of the fine grained unalloyed Mg sample.

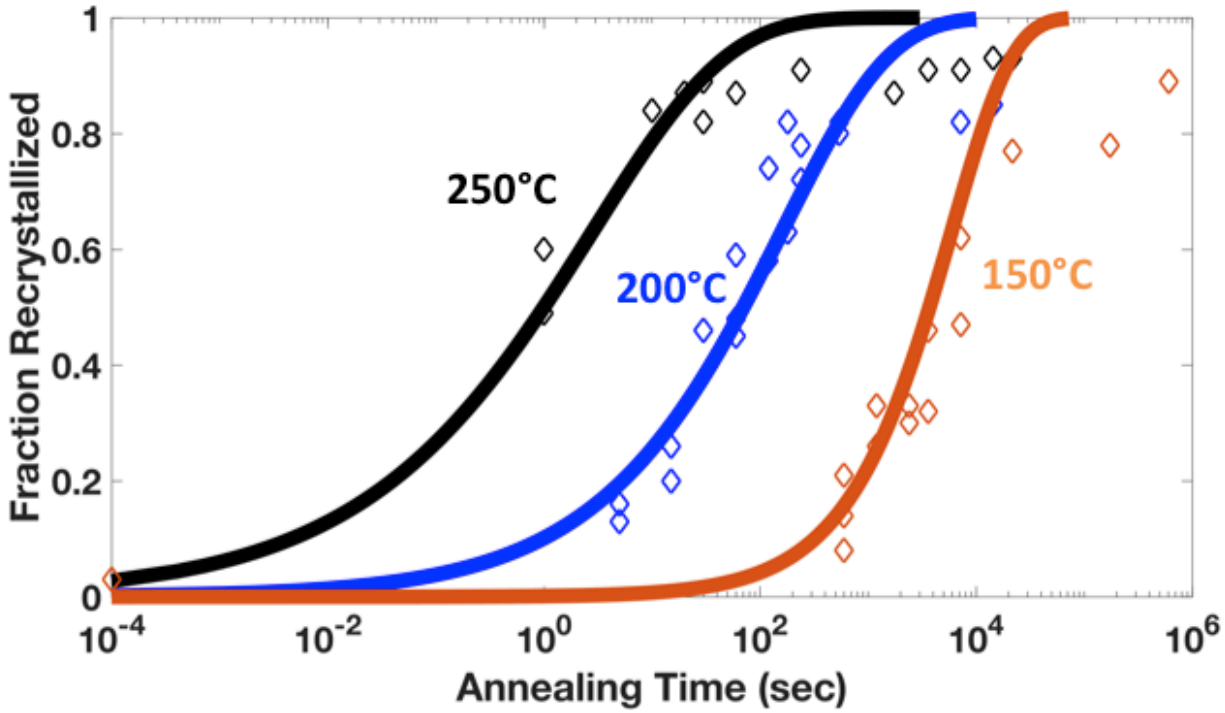

Figure 6.13: Fraction recrystallized versus annealing time for 150°C, 200°C, and 250°C for Unalloyed Mg. The solid lines represent the corresponding JMAK relationships for each condition.

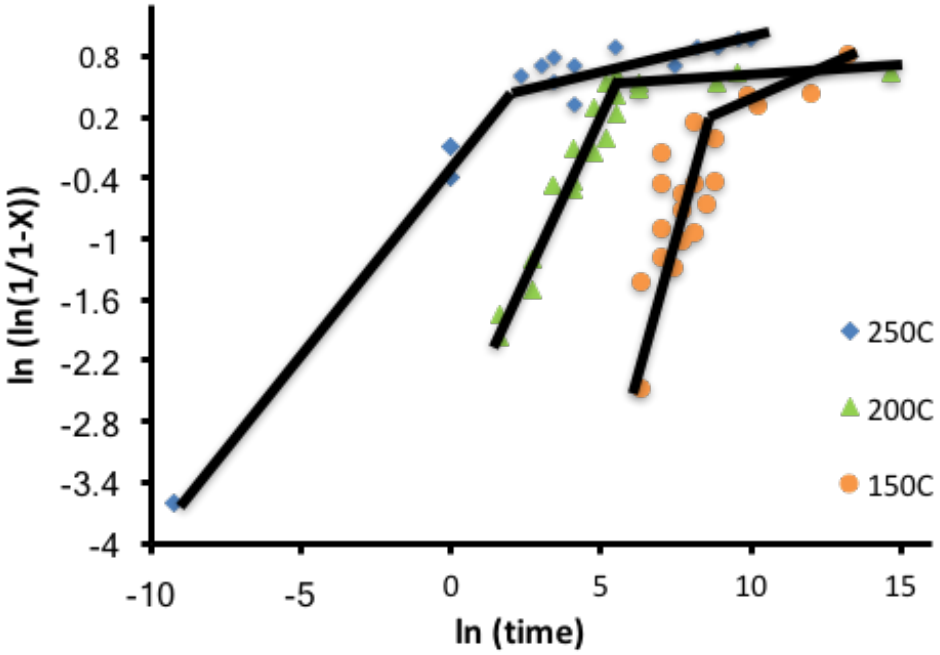

Figure 6.14: A plot of ln(ln(1/1-X)) versus ln(annealing time) results used to determine the Avrami exponents at each annealing temperature in fine-grained unalloyed Mg.

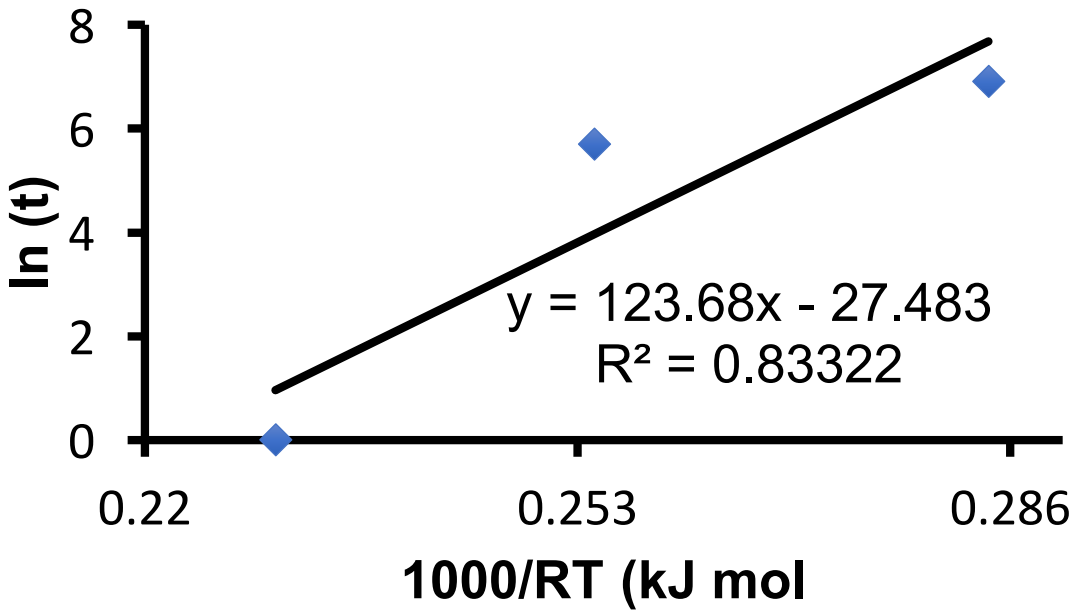

Figure 6.15: A plot of $\ln(t_{0.5})$ vs. 1000/RT results used to determine the activation energy for recrystallization in unalloyed Mg.

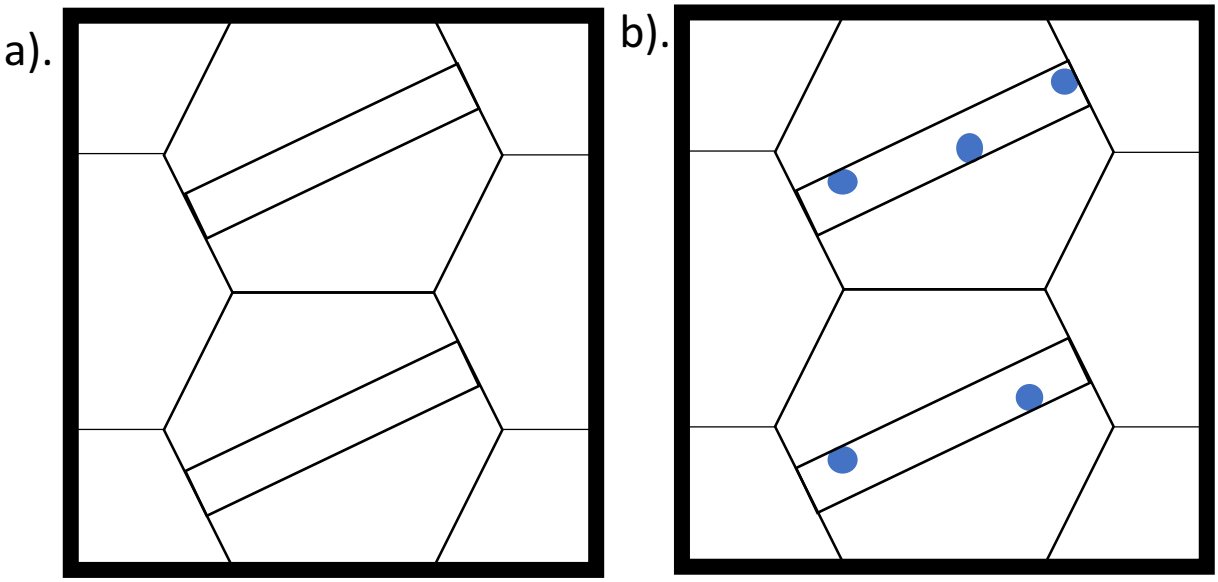

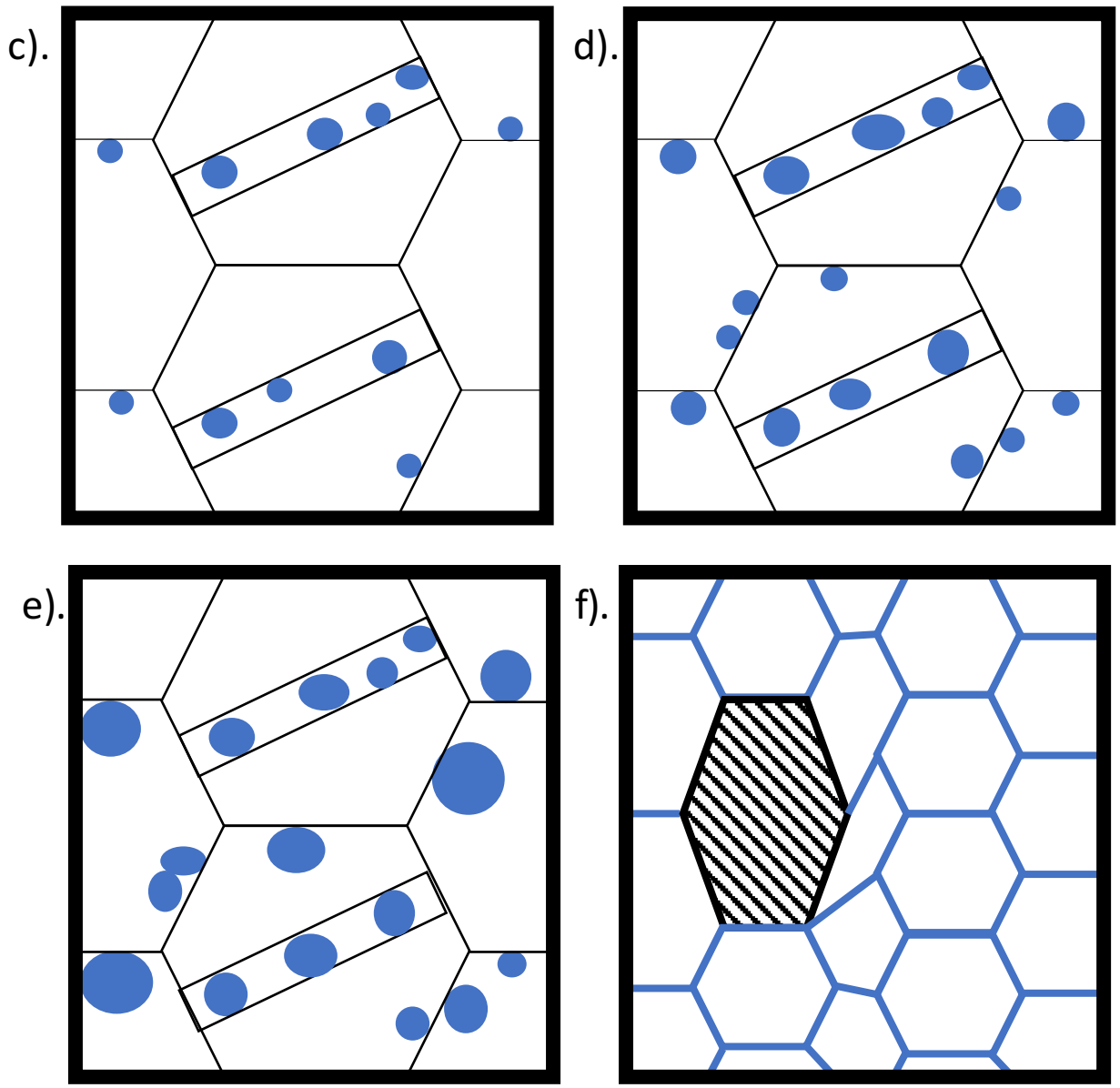

Figure 6.16: Schematic of the microstructural evolution during annealing: a). as-deformed state showing deformation twins and deformed grains, b). beginning of Stage 1 where new, strain-free grains (blue circles) grow from deformation twins, c-d). nucleation and growth of recrystallized grains from both deformation twins and grain boundaries, e). growth of recrystallized grains from twins and grain boundaries, and f).Stage 2 where the complete growth of recrystallized grains occurs (grains outlined in blue) while un-recrystallized grains remain in the material (filled with black dashed lines). In these regions the strain energy is not sufficient to cause further recrystallization.

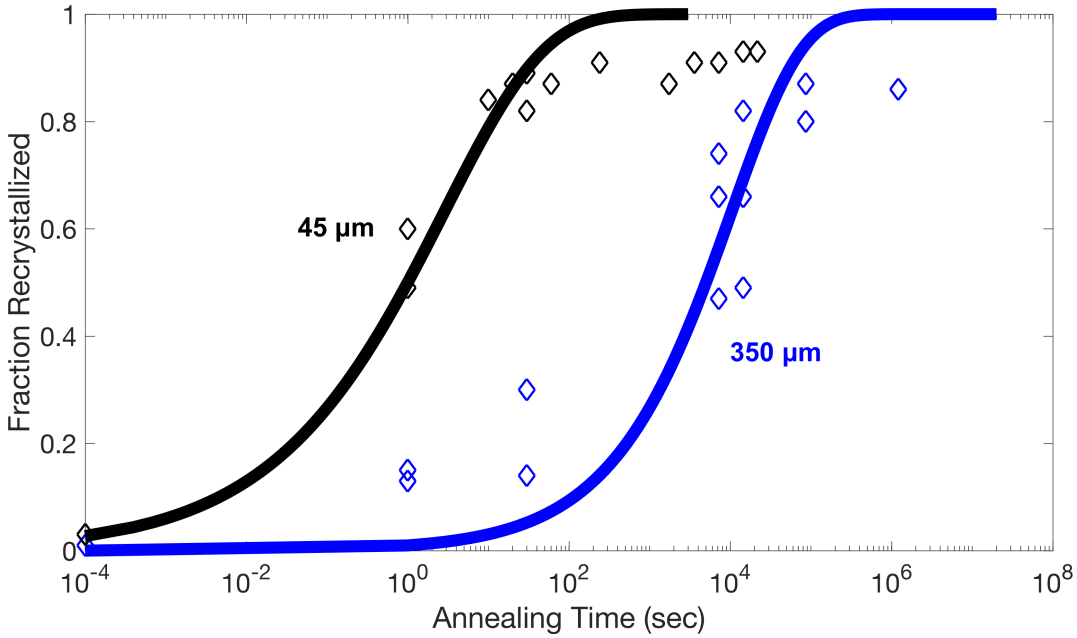

Figure 6.17: A comparison of the recrystallization kinetics for both the fine and coarse-grained unalloyed Mg annealed at 250°C.

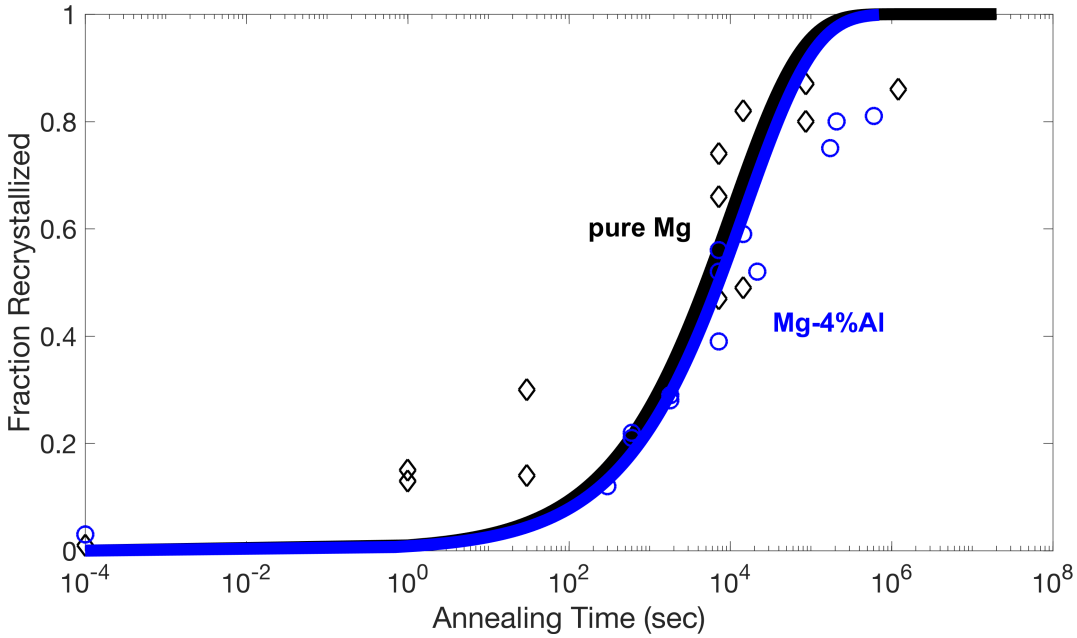

Figure 6.18: The fraction recrystallized versus annealing time for unalloyed Mg (black diamond) and coarse-grained Mg-4%Al (blue circle) at 250°C.

References

1. S.R. Agnew, J.F. Nie. Preface to the viewpoint set on: the current state of magnesium alloy science and technology. Scripta Materialia 63 (2010) 671-673
2. B.C. Suh, M.S. Shim, K.S. Shin, N.J. Kim. Current issues in magnesium sheet alloys: where do we go from here? Scripta Materialia 84-85 (2014) 1-6
3. F.A Mirza, D.L. Chen. Fatigue of rare earth containing Mg alloys: a review, Fat. Fract. Eng. Mater. Struct. 37 (2014) 831-853
4. W.J. Joost. Reducing the vehicle weight and improving US energy efficiency using ICME. JOM 64 (2012) 1032-1038
5. S. Sandlobes, Z. Pei, M. Friak, L.F. Zhu, F. Wang, S. Zaefferer, D. Raabe, J. Neugbauer. Ductility improvement of Mg alloys by solid solution: Abinitio modeling, synthesis and mechanical properties. Acta Materilia 70 (2014) 92-104
6. H.Y. Chao, H.F. Sun, W.Z. Chen, E.D. Wang. Static recrystallization kinetics of a heavily cold drawn AZ31 magnesium alloy under annealing treatment. Materials Characterization 62 (2011) 312-320
7. D.Griffiths. Explaining texture weakening and improved formability in magnesium rare earth alloys, Mat. Sci. Tech. 31 (2015) 10-24
8. Z.R. Zeng, Y.M. Zhu, S.W. Xu, M.Z. Bian, C.H.J. Davies, N. Birbilis, J.F. Nie. Texture Evolution during static recrystallization of cold-rolled magnesium alloys. Acta Materialia 105 (2016) 479-494
9. J. Hirsch, T. Al-Samman Superior light metals by texture engineering: optimized aluminum and magnesium alloys for automotive applications. Acta Materialia 61 (2013) 818-843
10. A.G. Beer, M.R. Barnett. The post deformation recrystallization behavior of magnesium alloy Mg-3Al-1Zn. Scripta Materialia 61 (2009) 1097-1100
11. F.J. Humphreys , M. Hatherlys. Recrystallization and Related Annealing Phenomena. Pergman (2004).
12. C. Drouven, I. Basu, T. Al-Samman, S. Korte-Kerzel. Twinning effects in deformed and annealed magnesium-neodymium alloys. Mat. Sci. Eng. A 647 (2015) 91-104
13. C.W. Su, L. Lu, M.O. Lai. Recrystallization and grain growth of deformed magnesium alloy. Philisophical Magazine 88 (2008) 181-200
14. J. Su, M. Sanjari, A.S.H. Kabir, J.J. Jonas, S. Yue. Static recrystallization behavior of magnesium AZ31 alloy subjected to high speed rolling. Mat. Sci. Eng. A 662 (2016) 412-425
15. D. Guan, W.M. Rainforth, L. Ma, B. Wynne, J. Gao. Twin recrystallization mechanisms and exceptional contribution to texture evolution during annealing in magnesium alloy. Acta Materialia 126 (2017) 132-144
16. M.M. Myshlyaev,H,J. McQueen, A. Mwembela, E. Konopleva. Twinning, dynamic recovery and recrystallization in hot worked Mg-Al-Zn alloy. Mat. Sci. Eng. A 337 (2002) 121-133
17. X. Li, P. Yang, L.N. Wang, L. Meng, F. Cui. Orientational analysis of static recrystallization at compression twins in a magnesium alloy AZ31. Mat. Sci. Eng. A 517 (2009) 160-169

18. T. Al-Samman, K.D. Molodov, D.A. Molodov, G. Gottstein, S. Suwas. Softening and dynamic recrystallization in magnesium single crystals during c-axis compression. Acta Materialia 60 2012 537-545
19. I. Basu, T. Al-Samman. Twin recrystallization mechanisms in magnesium-rare earth alloys. Acta Materialia 96 (2015) 111-132
20. K.D. Molodov. T. Al-Samman, D.A. Molodov, G. Gottstein. Mechanisms of exceptional ductility of magnesium single crystal during deformation at room temperature: multiple twinning and dynamic recrystallization. Acta Materialia 76 (2014) 314-330
21. M.H. Yoo. Slip, twinning, and fracture in hexagonal close-packed metals. Met. Trans. A 12 (1981) 409-418
22. A. Levinson, R.K. Mishra, R.D. Doherty, S.R. Kalidindi. Influence of deformation twinning on static annealing of AZ31 Mg alloy. Acta Materialia 61 (2013) 5966-5978
23. I. Basu, T. Al-Samman, G. Gottstein. Shear band-related recrystallization and grain growth in two rolled magnesium-rare earth alloys. Mat. Sci. Eng. A 579 (2013) 50-56
24. N. Stanford, M.R. Barnett. The origin of “rare earth” texture development in extruded Mg-based alloys and its effect on tensile ductility. Mat. Sci. Eng. A 496 (2008) 399-408
25. L.W.F. Mackenzie, M. Pekguleryuz. The recrystallization and texture of magnesium-zinc-cerium alloys. Scripta Materialia 59 (2001) 665-668
26. M. Oyarz’abal, A Martinez-de-Guerenu, I. Gutierrez. Effect of stored energy and recovery on the overall recrystallization kinetics of a cold rolled low carbon steel. Mat. Sci. Eng. A 485 (2008) 200-209
27. J.A. Valle, M.T. Perez-Prado, O.A. Ruano. Texture evolution during large strain hot rolling of Mg AZ61 alloy. Mat. Sci. Eng. A 355 (2003) 68-78
28. A. Galiyev et.al. Correlation of plastic deformation and dynamic recrystallization in magnesium alloy ZK60. Acta Materialia 49 (2001) 1199-1207
29. E. Martin et.al. Effect of twinning on recrystallization textures on recrystallization textures in deformed magnesium alloy AZ31. Philos. Mag. 91 (2011) 3613-3626
30. Q. Ma, B. Li, W.R. Whittington, A.L. Oppedal, P.T. Wang, and M.F. Horstemeyer: Texture evolution during dynamic recrystallization in magnesium alloy at 450C, Acta Materialia 67 (2014) 102-115
31. S.I. Wright, N.M. Nowell, and D.P. Field A review of strain analysis using electron backscatter diffraction. Microsc. Microanal. 17 (2011) 316-329
32. K. Kunze, S.I. Wright, B.L. Adams, and D.J. Dingley: Advances in automatic EBSP single orientation measurements. Text. Microstruc. 20 (1993) 41-54
33. M. Knezevic, M.R. Daymond, and I.J. Beyerlein: Modeling discrete twin lamellae in a microstructural framework. Scripta Materialia 121 (2016) 84-88
34. M. Knezevic, A. Levinson, R. Harris, R.K. Mishra, R.D. Doherty, and S.R. Kalidindi Deformation twinning in AZ31: Influence on strain hardening and texture evolution. Acta Materialia 58 (2010) 6230-6242
35. P P. Dobren, F. Chmelik, S. Yi, K. Parfenenko, D. Letzig, and J. Bohlen Grain size effects on deformation twinning in an extruded magnesium alloy tested in compression. Scripta Materialia 65 (2011) 424-427

36. G. Li, T.M. Maccagno, D.Q. Bai, and J.J. Jonas, Effect of initial grain size on the static recrystallization kinetics of Nb Microalloyed Steels. ISIJ Inter. 36 (1996) K. Kim and T.K. Ha Effect of aluminum addition on the static recrystallization behavior of magnesium. Mat. Sci. Forum 724 (2012) 163-168
37. K. Kim and T.K. Ha, Effect of aluminum addition on the static recrystallization behavior of magnesium, Mater. Sci. Forum, 2012, vol. 724, pp. 163-168
38. X. Yang, Static recrystallization behavior of hot-deformed magnesium alloy AZ31 during isothermal annealing. Trans. Nonferrous Met. Soc. China 20 (2010) 1269-1274
39. A. Trump and J. Allison, " The influence of aluminum content and annealing temperature on static recrystallization in α-titanium alloys", in review, Met Trans (2016).
40. J.W. Cahn. The impurity-drag effect in grain boundary motion. Acta Metallurgica 10 (1962) 789-798
41. Z. Aretxabaleta, B. Pereda, and B. Lopez Analysis of the effect of Al on the static softening kinetics of C-Mn Steels Using a Physically Based Model. Met. Mat. Trans. A 45 (2014) 934-947
42. H.S. Zurob, G. Zhu, S.V. Subramanian, G.R. Purdy, C.R. Hutchinson, and Y. Brechet Analysis of the effect of Mn on the recrystallization kinetics of high Nb steel: an example of physically-based alloy design. ISIJ Int. 45 (2005) 713-722

CHAPTER 7
GRAIN GROWTH BEHAVIOR OF UNALLOYED MG AND MG-4AL

7.1. Introduction

Grain refinement achieved via recrystallization is a method for improving strength and ductility of Mg and Mg alloys and has been the topic of recent studies [1-3]. In Mg alloys, a smaller grain size results in a higher yield strength and follows the well-known Hall-Petch relationship [3]. Therefore, it is important to know the kinetics that drive the growth of these recrystallized grains after recrystallization is complete. In this work, the influence of temperature and alloying on grain growth kinetics in un alloyed Mg and a Mg-4Al alloy has been characterized.

Deformation during processing increases the strain energy in the material [3]. This strain energy is stored in the form of dislocations and increases as deformation proceeds. During subsequent annealing, this stored strain energy is reduced by the nucleation and growth of new, strain-free grains [3]. When recrystallization is complete, the structure is still unstable and continued growth of recrystallized grains can occur. The driving force for grain growth is the reduction of interfacial energy which is stored in the form of grain boundaries [3]. Since the driving force for grain growth is small, significant grain growth usually occurs only at very high temperatures [3]. Ma et al found that grain growth was limited at low temperatures, but increased significantly with temperature. The addition of solutes and second phase particles limits grain growth by slowing down grain boundary mobility during annealing [4]. Wang et al showed that the activation energy for grain

growth in AZ31 was 18 kJ/mol higher than that of as-cast unalloyed Mg due to alloying effects [5].

In the current investigation, the grain growth behavior of unalloyed Mg and a binary Mg-4wt%Al alloy was examined. This study focuses on the effect of solute concentration and temperature on the grain growth behavior after recrystallization is complete. A complete manuscript on the recrystallization behavior of these materials is published elsewhere [2].

7.2. Experimental Procedure

7.2.1 Materials

The two materials used in this study, unalloyed Mg and Mg-4%Al, were provided by Canmet Materials in the form of extruded bars. Each bar was extruded from an 85-mm cast billet at 300C (unalloyed Mg) and 413ºC (Mg-4%Al) at a speed of 254mm/min to a final diameter of 15mm. The Mg-4Al cast billet was solution treated at 413ºC for 15 hours prior to extrusion to homogenize the Al concentration. To determine the initial grain size and level of recrystallization in the as-extruded bar, samples were inserted into a Tescan Mira 3 scanning electron microscope equipped with an EDAX Hikari XP EBSD detector. Each EBSD scan was taken at a voltage of 30kV and a beam intensity between 18-20 with an average step size of 1.0±0.2μm. The starting grain size of the unalloyed Mg and Mg-4%Al was 45±15μm and 33±10μm, respectively. Using the OIM Analysis 7 software via the grain orientation spread technique [2] it was determined that the unalloyed Mg and Mg-4%Al bars were 98 and 95 percent recrystallized, respectively. Figure 7.1 shows the inverse pole figure maps of the as-extruded microstructure for both unalloyed Mg and Mg-4Al. Since the as-

extruded bars were fully recrystallized all of the grain growth studies were performed using the as-received materials for both alloys.

7.2.2 Experimental Methods

7.2.2.1 Annealing

Rectangular specimens, 5mmx5mmx6mm, were machined from the as-extruded bars using electrical discharge machining (EDM). The samples were then annealed at 350ºC, 435ºC and 515ºC for various times in a Thermolyne box furnace to characterize the grain growth kinetics. To determine the time required to reach the annealing temperature, tests were performed by drilling a thermocouple in the center of various rectangular specimens. It was found that the heat up time for the 5mmx5mmx6mm sample in the box furnace was 10 seconds for each material.

7.2.2.2 Microstructural Characterization

After annealing, the samples were water quenched and sectioned for further examination. Metallographic specimens were prepared using standard techniques, finishing with 0.05μm polycrystalline diamond solution. A picric acid solution (5 g picric acid crystals, 10mL water, 5mL acetic acid, and 90mL ethanol) was used to etch the specimens for 3-5 seconds, which revealed grains and other features under optical microscopy. From the optical micrographs, the grain size was determined using the line intercept method outlined by ASTM E112.

7.3. Results

7.3.1 Grain Growth Behavior of unalloyed Mg

In the present study, three different annealing temperatures: 350ºC, 435ºC, and 515ºC were chosen to study the influence of temperature on grain growth behavior in

unalloyed Mg. The experimental results for each temperature are shown in Figure 7.2a. The microstructural evolution during annealing at 435ºC and 515ºC is shown in Figures 7.3 and 7.4. It was found that at 435ºC and 515ºC the grain size increases with both annealing temperature and time. At 435ºC the grain size has more than doubled after 1 minute of annealing and increased by one order of magnitude after 240 minutes of annealing. At 515ºC the grain size more than quadruples after annealing for 60 minutes. At 350ºC the grain size did not change with time. The lack of grain growth at this temperature is presumably due to the low driving force for grain growth, which requires higher temperatures to activate.

7.3.2 Grain Growth Behavior of Mg-4Al

For Mg-4Al, two different annealing temperatures: 435ºC and 515ºC, were selected to study the effect of temperature on grain growth. The experimental results for each temperature are shown in Figure 7.2b. The grain size significantly increased at 515ºC, where it increased from 33μm to 275μm after 240 minutes of annealing. At 435ºC, grain growth was significantly slower and after 1,440 minutes the grain size only increases to 92μm.

7.3.3 Grain Growth Kinetics

The kinetics of grain growth can be expressed as a linear relationship between the growth rate and the inverse grain size [3,6]. This linear relationship can be expressed as a differential equation as follows:

$$\frac{dD}{dt} = \frac{k}{D}$$

Where D is the average grain size at a given annealing temperature and time and k is the grain growth constant. After integrating equation 1, it can be expressed as:

$$D - D_o = kt^{1/n}$$

where D_o is the initial grain size, t is the annealing time, and n is the grain growth exponent [3,6]. The grain growth exponent can be determined by linearizing equation 2 as follows:

$$\ln(D - D_o) = \frac{1}{n} ln(t) + \ln(k)$$

Therefore, the value of n can be determined by calculating the slope of the plot $\ln(D\text{-}D_o)$ vs. ln(t). The plots for both unalloyed Mg and Mg-4%Al are shown in Figure 7.5 and the grain growth exponents can be found in Table 7.1. The grain growth exponent varies between 2 and 8 for Mg and Mg alloys. It was found that n increases with increasing temperature and decreases with the addition of aluminum (Table 7.1).

Table 7.1: Grain growth exponents for unalloyed Mg and Mg-4Al.

Material		**435°C**	**515°C**
Unalloyed Mg	**n**	**4.3**	**6.6**
Mg-4Al	**n**	**1.6**	**2.9**

7.4. Discussion

The grain growth behavior of unalloyed Mg and Mg-4Al was investigated. The grain growth exponent is a measure of the resistance to grain boundary motion. The grain growth kinetic equation developed by Burke and Turnbull makes two key assumptions: 1) the driving pressure on a boundary arises only from the curvature of that boundary and 2) the boundary velocity is proportional to the driving pressure [7]. When these conditions are met the ideal value for the grain growth exponent is 2 and remains constant for a given alloy [3,7]. In this study, the grain growth exponent for both unalloyed Mg and Mg-4Al differs from 2 and depends on the annealing temperature (Table 7.1).

Similar to the results found here, previous studies have shown that the value for n ranges from 2 to 8 for different Mg alloys and Mg-based composites [4,5,8]. In the case of unalloyed Mg, the grain growth exponents (Table 7.11) are within the range of n-values found elsewhere and lower than the ideal value of 2. Miao et al determined that the grain growth exponent for the Mg alloy, AZ31 was 4 [8]. There are many factors that affect grain growth kinetics which are not included in the original assumptions made by Burke and Turnbull such as impurity drag and crystallographic texture [3]. The deviation from the ideal value could be related to the trace amounts of solute as listed in Table 7.2. Solutes may pin grain boundaries during grain growth and therefore, inhibit further growth of grains [3]. The strong basal texture found perpendicular to the extrusion may also play a role (Figure 7.6). Strongly textured materials contain low angle grain boundaries of low energy which reduces the driving force for grain growth [3].

Table 7.2: Chemical composition of unalloyed Mg

Element	Na	Al	P	K	Ca	Cr	Mn	Fe	Ni	Cu	Zn	Ag	Ba	Pb
Average (µg/g)	173	38.7	411	104	530	0.41	25.4	17.2	2.99	5.76	93.9	0.17	0.52	1.08

For Mg-4Al the grain growth exponent also deviates from the ideal value. This difference could be due to solute drag effects from the addition of aluminum. During solute drag, solute atoms slow down grain boundary migration. In diffusion studies by Zhong et al, it was found that the impurity diffusion coefficient of Al in Mg could be measured using the Arrhenius relationship $D_{Al\ in\ Mg} = 2.1 \times 10^{-4} e^{-146000/RT}$. Using this relationship, they determined that Al diffuses slower than the self-diffusion of Mg for temperatures ranging

from 450ºC to 630ºC [9]. Grain growth is a diffusion controlled process where atoms must diffuse across the grain boundary in order for that grain boundary to migrate. Therefore, when the diffusion of solute atoms across the grain boundary is slower than the diffusion of the bulk atoms, grain growth kinetics is slowed down.

For both unalloyed Mg and Mg-4Al grain growth occurring more rapidly at higher temperatures when compared to lower temperatures (Figure 7.2) and the grain growth exponent increases as temperature increases. In Mg-4Al the grain growth exponent almost doubles with an increase in temperature. The grain growth exponent also decreases with the addition of Al, where the grain growth exponent is reduced by more than double in this condition compared with the unalloyed Mg. As stated earlier the addition of solute atoms slows down grain boundary migration and therefore reduces grain growth kinetics. This is particularly interested because a previous study [2] showed that the addition of 4 w/o Al to Mg did not affect the recrystallization kinetics. The effect of solutes on grain growth has been observed in titanium alloys [10,11]. Both these studies found that the addition alloying elements decreased the grain growth exponent in titanium [10,11].

7.5. Conclusions

The influence of Al content and annealing temperature on grain growth behavior in unalloyed Mg and Mg-4Al was examined in this study. The major conclusions are:

- In both unalloyed Mg and Mg-4Al, an increase in annealing temperature speeds up grain growth kinetics. In unalloyed Mg, the grain size increases from 45 to 410 **μ**m after annealing for 360 minutes at 515ºC.

- The addition of Al slows down grain growth in Mg. At 435ºC the grain growth exponent is lowered from 4.3 to 1.6 when the Al content is increased.

Figures

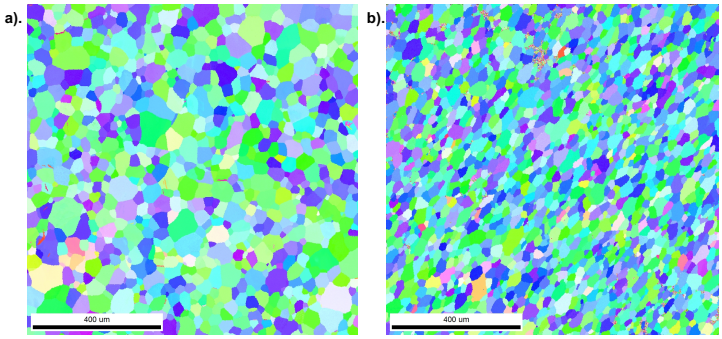

Figure 7.1: Inverse pole figure maps of the as-extruded microstructure for a). unalloyed Mg and b). Mg-4Al

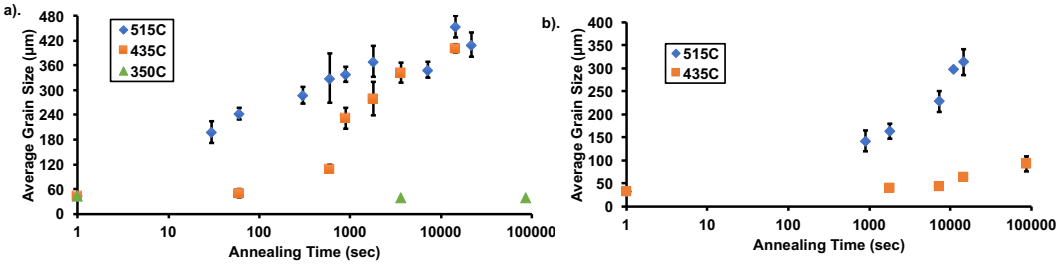

Figure 7.2: Average grain size as a function of annealing time for a). unalloyed Mg at 350ºC, 435ºC, and 515ºC and b). Mg-4%Al at 435ºC and 515ºC

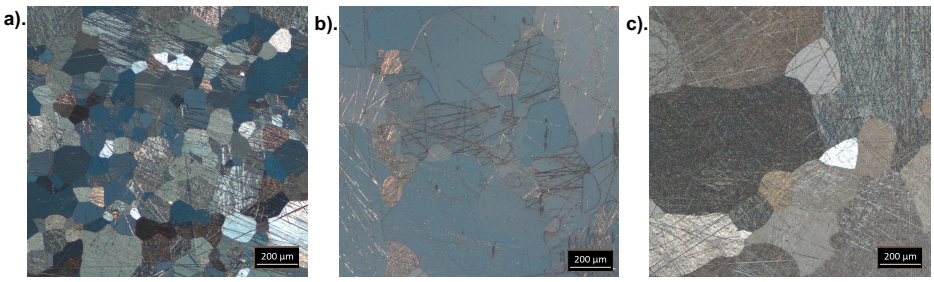

Figure 7.3: Optical micrographs showing the evolution of grain growth for unalloyed Mg at 435ºC at annealing times of a). 1 minute, b). 30 minutes, and c). 240 minutes. The grain size increases from left to right.

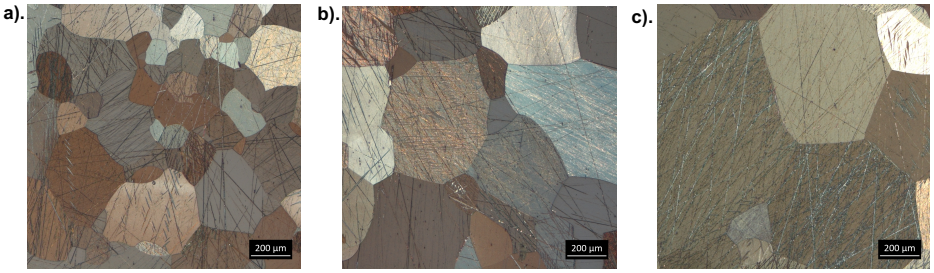

Figure 7.4: Optical micrographs showing the evolution of grain growth for unalloyed Mg at 515ºC at annealing times of a). 1 minute, b). 30 minutes, and c). 240 minutes. The grain size increases from left to right.

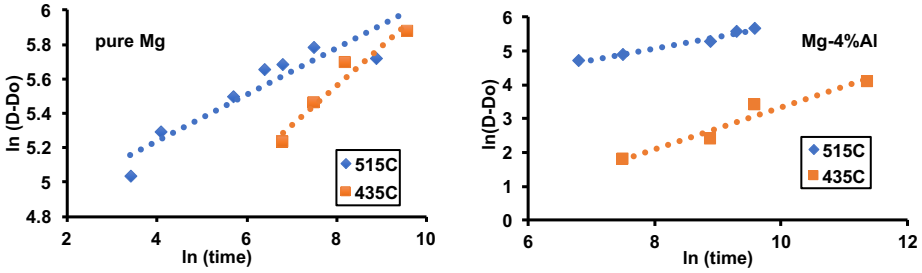

Figure 7.5: A plot of $\ln(D-D_o)$ vs. ln(time) used to determine the grain growth exponent for unalloyed Mg and Mg-4Al at 435ºC and 515ºC.

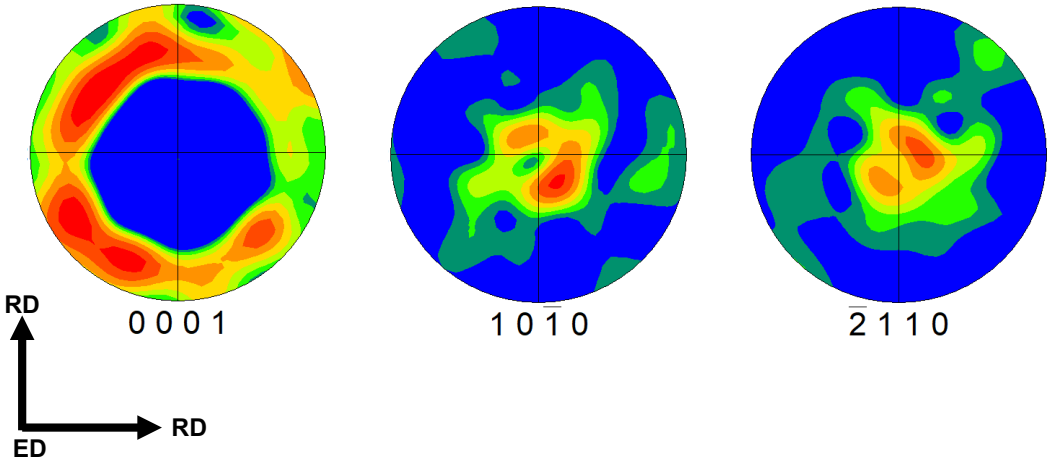

Figure 7.6: Pole figures showing the initial texture with the basal poles aligned normal to the extrusion direction.

References

1. B.L. Mordike et al., Mater. Sci. Eng. A 302, 2001, 37:45
2. A. Murphy et al. Met. Trans A, 2018
3. F.J. Humphreys and M. Hatherlys: Recrystallization and Related Annealing Phenomena, 2nd ed., Elsevier, Kidlington, Oxford, 2004
4. J. Ma et al., Mat. Design 47, 2013, 505:509
5. X. Wang et al., J. Alloys Compounds 527, 2012, 193:196
6. Z. Huda et al., J. Alloys Compounds 478, 2009, 128:132
7. J.E. Burke et al., Prog. Met. Phys. 3, 220, 1952
8. Q. Miao et al., J. Alloys Compounds 493, 2010, 87:90
9. W. Zhong et al., Scripta Mat 127, 2017, 92:96
10. F.J. Gil et al., J. Alloys Compounds 260, 1997, 147:152
11. A. Trump and J. Allison, manuscript in preparation, 2018.

CHAPTER 8
SUMMARY AND CONCLUSIONS

The goal of this thesis work was to understand the influence of grain size and alloying on the microstructural evolution that occurs during recrystallization and grain growth as well as determine how grain size and alloying effect the fatigue life and cyclic stress-strain behavior during low cycle fatigue. The final summary and conclusions are presented below.

8.1. LCF and CSS Behavior

The low cycle fatigue and cyclic stress-strain behavior was investigated under strain-controlled, LCF conditions using both ex-situ and in-situ techniques. In-situ HEXD was used to characterize the alternate occurrence of twinning and detwinning during cyclic loading. During loading the evolution of x-ray diffraction peaks associated with the basal {0002} planes were monitored throughout an entire fatigue cycle. In fine-grained unalloyed Mg (45μm) three different strain amplitudes: 0.4%, 0.52%, and 0.75% were employed and it was found at strains above 0.5%, twinning occurs during the compression portion of the cycle and at early stages of fatigue, most twins are removed (detwinned) under reversed loading during the tensile portion of the cycle. After 100-200 fatigue cycles, the complete detwinning process was no longer observed and a significant volume fraction of residual twins remained in the material and increased with cycling. The stress needed to initiate twins decreased with cycling indicating that as cycling continues twinning becomes easier as a result of increase plasticity near grain

boundaries since it is well-understood that twins nucleate from sources with high internal stresses such as grain boundaries, triple and quadruple joints. The twin volume fraction was calculated from diffracted intensities and it was determined that it increases with increasing cycles. The stress at the exhaustion of detwinning is closely related to the twin volume fraction where it also increased with cycling. At lower strain amplitudes (0.4%) it was found that loop shape asymmetries and diffracted basal peak intensities

associated with twinning were not observed indicating that when dislocation slip is dominant the resulting loop shape is symmetric.

The same in-situ HEXD techniques were used to investigate the influence of Al on twinning and detwinning during LCF of Mg-4Al (52μm). Three different strain amplitudes were investigated: 0.65%, 0.75%, and 0.85% and it was found that twinning and detwinning occurred alternately throughout a fatigue cycle. The stress needed to initiate twinning was increased with the addition of Al. This is because as Al concentration increases the CRSS for twin dislocation motion also increases and therefore, a higher stress is needed to initiate a twin in the alloy. Similarly, to unalloyed Mg, the compressive stress at which twins initiate decreases with cycling suggesting that the associated plastic flow is increasing on every cycle resulting in twins forming earlier during compression. In Mg-4Al the twin volume fraction remains stable and thus, the detwinning exhaustion stress also remains stable indicating that the detwinning stress is closely related to the amount of twins initiated during the previous compression cycle. The detwinning exhaustion stress was higher in the Mg-4Al alloy when compared to unalloyed Mg and the observed behavior was due to the increased twin volume fraction in Mg-4Al. Ex-situ results found that the stress amplitude was increased in the Mg-4Al and coarse-grained unalloyed Mg while the plastic strain amplitude was significantly lowered in Mg-4Al.

8.2. Recrystallization and Grain Growth

The static recrystallization kinetics of fine-grained unalloyed Mg (45μm) and coarse-grained Mg-4Al (360μm) were analyzed by quantifying the area of recrystallized grains throughout the entire recrystallization process. The grain orientation spread

method was used to determine the fraction of recrystallized grains. This method uses crystallographic orientation information provided by EBSD to determine the misorientation for each grain. The evolution of recrystallization was monitored at three different annealing temperatures for both unalloyed Mg and Mg-4Al and it was found that as the annealing temperature decreased, recrystallization was slower. In unalloyed Mg, $t_{0.5}$ decreased from 1000 seconds at 150C to 1 second at 250C. The observed behavior is due to the effects of temperature on diffusion. At lower temperatures, the diffusion rate is reduced resulting in a reduction of the mobility of high angle grain boundaries surrounding recrystallized grains. The relationship between $t_{0.5}$ and annealing temperature was used to calculate the activation energy for static recrystallization. In unalloyed Mg, the activation energy for unalloyed Mg (122kJ/mol) was consistent with that for bulk self-diffusion (135kJ/mol) indicating that the recrystallization rate is dependent on the diffusivity of Mg atoms. In the Mg-4Al alloy, the activation energy was increased to 177kJ/mol. In both materials, it was found that a two-stage recrystallization process exists where rapid initial recrystallization occurred followed by an abrupt retardation of recrystallization at longer annealing times after 65-80% recrystallization. The two-stage process was characterized by the JMAK relationship where the Avrami exponent was in the range of 0.35-0.6 for Stage 1 and a factor of two to ten lower for Stage 2. The Avrami exponents are much lower than the ideal value of 3 which is derived from the assumptions of site-saturated nucleation and a constant growth rate throughout recrystallization. EBSD analysis revealed that during Stage 1, heterogeneous nucleation of strain-free grains was observed at twins and grain boundaries suggesting that the stored energy was higher in those regions. The low

Stage 1 JMAK exponents and two stage recrystallization process are attributed to these heterogeneous nucleation processes.

To characterize the influence of grain size on static recrystallization in unalloyed Mg, a solution treatment was performed on the material to increase the grain size from 45μm to 350μm. The recrystallization kinetics of the coarse-grained material was investigated at 250C and it was observed to be significantly enhanced in the fine grain size condition compared to a coarse grain size condition. This suggests that, although nucleation of recrystallized grains at twins is important, grain boundary nucleation plays a dominant role during recrystallization. The recrystallization kinetics of the Mg-4Al and coarse-grained unalloyed Mg was also investigated at 250C and it was found that the addition of Al had a minimal effect on recrystallization in Mg.

The grain growth kinetics of the fine-grained unalloyed Mg and fine-grained Mg-4Al was characterized using optical microscopy where rapid growth occurred at early annealing times followed by slower growth at longer annealing times due a decreasing driving force. The evolution of grain growth was analyzed at three different annealing temperatures and it was found that grain growth was more rapid at higher annealing temperatures. In unalloyed Mg, the grain size increased from 45 to 410μm after annealing for 360 minutes at 515C. Similar to recrystallization, grain-growth is a diffusion-based process, where diffusivity of atoms is increased at higher temperatures. The addition of Al was found to significantly retard grain growth kinetics which is generally attributed to solute drag where solute atoms exert a force on grain boundaries as they migrate decreasing their mobility during grain growth. In both materials, the grain growth exponent was different from the ideal value which was attributed to the

addition of solute in the Mg-4Al alloy and the strong basal texture in the unalloyed Mg. Strongly textured materials usually contain many low angle boundaries of low energy which leads to a reduced driving force for grain growth during annealing.

8.3. Recommendations For Future Work

Based on the results and conclusions discussed throughout this dissertation, the following recommendations are made for future work:

1. In this study, it was determined that for a given plastic strain amplitude, the fatigue life was independent of grain size and decreased with the addition of Al. It is generally accepted that both twins and cracks initiate from regions with high internal stresses (or stress concentrations) and therefore, a more thorough investigation on fatigue damage development during LCF should be conducted. A study investigating crack initiation and propagation as a result of the twinning-detwinning process should provide more insight on the role of twin boundaries, twin tips as well as grain boundaries on crack initiation and growth during LCF. Understanding the influence that both grain size and alloying have on cyclic damage accumulation will provide a quantitative analysis on fatigue life. Favorable crack initiation sites such as twin tips, twin and grain boundaries and other microstructural features such as hard and soft grains and texture can be identified in this study. These experiments could then be used to further improve predictive models on crack initiation and growth during LCF.
2. In-situ HEXD experiments provided critical information on the cyclic stress-strain behavior in both fine-grained unalloyed Mg and Mg-4Al, however, experiments involving the coarse-grained condition should be performed to provide further

insight on grain size effects on twin volume fraction evolution during LCF as well as the stresses needed to initiate twinning and exhaust detwinning. These experiments could be used to create CPFE models that accurately predict grain size influence on CSS behavior during LCF of Mg. Currently there are no CPFE models that examine the influence of solute on the CRSS needed for twin initiation in Mg and the current grain size models only examine twin behavior during monotonic experiments and not cyclic tests. CPFE models that expand on the stresses needed for twin initiation during fatigue in both solute and solute-free Mg alloys is required in order to accurately predict the LCF and CSS behavior of these materials.

3. An important next step is to use analytical models such as the Cahn Model to quantify static recrystallization and grain growth kinetics in Mg-4%Al and Mg-0%Al (unalloyed Mg) as well as Mg-Al alloys at lower concentrations such as 0.5-2wt%. This will provide comparative information between 0wt% and 4wt% and lower concentrations to determine trends in the $t_{0.5}$, driving force and grain boundary mobility for recrystallization as well as the grain boundary mobility for grain growth.
4. The addition of Al had a minimal effect on recrystallization at 250°C in magnesium. However, it was determined that twins play an important role in the RX kinetics in both materials. Since the materials used in this study were in the as-cast condition, an important next step would be to use either synchrotron diffraction or EBSD to study the twin volume fraction evolution that occurs during monotonic compression tests in this condition.

5. Grain growth studies found that grain growth was significantly retarded with the addition of Al solute and the observed behavior was attributed to the solute drag effect. During solute drag, solutes segregate at grain boundaries and when the diffusivity of the solute atoms is slower than that of solvent atoms, the grain boundary must drag the solute atoms along resulting in a lowered grain boundary mobility. To confirm the solute drag hypothesis, scanning transmission electron microscopy (STEM) combined with energy dispersive spectroscopy (EDS) mapping should be used to experimentally determine if solute segregation is the reason for the reduction in grain growth for the Mg-4%Al alloy. Atom probe tomography can also be used to study solute segregation at grain boundaries since the technique provides elemental distribution information. This would provide a more quantitative understanding of the reduction in grain growth as well as provide a mechanism for the observed behavior. The grain boundary migration in the presence of solute segregation can also be examined using phase field simulations, where the effects of solute drag on grain boundary velocity and grain-size distributions can be calculated.

APPENDIX A
CRYSTAL PLASTICITY FINITE ELEMENTS SIMULATION OF TWINNING AND DETWINNING BEHAVIOR OF UNALLOYED MG DURING CYCLIC LOADING

AUTHORED BY MOHAMMADREZA YAGHOOBI, PRISMS CENTER, UNIVERSITYOF MICHIGAN

A.1. Introduction

Crystal plasticity simulation of cyclic behavior of HCP materials is a great challenge in material science due to the complexity of the twinning and detwinning phenomena occurring during the cyclic loading. Accordingly, not many researchers have investigated this topic. Guillemer et al incorporate a mean fields model and a crystal plasticity based constitutive model to capture cyclic behavior of extruded Mg by incorporating a twinning –detwinning model [2]. Qiao et al incorporated the elasto-viscoplastic self-consistent (EVPSC) model and incorporated a twinning-detwinning model to capture the cyclic behavior of Mg alloy ZK60A [3]. Here, the crystal plasticity simulation (CPFEM) is incorporated along the twinning-detwinning model to capture the cyclic behavior of unalloyed Mg. The PRISMS-Plasticity code is incorporated, which is a parallel open-source numerical framework for implementing continuum and crystal plasticity models [1]. For PRISMS-Plasticity crystal plasticity code, HCP, BCC and FCC single crystal elasto-plastic constitutive models are implemented. The material deformation is solved based on a constitutive response driven by mechanisms of dislocation slip, twinning and crystal reorientation. Ganesan presented the implemented framework of crystal plasticity finite element including the theory and implementation [1].

A.2. Twinning model

The crystallography of a twinning phenomenon is depicted in Fig. A.1 which shows the parent grain and the twinned region and their corresponding orientations. The incorporated twinning-detwinning model is the extension of the Predominant Twin Reorientation scheme (PTR) developed by Tomé et al. [5]. The kinematics of the twinning model is shown in Fig. A.2. The PTR method is extensively elaborated by Staroselsky and Anand [4]. Here, the PTR scheme is extended to capture both twinning and detwinning in the framework of crystal plasticity finite elements (CPFEM). In the case of CPFEM, the twinning-detwinning model is applied for all quadrature points. In the absence of twinning-detwinning, the plastic deformation gradient tensor $\mathbf{F}^p$ can be obtained as follows:

$$\mathbf{F}^p(\tau) = \boldsymbol{I} + \sum_i \Delta\gamma^i \, \boldsymbol{S}_\mathbf{0}^i \tag{A.1}$$

Where $\Delta\gamma^i$ is the slip increment of the ith slip system, and $\boldsymbol{S}_\mathbf{0}^i$ is the Schmid tensor for the ith slip system. τ is the psudo-time incorporated to numerically integrate the rate-independent model using an iterative procedure [1]. In the case of model with twinning-detwinning, the basic kinematic expression of crystal plasticity presented in Eq. (A.1) is modified to include twinning as follows:

$$\mathbf{F}^p(\tau) = \boldsymbol{I} + \sum_i \Delta\gamma^i \, \boldsymbol{S}_\mathbf{0}^i + \sum_\alpha \Delta\gamma^\alpha \, \boldsymbol{S}_\mathbf{0}^\alpha \tag{A.2}$$

where $\Delta\gamma^\alpha$ is the slip increment of the αth twin system, and $\boldsymbol{S}_\mathbf{0}^\alpha$ is the Schmid tensor for the αth twin system. Eq. (A.2) states that the part of the plastic deformation is accommodated through the shear strain occurring in twinning slip systems. Accordingly, the total shear strain occurring in the twinning slip system α can be defined as follows:

$$\Gamma^{\alpha}(\tau) = \int_0^{\tau} \Delta\gamma^{\alpha}(t)dt \tag{A.3}$$

Finally, in the case of CPFEM, the total twin fraction in a quadrature points can be defined as follows:

$$f^{\alpha}(\tau) \equiv \frac{\Gamma^{\alpha}(\tau)}{\gamma_0} \tag{A.4}$$

where γ_0 is the twinning shear which is 0.126 for Mg. Next, the twin system with the maximum twin fraction $f^{\alpha_{\max}}(\tau)$ should be defined in each quadrature point. In the next step, $f^{\max}(\tau)$ in each quadrature point should be compared against the predefined limit ξ in a way that if $f^{\alpha_{\max}}(\tau) \geq \xi$ in a quadrature point, the crystal structure of that quadrature point should be rotated according to the crystallographic characteristics of the twin system with maximum twin volume fraction, i.e., $\alpha_{\max}$. Fig. A.3 depicts the reorientation due to twinning. In the case of a quadrature point with $f^{\alpha_{\max}}(\tau) \geq \xi$, following steps should be conducted:

- The rotation matrix that brings the crystal coordinates to sample coordinates, i.e., $\mathbf{R}_1$ should be obtained from the initial quadrature point Rodrigues vector.
- The rotation matrix to apply the rotation on crystal frame about the twin system with maximum twin volume fraction i.e., $\mathbf{R}_{\alpha_{\max}}$, should be calculated as follows:

  $$\mathbf{R}_{\alpha_{\max}} = 2\boldsymbol{n}_{\alpha_{\max}} \otimes \boldsymbol{n}_{\alpha_{\max}} - \boldsymbol{I} \tag{A.5}$$

  where $\boldsymbol{n}_{\alpha_{\max}}$ is the normal vector corresponding to the twin system with the maximum twin fraction $f^{\alpha_{\max}}(\tau)$.
- The resulting rotation matrix $\mathbf{Q} = \mathbf{R}_1 . \mathbf{R}_{\alpha_{\max}}$ should be calculated.

- The rotation matrix $\mathbf{Q}$ should be converted to the fundamental region and then Rodrigues vector. The newly calculated Rodrigues vector is the new crystal crystallographic character for the twinned quadrature point.

In the case of cyclic loading, two separate governing equations are incorporated to capture twinning and detwinning, both following the twinning model presented here, but with two different sets of twin parameters of critical twinning volume fraction of ξ and initial critical resolved shear stress s_0. In other words, ξ^T and s_0^T governs the twinning procedure, and ξ^{DT} and s_0^{DT} controls the detwinning evolution. Based on the current experimental observations, twinning is occurring during the compressive part of the loading cycle while detwinning is occurring during the tensile loading. Accordingly, the twinning model captures the compressive loading, while the detwinning model governs the tensile part of the loading cycle. Furthermore, the detwinning evolution law is solely applied to those quadrature points which has been twinned. In this work, the values of $\xi^T = 0.1$ and $\xi^{DT} = 0.05$ is selected to capture the twinning-detwinning phenomena in unalloyed Mg during the cyclic loading.

The critical resolved shear stress hardening can be defined as follows [1]:

$$h^{\alpha\beta}(\tau) = \begin{cases} \text{If } \alpha = \beta \;\; \rightarrow \;\; h_0^\alpha \left[1 - \dfrac{s^\alpha(\tau)}{s_s^\alpha}\right]^{\theta^\alpha} \\ \text{If } \alpha \neq \beta \;\; \rightarrow \;\; h_0^\alpha q \left[1 - \dfrac{s^\alpha(\tau)}{s_s^\alpha}\right]^{\theta^\alpha} \end{cases} \tag{A.6}$$

where h_0^α denotes the initial self-hardening rate, $s^\alpha(\tau)$ is the critical resolved shear stress for slip system α, s_s^α is the saturation critical resolved shear stress for slip system α, θ^α is the exponent governs the saturation rate for the slip system α, and q is the latent hardening parameter, which is selected as 1.1 in the current work. Table A.1 presents the

parameters incorporated to model the cyclic behavior of unalloyed Mg. One should note that the required critical resolve shear stress to activate detwinning is lower than that of the twinning [3].

A simple backstress model is incorporated to capture the kinematic hardening of uniaxial cyclic loading. In this model, at strains at which the sign of loading changes, the critical resolved shear stress value of the slip (or twinning) system α, i.e., s^{α}, are governed as follows:

$$s^{\alpha} = s_0^{\alpha} + \chi(s^{\alpha} - s_0^{\alpha}) \tag{A.7}$$

where χ is the backstress factor. In the current work, the backstress value of $\chi = 1$ is incorporated. Due to the simplicity of the implemented kinematic hardening models, the simulation takes some cycle to stabilize the response. Accordingly, the model can capture the stabilized cyclic behvaiour of unalloyed Mg sample and not the initial cycles. The implementation of a more general kinematic hardening to capture the initial cycles is under study research.

In the case of CPFEM simulation, a cubic sample with the unit dimension is discretized using a $4\times4\times8$ mesh network. Each grain orientation, which is obtained using the EBSD data of the fine grained unalloyed Mg, is assigned to a quadrature points to reproduce the microstructure of the unalloyed Mg sample. The simulation is then performed using the implemented twinning-detwinning model in PRISMS-Plasticity crystal plasticity code. The cyclic loading is then applied with the total strain amplitudes of 0.75%.

Fig. A.4 compares the stabilized stress-strain loop of experiment versus the CPFEM simulation for tests conducted at a total strain amplitude of 0.75%. The results

show that the simulation can capture most of the features of the experimental results. The biggest deviation is the difference between the simulation and experiments during the start of unloading, which the slope is different. This is the topic under research which is tried to be handled using more appropriate kinematic hardening. Fig. A.5 compares the experimental x-ray peak intensity of the basal {0002} peak versus twinning volume fraction obtained from CPFEM simulation in the case of the stabilized loop for test conducted at a total strain amplitude of 0.75%. The CPFEM simulation capture important aspects of experiment including starting from residual twins, following by detwinning and next another twinning cycle, and finally a detwinning phase. CPFEM captures many aspects of the cyclic curve corresponding to the stabilized cycle. However, more accurate kinematic hardening should be implemented to capture the initial cycles accurately.

Figures

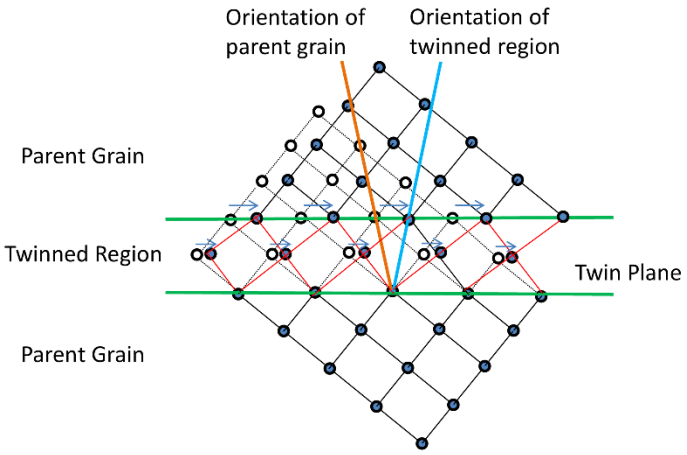

Figure A.1. Crystallography of twinned region [1]

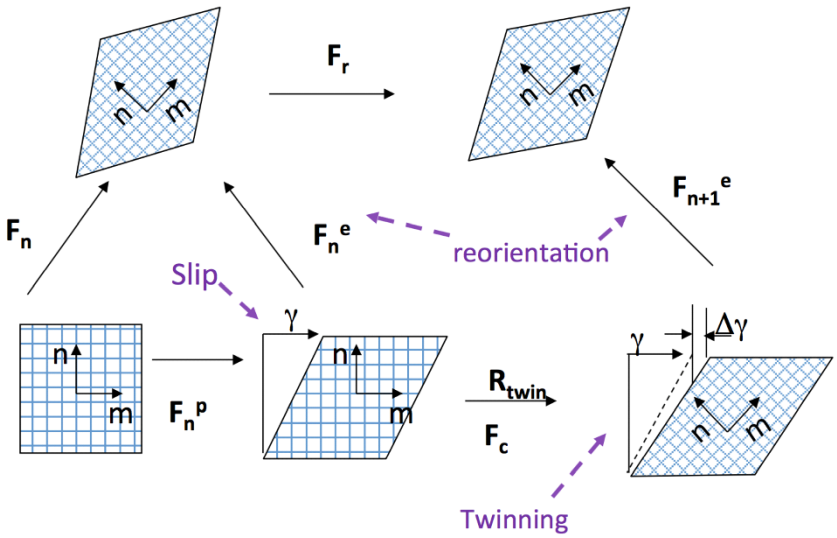

Figure A.2. Kinematics of slip and twinning [1]

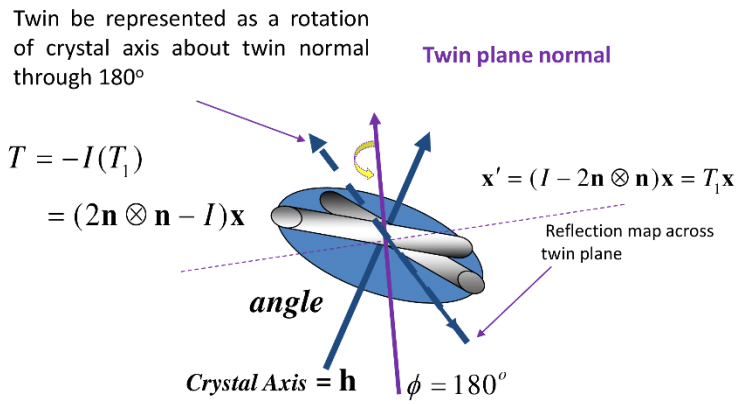

Figure A.3. Reorientation due to twinning [1]

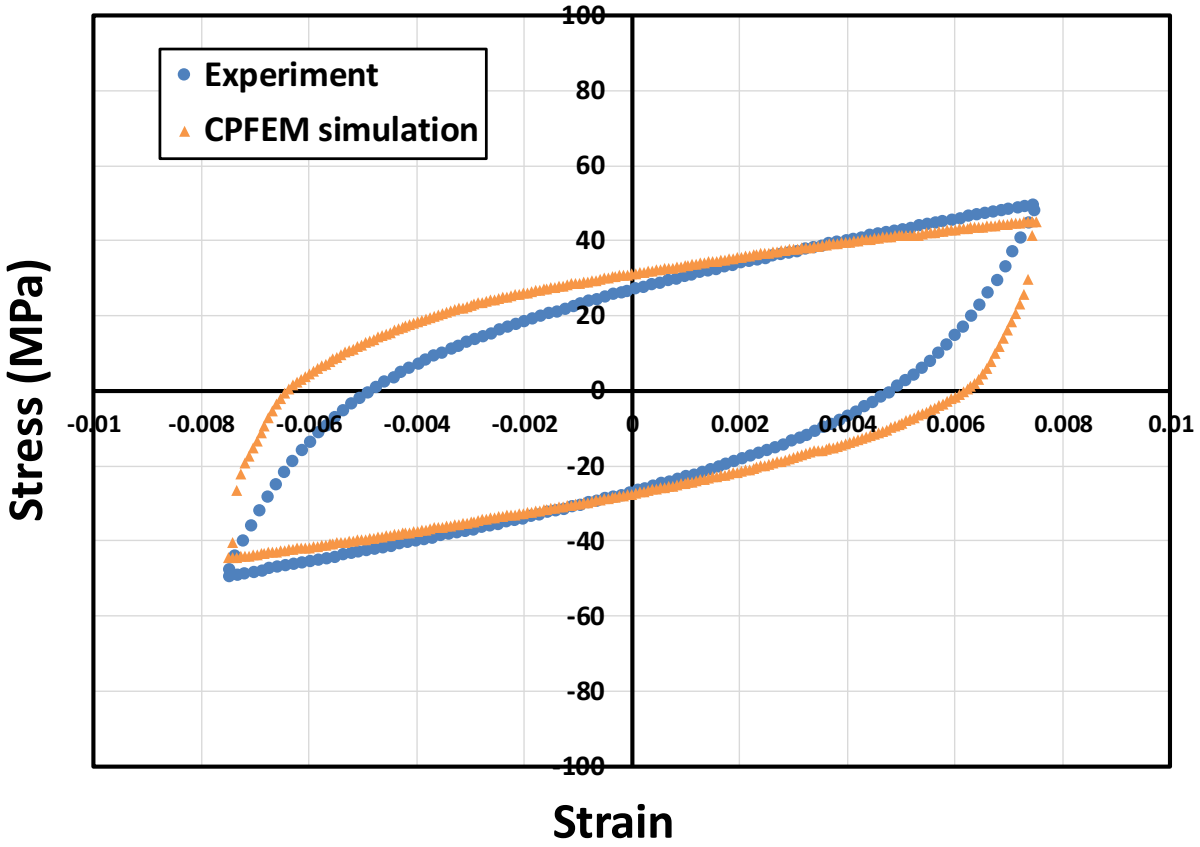

Figure A.4. Stabilized stress-strain loop: Experiment versus the CPFEM simulation for tests conducted at a total strain amplitude of 0.75%.

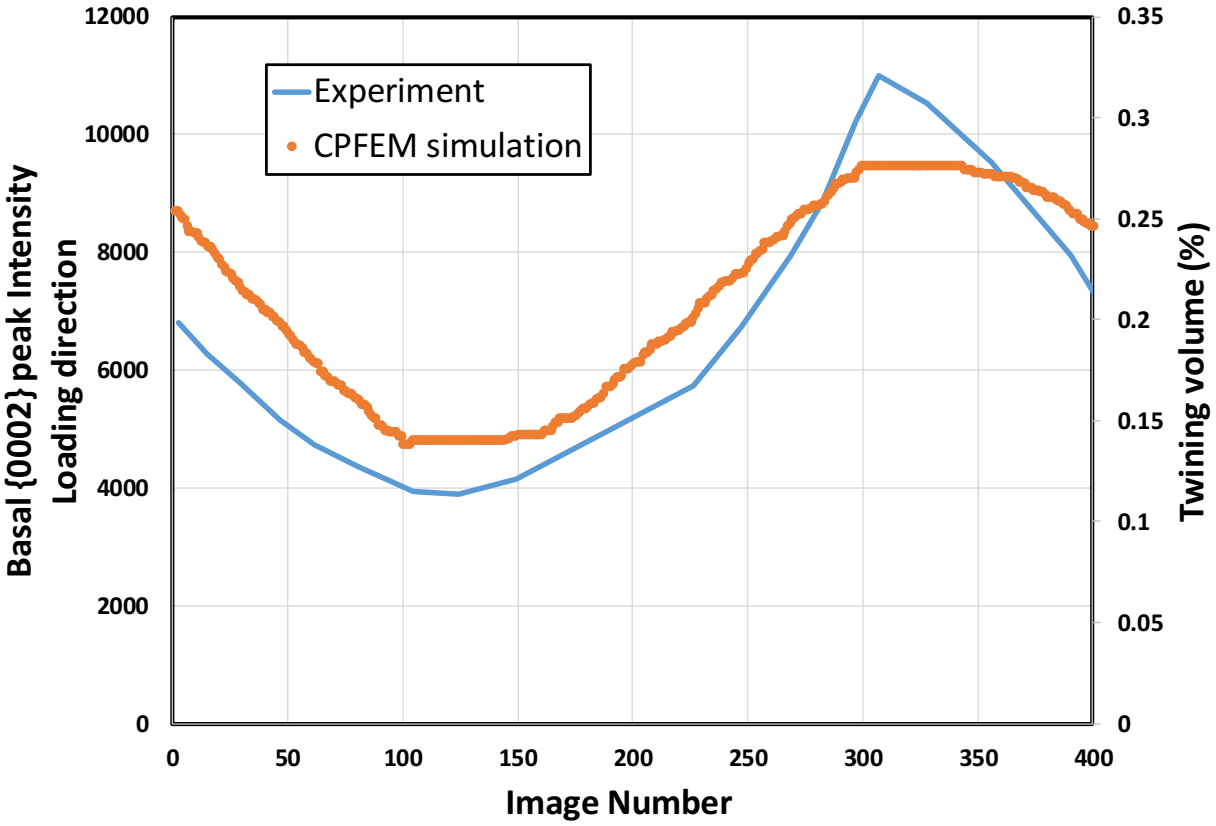

Figure A.5. Comparison between the experimental x-ray peak intensity of the basal {0002} peak and twinning volume fraction obtained from CPFEM simulation in the case of the stabilized loop for test conducted at a total strain amplitude of 0.75%.

Table. A.1. Crystal plasticity parameters of unalloyed Mg for different slip and twin system.

Mode	s_0^α (MPa)	h_0^α (MPa)	s_s^α (Mpa)	θ^α
Basal	0.5	10	20	0
Prismatic	8	100	60	2
Pyramidal<a>	8	300	60	2
Pyramidal<c+a>	40	100	155	2
Twinning	7	1000	-	0
Detwinning	3.5	1000	-	0

References

1. S. Ganesan, Microstructural Response of Magnesium Alloys: 3D Crystal Plasticity and Experimental Validation. University of Michigan, 2017.
2. C. Guillemer, M. Clavel, G. Cailletaud, Cyclic behavior of extruded magnesium: Experimental, microstructural and numerical approach. International Journal of Plasticity 27 (2011) 2068–2084.
3. H. Qiao, S.R. Agnew, P.D. Wu, Modeling twinning and detwinning behavior of Mg alloy ZK60A during monotonic and cyclic loading. International Journal of Plasticity 65 (2015) 61–84.
4. A. Staroselsky, L. Anand, A constitutive model for hcp materials deforming by slip and twinning: application to magnesium alloy AZ31B, International Journal of Plasticity 19 (20013) 1843-1864.
5. C. Tome, R.A. Lebensohn, U. Kocks, A model for texture development dominated by deformation twinning: application to zirconium alloys, Acta Metallurgica Et Materialia, 39 (1991) 2667-268.

APPENDIX B
ADDITIONAL FIGURES

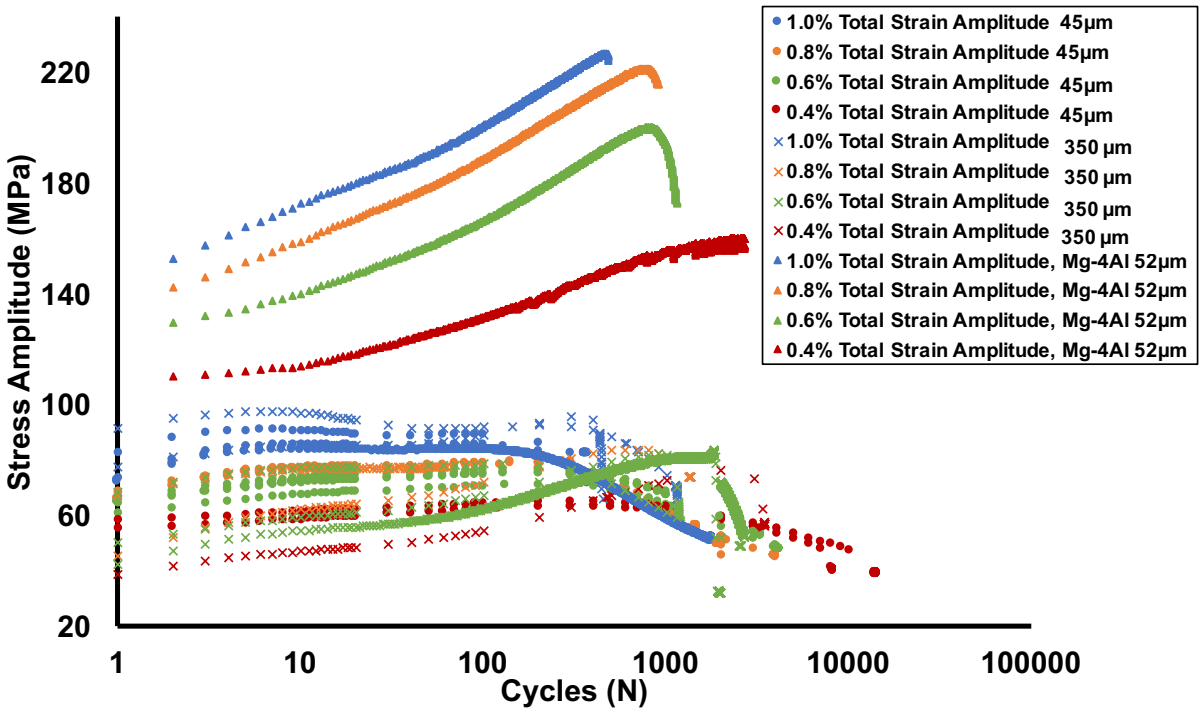

Figure B.1: A comparison of stress amplitude vs number of cycles for the 45µm and 350µm unalloyed Mg conditions and Mg-4Al showing the difference in hardening behavior between the two conditions at each total strain amplitude

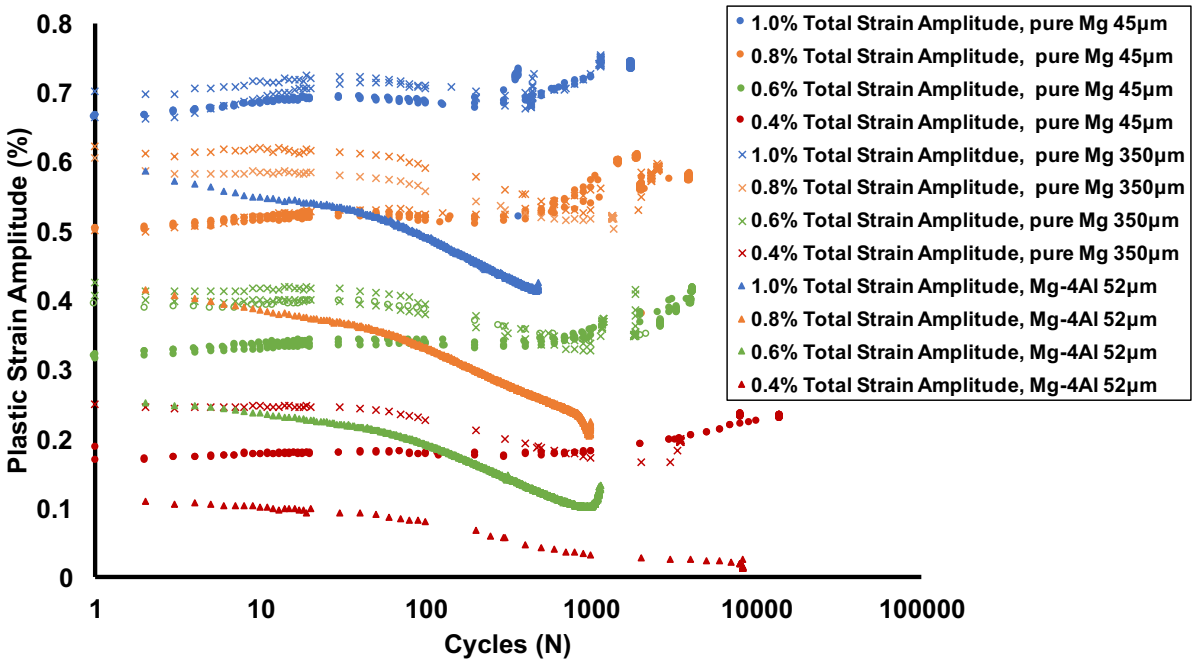

Figure B.2: A comparison of the plastic amplitude vs number of cycles for the 45µm and 350µm unalloyed Mg conditions and Mg-4Al showing the difference in hardening behavior between the two conditions at each total strain amplitude